UNIVERSITY OF
BIRMINGHAM

Fatigue crack propagation threshold in lamellar TiAl alloys

By

JING YANG

A thesis submitted to the University of Birmingham

For the degree of

DOCTOR OF PHILOSOPHY

School of Metallurgy and Materials

University of Birmingham

November 2014

Abstract

In the present study, the effect of lamellar spacing, volume fraction of equiaxed gamma grains and lamellar orientation on fatigue crack propagation threshold have been assessed for three as-cast γ-TiAl alloys, Ti45Al2Mn2Nb1B (4522XD), Ti45Al2Mn2Nb (4522) and Ti46Al8Nb (at %). The influence of alloying elements, Nb and Ta on fatigue threshold was also studied with five forged alloys, Ti45Al2Mn2Nb1B, Ti45Al2Nb2Ta1B, Ti45Al2Mn2Ta1B, Ti45Al2Mn4Ta1B and Ti45Al2Mn4Nb1B. The fatigue crack propagation threshold tests were carried out at 650°C in air at a stress ratio R=0.1 and frequency of 10HZ. In addition, the microstructural characterisation of fatigue crack growth fracture surface was also examined by SEM.

The samples assessed for fatigue crack propagation threshold failed mainly by translamellar fracture and interlamellar fracture. Interlamellar cracking occurs in lamellar colonies at any lamellar orientation at high stress intensity factor, ΔK, while at low ΔK cracking occurs in lamellar colonies only when the lamellar interface is parallel to the fracture plane. Therefore, the fracture behaviour is determined by both lamellar orientation and ΔK.

The fatigue crack propagation threshold shows little sensitivity to lamellar spacing and volume fraction of equiaxed gamma grains with 4522XD variants in the studied range. However, it shows a strong dependence on lamellar orientation with coarse-grained 4522 and Ti46Al8Nb. The highest threshold was obtained in lamellar colonies with the lamellar interface parallel to the stress axis while low threshold was obtained in colonies with an orientation about 30º-50º to the stress axis. The results show that slip or twinning parallel to

a lamellar interface may help to open up new cracks ahead of the main crack by intersection with cross-lamella slip or twinning. The alloying elements, Nb and Ta do not influence the fatigue properties for samples with similar microstructures, confirming that the fatigue properties are controlled mainly by microstructure and that composition is of secondary importance.

ACKNOWLEDGEMENTS

I wish to express my deepest gratitude and appreciation to my supervisors, Dr. D. Hu and Dr. H. Y. Li, in the first place for giving me this great opportunity to have this amazing experience of study. Thanks for their patient supervision, excellent guidance, constant encouragement and continuous support throughout the research and study. I also would like to thank School of Metallurgy and Materials for the provision of research facilities, EPSRC for the Dorothy Hodgkin Postgraduate Awards and Rolls-Royce Plc. for additional financial support.

Special thanks must go to Prof. M. H. Loretto for his valuable advice and his precious time to read this thesis. The involvement of M. Dixon, A. Huang and N. Martin from Royce-Rolls Plc. was extremely beneficial to the project and I wish to express my appreciation for their helpful discussions. I am grateful to Dr T. Doel and Mr. D. Price for training and assistance of the mechanical testing. I also wish to thank the staff within EM centre, Dr. M. Chu, Mr. P. Stanley and Mrs. T. Morris for their training for the electronic microscopes. I am appreciative of all the technical staff for their help and assistant.

Finally, I would like to thank my parents for their constant love and support. Many thanks to my friends and colleagues during my time in University of Birmingham for their friendship, kindness and encouragement.

Table of Contents

Chapter 1. Introduction

Titanium aluminides have been studied for over twenty years because their low density, high specific strength and good oxidation resistance suggested that they would be excellent materials for low pressure turbine blades. GE formally announced that two stages of GEnx (General Electric Next-generation) LPT (low pressure turbine) blades would be in TiAl material in 2006 and the engine was certified in the following year with TiAl blades. Rolls-Royce also defined a strategy to apply TiAl in their Trent XWB LPT blades using the alloy Ti45Al2Mn2Nb1B (Ti4522XD), which is the main alloy studied in this thesis.

Due to the intrinsic brittleness of TiAl material, the design method for TiAl applications is based on damage tolerance of the material and fatigue crack growth threshold is the most important property. Previous research in this area was mainly focused on the effect of microstructure on crack propagation under various stress conditions in a number of individual alloys. The major conclusion was that the lamellar microstructure offers better crack propagation resistance than other microstructures such as duplex and near gamma microstructures. In this earlier work there was little emphasis on cross-alloy studies on crack propagation behaviour because almost all the properties in TiAl are sensitive to microstructures and it is difficult to obtain identical microstructures in different alloys. Therefore, the work described in this thesis aims to achieve a fundamental understanding of factors which influence the FCG threshold properties in a number of alloys which have either different composition, closely similar microstructures or same composition, different microstructural parameters.

Chapter 2 presents the overall literature review including a general introduction to intermetallics and titanium aluminides (TiAl) including crystallography, phase diagrams, microstructure and mechanical properties. Since the fatigue crack propagation threshold is the main topic of this thesis, the literature review on fracture mechanics in fatigue and fracture, and the fatigue crack propagation behaviour in TiAl alloys is highlighted. As Ti4522XD and Ti46Al8Nb are the main alloys in this study, an introduction to these two alloys is given after that. Finally, the background and the aim of this project are summarised.

Chapter 3 describes the experimental methods used in this project, which includes the materials and the main analytical methods. Ti4522XD is the baseline alloy, and four modifications containing Nb and Ta are studied to assess the effect of alloying elements on properties. Different heat treatments were carried out to provide different microstructures. Both coarse Ti4522 and Ti46Al8Nb have been studied in order to define the effect of lamellar orientation. The details on sample preparation, microstructural analysis, mechanical tests and fractography are described.

The results and discussion are divided into three chapters considering the different studies on fatigue crack propagation threshold. In Chapter 4, the microstructure and mechanical properties of the main alloy Ti4522XD with slightly to moderately different lamellar microstructures are presented. The mechanisms of fatigue crack propagation behaviour of TiAl alloys and the microstructural characterisation of fracture surfaces are discussed. The comparison of different microstructures was designed to study the influence of lamellar spacing, colony size and volume fraction of equiaxed gamma grains on fatigue crack propagation threshold. In Chapter 5, five alloys with different compositions but similar microstructures are presented. The effect of alloying elements Nb and Ta on both tensile

properties and fatigue crack propagation threshold are given. In Chapter 6, the microstructures of coarse Ti4522 and Ti46Al8Nb are presented, and the influence of lamellar orientations of fatigue testing samples of both alloys is determined. The test results and the relationship between lamellar orientation and fatigue threshold are given. Possible mechanisms of lamellar orientation effect on fatigue threshold are discussed.

The main findings and conclusions are summarised in Chapter 7 together with suggestions for future work which could be carried out for further understanding in the research area.

Chapter 2. Literature review

2.1 Introduction

2.1.1 Intermetallics

Intermetallics, or intermetallic compounds are clearly defined as the solid phases, which contain two or more metallic elements and optionally one or more non-metallic elements with different crystal structure from other constituents by Schulze in 1967 [1]. Intermetallic phases are formed when the metallic bonding between unlike metal atoms is stronger than that between the like. The intermetallic compounds, with ordered crystal structures, have particular properties which may include high strength, elastic stiffness, creep resistance and low density. However, accompanying these advantages, there are also some disadvantages. The main disadvantage, common to virtually all intermetallics is their poor deformability (brittleness). Overall, the properties of intermetallics are between those of metals and ceramics.

2.1.2 Titanium aluminides

Titanium aluminides are recognized as the most promising candidate materials for low pressure turbine blade because of their low density, high elastic modulus, excellent oxidation and creep resistance and good high temperature strength. There are four types of titanium aluminides in the TiAl system: α_2-Ti_3Al, γ-TiAl, $TiAl_2$ and $TiAl_3$, depending on their Ti/Al ratio, with their own ordered crystal structure. However, $TiAl_2$ and $TiAl_3$ compounds get least attention, while γ-TiAl and α_2-Ti_3Al are the main intermetallics which have been the subject

of intensive investigations for over twenty years. Table 2.1 illustrates the comparison of physical and mechanical properties of titanium alloys, titanium aluminides and nickel-based super alloys [2]. Obviously, compared with titanium alloys and Ti_3Al based alloys, γ-TiAl based alloys show better high temperature properties, and the operational temperature can be over 750°C, which makes it possible to replace some nickel-based superalloy components in aircraft turbine engines. Nevertheless, due to the intrinsic brittleness of TiAl-based alloys, they suffer from low room temperature ductility, poor fracture toughness and high crack growth rate, which increase the possibility of failure, and design of components made from these alloys has to take these factors into account.

The compressor, the combustion chamber and the turbine make up a gas turbine engine. For each part, there is a particular function and a specific material requirement. The primary categories of the materials used in turbine engine are nickel-based superalloys, high strength steels and titanium alloys, as shown in Fig.2.1[3]. Titanium alloys are normally used in the compressor section of the engine near the air inlet as their operating temperature is well below 600°C, while nickel-based superalloys are used as the compressor blades in the hottest and high-pressure part of the compressor and also as the turbine blades. Titanium aluminides are the potential alloys for some components, such as low pressure turbine blades and high pressure compressor stators. In fact Ti48Al2Cr2Nb (Ti4822) has been used in the latest engines by GE recently and Ti45Al2Mn2Nb with addition of B (Ti4522XD) will be introduced as low pressure turbine blades by Rolls-Royce. Apart from aerospace, TiAl alloys are also used in the automotive industry. The most successful application of titanium aluminides is that more than 20,000 turbochargers have been fitted to top of the range Lancia cars in Japan by the end of 2003. The alloy is melted using a cold wall furnace and the

turbochargers are cast using counter gravity casting, which builds up experience of casting technology, and eventually, safety-critical components can be manufactured by this route. Thermo-mechanically processed valves have been used in Formula 1 cars for many years (where cost was not an issue), but revised Formula 1 regulations no longer allow their use. Engine tests show that TiAl valves will give a power increase over stainless steel valves of 8% due to the increase in rpm allowed. However, the costs of TiAl valves are significantly higher than those of 21-2N steel for normal cars because of the large amount of scrap and the increasing cost of raw materials [4, 5]. With the developments of casting and melting achieved by the aerospace industry these problems will no doubt soon be overcome.

2.2 Gamma titanium aluminide (γ-TiAl) based alloys

As mentioned above, there are three main intermetallics in the TiAl system: γ-TiAl, α_2-Ti_3Al and $TiAl_3$. Nevertheless, gamma titanium aluminides (TiAl-based alloy), normally, refer to alloys that contain both single phase (γ) and two phases (γ and α_2) [6]. Therefore, the crystallography of these two main phases is reviewed.

2.2.1 Crystallography and phase diagram

According to the accepted binary Ti-Al phase diagram by Schuster in 2006 [7] (Fig.2.2), the two phases α_2-Ti_3Al and γ-TiAl exist over a wide range from about 22% to 55% at.% Al. In the region of interest, there are two peritectic reactions $L + \alpha \rightarrow \gamma$, $L + \beta \rightarrow \alpha$ and one eutectoid reaction $\alpha \rightarrow \alpha_2 + \gamma$. Because of the poor ductility and fracture toughness of single phase γ, attention has been focused on two-phase γ-based alloys, consisting of α_2 as a minor phase.

The crystal structures of α_2-Ti_3Al and γ-TiAl are shown in Fig.2.3[8]. α_2-Ti_3Al has an ordered Strukturbericht Designation $D0_{19}$ hexagonal crystal structure with a composition in a range of 22-39% at.% Al content. TiAl is the γ phase, and it has an ordered $L1_0$ face-centred crystal structure up to its melting point at about 1460°C which can exist with the aluminium content in a range of 48.5-66%. The α_2 phase and γ phase follow Blackburn's orientation relationship [9] during solid phase transformation:

$\{111\}\ \gamma\ //\ (0001)\ \alpha_2;\ <110>\gamma\ //\ <11\bar{2}0>\ \alpha_2$

2.2.2 Microstructures of titanium aluminides

Generally, gamma titanium aluminides are categorized into two groups – single γ phase alloys and two-phase ($\alpha_2 + \gamma$) alloys. The properties of single phase alloys cannot be changed by heat treatment in the way that multiphase alloys can and single phase alloys are therefore not useful for commercial application due to their low ductility and fracture toughness. Normally, after different heat treatment, a two-phase γ-TiAl has four distinctive types of room temperature microstructures, near γ (termed NG), duplex (termed DP), near lamellar (termed NL) and fully lamellar (termed FL), as shown in Fig.2.4 [10]. The mechanical properties of TiAl alloys are strongly dependent on their microstructure. Therefore, it is important to understand the characteristics of these microstructures.

2.2.2.1 Near γ microstructure

NG microstructure, consisting of equiaxed γ grains and a few α_2 grains, is obtained by hot working and subsequent heat-treatment at a temperature where the γ phase is the dominant phase, just above the eutectoid temperature [10]. The NG structure has poor fracture

toughness and poor elevated-temperature properties. The homogeneity of the NG microstructure depends strongly on the chosen hot working conditions.

2.2.2.2 Duplex microstructure

Heat-treatment in the (α + γ) phase region, after hot working, at a temperature where the volume fractions of γ phase and α phase are approximately equal leads to a duplex (DP) microstructure, which is composed of equiaxed γ grains and lamellar colonies. The growth of both γ grains and α grains is limited as expected in a two-phase alloy. Therefore, the competitive growth results in a fine mixture of grains. The α grains transform into lamellar colonies during cooling. The duplex microstructure, with homogeneous and fine grains, has the highest strength and best ductility but the poorest fracture toughness [11].

2.2.2.3 Near lamellar microstructure

Heat treatment near but below $T_{\alpha,}$ (α transus) where the predominant phase is α or slow cooling after solution treatment in the α phase region [4] leads to a near lamellar microstructure (NL). NL microstructure is composed of lamellar colonies, consisting of α_2 and γ plates following the Blackburn orientation relationship, as the dominant constituent and fine equiaxed γ grains as the minor phase at lamellar colony boundaries.

2.2.2.4 Fully lamellar microstructure

Heat treatment above T_α and not very slow cooling leads to a fully lamellar microstructure (FL) with large lamellar grains [10]. The fully lamellar microstructure has good fracture toughness and creep resistance, but reduced strength and ductility compared to duplex microstructures, because of its large grain size. It has been established that these alloys with a

fine fully lamellar (FFL) microstructure exerts good balanced mechanical properties such as strength, toughness and ductility. Therefore, grain refinement of fully lamellar microstructure is very important.

A lot of work has been done to control the grain size. By small additions of B, the grain size can be refined and also the homogeneity can be improved [12-15]. Alloy elements, such as Ta, Nb, W and Al concentration, also affect grain refinement in TiAl-based alloys [16]. Thermo mechanical treatment, such as control of cooling and heating rate, is used to obtain a fine lamellar microstructure [17-19]. In addition, different cooling rates can also produce different microstructures, such as massive, feathery, Widmanstätten lamellar, lamellar or granular gamma, as shown in Fig.2.5 [20].

2.2.3 Development of gamma titanium aluminides and effects of alloying elements

2.2.3.1 Development of gamma titanium aluminides

During the early 1950s, American researchers found the outstanding high temperature properties of binary alloy Ti-50Al, but the research was given up because of the low room temperature ductility. After intensive investigations of alloys with different compositions, a two-phase TiAl alloy, Ti-48Al-1V (0.1C) (at %), which shows an elongation up to 2% at room temperature was developed by Blackburn in the early 1980s. However, the overall properties of this alloy were not competitive with the aerospace engine materials at that time. Extensive research was carried out in late 1980s and early 1990s and several alloys based on Ti-(44-48)Al were found of engineering importance, such as Ti-48Al-2Nb-X (X=Cr, Mn, V, etc.) and their modifications. A new TNB alloy family with high content of Nb, having a

general composition of Nb about 5–10 at.% with small addition of C or B was studied for their superior mechanical performance compared to traditional TiAl based alloys, and its foreign object damage (FOD) tolerance appears even better than the nickel alloy IN718 [21, 22]. A TNM alloy, with the composition of Ti-(42–45)Al-(3–5)Nb-(0.1–2)Mo-(0.1–0.2)B), was designed to offer a better hot working capability with the benefit of removing most of the beta phase through heat treatment for improved creep resistance [23, 24]. Ti-46Al-8Ta is a cast alloy, developed around 2007, transforming massively from alpha to gamma at low cooing rates, allowing samples up to 20mm in diameter to have fully massive gamma microstructures after air cooling which could be converted into fine convoluted microstructures through simple ageing or HIPping to improve room temperature ductility [25, 26].

2.2.3.2 Alloying effect on properties

The properties of TiAl alloys which are affected by alloying can be divided into two groups according to the apparent effectiveness of alloying. In one group the properties show obvious improvement after alloying regardless of their microstructures. These properties are oxidation/corrosion resistance, creep resistance and tensile strength and ductility in the case of precipitation hardening. Even though the creep resistance of TiAl alloys is strongly dependent on microstructure, the alloying effect is still applicable. Properties in another group show less alloying effect or alloying effect is closely related to microstructures. Such properties are tensile strength and ductility, fatigue strength, fracture toughness and fatigue crack growth behaviour.

The refractory elements, such as Nb and Ta are added to improve the high temperature capability of γ-TiAl alloys by enhancing high temperature strength by solid solution strengthening, increasing the oxidation resistance and creep resistance, regardless of the microstructure [27-30]. Of these elements, Nb is the most important and it improves the oxidation resistance significantly up to 900°C. The effects of Nb on oxidation can be summarised as follows: (a) Nb substitutes for Ti in TiO_2, resulting in a decrease of the concentration of oxygen vacancies, which retards the diffusion of oxygen; (b) Nb promotes the formation of TiN at the scale/subscale interface, impeding the diffusion of titanium and oxygen ions; (c) Nb increases the thermodynamic activity of Al, and thus promotes the formation of a stable alumina scale. However, when the content of Nb in TiAl alloys is too high, Nb decreases the oxidation resistance because of the formation of $TiNb_2O_7$ or $AlNbO_4$ in the scale [27, 28, 31-33]. In most researches, Ta has been found to have a weaker influence on the oxidation resistance than Nb [29, 34].

Apart from the significant improvement of oxidation resistance, these refractory elements are also reported to enhance the strength of the alloy by solid solution strengthening; especially Nb. Liu studied the effect of Nb addition on the microstructural characteristics and properties of fully lamellar, near fully lamellar and duplex microstructures. The results show that only slight influences of lamellar spacing and volume fraction of α_2 phase are caused by Nb additions of 8% and 10%, but the yield strength of TiAl-based alloys is significantly increased [35, 36]. Nb is also found to benefit creep resistance by increasing the activation energy of diffusion [37].

Small additions of Mn can improve the ductility in two-phase γ-TiAl alloys, increasing the ductility of γ-TiAl alloys for duplex microstructures at room temperature, but having no

obvious influence in single-phase TiAl alloys. One explanation is that the Mn addition occupies Al sites and reduces the *c/a* ratio by decreasing the *c* value of the γ crystal, suggesting that the covalent-like bonding is weakened. Mn is also reported to promote the formation of deformation twins. However, more Mn addition does not further enhance the properties [38].

Al has significant effects on microstructure and mechanical properties and the effects on mechanical properties are through its influence on the amount of α_2 phase, for both duplex and lamellar microstructures. With decreasing content of Al, the volume fraction of α_2 phase increases, and decrease average lamellae spacing. It was reported that with a reduced Al-content, the alloys have smaller grain size, higher yield strength and strain to fracture [30][39]. However, there is some debate whether the existence of α_2 phase or the refined microstructure contributes to the improved strength. It is reported that the fracture toughness decreases with the increase of Al content in the wrought TiAl alloys with both duplex and lamellar microstructures [40]. However, no microstructural parameters, such as colony size and lamellar spacing, were given in the reference. Therefore, it is controversial that whether Al content or microstructural parameters contribute to the influence of fracture toughness.

β-stabilising elements, such as Cr, W, Mo, Ta and Nb, can introduce a third phase, β or B2, in γ TiAl alloys. B2 phase can improve the workability of γ TiAl alloys. Moreover, it is found that the existence of B2 grains is favourable for the refinement of the microstructure and high temperature deformation. However, different elements show different beta stabilising strength. A small addition of W can give rise to the formation of B2 phase, while for the same effect, a large amount of Nb is needed. However, large additions of these elements can cause serious segregation [41].

Boron addition has a pronounced effect on grain refinement for as-cast TiAl alloys, and the critical level of boron content required to refine the grain size varies with Al concentration and alloying elements [12]. Possible mechanisms of grain refinement have been widely debated. All mechanisms for the refining of the microstructure consider the behaviour of borides or boron during solidification and the importance of the boron content. Larsen pointed out that more than 1.0 volume percent TiB_2 in Ti-47.5Al-2Nb-2Mn (at %) refined the microstructure because of the insolubility of the boride particles during melting[42]. Inkson proposed that the borides precipitated first during melting and then these precipitations served as the nuclei for the solidification [43]. Godfrey observed the shrinkage at the base of dendrite arms and inferred that the broken-off fragments of dendrites contributed to the nucleation [44]. These three mechanisms cannot explain the role of B in all alloys. Cheng proposed a mechanism based on constitutional undercooling in the liquid ahead of the solidification front associated with the different solubility of B in the liquid and solid phases. This results in the formation of borides but more importantly to the nucleation of new grains ahead of the solidification front, which leads to grain refinement [12]. Titanium borides have a significant influence on the tensile ductility of TiAl alloys. The ductility is relatively low when large sized titanium borides precipitate, which is often observed in highly-alloyed TiAl alloys (such as Ti–44Al–8Nb–1B). The large titanium borides cause premature failure in as-cast samples leading to a poor tensile ductility. Refinement of titanium boride precipitates, will give rise to a much better tensile ductility.[45].

Small additions of C and N can also refine the microstructure, thus increasing the yield strength [46]. Another important impact of C is its remarkable effect on improvement in

creep resistance through C in solution and precipitated carbides. Si can also benefit creep resistance in the same way as C, by Si in solution and by precipitating silicide [42, 47, 48].

2.3 Mechanical properties

2.3.1 Deformation mechanisms

The deformation behaviour of TiAl alloys suffers from typical characteristics of other intermetallic compounds, such as low ductility, strong dependence of yield stress on temperature (relative to the brittle to ductile transition temperature) and orientation [49, 50]. The deformation behaviour of gamma titanium aluminides is closely related to its $L1_0$ structure. Fig.2.6 [51] illustrates the potential slip and twinning systems in γ phase. Dislocation of Burgers vectors 1/2<110>, 1/2<$11\bar{2}$ > and <011> glide on {111}. Plastic deformation of γ-TiAl can also be achieved by mechanical twinning 1/6<$11\bar{2}$ > {111}.

Mercer et al. [52] found that for quaternary and quinternary TiAl based alloys, twin boundaries generated upon crack loading during fatigue, served as barriers to reversed dislocation motion during unloading. These barriers cause an increase in the irreversibility of slip when both slip and twinning occur as a crack tip deformation mechanism. It is also proposed that the fatigue crack tip deformation in quaternary and quinternary TiAl based alloys occurs either by a combination of conventional slip and twinning or solely by conventional slip, and this mechanism is determined by either alloy composition or material fabrication.

2.3.2 Tensile properties

The tensile properties of γ-TiAl depend largely on the microstructure and grain/ colony size, lamellar orientation and to a lesser extent on the alloy additions. The yield strength of TiAl alloys varies between about 300 MPa to 650 MPa at room temperature. Fig.2.7 shows the effects of microstructure and grain/colony size on the tensile properties [10]. Obviously, the reduction of lamellar colony size of FL microstructure from ~1300μm to ~250μm can increase the yield strength from ~300MPa to ~ 500MPa. This observation is also appropriate for near gamma and duplex microstructure [51]. The yield strength at room temperature indicates the Hall-Petch relationship between yield stress ($\sigma_{0.2}$) and grain size (d): $\sigma_{0.2}=\sigma_0+k_y d^{-1/2}$, thus grain size refinement can lead to strength improvement. However, for lamellar microstructures, there is some debate whether the lamellar colony size or the lamellar spacing acts as the microstructural length parameter d to affect the yield strength. The yield strength is sensitive to lamellar spacing at both room temperature and elevated temperature, exhibiting increasing strength with decreasing lamellar spacing [53].

The tensile properties are also affected by lamellar orientation. For polysynthetically twinned (PST) crystal alloys, k_y^{PST} is also determined from a relationship of φ-dependent flow stress, where φ is the angle between lamellar interface and the loading axis, as shown in Fig.2.8. As the deformation occurs on {111} planes, when the stress is applied parallel or perpendicular to the lamellar planes, φ = 0° or 90°, representing the hard orientations, the shear deformation proceeds across the lamellae. Therefore, the specimens are very strong, showing yield strength of 200-400MPa and 550-750MPa, respectively. However, when the stress is applied at intermediate angles, e.g. φ = 45°, represents the soft orientation, the shear deformation is

less or not impeded by the lamellar boundaries, low yield strength of about 100-200MPa is observed [49].

The tensile ductility of two-phase γ-TiAl is characterised by a brittle-to-ductile transition at BDTT which ranges from about 620 to 800°C for the typical strain rate of 1×10^{-4} s^{-1}, depending on the microstructure. A brittle-to-ductile transition temperature (BDTT) is defined as the temperature at which the elongation rises to 7.5% [50]. As shown in Fig.2.9, the elongation remains stable and increases gradually with increasing temperature below BDTT, but increases rapidly above BDTT. The yield strength only decreases slightly with increasing temperature below BDTT, regardless of alloy composition and microstructure. However, the yield strength drops rapidly above BDTT [51]. That is because of the acceleration of twinning when the testing temperature is over BDTT. Recrystallisation also occurs, and fine equiaxed grains are formed. Actually, the fracture mode is strongly affected by testing temperature. At low temperatures, transgranular cleavage, including translamellar cleavage and delamination is dominant although intergranular failure is still found. Around BDTT, dimples start to appear on the fracture surface and tend to take the place of transgranular cleavage. Above BDTT, dimple fracture and intergranular failure become the main fracture mode [50].

The alloying elements play a significant role in the tensile properties. As stated in section 2.2.3, the addition of Nb [35, 54, 55], Ta [54], Mo [56] and W [53] is reported to improve the tensile strength by solid-solution strengthening. Cr, Mn and V are reported to improve the ductility of TiAl alloys. Liu indicates that the increase of high temperature strength caused by high Nb content is mainly because of the stronger friction stress of moving dislocations compared with the titanium aluminides with lower Nb content [36].

2.3.3 Creep properties

The creep properties of TiAl-based alloys are strongly dependent on grain size [57-59], microstructure [60-62], alloy composition [48, 57, 62] and applied stress [60]. The addition of C, N and W improves the creep resistance of gamma titanium aluminides [48, 57, 62]. Fully lamellar forged and cast TiAl based alloys have far better creep properties than other microstructures [60-62]. Zhu found that compared to near lamellar microstructure, the stabilized fully lamellar microstructure showed a lower minimum creep rate and a longer rupture life, as a result of the lower number of γ grains. γ grains are claimed to accelerate dynamic recrystallization and onset of grain boundary sliding (GBS), therefore increasing creep strain rate [60]. Es-Souni also found fully lamellar microstructure showed the lowest creep rate but highest extent of primary creep, shown in Fig.2.10 [62]. This is because of the relaxation of the mismatch structures and coherency stresses present at the lamellar interfaces as a result of the emission of dislocations from the interfaces, as discussed by Appel [63]. Maruyama[58] studied the influence of lamellar spacing on creep strength of fully lamellar TiAl alloys, pointing out that decreased lamellar spacing leads to slow creep rate, especially at high stresses, as shown in Fig.2.11. However, the effect of lamellar spacing reduction on creep rate diminishes when the stress is lower because of the increasing contribution of dynamic recrystallisation and interface sliding. Chen [64] indicates that small lamellar spacing and planar grain boundaries increase the creep resistance, while larger lamellar spacing and interlocked grain boundaries decrease creep life, increase the minimum creep strain rate and tertiary creep strain. Especially the creep behaviour in tertiary stage is affected by the grain boundary morphology, with plannar grain boundaries susceptible to intergranular cracking.

2.3.4 Oxidation behaviour

The oxidation behaviour in γ-TiAl alloys is affected by several factors, such as alloy composition [65, 66], oxygen partial pressure and environmental atmosphere [67, 68], surface status [69] and microstructure[70]. Maurice [71] studied the initial stages of oxidation behaviour of two phase γ-TiAl alloys at 650°C under low pressure conditions and found that there were three stages in this process. The first stage is called pre-oxidation stage and it is characterised by the adsorption of oxygen species. When saturation is reached, the oxidation of aluminium occurs, which is the second stage. During the second stage, an ultrathin alumina layer forms and grows. Due to the limitation of transport of Al in the alloy, the growth kinetics of alumina layers is restricted, so Al is depleted in the metallic phase underneath the oxide. When a critical concentration ($Ti_{82}Al_{18}$ and $Ti_{75}Al_{25}$ on α_2-Ti_3Al and γ-TiAl, respectively) is reached, titanium oxidation occurs, and the third stage starts, corresponding to the oxidation of both aluminium and titanium. The oxidation behaviour also has an influence on mechanical properties in γ-TiAl alloys, such as the reduction of tensile strength and ductility at both ambient temperature and elevated temperature, especially ductility [72, 73].

2.4 Fracture mechanics in fatigue and fracture

2.4.1 Introduction of fracture mechanics

Fracture mechanics is a branch of engineering science that is concerned with failure of materials due to crack initiation and propagation. There are two fundamental approaches for fracture standards: the energy balance approach and the crack tip stress field approach [74].

2.4.1.1 Griffith's energy balance approach

Griffith's pioneering work on brittle fracture of glass in the 1920s exploited a new field of mechanics of materials, fracture mechanics. Before Griffith's work, it was known that the theoretical fracture strength of glass was based on the breaking of atomic bonds but the laboratory fracture strength was far below the theoretical fracture strength. Griffith believed that this discrepancy was due to micro cracks in the glass and these micro cracks which acted as stress concentration generators could propagate when the applied load level was far below the theoretical strength [75]. In Griffith's energy balance theory, the total energy U of semi-infinite plate of unit thickness containing a through-thickness crack of a length of $2a$ is considered to be subject to a constant tensile stress σ, as shown in Fig.2.12, and the equation is obtained as follows:

$$U = U_0 + U_a + U_r - F \qquad (2.1)$$

Where

U = Total energy

U_0 = Elastic energy of the loaded uncracked plate (constant)

U_a = Change in the elastic energy caused by introducing the crack in the plate

U_r = Change in the elastic surface energy caused by the formation of the crack surface

F = Work performed by external forces

The change of elastic energy U_a caused by inducing a crack in the plate can be formulated as:

$$U_a = (\pi\sigma^2 a^2)/E \tag{2.2}$$

where *E* is Young's modulus.

The change of elastic surface energy U_r caused by the formation of crack surface is equal to the product of the unit elastic surface energy of the material γ and the new dimension of the crack

$$U_\gamma = 2(2a\gamma_e) = 4a\gamma \tag{2.3}$$

As the glass is under the fixed grip condition, no work is done by external forces, therefore, F=0. The elastic strain energy is negative because it is released. Thus the total energy of the cracked plate is

$$U = U_0 + U_a + U_r = U_0 - (\pi\sigma^2 a^2)/E + 4a\gamma \tag{2.4}$$

As U_0 is constant, dU_0/da is zero. When the equilibrium condition is reached, dU/da is equal to zero, accordingly

$$\frac{dU}{da} = \frac{d(4a\gamma)}{da} - \frac{d\left(\frac{\pi\sigma^2 a^2}{E}\right)}{da} = 0 \tag{2.5}$$

$$2\pi\sigma^2 a/E = 4\gamma \tag{2.6}$$

The stress required to create new crack surface can be given as follows:

$$\sigma_F = \sqrt{\frac{2E\gamma}{\pi a}} \qquad (2.7)$$

where σ_F is the failure stress. This is the Griffith strength relation. When σ reaches a critical value, the crack starts to propagate. The above equation is of the same form as the theoretical fracture strength, but with an important difference. In the equation of theoretical fracture strength, *a* stands for lattice parameter, while in the Griffith equation, *a* means half length of the micro crack. Therefore, the strength obtained from the Griffith strength equation is much smaller than the theoretical fracture strength as the dimension of a micro crack is much larger than lattice parameter.

2.4.1.2 Irwin's modification to Griffith Theory

Although Griffith's theory has already provided excellent agreement with the laboratory results for brittle materials, it is usually impractical for ductile materials. In ductile materials, or even in materials which appear to be brittle, there is a plastic zone at the crack tip. Irwin's group at U.S. Naval Research Laboratory (NRL) suggested that plasticity should play a vital part in the fracture of ductile materials. Irwin's modification is to divide the energy to two parts:

$$(\pi\sigma^2 a)/E = 2\gamma + 2\gamma_p \qquad (2.8)$$

where γ_p is the plastic work.

The left hand term is defined as the energy release rate G which is the elastic energy per unit crack surface area required for crack propagation. The right hand term is defined as the surface energy needed for crack extension or the crack resistance R.

$$G = (\pi\sigma^2 a)/E \geq 2\gamma + 2\gamma_p = G_c = R \qquad (2.9)$$

Unstable crack propagation will occur when G is equal to R. Fracture will happen if G exceeds the critical level G_c. For brittle materials, $\gamma >> \gamma_p$, the plastic work can be neglected and R is mainly equal to the surface energy. For ductile materials, $\gamma_p >> \gamma$, thus the surface energy can be ignored and the plastic work dominates.

2.4.1.3 Stress intensity approach

Even though Irwin's modification has already considered the plastic energy, it still cannot explain the conditions needed for unstable and stable crack propagation. This leads to the stress intensity approach for fracture mechanics by Irwin and his group. A new method was been found to calculate the amount of stress applicable for fracture in the vicinity around the crack front in a linear elastic solid, which can be denoted as follows

$$\sigma_{ij} = (K/\sqrt{2\pi r}) f_{ij}(\theta) \qquad (2.10)$$

where σ_{ij} is the stress distribution near the crack tip; r is the distance from the crack tip, and θ is the angle with regard to the plane of the crack, as shown in Fig.2.13 [76]. f_{ij} is a dimensionless quantity depending on the load and geometry. K is the stress intensity factor, which is used to describe the stress state (stress intensity) near the crack front caused by a

distant load or residual stresses. Irwin defined the general formula of the stress intensity factor

$$K = \sigma\sqrt{\pi a}\, f(a/W) \qquad (2.11)$$

Where $f(a/W)$ is a dimensionless parameter with respect to the size of crack and specimen.

There are three modes of crack according to the applied force and deformation type, opening mode, in-plane mode and out-of-plane shear mode, as shown in Fig.2.14. K_I, K_{II} and K_{III} are designated for the stress intensity factors of mode I, II and III, the crack opening mode, crack sliding mode and crack tearing mode, respectively. The stress intensity factor K_I is shown as

$$K_I = \sigma\sqrt{\pi a} \qquad (2.12)$$

When the critical value of K is obtained, fracture occurs. Irwin showed the relationship of the stress intensity factor and the strain energy release rate for a mode I crack (opening mode) as:

$$G_I = K_I^2/E \qquad \textit{plane stress} \qquad (2.13)$$

$$G_I = K_I^2(1-\upsilon^2)/E \qquad \textit{plane strain} \qquad (2.14)$$

where υ is Poisson's ratio.

The significance of the stress intensity approach lies in the assumption that a crack starts to propagate when a unique value of K is achieved, which is material-dependent and can be measured via experiment.

2.4.1.4 Crack tip plasticity

According to equation 2.10, the elastic stress distribution at the crack front becomes infinite or approaches a singularity when the value of r approaches to zero. However, for most metals, plastic deformation will occur when the stress exceeds the yield stress of the material, and a plastic zone will appear around the crack tip. As fracture is the extension of cracks, and the energy required for the propagation of cracks is mainly consumed in the plastic work, the plastic work required increases with the size of the plastic zone. Therefore, the study of plastic zone around the crack tip is very important.

The actual crack length was supposed to be extended by a distance $r_{y,}$ the plastic zone radius, by Irwin. Thus it can be considered that the crack has a notional crack tip with a distance r_y ahead of the real crack front. For the crack under monotonic tensile loading, the plastic zone size at the crack tip was

$$r_y = \frac{1}{\pi} \cdot (\frac{K}{\sigma_{ys}})^2 \qquad plane\ stress \qquad (2.15)$$

$$r_y = \frac{1}{3\pi} \cdot (\frac{K}{\sigma_{ys}})^2 \qquad plane\ strain \qquad (2.16)$$

The circular plastic zone is with a diameter of 2 r_y, as shown in Fig.2.15 (a). As mentioned above, Irwin considered a notional crack tip ahead of the real crack tip; therefore the correction is shown in Fig.2.15 (b).

According to equations 2.15 and 2.16, it can be seen that the plastic zone size varies in a finite plate along the crack tip. At the surface of the plate, there are no stresses in the

thickness direction, so a biaxial condition of plane stress exists. Towards the centre of the specimen, there is an increasing degree of triaxiality that may eventually become plane strain. This leads to a variation of the plastic zone size and shape through the thickness of the plate, as shown in Fig.2.16.

For most metals, when the stress exceeds their yield stress, plastic deformation will occur and a plastic zone will appear around the crack tip. It is indicated that linear elastic fracture mechanics can only be applied when the plastic zone size is smaller than the crack size and the cracked body behaves in a predominantly elastic manner. Hence a more general theory, elastic-plastic fracture mechanics (EPFM) is developed when the above conditions cannot be fulfilled. Two concepts of EPFM are used, one is the crack opening displacement (COD) approach based on the crack tip strain mainly developed in UK, the other is the J integral energy balance concept largely developed in US [77].

2.4.1.5 Fracture toughness

Fracture toughness is a property which defines the ability of a material to resist fracture when a crack exists; it is one of the most important properties of a material and is very crucial to the design of engineering components. It can be expressed as K_C under plane stress conditions or K_{IC} under plane strain conditions for mode I loading. The value of K_C is a function of material microstructure, testing temperature and environment, loading mode, strain rate and stress state (plane stress or plane strain) [78]. It varies with different specimen thickness. When the thickness of the specimen reaches the plane strain state, the value of K_C approaches a stable minimum value, expressed as K_{IC}. Plain strain conditions can be reached when the thickness of the test piece is 25 times or more than the monotonic plastic zone size,

shown in Fig.2.17. Therefore, K_{IC} is considered as a material property, revealing the resistance of a material to crack propagation. It should not be affected by the specimen geometry, crack size and shape; therefore, it can be used as a criterion for the prediction of the failure of a material with different geometries.

2.4.2 Fatigue

2.4.2.1 Introduction

The word ‘fatigue’ is regarded as a terminology for the damage and failure of materials caused by the repeated application of stresses or strains, which has been known for over one hundred and eighty years since it was first studied by a German mining engineer U.A.J. Albert around 1829 [78]. Now fatigue has become a progressively common technology area of study since most of the causes of mechanical failure are because of fatigue.

The total fatigue life is composed of both crack initiation and crack propagation stages. The definition of fatigue crack initiation strongly depends on the size scale of observation. Scientists would like to consider the nucleation of flaws as the initiation of the crack, while mechanical engineers prefer to associate crack detection with the threshold for the crack nucleation. After that, there will be stable crack propagation progress until the final fracture.

For fatigue tests, the results can be shown in terms of a linear / log plot termed *S-N* curves, which present the relationship between stress amplitude (σ_a) or stress range ($\Delta\sigma$) and the number of cycles to failure (N_f), as shown in Fig.2.18. The stress range and stress amplitude are the algebraic difference between the maximum and minimum stresses and half stress range, respectively.

$$\Delta\sigma = \sigma_{max} - \sigma_{min} \tag{2.17}$$

$$\sigma_a = \frac{\sigma_{max} - \sigma_{min}}{2} \tag{2.18}$$

2.4.2.2 Fatigue crack propagation and da/dN-ΔK curve

Paris, Gomez & Anderson proposed that the fatigue crack growth rate should be based upon the stress intensity factor range Δ*K* [78].

$$\Delta K = K_{max} - K_{min} \tag{2.19}$$

K_{max} and K_{min} are the maximum and minimum values of stress intensity factor, respectively. For an edge-cracked test piece,

$$K_{max} = Y\sigma_{max}\sqrt{\pi a}$$

$$K_{min} = Y\sigma_{min}\sqrt{\pi a}$$

$$\Delta K = K_{max} - K_{min} = Y\Delta\sigma\sqrt{\pi a} \tag{2.20}$$

where *Y* is a geometrical factor for the test specimen dependent on the ratio of crack length *a* to the width of the specimen *W*. The relationship between the fatigue crack growth increment *da/dN* and stress intensity factor range Δ*K*, the Paris law relation, can be expressed as

$$\frac{da}{dN} = C(\Delta K)^m \tag{2.21}$$

where C and m are constants, which are affected by a number of factors, such as microstructure, loading frequency, testing temperature and environment, waveform and stress ratio R, expressed as the ratio of the minimum to the maximum stress or stress intensity factor.

$$R = \frac{\sigma_{min}}{\sigma_{max}} = \frac{K_{min}}{K_{max}} \qquad (2.22)$$

For most engineering materials, the plot of *log da/dN* versus *log* ΔK shows a sigmoidal shape, and the curve can be divided into three regimes: Regime A, Regime B and Regime C, as shown schematically in Fig.2.19. In Region A, the crack grows very slowly, with an average crack growth rate less than lattice spacing per cycle. When the stress intensity factor range is below a threshold value ΔK_{th}, the crack remains dormant or the crack growth rate cannot be detected. Above ΔK_{th}, the crack grows rapidly, with a steep increase of *da/dN* with ΔK. The fatigue crack propagation threshold is affected by many factors, such as microstructure, grain size, stress ratio, testing temperature and environment. Overall; the crack propagation behaviour in this region is discontinuous. Region B is known as the Paris Region, with a linear relation of *log da/dN* versus *log* ΔK, which can be expressed as the Paris equation (equation 2.21). During this period, the crack grows continuously. Stable crack propagation occurs when the maximum stress intensity factor $K_{max} = \Delta K/(1-R)$ is far below the quasi-static fracture toughness K_{IC}. In Region C, the crack growth rate increases rapidly until the final failure when K_{max} reaches the critical stress intensity factor K_c. Forman developed a relation associated with ΔK and K_C for the crack growth rate expression in this period [78].

$$\frac{da}{dN} = \frac{C(\Delta K)^m}{(1-R)K_C - \Delta K} \qquad (2.23)$$

This equation is a modification of the Paris Law by $[(1-R)K_C - \Delta K]$, in which the crack growth rate increase with increasing stress ratio R and decreasing fracture toughness K_C at a given ΔK level.

As mentioned above, the fatigue crack propagation behaviour is generally described by the Paris Law, equation (2.21). The constants C and m are very sensitive to stress ratio R, microstructure and environment. However, there is a controversy about whether the fatigue crack growth is more dependent on ΔK or $K_{max.}$ Many researchers have carried out systematic experiments and a modification of the Paris Law has been developed to depict the dependence of crack growth rate, da/dN on ΔK and K_{max}.

$$\frac{da}{dN} = C'(\Delta K)^p (K_{max})^q \qquad (2.24)$$

where C' is a scaling constant and p and q are determined by experiment to estimate the dependence of crack growth. Compared with Equation (2.21), it is found that $m = p + q$, and $C = C'(1-R)^q$. For most ceramics, $p<<q$, revealing that K_{max} is the controlling parameter for fatigue crack growth, while for metals, $p>>q$ [78, 79].

2.4.2.3 Near-threshold fatigue crack growth

Although the design based on fatigue crack propagation threshold may be exceedingly conservative for ductile materials, the threshold is still necessary for the analysis of the failure in components in the aeronautic and automotive industries, and also it is extremely important for the fatigue design of brittle materials. The values of fatigue crack growth

threshold can be affected by lots of factors, such as microstructure, R ratio, temperature, environment and crack size.

The assumed relationship between the fatigue threshold and the cyclic plastic zone size has been established. The model was developed by Donahue et al on the basis of the concept that the fatigue threshold can be attained when the crack tip opening displacement reaches a value which is analogous to a critical microstructural dimension [80].

$$\Delta K_{th} \propto \sqrt{\sigma_y E' l^*} \qquad (2.26)$$

where σ_y is the yield stress, E' is the Young's modulus in plain strain, and l^* is the microstructural size scale such as grain size. However, in ductile materials, different fatigue threshold values can be achieved even when the cyclic plastic zone size ahead of the crack tip is the same, due to different slip characteristics.

Another postulate by Sadananda and Shahinian is that the threshold is attained with a critical shear stress τ for the nucleation and movement of a dislocation from the crack tip [78].

$$\Delta K_{th} \propto \tau\sqrt{b} \qquad (2.27)$$

where b is the magnitude of the Burgers vector.

It is proposed that the appearance of the fatigue crack propagation threshold directly results from the crack closure phenomenon, which is extremely important in the near threshold region. Crack closure is the consequence of residual plastic deformation left in the wedge of fatigue crack tip and the accompanying reduction in crack opening displacement leads to

premature contact between the mating crack faces even during far-field tensile fatigue loading. It is one of the most important factors leading to the dependence of fatigue thresholds on microstructural, mechanical and environmental variables.

Many researchers studied different types of crack closure phenomena and classified many forms of fatigue crack closure based on their own results. Possible modes of fatigue crack closure are plasticity-induced crack closure, oxide-induced crack closure, roughness-induced crack closure, viscous fluid-induced crack closure and transformation-induced crack closure. Apart from the above mechanisms of fatigue crack closure in conventional metals, work has also been carried out on fatigue of advanced metallic systems and non-metallic materials. They are: (1) crack deflection, (2) crack-bridging (trapping), (3) crack-shielding caused by microcracking, phase transformations and dislocations, shown in Fig.2.20 [78].

When these fatigue crack closure phenomena are considered, it can be seen that fatigue crack growth is not only influenced by the conditions ahead of the crack tip, but is also influenced by the contact of mating crack faces behind the crack tip. Thus, Elber proposed that the crack propagation occurs only during the period of fatigue loading cycle when the crack faces are fully separated. To measure the displacement of the crack faces, strain gauges are used above and below the crack plane, shown in Fig.2.21 (a). A schematic of the relationship between the applied stress σ and the displacement from the monitor δ during fully unloading from the fat-field stress is obtained in Fig.2.21 (b). In this curve, the crack is fully open until the stress drops from σ_{max} to σ_{op} from point A to B; the region B to C is caused by the crack closure phenomenon; the crack is fully closed beyond point C [78]. Therefore, the crack can propagate when the stress σ_{op} needed for fully open is reached, with a corresponding stress intensity factor K_{op}, and the effective stress intensity factor range ΔK_{eff} is defined as follows

$$\Delta K_{eff} = K_{max} - K_{op} \quad (2.28)$$

2.5 Fatigue crack propagation in γ-TiAl

Fatigue crack propagation of gamma titanium aluminides has been studied for many years since early 1990s [81-88]. Fatigue crack propagation behaviour of γ-TiAl alloys depends not only on extrinsic factors, but also depends on different intrinsic factors [89-92]. Ritchie states that the process of the fatigue crack propagation is a mutual competition between intrinsic microstructural damage mechanisms which promote crack growth ahead of the crack tip and extrinsic mechanisms which impede crack growth behind the crack tip, as shown in Fig.2.22. For brittle materials, extrinsic mechanisms are more important in the toughening of materials. Extrinsic mechanisms impeded the crack growth by crack deflection, crack tip shielding by inelastic zone or contact between the crack surfaces, in the form of crack closure [93]. Since the crack growth rate of TiAl alloys is rather fast compared with ductile alloys, the fatigue design of titanium aluminides is mainly based on fatigue crack propagation threshold [86].

2.5.1 Effect of microstructure on fatigue crack propagation

It is found that fatigue crack propagation behaviour in gamma titanium aluminides is very sensitive to microstructure and lamellar microstructure provides better fatigue crack propagation resistance than duplex and equiaxed gamma microstructures [83, 94-98].

Fig.2.23 presents a comparison of crack growth rates as a function of effective stress intensity factor ΔK for two microstructures (lamellar and duplex) at ambient temperature in air. Obviously, the threshold value of duplex microstructure is lower than that of lamellar

microstructure. It can be seen that, in the crack initiation region, the fatigue crack growth rate of both microstructures is very fast. However, the effect of microstructure on the fatigue crack growth behaviour is noticeable for $da/dN>10^{-8}$m/cycle. The fast crack growth rate and low threshold value of the duplex microstructure is due to its fine grain size, leading to a comparatively flat crack growth path and less crack tip shielding from crack deflection, branching, micro cracking ahead of the crack tip and shear-ligament bridging in the crack wake [95]. The respective contribution of the impact of bridging effect and crack closure effect on fatigue crack growth rate is not clear. Zhu stated that the superior crack growth resistance of fully-lamellar microstructure compared with duplex was due to crack closure [79]. Mutoh et al pointed out that bridging is more influential on FCG rate because of the observed micro cracks, which were formed near the crack tip. Some of these micro cracks coalesced to the main crack, while the rest of them remained unbroken in the crack wake, leading to the improvement of crack tip stress shielding effect [98]. Larsen also showed that the fatigue crack growth rate of TiAl alloys with lamellar microstructure was slower than that with duplex microstructure at the same ΔK level [99]. The fracture toughness is reported much higher with refined lamellar microstructure compared with refined duplex microstructure by Liu et al [100].

However, the above comparison may be influenced by environmental effects. Therefore, the effective stress intensity factor range of a selected microstructure, which reveals the intrinsic fatigue crack growth behaviour, has been introduced and is evaluated in an inert atmosphere like high vacuum and corrected from closure effects. Hénaff summarised the intrinsic fatigue crack growth behaviour at room temperature with different microstructures of gamma titanium aluminides. Their fatigue crack resistance is shown in Fig.2.24, which confirms the

above trends observed in air with a better fatigue crack growth resistance of lamellar samples than equiaxed gamma and duplex samples [89]. A similar trend is also found at elevated temperatures [83, 97, 98].

Equiaxed gamma grains influence crack growth resistance. Fractographic studies indicate that the gamma grains fail by brittle intergranular decohesion with test temperatures over 500°C and transgranular cleavage with test temperatures below 500°C under cyclic load. Both of these fracture modes reduce the fatigue crack growth resistance and increase crack growth rate [82].

The fracture modes of lamellar microstructure in two-phase gamma titanium aluminides are generally classified into two main categories: translamellar fracture and interlamellar fracture, as shown in Fig.2.25 [101-103]. Translamellar fracture mode is a cleavage failure, which propagates perpendicularly or angularly to the lamellar interface, while interlamellar fracture mode always occurs along the lamellar interfaces. The translamellar fracture surface is uneven since the crack crosses different lamellae as it propagates; the interlamellar facture surface is relatively flat and smooth with small area of facet. Translamellar fracture tends to be the main fracture mode at elevated temperatures, which can be confirmed by a less tortuous crack path observed on the fracture surface [99]. It is observed that most micro cracks are formed at the γ/α_2 interfaces within the colonies and gather at colonies with soft orientation [104]. However, Bowen reported that interlamellar fracture mainly occurs at γ/γ interfaces, although some γ/α_2 interface fractures are still observed under cyclic load [82].

Despite the above two main fracture modes, there are still small amounts of intralamellar fracture observed on the fracture surface of lamellar gamma titanium aluminides. The

intralamellar fracture surface is very similar to interlamellar fracture surface, which is also parallel to the lamellar interface, but with a geometric pattern consisting of a large amount of parallel ridges or markings on consecutive lamellar plates. These parallel markings are observed either at inclined angles of 60° (or 120°) to each other or in a direction parallel to each other, showing as a geometric pattern of three-fold symmetry, regardless of whether they stay on the same place or on different neighbouring plates, as shown in Fig.2.26 [105].

2.5.2 Effect of colony size on fatigue crack propagation

Choi [91] investigated the influence of colony size on the fatigue crack propagation behaviour of gamma titanium aluminides Ti-46.5Al-2Cr-3Nb-0.2W and Ti-47Al-1.5Cr-0.5Mn-2.5Nb-0.18B with fully lamellar microstructures. The results shown in Fig.2.27(a) reveal that with similar lamellar spacing, when the colony size is below 400μm, there is no significant influence of colony size (90μm, 290μm and 400μm) on the value of fatigue crack propagation threshold for both alloys, exhibiting a constant value around 8-9MPa√m. However, when the lamellar colony is very coarse, with a colony size over 1400μm, the fatigue crack propagation threshold is much lower around 6.5 MPa√m, showing that the fatigue crack propagation resistance of coarse lamellar microstructure is much lower than that of fine lamellar microstructure. Alloys with a medium colony size show the fastest crack growth rate, while alloys with a coarse colony size show the slowest crack growth rate. The coarse alloy also shows the highest fracture toughness, which is the opposite to the results reported by Chan and Kim [106], who point out that the fracture toughness reaches a maximum value with a colony size around 500μm. This can be possibly explained by the presence of small amount of equiaxed γ grains in Choi's alloy [91]. When fatigue crack closure effect is considered, the alloy with coarse lamellar colonies still exhibits lower fatigue

crack propagation threshold (around 4 MPa√m) than fine colony microstructure, shown in Fig.2.27 (b).

2.5.3 Effect of lamellar spacing on fatigue crack propagation

The fatigue crack propagation behaviour of gamma titanium aluminides with lamellar microstructure is also affected by the lamellar spacing [90, 91]. Mine studied the influence of lamellar spacing on fatigue crack growth by comparing the FCG behaviour of air-cooled and furnace-cooled materials with similar colony size and proposed that the decrease of lamellar spacing leads to a general trend of improvement of fatigue crack growth resistance, shown in Fig.2.28 [90]. The average lamellar spacing of air-cooled and furnace-cooled materials is 0.91μm and 3.84μm, respectively. Similar results are also found by Choi with lamellar spacings of 0.4μm and 5.5μm [91]. The mechanisms of interlamellar fracture which occur in both air-cooled and furnace-cooled specimens are illustrated in Fig.2.29 [90]. When the crack propagates in the air-cooled specimen with a thin lamellar spacing, the crack traverses the lamellae by linking of the micro cracks formed in a small area in front of the crack tip, while in furnace-cooled specimens the crack primarily propagates on the planes along the lamellar interfaces as the lamellar spacing here is in the range of the critical lamellar thickness to form a micro crack. Only a few steps are observed in the fracture surfaces as the crack occasionally propagates across the lamellar plates.

Chan showed that the fracture toughness of lamellar TiAl was improved with decreasing lamellar spacing by the influence of translamellar micro cracking and the size of the shear ligaments as with the Hall-Petch relationship. Translamellar micro cracking is favoured in specimens with thick lamellae, and the linkage of the main crack with translamellar and

interlamellar micro cracks becomes considerably easier, leading to a smaller ligament size and lower shear ligament toughening. While the translamellar micro cracking is hindered with thin lamellae, and the linkage of the main crack becomes difficult, giving rise to a larger ligament size and high shear ligament toughening. However, it is reported that when the lamellar colony size exceeds 600μm, the fracture toughness is not only controlled by the lamellar spacing, but also controlled by the lamellar orientation. [106].

2.5.4 Effect of lamellar orientation on fatigue crack propagation

The properties of gamma titanium aluminides with a lamellar microstructure are influenced by the orientation of lamellar colonies because of its anisotropic nature. The dependence of various properties and behaviour of lamellar gamma titanium aluminides on lamellar orientation has been successfully studied with polysynthetically twinned (PST) TiAl. The plastic deformation in each lamella was shown to be dictated by the lamella's orientation, and the properties, such as tensile and compression strength, fatigue crack propagation resistance, creep resistance and fracture toughness of PST crystals are influenced by the lamellar orientation. This is defined by the angle between the stress direction and the lamellar interface normal. It has been shown that low fracture toughness is obtained with lamellar orientation parallel to the crack plane, while the fracture toughness is much higher with lamellar orientation perpendicular to the crack plane. However, although the yield strength is lower when the lamellar plane is parallel to the loading axis than when it is perpendicular, the lowest value is observed at the intermediate angle between the loading axis and lamellar plane [107-110].

Although no dedicated research on fatigue crack propagation has been reported using PST TiAl crystals, the strong influence of lamellar orientation on fatigue crack propagation behaviour has been illustrated by using as-cast TiAl alloys with coarse columnar structures [82-84, 111]. Zhu pointed out that the influence of lamellar orientation on fatigue crack propagation behaviour can be shown through the scatter in fatigue crack growth data observed with lamellar microstructures which is larger than other microstructures [79]. The definition of the relation between lamellar orientation and fatigue crack growth direction is shown in Fig.2.30 where the lamellar orientation of type A and B specimen is perpendicular to the crack growth direction while that of type C specimen is parallel to the crack growth direction [111].

For type A and B alloys, the lamellar orientation is perpendicular to the crack growth direction, but the crack propagates across different lamellae in type A alloy, while the crack propagates within each lamellae in B. Tsutsumi studied the fatigue crack propagation behaviour at high temperatures with type A and B samples and showed that: (a) the crack was not arrested at the grain boundaries and lamellae, but propagated smoothly; (b) a slight difference was observed in the relationship of crack growth rate da/dN and stress intensity factor range ΔK for the two types of alloys, shown in Fig.2.31, which might be due to the fact that the cracks in both alloys propagate in the direction perpendicular to the stress, traversing the lamella boundaries [84]. Hénaff also studied the fatigue crack propagation behaviour of these two types of alloys at room temperature in air and vacuum. It is found that for type A orientation, translamellar fracture is always the most common feature either in air or in vacuum. However, the general aspect of type B orientation is different. From the fractography, especially from the fracture surface of a specimen tested in vacuum, few

translamellar fractures are observed, while lots of crystallographic facets among large cleavage-like fracture are observed throughout the surface. Such crystallographic aspect features are not so pronounced for the specimen with the same B orientation tested in air [111].

Wissuchek showed that the fatigue crack propagation threshold ΔK_{th} was strongly influenced by the orientation of lamellae with respect to the crack propagation direction. The threshold value required for crack propagation perpendicular to lamellar interfaces is about 11.5 MPa√m, while that to propagate a crack parallel to lamellar interfaces is only about 6.5 MPa√m, which is about 60% of the maximum value [112]. Fig.2.32 shows typical da/dN- ΔK curve for the specimens with lamellar orientation perpendicular and parallel to the crack growth direction, respectively [92]. As can be seen from the curve, both orientations show a considerably large scatter of da/dN, and type C indicates much faster crack growth rate than type B. This tendency still remains even after taking crack closure into consideration, i.e., when the graphs are plotted as a function of ΔK_{eff}. For the specimen with lamellar orientation perpendicular to the crack growth direction, just one main crack started from the notch without noticeable deflections and branching is observed from both specimen surfaces, shown in Fig.2.33 (a). The crack propagates across the lamellae, seen from profile on the longitudinal section, Fig.2.33 (b), and translamellar fracture is observed from the fracture surface in this type of specimen. While for the specimen with lamellar orientation parallel to the growth direction, a crack from the notch is arrested and new cracks initiate away from the crack tip, thus several cracks are observed on the sample surface. Most cracks are not connected to each other as the crack faces are not coplanar, shown in Fig.2.33 (c). These cracks are found to be along the lamellar interface, seen from the profile on the longitudinal

section, Fig.2.33 (d), so interlamellar fracture is observed from the fracture surface. An earlier post mortem TEM study on crack tip deformation showed that cracks severing lamellae were formed on the cross-lamella {111} planes through twinning and banding of ordinary and superdislocation slip [113]. Microcracks are also shown to be formed at cross-lamellar twin boundaries and slip bands by in-situ TEM examination on tensile specimens of TiAl [114, 115]. Microcracks along the interfaces ahead of the main crack are only nucleated when the crack growth direction is roughly parallel to lamellar interface and the crack propagates by ligament fracture [116]. Bridging is found to be very important during fatigue crack growth process, shown in Fig.2.34. The crack propagates continuously through the colony on the left. However, it stops at the boundary. As the increase of ΔK, re-nucleation occurs in the next grain and crack growth resumes almost at the same time. The bridging ligament formed during crack re-nucleation restricts the crack propagation [112].

2.6 Ti4522XD and Ti46Al8Nb alloys

2.6.1 Ti4522XD alloy

Ti4522XD, which is a commercially available gamma titanium aluminide with a composition of Ti-45Al-2Mn-2Nb-1B (at. %) composed of $\alpha_2 + \gamma$ two phases, is one of the two main alloys used in this study. As mentioned in 2.2, Mn is added to improve the ductility. However, larger addition of Mn does not further improve the property [38]. Nb is introduced to enhance the tensile strength and oxidation resistance. B is added most importantly for the grain refinement, thus benefitting tensile strength and ductility, and reducing hydrogen-induced embrittlement [117].

XD (exothermal dispersive), or XD^{TM,} is a trade name used for a method of processing technology to form ceramic particles such as borides, carbides, nitrides and silicides in a metallic or intermetallic matrix by in-situ precipitation invented and developed by Martin Marietta Laboratories [118]. Although thermo-mechanical processing is recognized to offer potential improvement of properties, the XD route is used to cast the original ingots as it reduces grain size, enhances specific tensile and fatigue strength and fire resistance. It also improves castability as well as microstructural uniformity because of the fine dispersion of TiB_2 particles [119, 120].

Ti4522XD has been used to make a number of different trial aero-engine components by Rolls-Royce, such as compressor stator vanes and blades, low pressure turbine blades and large complex cast components. Although the low pressure turbine blades have been successfully cast and machined, the temperature capability of Ti4522XD has limited its application because, even though it is currently suitable for the ultimate stage blades, future trends are towards higher temperatures and towards its additional requirement for the penultimate stage [120]. In this thesis, refractory alloying elements, e.g. Nb and Ta, which are potentially able to increase temperature capability of γ-TiAl alloys, are added into the traditional Ti4522XD to study the effects of alloy composition on the properties of this series of alloys.

2.6.2 Ti46Al8Nb alloy

The more advanced gamma titanium aluminides (TNB), with the alloy addition of Nb (5-10 at. %), is developed to further increase the high temperature properties of TiAl alloys and has a potential for industrial applications. Nb is recognized as an essential additive in gamma

titanium aluminides as the ductility and high temperature strength is found to be improved with the addition of niobium. In addition, Lin et al. have proven that the oxidation resistance is also greatly improved by niobium. Furthermore, the alloys with addition of 5 to 10 at. % niobium exhibit significant increase on the creep resistance. Thus, this range of gamma titanium aluminides is an alternative to nickel-bases superalloys for some components up to temperatures of about 800˚C [32, 36, 121-123]. Therefore, alloy Ti46Al8Nb has been chosen in this thesis to study its fatigue crack propagation behaviour.

2.7 Background and aim of this project

Crack propagation in TiAl alloys has been under investigation in the aerospace industry since 1990 but the activities were substantially reduced after 2000, probably mainly due to the lack of near-term application. The main factor which was constraining the application of these alloys was the difficulty of producing components cost-effectively [4]. However, GE formally announced that two stages of Genx LPT blades would be in TiAl material in 2006 and the engine was certified in the following year with TiAl blade. R-R also defined a strategy to apply TiAl in their Trent XWB LPT blades later on.

Due to the intinsic brittleness of TiAl-based alloys, the design method for the applicaion of TiAl-based alloys is based on damage tolerance of the material and fatigue crack growth (FCG) threshold is one of the most important properties. The focus of this project is to achieve a fundamental understanding of factors which influence the FCG threshold by focusing mainly on the effects of alloy elements and microstructural parameters on crack propagation under various stress conditions in a number of alloys. The current situation is that studies have shown that the lamellar microstructure offers better crack propagation

resistance than other microstructures such as duplex and near gamma microstructures [101], but the influence of alloy composition has not been studied. This may be because the properties of TiAl-based alloys are sensitive to microstructure and it is difficult to obtain identical microstructures in different alloys. In other words, property difference in different alloys may be buried by the variation in microstructures in different alloys. Hence one aspect of the present study, where the influence of alloy composition on FCG is to be determined, will be to characterise the microstructures of the different alloys very carefully so that comparisons can be made. Also, lamellar TiAl-based alloys with different microstructural parameters are chosen to understand the influence of microstructural parameters on fatigue crack propagation behaviour.

In this thesis, Ti4522XD and its four modifications, Ti-45Al-2Mn-2Ta-1B, Ti-45Al-2Mn-4Nb-1B, Ti-45Al-2Mn-4Ta-1B and Ti-45Al-2Nb-2Ta-1B, are selected to understand the effects of alloy composition, especially refractory alloying elements, e.g. Nb and Ta, which are potentially able to increase temperature capability of γ-TiAl alloys, on fatigue crack propagation threshold. Some other mechanical tests, such as tensile and hardness tests will also be conducted to get a comprehensive view of mechanical properties of these modified alloys. Different heat treatments are applied and different amount of B is added into the alloy to obtain different colony sizes, lamellar spacing, and volume of γ grains. Consequently, the influence of these microstructural factors on fatigue crack propagation threshold will be studied. Finally two series of alloys, Ti4522 and Ti46Al8Nb, with extremely coarse lamellar microstructures have been selected to understand the lamellar orientation effect on fatigue crack propagation threshold.

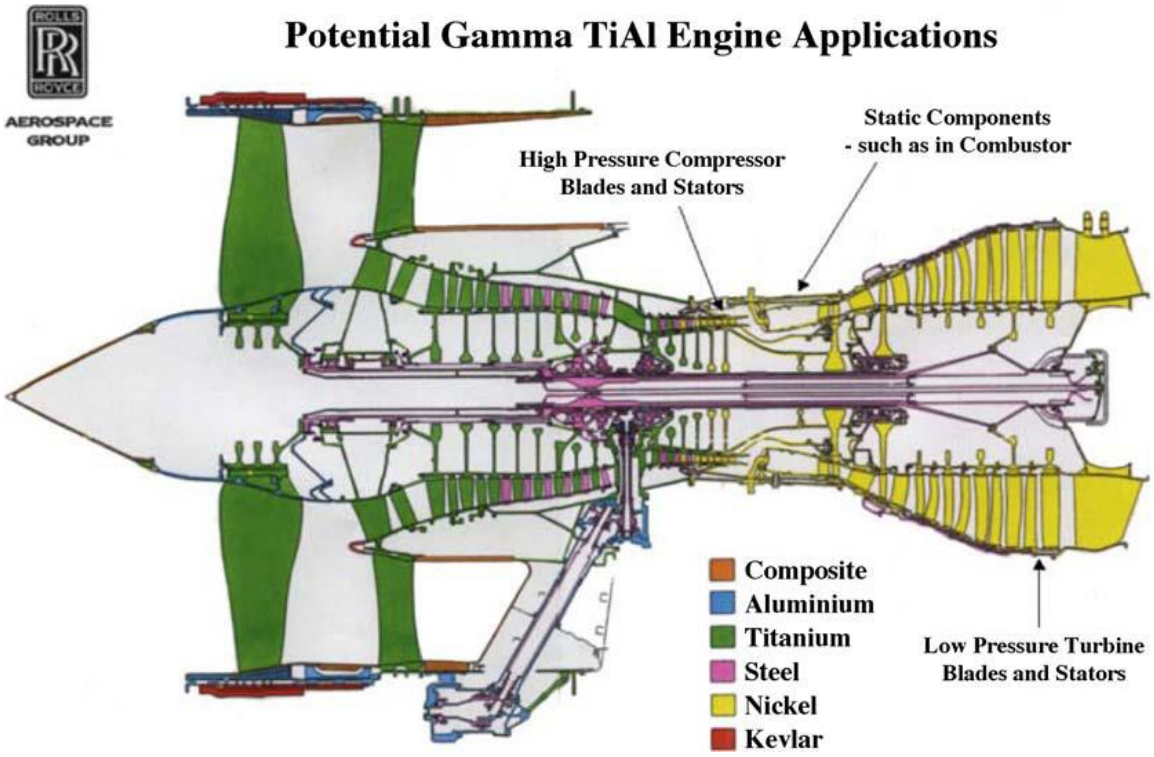

Fig.2.1. Cross-section through a Trent aero-engine, showing potential TiAl engine applications (courtesy of Rolls-Royce plc, UK) [3].

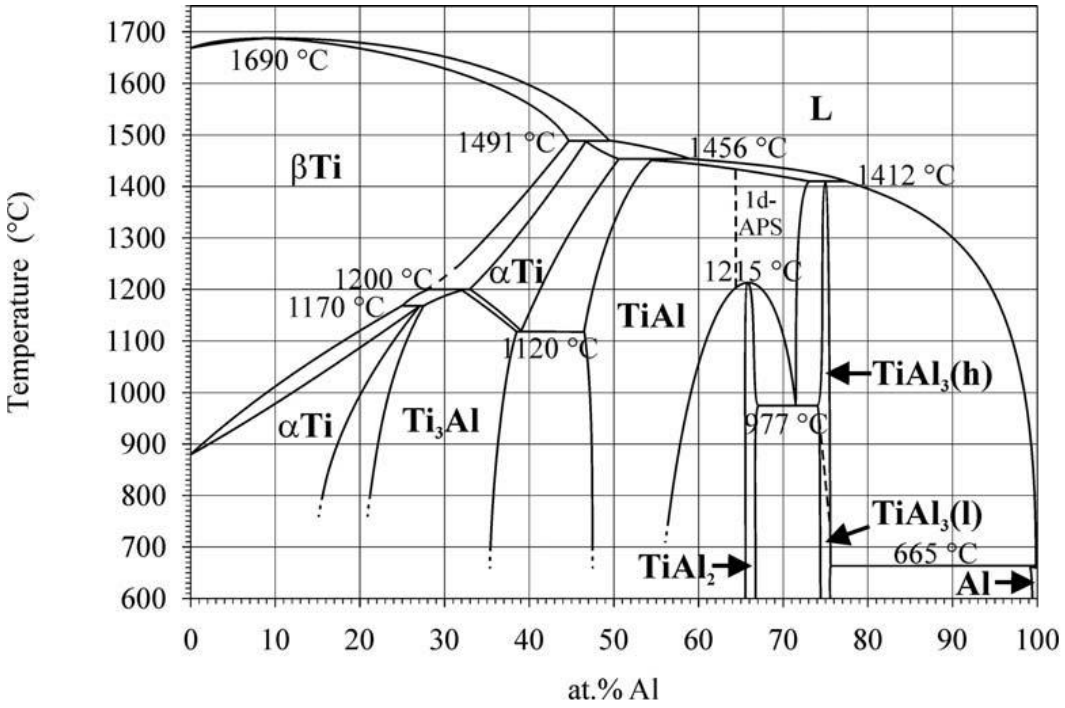

Fig.2.2 Binary Ti-Al phase diagram (Schuster and Palm, 2006) [7].

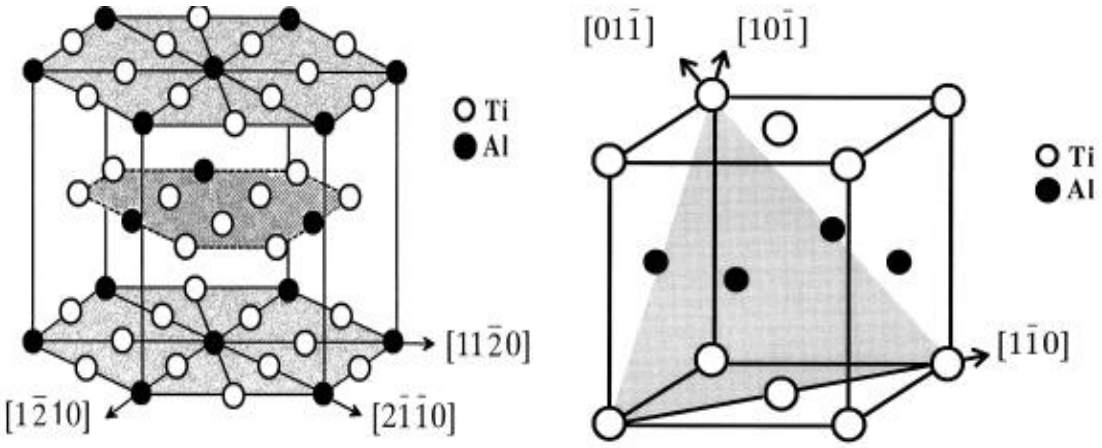

a b

Fig.2.3 Crystal structure of (a) α_2-Ti_3Al and (b) γ-TiAl [8].

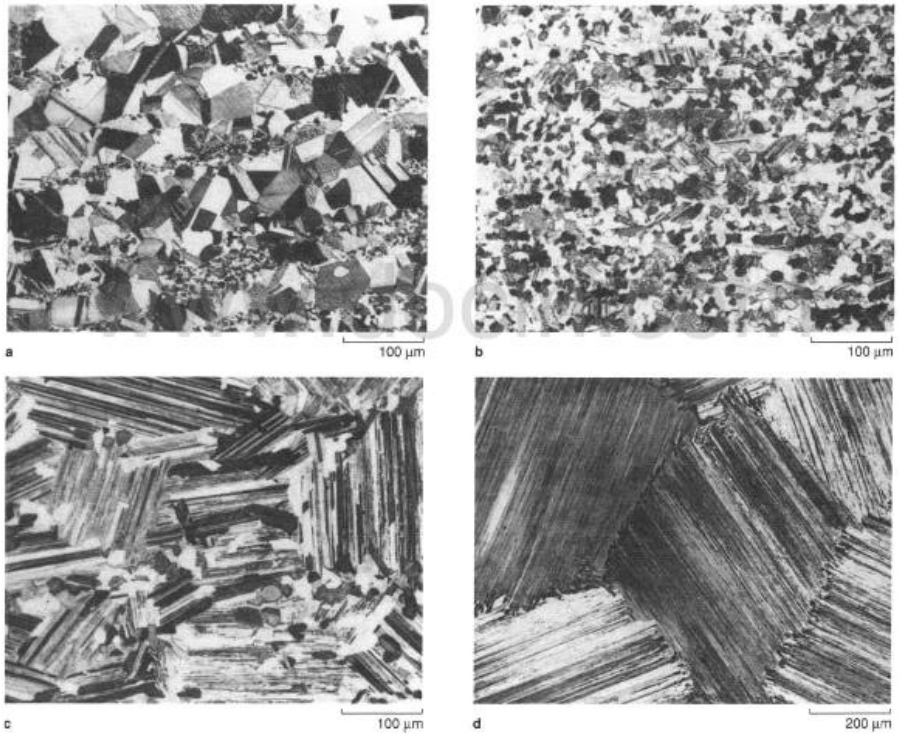

Fig.2.4 Typical microstructure of gamma titanium aluminide. (a)NG; (b) DP; (c) NL; (d) FL [11].

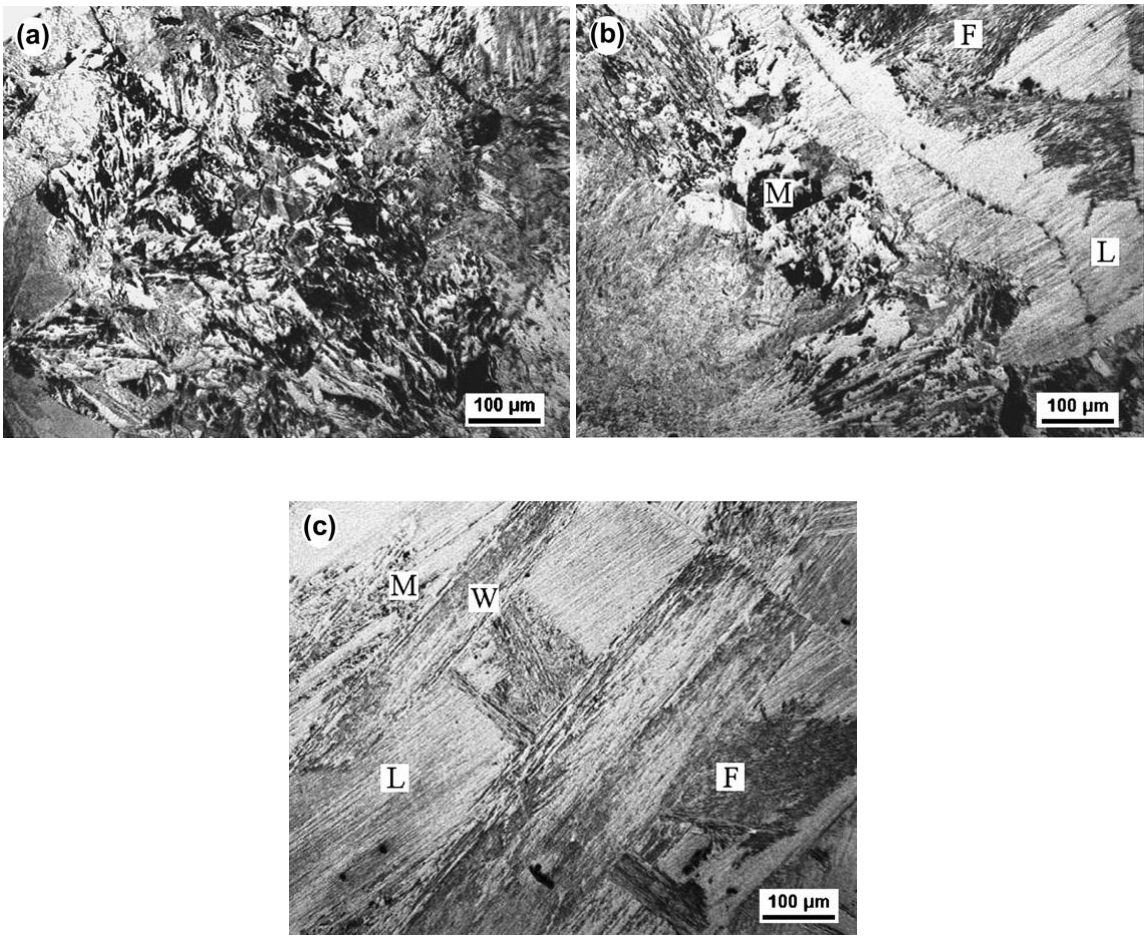

Fig. 2.5 Typical optical microstructures in continuously cooled Ti-46Al-8Nb from 1360° C (alpha phase field). (a) Fully massive γ obtained at a cooling rate of 180°Cs^{-1}, (b) a mixture of massive γ + feather + lamellar microstructure obtained at a cooling rate of 25°Cs^{-1} and (c) a mixture of feathery + Widmanstätten + lamellar microstructures obtained at a cooling rate of 10°Cs^{-1} (there is still a tiny fraction of massive γ at this cooling rate). Letters M, F, W and L stand for massive, feathery, Widmanstätten and lamellar microstructures, respectively [20].

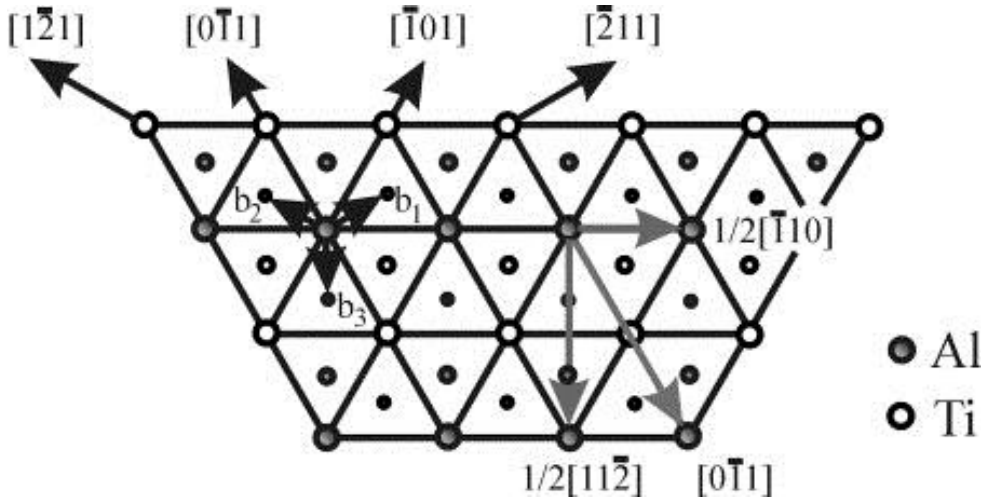

Fig.2.6 Potential slip and twinning system of the $L1_0$ structure, schematic drawing of three-layer sequence of atom stacking on the (111) plane shown by small, medium and larger circles. $b_1 = 1/6[\bar{2}11]$, $b_2 = 1/6[1\bar{2}1]$ and $b_3 = 1/6[11\bar{2}]$ are the Burgers vectors of partial dislocations. b_3 is perpendicular to the Burgers vector $b = 1/6[\bar{1}10]$ for ordinary dislocations represent the Shockley partial dislocation for true twinning , where b_1 and b_2 represent pseudo-twinning [51].

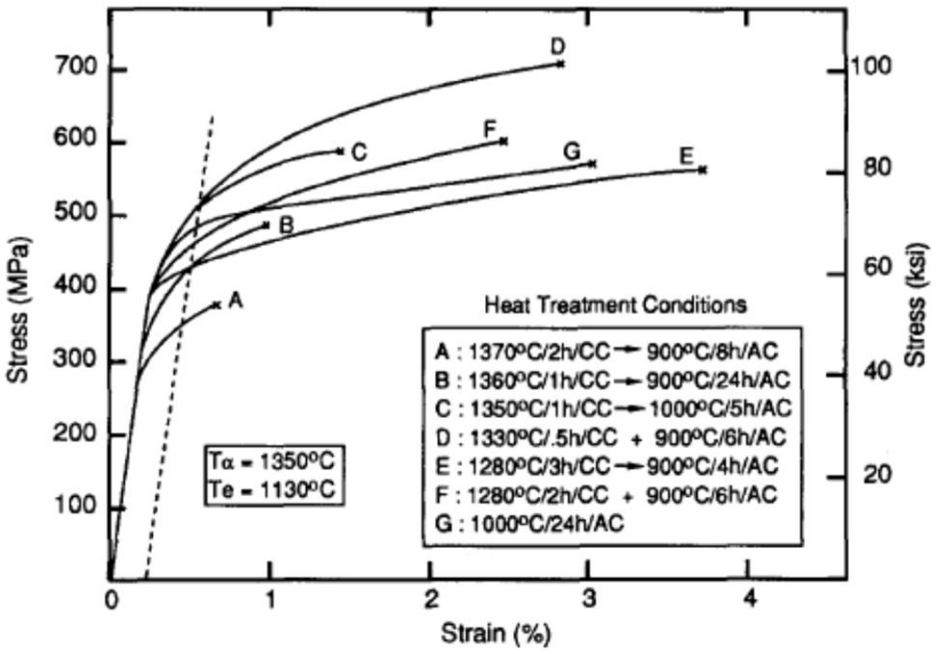

Fig.2.7 Stress strain curves of different γ-TiAl alloys at room temperature. The materials are all Ti-47Al-1Cr-1V-2.5Nb but different microstructures. Samples A, B and C have FL microstructures with colony sizes decreasing from 700-1300μm (A) to 250-500μm (C); D has a NL microstructure with a lamellar colony size of 70-140μm and γ grains of 10-30μm; E and F have a duplex microstructure with grain size of 15-40μm and 10-30μm, respectively; sample G has a near gamma microstructure with γ grain size of 5-100μm and α_2 grain size of 1-5μm [10].

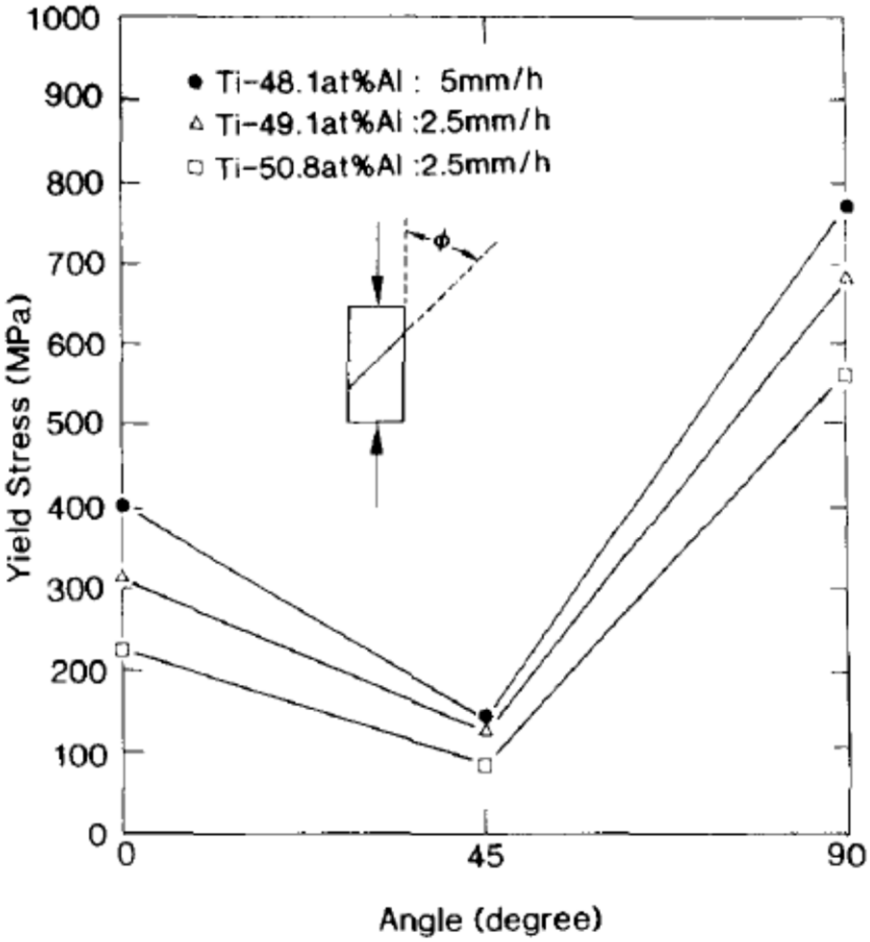

Fig.2.8 Variation of the room temperature yield stress with orientation angle φ of various alloys, φ is the angle between the compressive axis and the lamellar planes [49].

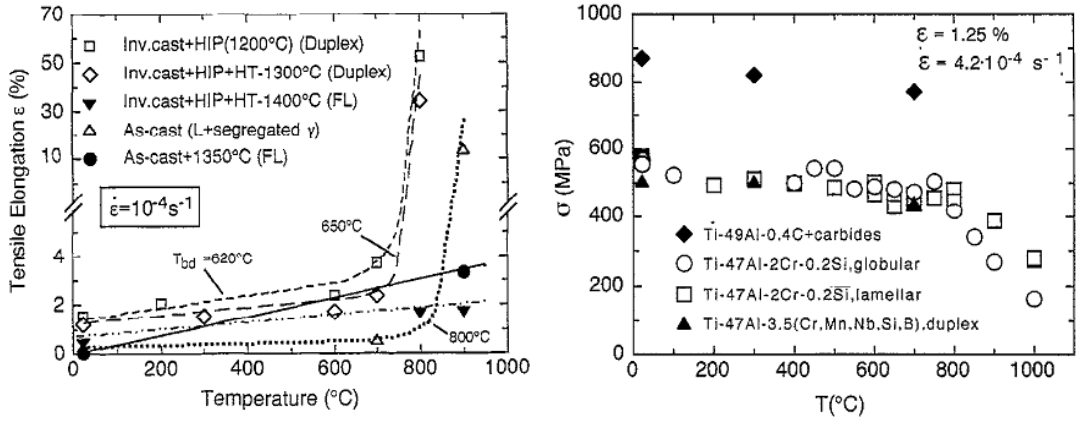

Fig.2.9 Comparison of tensile properties of different alloys and microstructures at different testing temperatures [51].

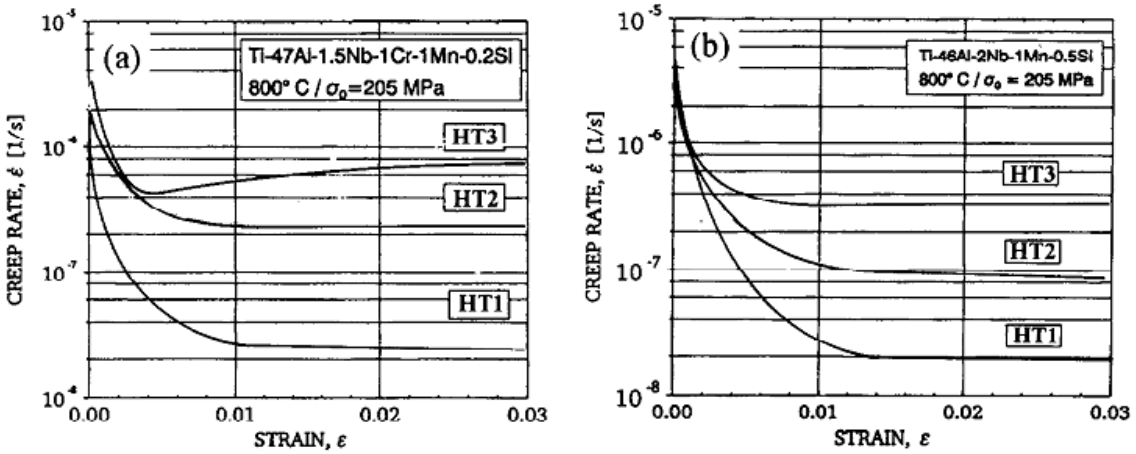

(a) (b)

Fig.2.10 Creep strain rate vs. true strain curves of alloy 1 (Ti – 47Al – 1.5Nb – 1Cr – 1Mn – 0.2Si) (a) and alloy 2 (b) in the different heat treatment conditions at an initial stress of 205MPa. HT1, isothermal annealing at 1400° C + ageing, fully lamellar; HT2, isothermal annealing at 1300° C + ageing, duplex; HT3, isothermal annealing at 1250° C + ageing, globular [62].

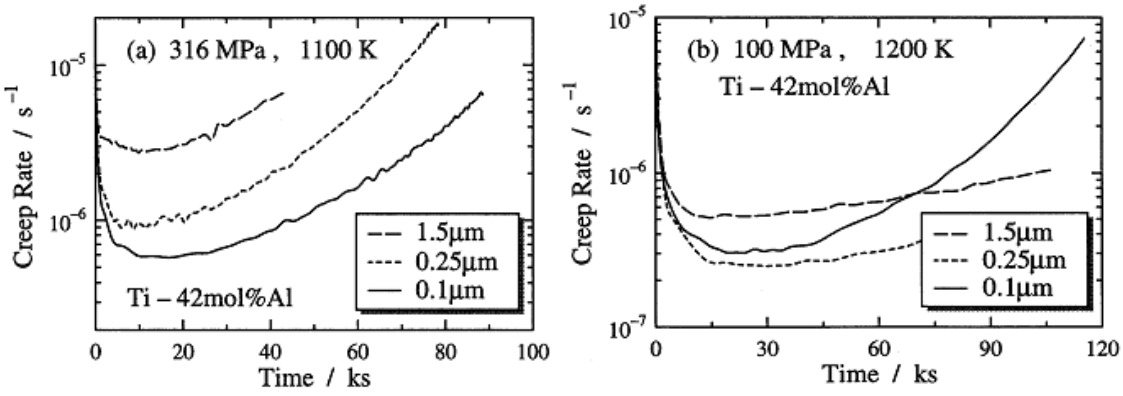

Fig.2.11 Representative Creep curves of Ti–42mol%Al with the three different lamellar spacings; (a) at a high stress and (b) at a low stress [58].

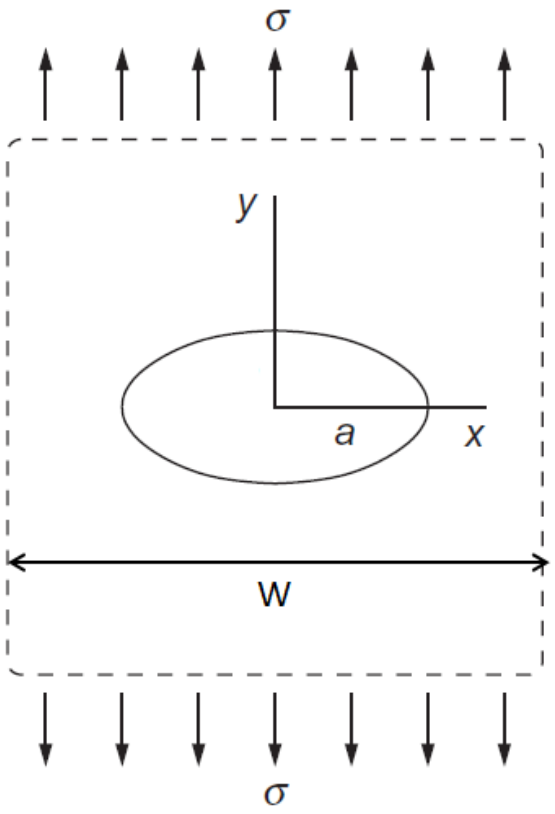

Fig.2.12 A through-crack infinite plate of unit thickness and 2a<<W [74].

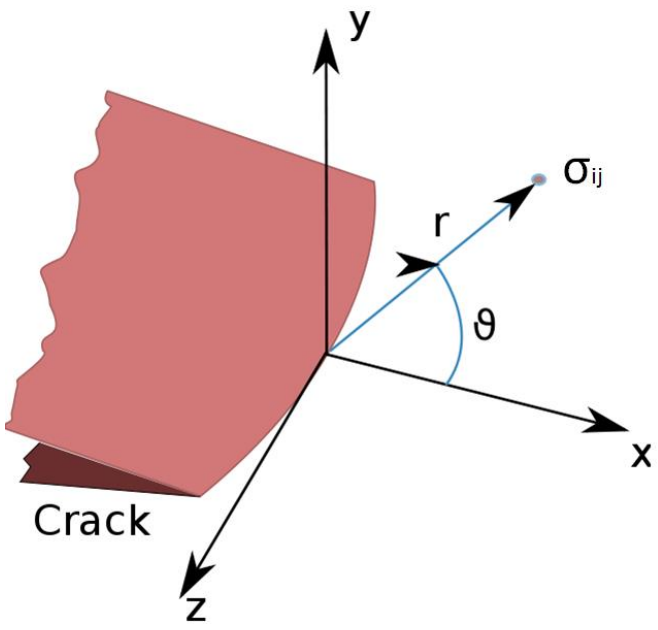

Fig.2.13 Polar coordinates ahead of the crack tip [76].

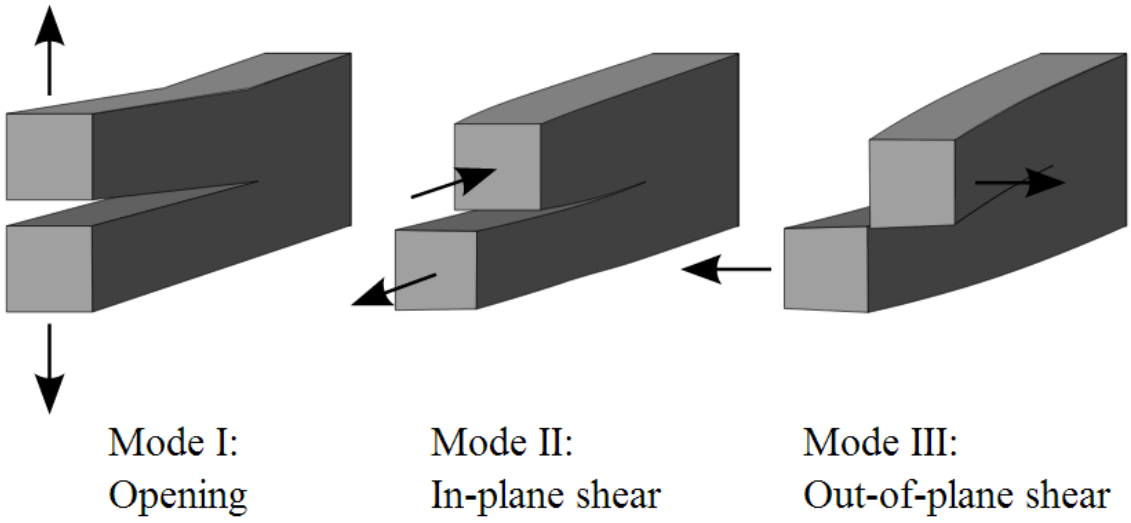

Fig.2.14 Illustration of crack mode [76].

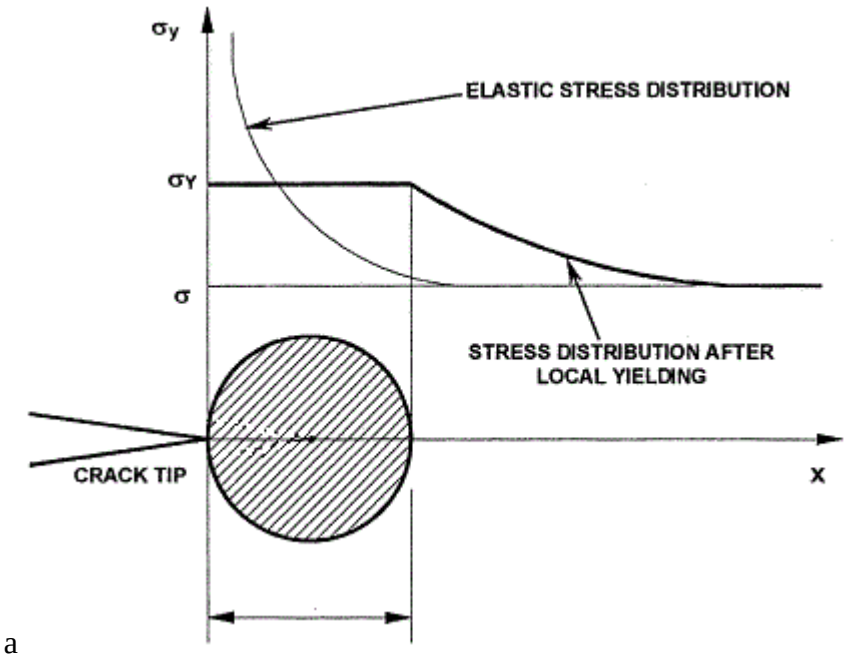

a

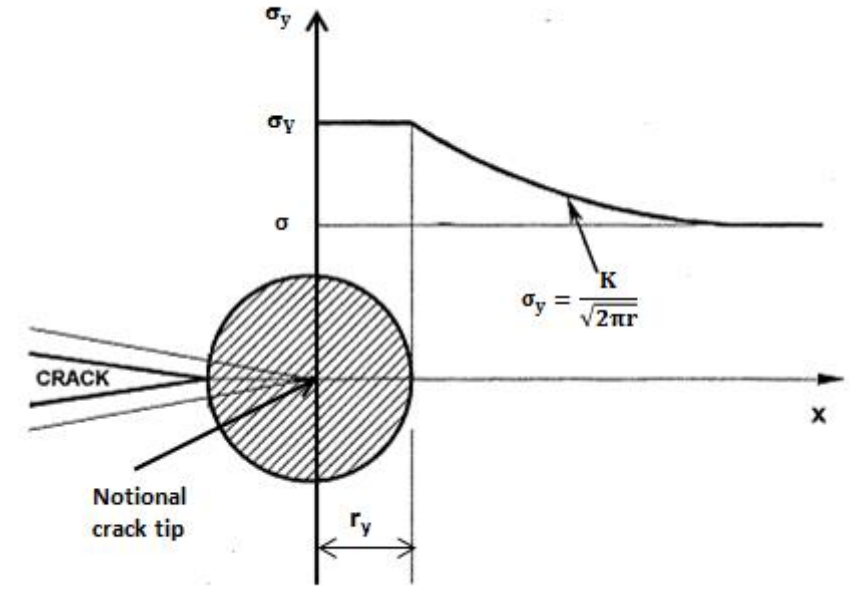

b

Fig.2.15 (a) plastic zone ahead of the crack tip; (b) Irwin's correction [74].

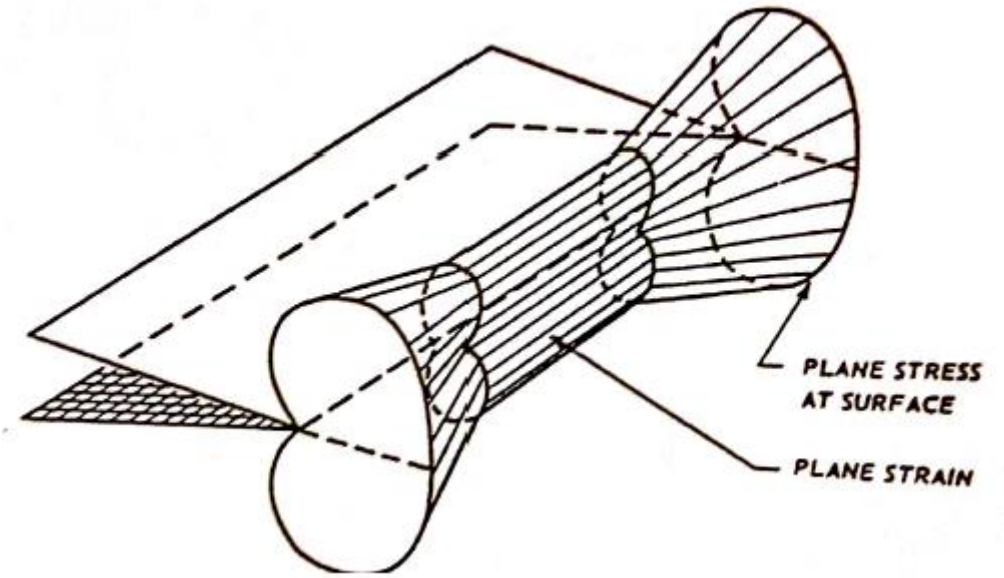

Fig.2.16 Schematic through-thickness plastic zone size and shape in a finite plate [74].

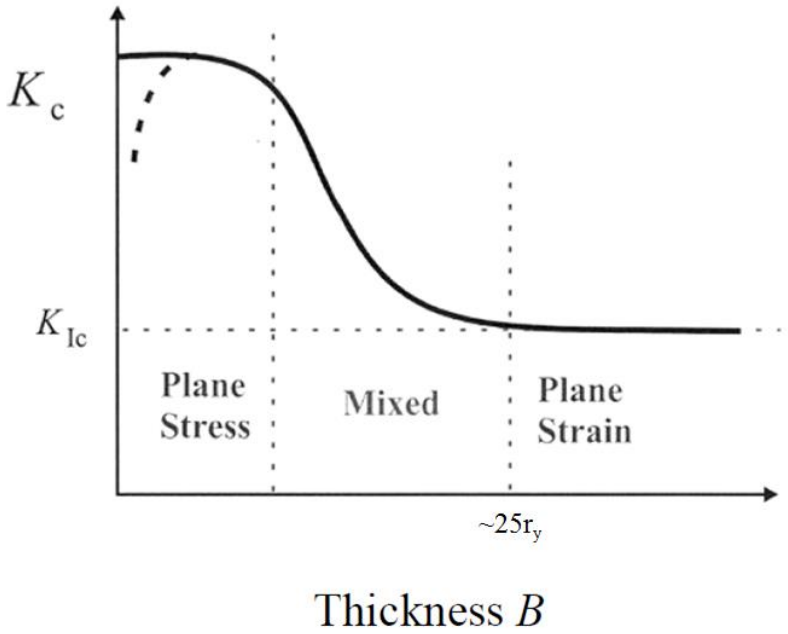

Fig.2.17 Relationship between specimen thickness B and fracture toughness K_C [74].

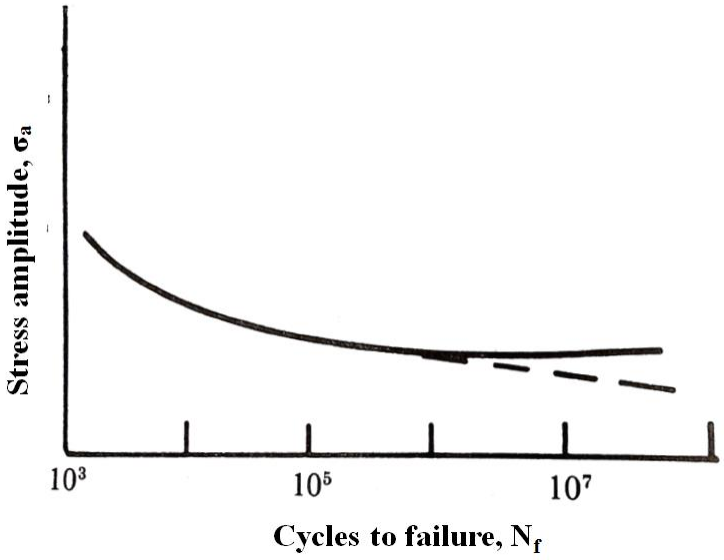

Fig.2.18 Typical S-N diagram showing the variation of the stress amplitude for fully reversed fatigue loading as a function of the number of cycles to failure for ferrous and nonferrous alloys [78].

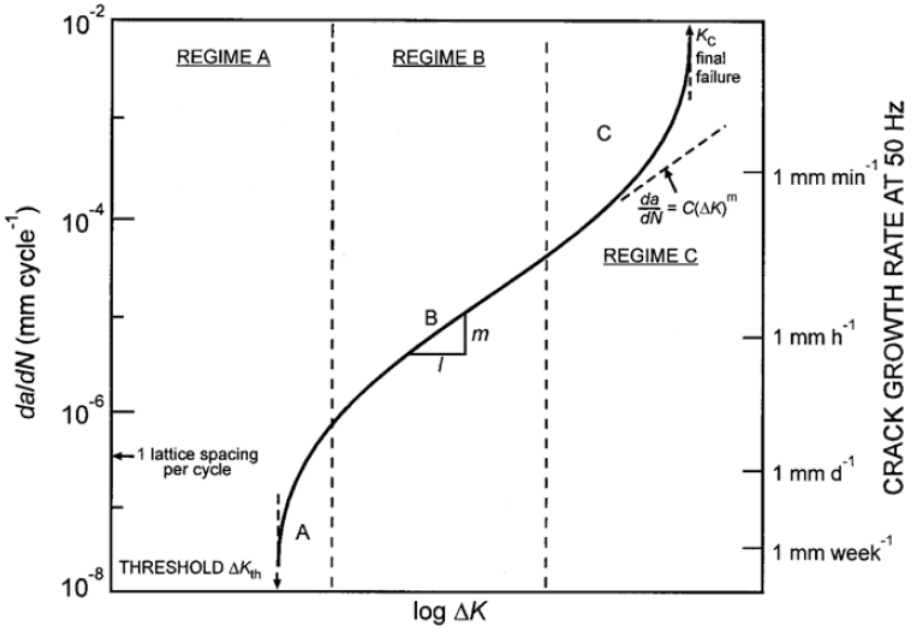

Fig.2.19 Schematic illustration of the different regimes of stable fatigue crack propagation [78].

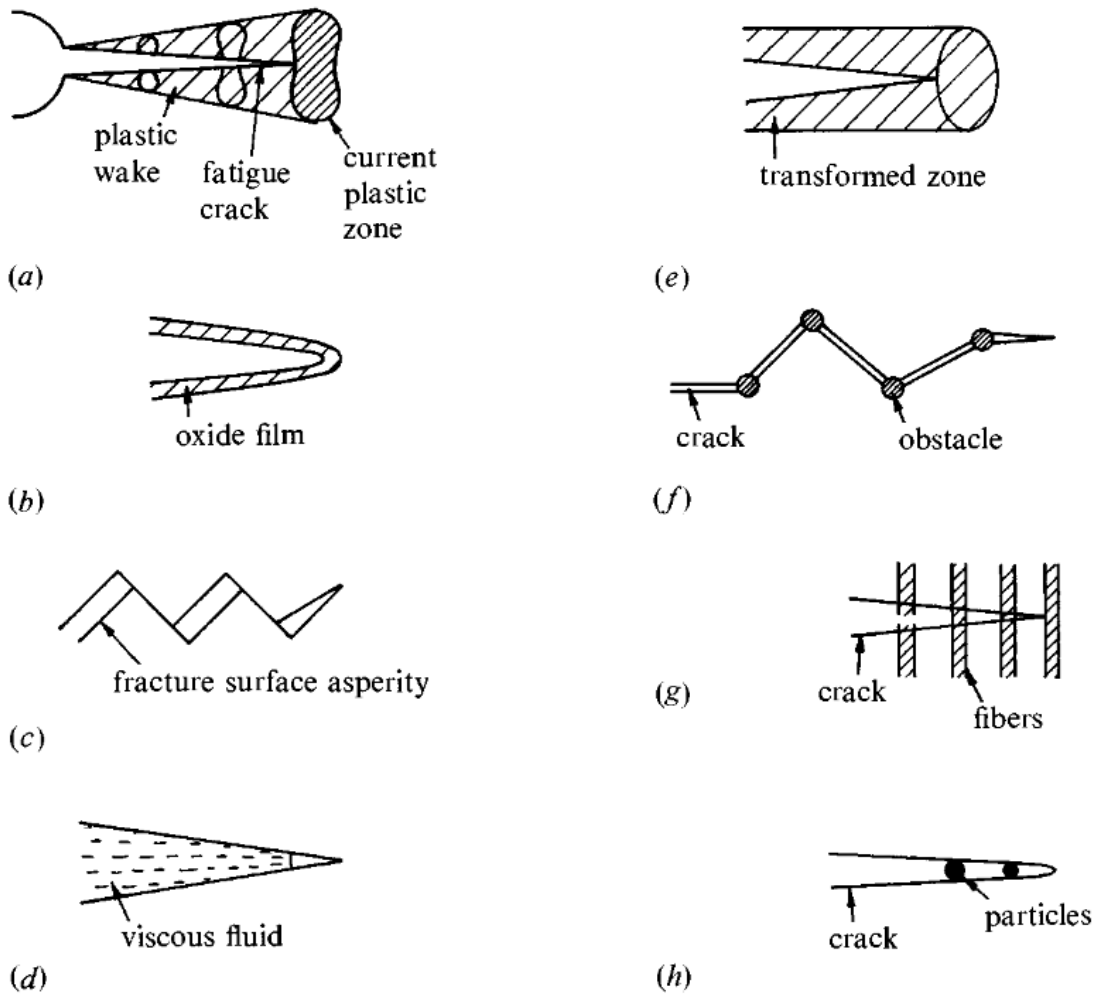

Fig.2.20 A schematic illustration of the mechanisms which promote retardation of fatigue crack growth in constant amplitude fatigue. (a) plasticity-induced crack closure; (b) oxide-induced crack closure; (c) roughness-induced crack closure; (d) fluid-induced crack closure; (e) transformation-induced crack closure; (f) crack deflection; (g) crack-bridging by fibres (h) crack-bridging (trapping) by particles [78].

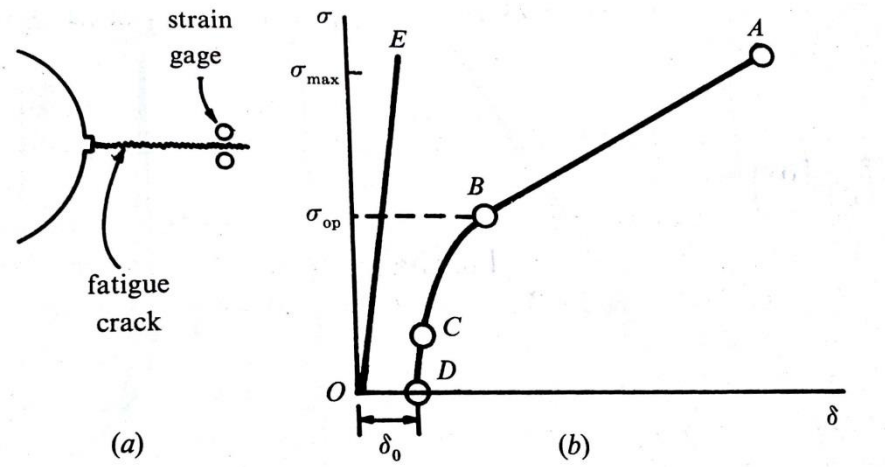

Fig.2.21 A schematic of the relationship between the applied stress and the displacement measured by strain gauges during loading from the far-field stress [78].

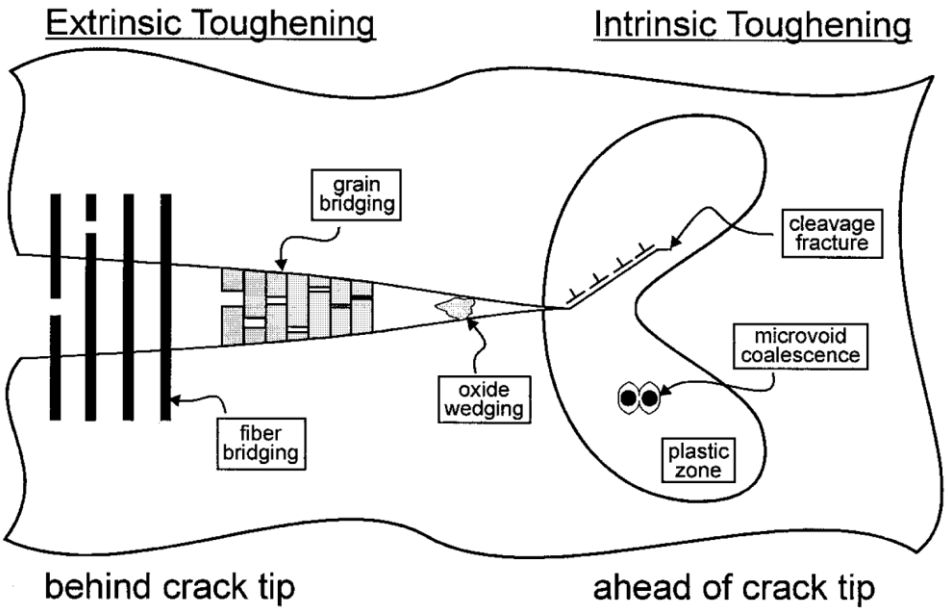

Fig.2.22 Schematic illustration of mutual competition between intrinsic mechanisms of damage/crack advance and extrinsic mechanisms of crack-tip shielding involved in crack growth [93].

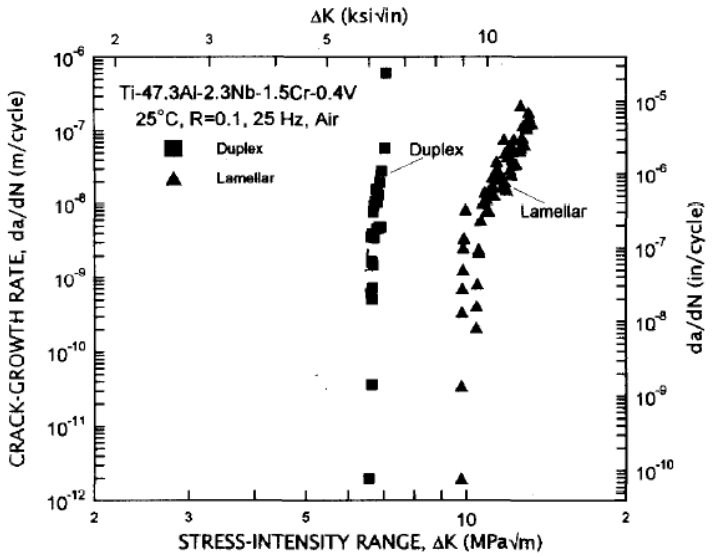

Fig.2.23 Fatigue-crack growth behaviour of two-phase γ-TiAl alloy in the duplex and lamellar microstructures at room temperature in air (R=0.l, 25 Hz) [95].

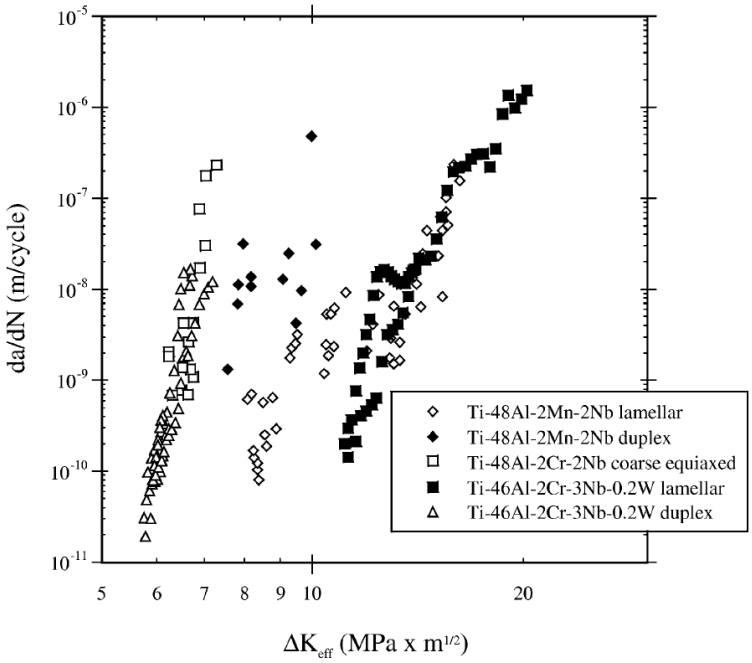

Fig.2.24 Intrinsic fatigue crack growth behaviour of various microstructures (Ti–48Al–2Cr–2Nb and Ti–48Al–2Mn–2Nb; Ti–46Al–2Cr–2Nb–0.2W) at room temperature in vacuum [89].

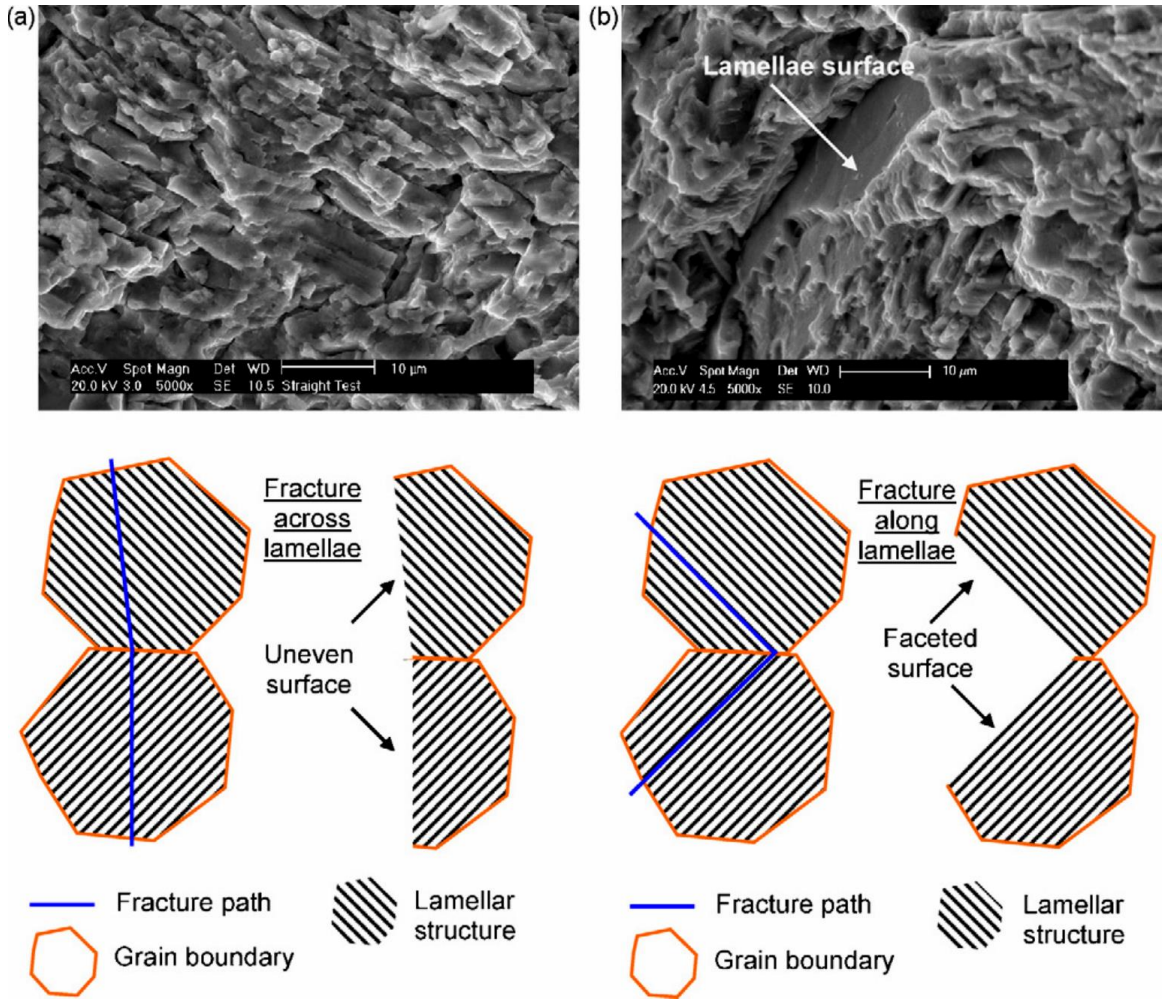

Fig.2.25 Illustration of (a) translamellar fracture (fracture across lamellae) and (b) interlamellar fracture (fracture along lamellae interface) of the fracture of lamellar microstructure of gamma titanium aluminides [102].

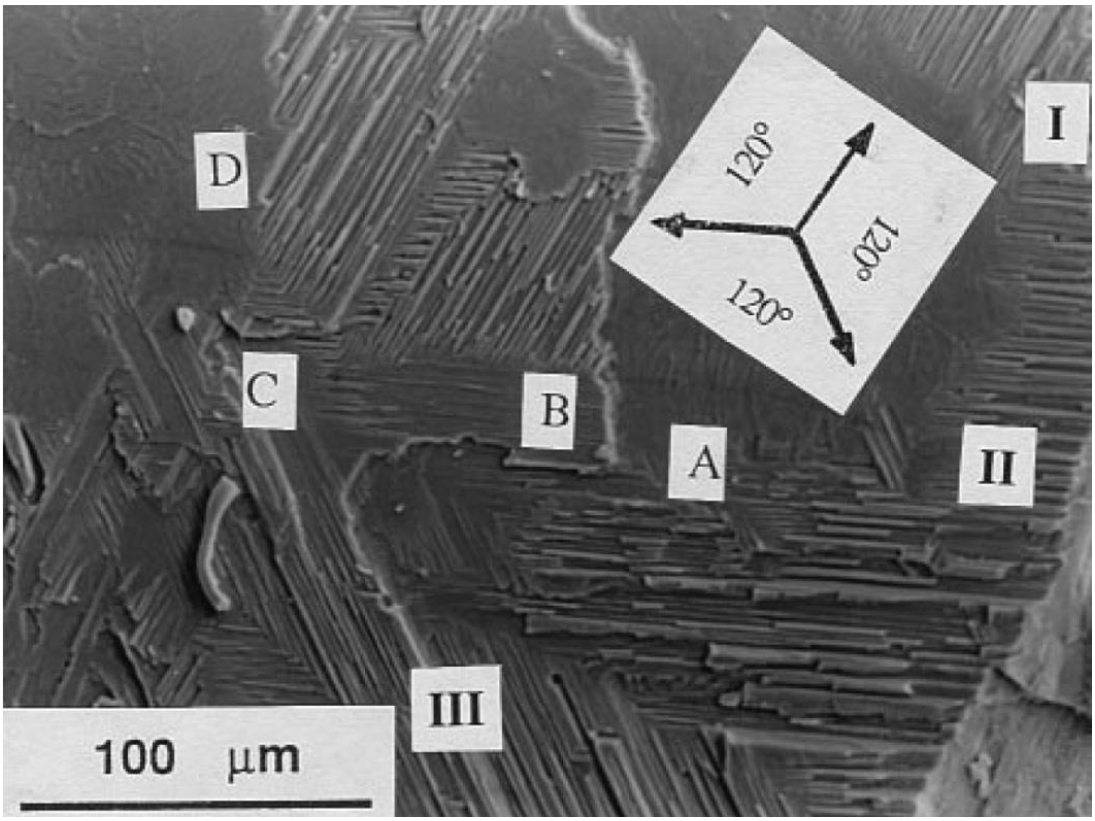

Fig.2.26 Intralamellar fracture surface taken from a low ΔK region showing the geometric patterns formed on the consecutive lamellar plates A, B, C and D. Not the three-fold symmetry located in three ordered γ domains designated as I II and III [105].

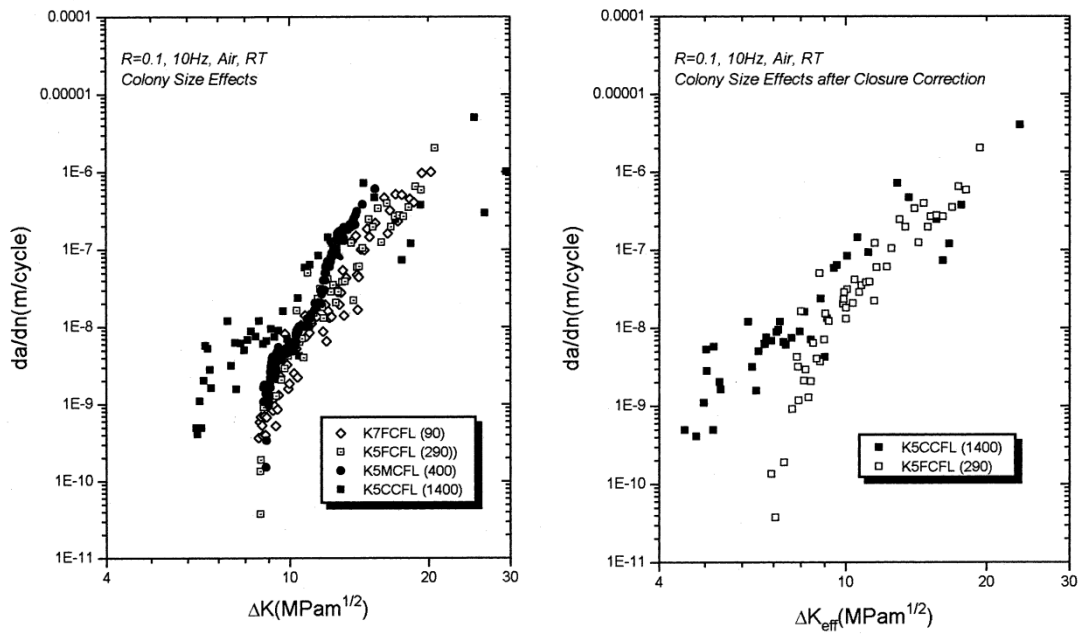

Fig.2.27 Fatigue crack propagation of Ti-46.5Al-2Cr-3Nb-0.2W (K5) and Ti-47Al-1.5Cr-0.5Mn-2.5Nb-0.18B (K7) with different colony sizes: (a) da/dN versus ΔK; (b) da/dN versus ΔK_{eff} [91].

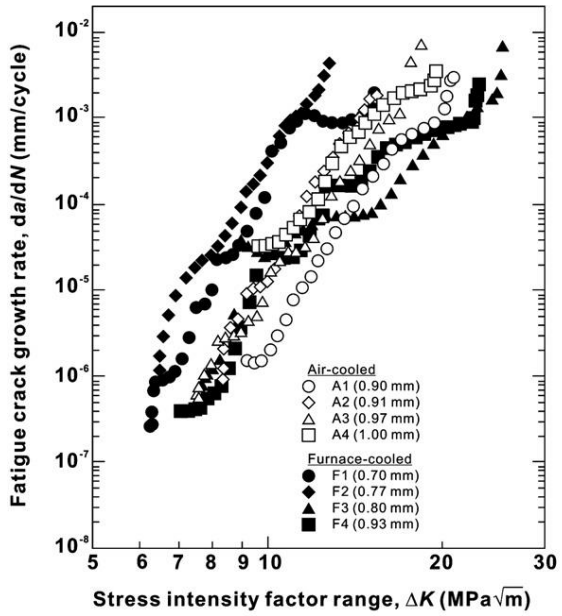

Fig.2.28 Fatigue crack growth resistance curves at room temperature: air-cooled and furnace-cooled specimens. The colony size of each specimen is given in the legend [90].

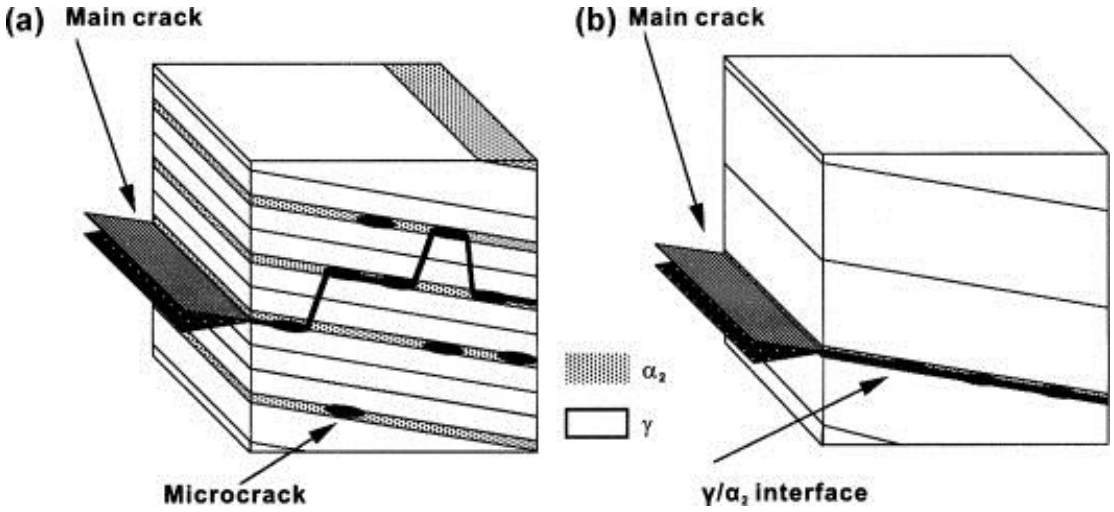

Fig.2.29 Schematic illustrations of interlamellar crack growth mechanisms in (a) air-cooled and (b) furnace-cooled specimens [90].

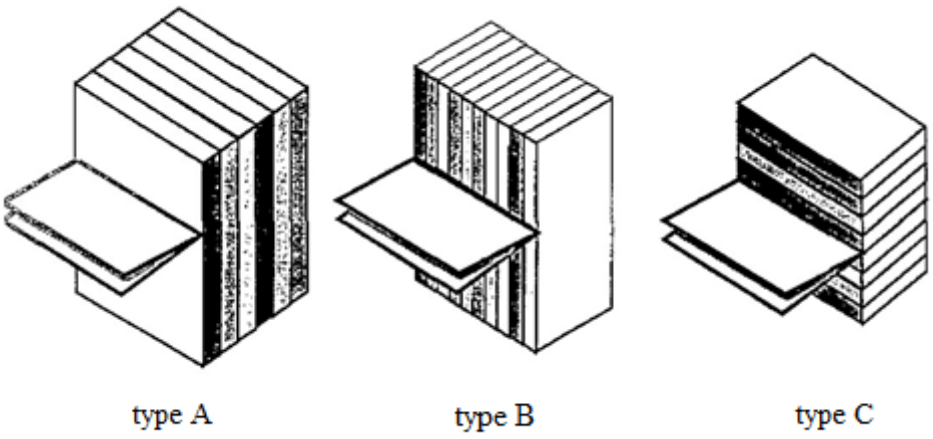

Fig.2.30 Definition of the crack growth direction with respect to lamellar orientation [111].

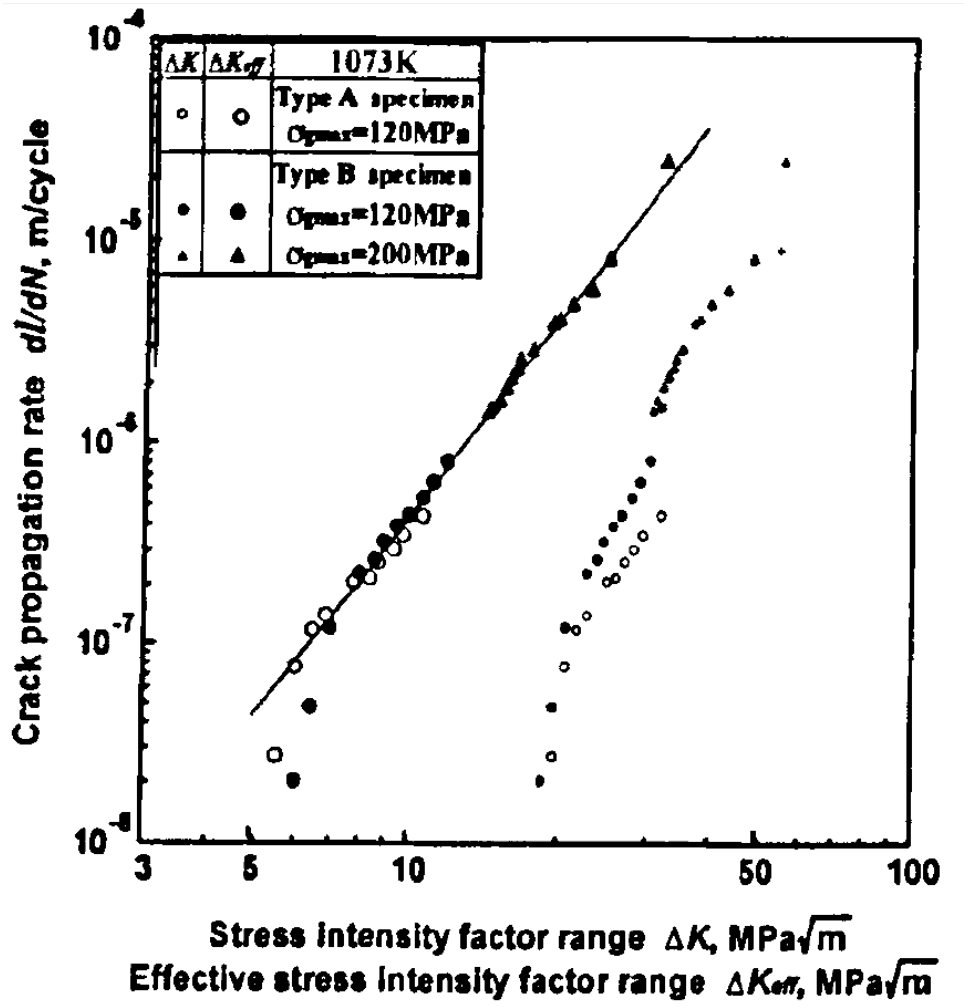

Fig.2.31 Effects of lamellar orientation on relationship between crack propagation rate and stress intensity factor range from cycle-dependent fatigue [84].

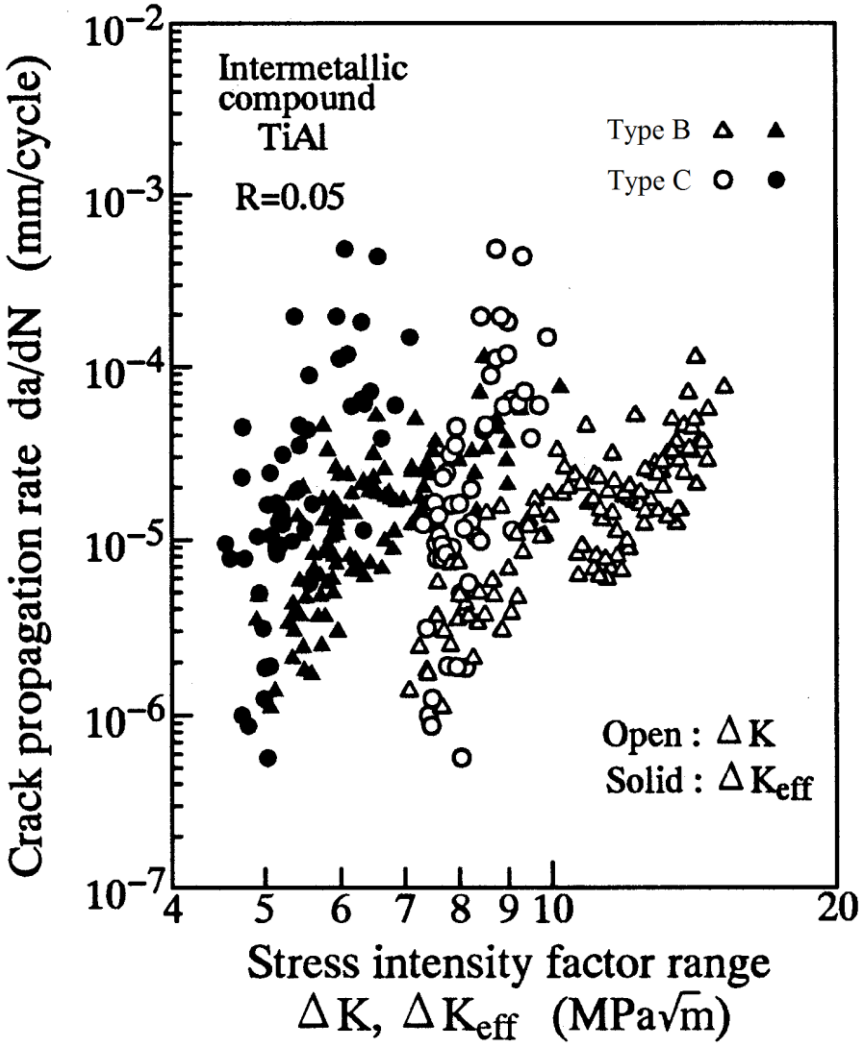

Fig.2.32 Relationship between crack propagation rate and stress intensity factor range at ambient temperature in air: type B with lamellar orientation perpendicular to crack growth direction; and type C with lamellar orientation parallel to crack growth direction [92].

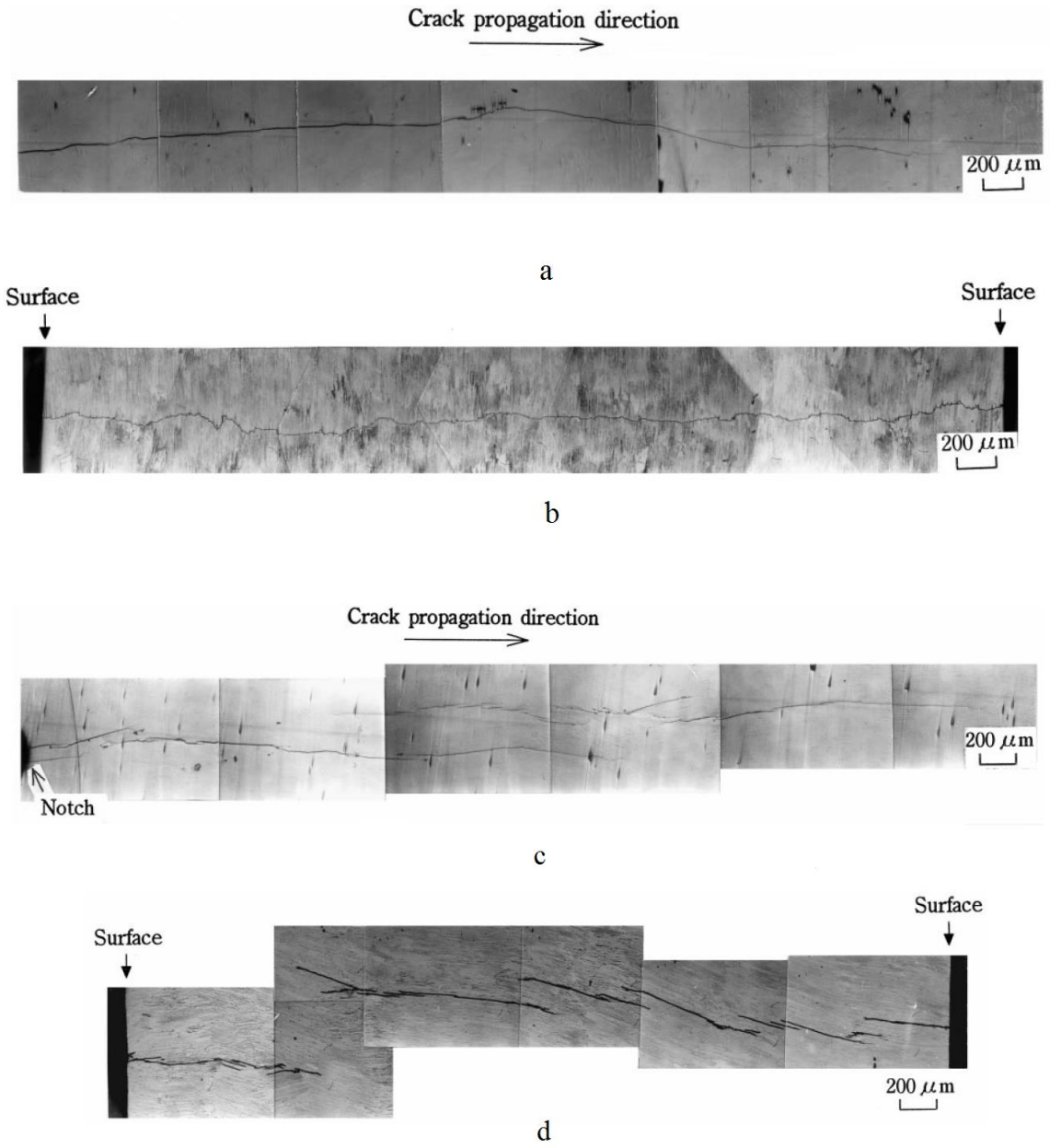

Fig.2.33 Crack propagation path on the specimen surface in specimen (a) lamellar orientation parallel to crack growth direction and (c) lamellar orientation perpendicular to crack growth direction; crack profile on the longitudinal section in specimen (b) lamellar parallel to crack growth direction and (d) lamellar orientation perpendicular to crack growth direction [92].

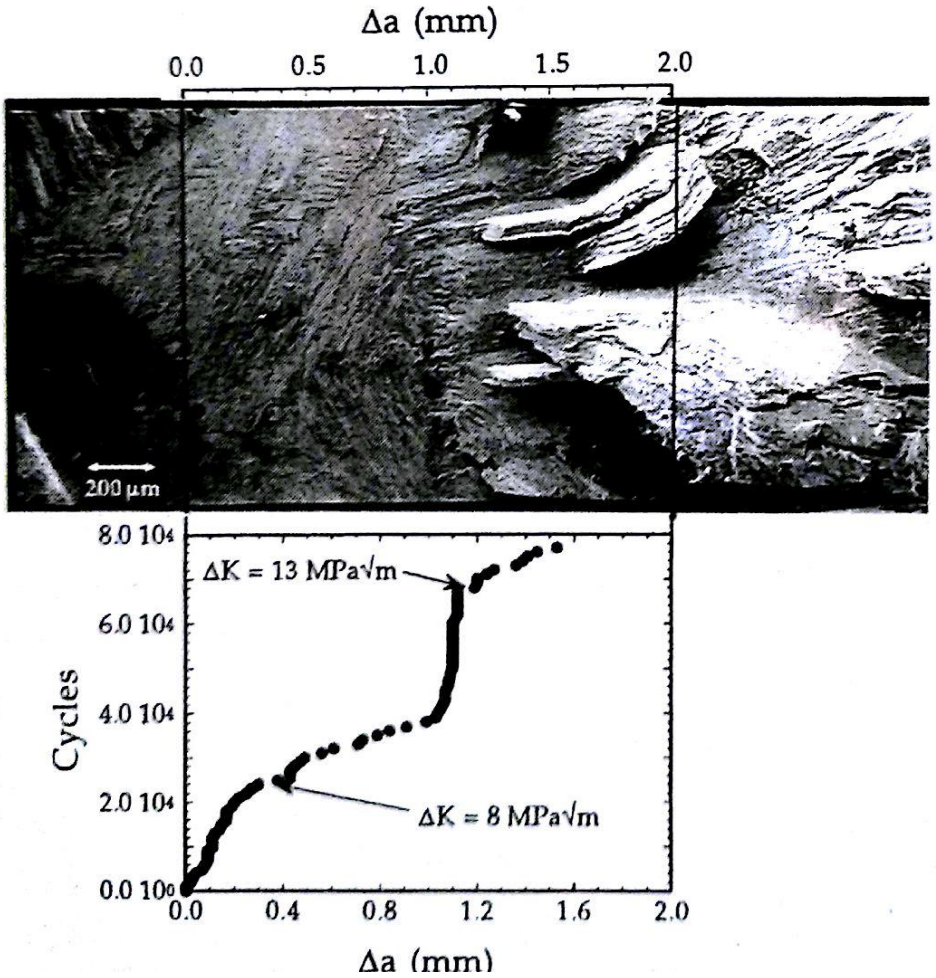

Fig.2.34 Fracture surface of a fatigue sample, where crack propagation direction is from left to right, with the corresponding crack growth curve plotted to scale. The crack stopped at the grain boundary until the applied ΔK was increased. There is extensive ligament formation in the next grain [112].

Table 2.1 Properties of titanium alloys, titanium aluminides and nickel based super alloys [2].

Property	**Ti-based**	**Ti_3Al-based**	**TiAl-based**	**Ni-based**
Structure	hcp/bcc	$D0_{19}$	$L1_0$	fcc/$L1_2$
Density (g/cm^3)	4.5	4.1-4.7	3.7-3.9	7.9-8.5
Modulus (GPa)	95-115	110-145	160-180	206
Yield Strength (MPa)	380-1150	700-990	350-600	800-1200
Tensile Strength (MPa)	480-1200	800-1140	440-700	1250-1450
Room-Temp. Ductility (%)	10-25	2-10	1-4	3-25
Room-Temp. Fracture Toughness (MPa$\sqrt{m}$)	12-50	13-30	12-35	30-100
Creep Limit (°C)	750	750	750[a]-950[b]	800-1090
Oxidation (°C)	650	650	800[c]-950[d]	870[c]-1090[d]

a Duplex microstructure. b Fully lamellar microstructure.
c Uncoated. d Coated/Actively cooled.

Chapter 3. Experimental Procedure

This chapter describes the experimental work in terms of the raw materials and the processing and heat treatment methods used in the study, types of mechanical tests, microscopy and analysis techniques to comprehend the microstructural characterization and fracture mechanisms.

3.1 Materials

3.1.1 Ti4522 (XD) and four modified forged Alloys

Ti45Al2Mn2Nb1B (at %) (4522XD) alloy is the baseline alloy and its modifications, Ti45Al2Nb2Ta1B, Ti45Al2Mn2Ta1B, Ti45Al2Mn4Ta1B and Ti45Al2Mn4Nb1B (at %), are also studied. The base alloy was from a 50kg ingot prepared by double cold hearth plasma arc melting and the modified alloys were prepared using plasma arc melting in the form of 1kg buttons. The buttons were melted 4 times to improve the microstructure homogeneity. The buttons were cut into forging billets with a height of 60mm. Isothermal forging of the billets and ingot section were carried out at 1150ºC and an initial strain rate of $1x10^{-3}$ s^{-1}. They were forged into packages with a reduction in height of about 70-80%. Heat treatment was carried out at 1320°C for 1 hour and then cooled at 20°C/min to get the refined lamellar microstructures.

3.1.2 Ti4522 (XD) as-cast Alloys

The as-cast Ti45Al2Mn2Nb0.4B ingot, of which the diameter is 50mm and the height is 200mm. It was cut into two pieces, and they were heat treated at 1320°C for 1hour. They are expected to give different lamellar spacing with different cooling rates, furnace cooling (FC) to get thick lamellar and air cooling (AC) to get thin lamellar.

Samples107 and 407 were Ti4522XD cast into slabs. The boron concentration was 0.3 and 1at% for 107 and 407 respectively. The difference in boron concentration was expected to give different lamellar colony size in cast slabs. The measured lamellar colony size was 70 and 90μm in average for 107 and 407 respectively. The slabs were HIPped at 1260°C/150MPa for 4h followed by ageing at 1000°C for 8h.

Samples containing equiaxed gamma grains were obtained by HIPping of investment cast bars containing cast defects like shrinkage and porosity. It has been demonstrated in an early work that the grains surrounding the pores underwent recrystallisation during HIPping and evolved into clusters of equiaxed gamma grains [119]. The cast Ti4522XD test bars were screened using X-ray and some with visible pores were HIPped. Two samples, 24-10-B-8 and 24-7-A-4 were chosen for fatigue crack growth threshold testing.

3.1.3 Coarse Ti4522 and Ti46Al8Nb

Two coarse columnar microstructure alloys, Ti45Al2Mn2Nb and Ti46Al8Nb alloy were prepared by using double cold hearth plasma arc melting in the form of 100mm diameter ingot. The ingots were hipped at 1280°C/150MPa for 4h. The composition of these alloys is very close to their nominal composition, and the oxygen concentration is about 600wtppm.

3.2 Microstructural characterisation

3.2.1 Specimen preparation

A small piece, approximately a 10mm cube, of each material was cut by the Struers Accutom-5 cutting machine using a silicon carbide cutting blade. They were hot mounted in conductive Bakelite powder in an OPAL 400 mounting machine for microstructure analysis. After that, they were ground by wet and dry silicon carbide abrasive grinding paper with water, step by step from grit 240 to grit 2500 about 3mins for each step before final polishing. The solution used for final polishing is activated colloidal silica, composed of OP-S suspension and 5% hydrogen peroxide. All the samples were polished for around 10mins with a MD-Chem polishing disc produced by Struers. Normally, for most cases, 10-mins polishing is good enough for microstructural characterisation by scanning electron microscope (SEM) with back scattered electron (BSE) imaging. However, another polishing procedure is needed with a smaller force to prepare samples for electron back scatter diffraction (EBSD) mapping. All the polishing and grinding was carried out in a Struers LaboPol-5 polishing unit fitted with a LaboForce-3 automatic polishing head. Finally, the polished samples were cleaned by cleaning agent, water and absolute ethanol, and dried.

3.2.2 Microscopy techniques

A Philips XL-30 and JOEL 7000 were the facilities used for microstructure investigation. The Philips XL-30 is Lanthanum hexaboride (LaB_6) scanning electron microscope (SEM), while JOEL 7000 is a field emission one. Both of them can be used for back scatter electron (BSE), secondary electron (SE) and electron back scattered diffraction (EBSD) analysis.

Since the secondary electrons are ejected from the top layers of the specimen surface, they are of low energy and cause topographic contrast. Therefore, the intensity depends on surface topography, rather than atomic number. SE imaging technique is used for the characterisation of fracture surface in this study. As the intensity of back scattered electrons is in proportion to atomic number, BSE imaging technique is used to distinguish different phases. The microstructure investigation for the supplied alloys is carried out by BSE imaging, as there is a big difference in atomic mass for α_2 and γ phases. The accelerating voltage used for both SE and BSE imaging is 20 KV.

As a microstructural-crystallographic technique, EBSD is widely used for grain boundary and morphology analysis, texture investigation, crystal orientation mapping and phase identification. To operate EBSD, the specimen has to be tilted 70°, the working distance must be 12-17mm and the accelerating voltage should be 20 KV.

3.2.3 Colony size measurement

The colony size is measured using the linear intercept method with SEM BSE images (Fig.3.1). The colony size is calculated on each transverse line, but the first colony and the last colony on each transverse line is not included.

3.2.4 Lamellar spacing measurement

The measurement of lamellar spacing includes the measurement ofα_2 lamellar spacing, γ lamellar thickness and lamellar spacing. The α_2 lamellar spacing is the distance between two adjacent α_2 lamellae; γ lamellar thickness is the thickness of γ lamellae and lamellar spacing

is the mean lamellar spacing including γ/α_2 as well as γ/γ interfaces, as shown in Fig.3.2. They are measured by using 3D stereographic SEM analysis, as shown in Fig.3.3. The specimen was cut from the thread of the fatigue crack propagation threshold test pieces and hot mounted, and then it was cut again to produce a transverse section, so two faces of the specimen can be observed. Both faces were ground and polished by using the standard grinding/polishing procedure mentioned above. The prepared samples were firstly observed with BSE to obtain the α_2/α_2 lamellar spacing, and then lightly etched with Kroll's reagent, which is 2%vol hydrogen fluoride (HF), 10%vol nitric acid (HNO_3) and balance water, in order to reveal the γ/γ interfaces by SEM evaluation. Finally α_2 lamellar spacing, γ lamellar thickness and lamellar spacing were corrected by a factor λ. The angles a and b are shown in Fig.3.2 (b) and Fig.3.2 (c) respectively.

$$\lambda = \frac{sinb\sqrt{(cosasinb)^2 + (sinacosb)^2 + (sinasinb)^2}}{|-1 + cosb^2cosa^2|}$$

3.3 Mechanical testing

3.3.1 Hardness testing

The hardnesses were measured by Vickers hardness method with polished samples and the applied load was 20Kgf. The Vickers hardness test method consists of indenting the test material with a diamond indenter, in the form of a right pyramid with a square base and an angle of 136° between opposite faces subjected to a load of 1 to 100kgf. The two diagonals of the indentation left in the surface of the material after removal of the load are measured using a microscope and their average calculated. The area of the sloping surface of the indentation

is calculated (Fig.3.4). The Vickers hardness is the quotient obtained by dividing the kgf load by the square mm area of indentation.

$$HV = \frac{2FSin\frac{136°}{2}}{d^2}$$

Where:

F= Load, in kgf;

d= Arithmetic mean of the tow diagonals, in mm;

HV= Vickers hardness.

3.3.2 Tensile testing

The ϕ9mm (diameter) × 60mm (length) cylinders were cut from the original blocks using EDM (electro discharge machine) and sent out to GTG Engineering Co. Ltd and machined by turning to the final shape with a 20mm gauge length and a diameter of 4mm, as shown in Fig.3.5. The tensile tests were carried out by a Zwick servo hydraulic testing machine at an initial strain rate of 1×10^{-4} s^{-1} in air, and an extensometer with a gauge length of 20mm was used to track the displacement. The load/displacement curves were converted to engineering stress/engineering strain curves, and then the ultimate tensile strength (UTS), yield stress and elongation were measured and calculated. The tensile test of the baseline alloy, forged Ti45Al2Mn2Nb1B (4522XD) were carried out at room temperature, 450°C and 650°C, while all other alloys were tested at 650°C to see the alloy elements effect on high

temperature capability. There are two test pieces for each condition. The facture surfaces of the failed tensile test pieces were investigated using the Philips XL30 SEM.

3.3.3 Fatigue crack propagation threshold testing

3.3.3.1 Specimen preparation

All tests were done with corner notched specimen, as shown in Fig.3.6 (a). The test pieces of all forged and cast 4522XD and modified alloys were machined by GTG Company. Cylinders were cut from the ingots and machined into test pieces containing a square cross sectioned gauge of 5x5 mm^2 in area and 25mm in length. From previous studies within the group, pre-cracking does not affect the threshold of this material, therefore, instead of pre-cracking, in this research; a notch was induced in the middle of the gauge by EDM using a fine wire (ϕ30μm) with a depth of 0.5mm and a length of 1mm shown in Fig.3.6.

The coarse Ti4522 and Ti46Al8Nb alloys were used to investigate the effect of lamellar orientation on fatigue crack propagation threshold. Therefore, it is crucial to choose the proper lamellar orientation when preparing the test pieces. For this part of the work, firstly, cylinders were cut from the ingot section longitudinally and sent to GTG Company to machine the thread. Then the machined specimens were sent back to IRC (interdisciplinary research centre) to machine the gauge by EDM cutting. After that, the final test pieces were ground about 40μm with grit 400 SiC grinding paper manually to remove any damage caused by EDM, then an additional hand grinding with grinding paper from grit 800 to grit 4000 and polishing with polish cloth was operated to all four faces of the gauge area. Finally, they were etched by Kroll's reagent for optical microscopy.

An Axioskop-2 MAT digitized optical microscope, combined with image analysis software Axiovision Rel.4.8 was used to examine the etched samples. The area of ±2mm of the middle of the gauge length shown in Fig.3.7 at each corner was observed to choose the position to induce a notch. Only the position of which the size of the lamellar colony perpendicular to the loading axis on both sides of the corner exceeds 0.7mm can be selected, so the notch can be made within one lamellar colony. The position was marked, and the specimens were sent to Department of Mechanical Engineering, University of Birmingham to make the notch by EDM, which can be accurate to 1μm.

3.3.3.2 Fatigue crack propagation threshold test

The fatigue crack propagation threshold tests were based on Rolls-Royce standard test procedure document (MMM31002) and British Standard BS 6835-1:1998. All the tests were carried out at 650°C in air at a stress ratio, R, of 0.1 and frequency of 10HZ with a servo-hydraulic Instron 8501 test machine with Instron 8500 control system and 10KN load cell, shown in Fig.3.8. The wave form employed during testing was a standard sinusoidal wave. Due to the brittleness of the material, the fatigue crack propagation tests were done using a method proposed by Suresh (1985) and Christman & Suresh (1986) [78], but without pre-crack. It is carried out by increasing the maximum load very carefully (0.2KN per step) from an initial value well below the anticipated threshold. The initial load was chosen corresponding to a ΔK which is about 20% lower than the expected threshold ΔK value, according to experience. At each load level, 5×10^4 cycles were spent as a minimum value. The test was stopped when consistent crack growth was observed and the crack was allowed to grow until it reached a predetermined crack length. After that, the number of cycles was recorded, and the specimen was cooled down to room temperature to break it.

The extension of the fatigue crack was automatically monitored with a Direct Current Potential Difference (D.C.P.D) technique by the potential drop. The D.C.P.D. technique is based on the principle that the electrical field applied on the specimen can be influenced by the change of crack length or shape. A pair of Pt wires, sheathed in braided silica to prevent contact with the chamber wall, was welded with spot welding machine MacGregor m1-10 as close as possible to the notch on both sides of the notch and the other end was connected to a chart recorder. When a constant direct current, provided by a power supply, is passing through the specimen, the potential drop caused by crack propagation is monitored by a data/chart recorder as a function of time, in proportion to the number of cycles. The typical current passing through the specimen was in a range of 6-8 amps, which generated an initial voltage of 200μv at room temperature. As the increase of crack length can cause the increase of electrical resistance, when the input current is constant, the output potential increases. Finally, the crack length was worked out. The principles are shown in Fig.3.9.

3.3.3.3 Data processing

The instantaneous voltage V was normalized by an initial reference potential, V_0, and the crack length was worked out by using the following relationship based on the in-house experimental calibration:

$$a/W = 0.000181(V/V_0)^3 - 0.000528(V/V_0)^2 + 0.109103\left(V/V_0\right) - 0.008636$$

However, the crack length worked out by D.C.P.D method maybe different from the actual crack length. Therefore, both the initial crack length and the final crack length are required to be calibrated before the data processing. . The actual crack length was measured from the

optical images by Axiovision Rel.4.8 using a seven point secant method. 7 points were selected on the initial front line and final crack front line at specific angles (1°, 15 °, 30 °, 45 °, 75 ° and 89 °), as shown in Fig.3.10. Then the average values were used for calculation of da/dN and ΔK values.

The crack growth rate was investigated by plotting the crack growth rate (da/dN) as a function of stress intensity factor range (ΔK). The crack length used for calculation is after correction. The number of cycles to that crack length is calculated from the corresponding PD value according to the chart. A five-point method was used to smooth the crack growth rate curve. Then stress intensity factor range (ΔK) for corner-notch specimen was calculated.

3.3.3.4 Fractography

The fracture surfaces of failed test specimens were studied by a scanning electron microscope (SEM). Two SEMs were used for fractographic analysis: Philips XL30 and JEOL 7000. The specimens failed from the notch were examined using secondary-electron images along a line at 45 ° to the specimen edge. Both microscopes were operated with an accelerating voltage of 20kv and a sample tilt angle of 0°.

3.3.3.5 Roughness

The fracture surface roughness was assessed using a LEXT OLS4000 3D Laser Measurement Microscope with a laser spot size of 0.2μm. The surface roughness, R_a, was measured within the fatigue region with a length of 1mm and a width of 160μm, shown in Fig.3.11. The R_a value is defined as the arithmetic mean value in microns.

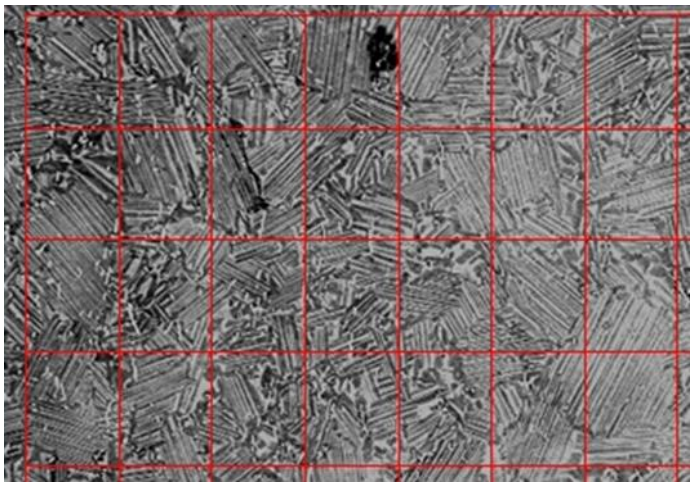

Fig.3.1 SEM BSE image showing the linear intercept methods for colony size calculation.

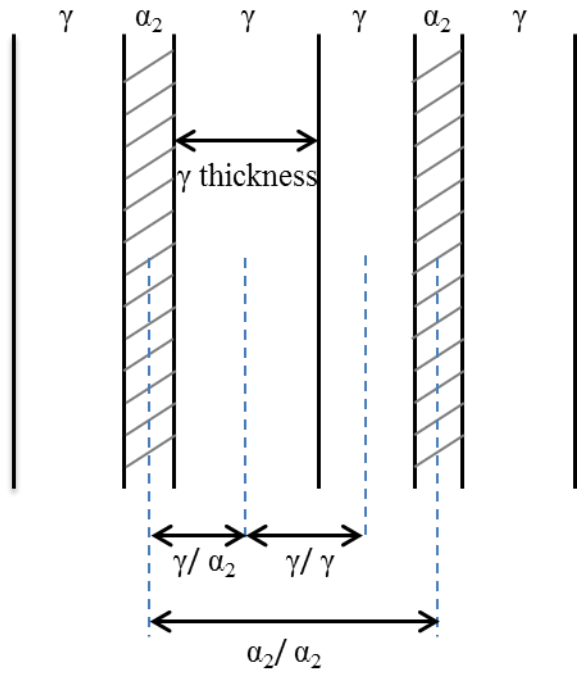

Fig.3.2 Schematic illustration showing the definition of γ lamellar thickness, γ/ α_2, γ/γ and α_2/ α_2 lamellar spacing.

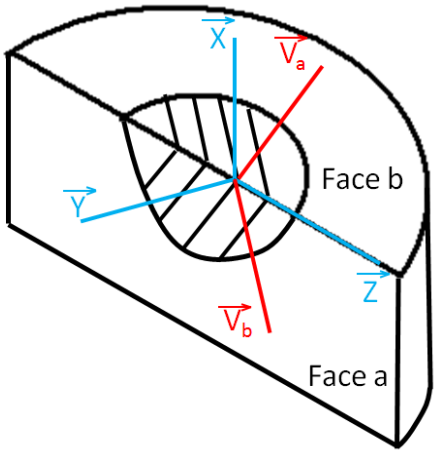

(a)

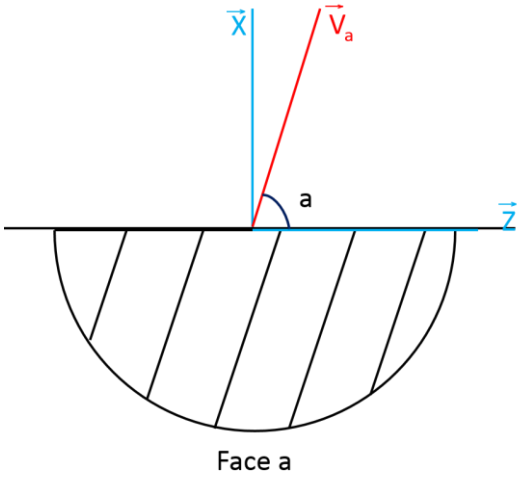

(b)

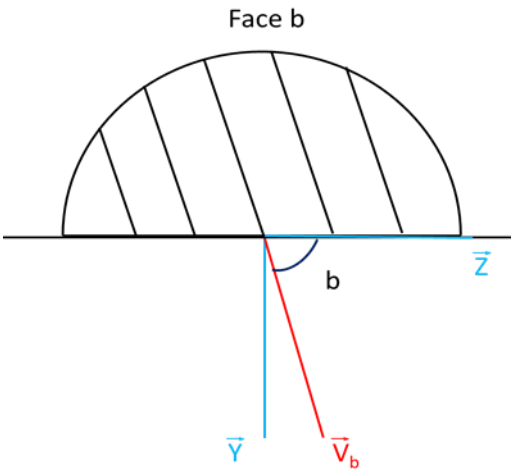

(c)

Fig.3.3 3D stereographic SEM analysis (a) Definition of coordinate system for lamellar orientation determination; (b) lamellar orientation on face a; (c) lamellar orientation on face b.

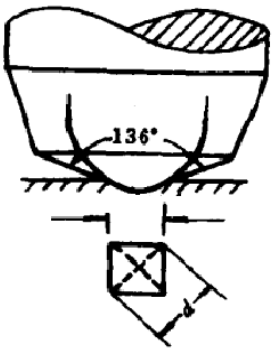

Fig.3.4 Vickers hardness test.

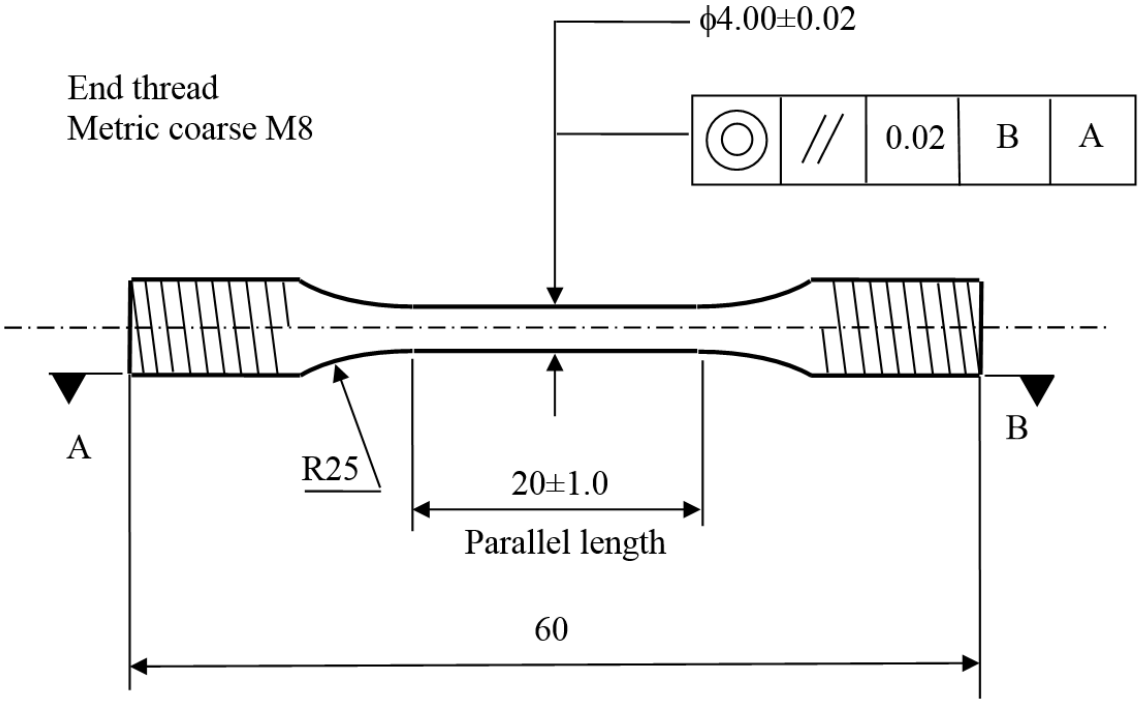

Notes: Roughness value for machined surfaces to be 1.6 micrometers unless otherwise stated; all dimensions and tolerances are in mm unless otherwise stated

Fig.3.5 Schematic dimension and machining requirement of round tensile test piece.

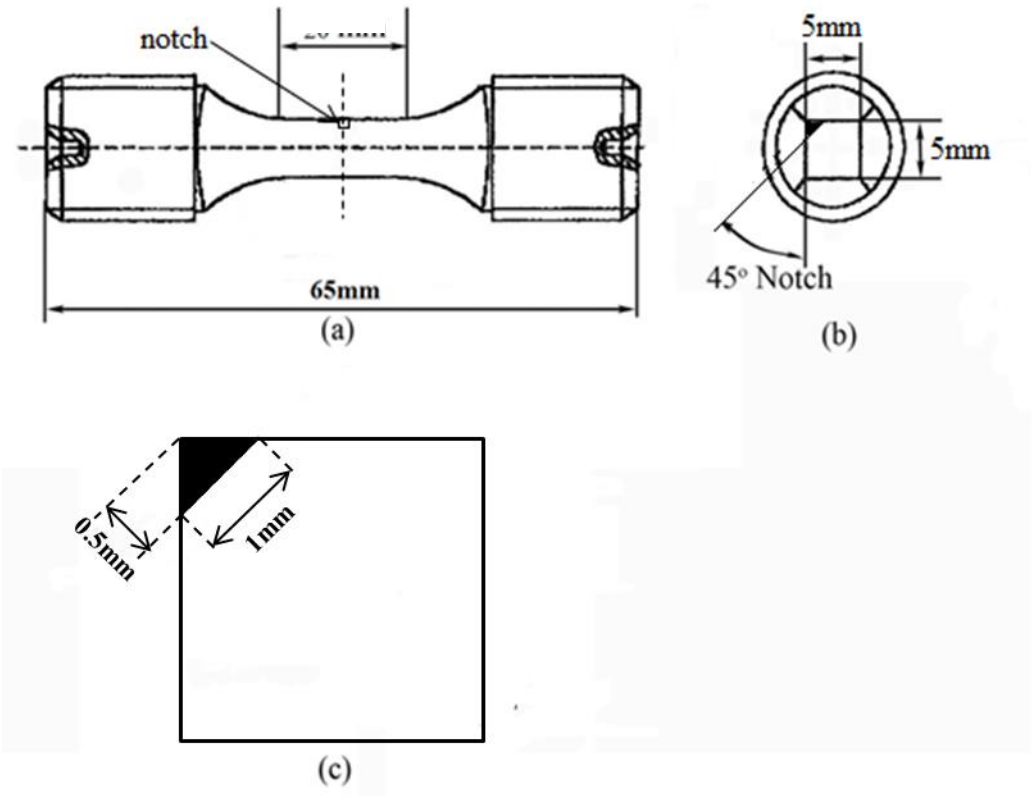

Fig.3.6 Schematic specimen geometry for fatigue threshold crack propagation testing: (a) geometry and dimension of the specimen; (b) position of the notch and cross section of the gauge; (c) depth and length of the notch.

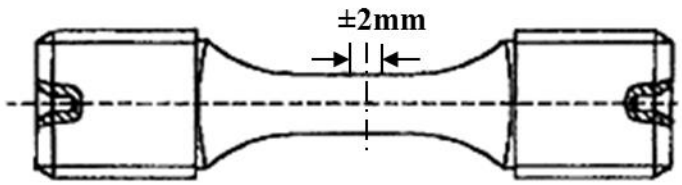

Fig.3.7 Optical microscopy region to choose the position to make a notch.

Fig.3.8 Installation of tension fatigue crack propagation threshold test in a servo hydraulic machine.

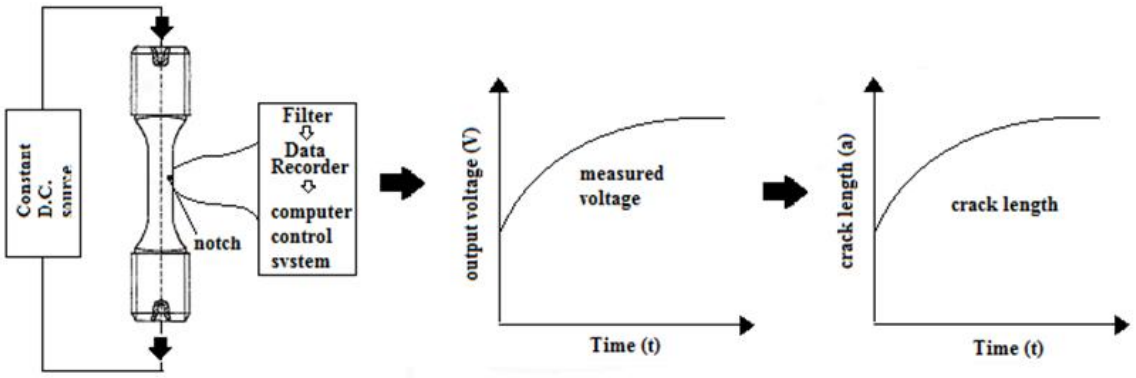

Fig.3.9 Schematic illustration showing the principle and data processing for D.C.P.D. technique used in testing.

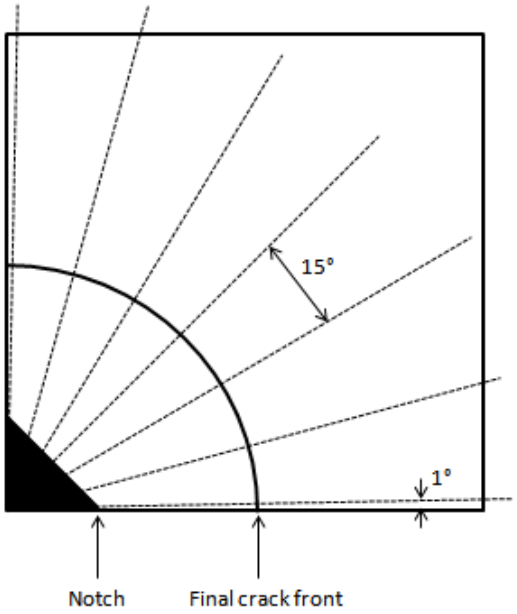

Fig.3.10 Schematic diagram of crack length measurement.

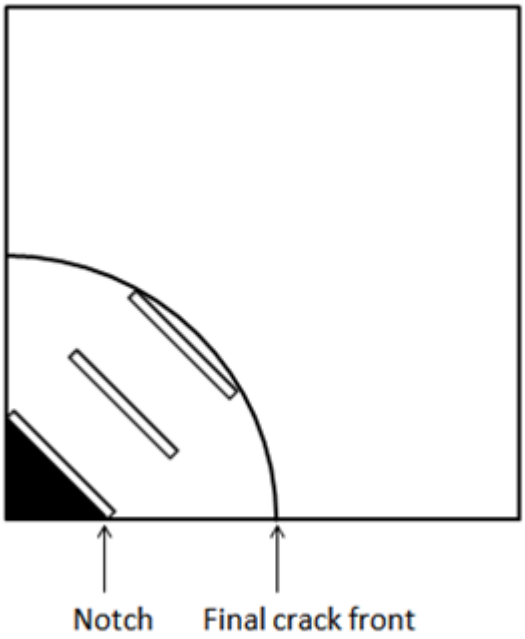

Fig.3.11 Schematic diagram of roughness measurement.

Chapter 4. Effects of microstructural parameters on Fatigue crack propagation threshold[1]

4.1 Microstructure evaluation

The material selection and heat treatment were carefully designed to provide different microstructural parameters in as-cast Ti4522XD alloys: thin lamellae by air cooling (AC), thick lamellae by furnaces cooling (FC), and large colony size by reducing the content of boron from 1% in the baseline alloy to 0.3% (107), small colony size (407) and the one which contains more equiaxed gamma grains (NL).

The microstructures were examined using the threaded part of the test pieces with scanning electron microscopy (SEM) using back scattered electron (BSE) microscopy. A typical BSE image of lamellar Ti4522XD is shown in Fig.4.1, with γ laths appearing dark, α_2 laths appearing grey and borides appearing bright. Small amounts of equiaxed gamma grains are observed to reside at colony boundaries.

The microstructures of these alloys are shown in Fig.4.2 (a)-(e). It is clear that the microstructures of most alloys are fully lamellar, except alloy NL, which contains a large amount of equiaxed gamma grains, exhibiting a near fully lamellar microstructure. Although

[1] The contents of this chapter are based on the paper by Yang J., Li H., Hu D., and Dixon M., Microstructural Characterisation of Fatigue Fracture Surfaces of a Lamellar TiAl Alloy. Intermetallics, 2014. 45: pp. 89-95. According to Elsevier's policy, the contents of published journal articles can be included in a thesis. *http://www.elsevier.com/authors/author-rights-and-responsibilities*

there are lots of equiaxed gamma grains in this alloy, the gamma grains are still dispersed. They are not evenly distributed but exhibit as the gamma grain clusters. The average lamellar colony sizes of alloy AC, FC, 107 and 407 are about 100μm, as shown in Table 4.1. The average colony size of alloy 107 and 407 is similar, which is not as intended. The lamellar colony size of alloy NL is much smaller; with the average colony size of about 40μm. The volume fraction of the equiaxed gamma grains is about 10%, and the size of the gamma grain clusters can be larger than 100 μm. From the SEM BSE images of the lamellar thickness of alloy AC and FC, it is obvious that the lamellar spacing of alloy FC is much larger than the AC sample. The average α_2 lamellar spacing (the distance between the α_2 plates), average thickness of γ laths and the average lamellar spacing (the mean lamellar spacing including γ/α_2 as well as γ/γ interfaces) are also studied and the summary of the data is given in Table 4.2. A decrease in the cooling rate during heat treatment, i.e., from air cooling to furnace cooling, increased the α_2 lamellar spacing, lamellae thickness of γ laths and the lamellar spacing. These three parameters of the furnace-cooled samples are almost double those of the air-cooled one. The volume fraction of α_2 phase is determined to be ~25% for the air-cooled samples and ~20% for the furnace-cooled samples. The α_2 lamellar spacing, γ lamellae thickness and lamellar spacing of alloy 107 and 407 are very close and between that of alloy AC and FC. The lamellar colony orientation was investigated by electron back-scattering diffraction (EBSD) and the (0001) pole figure of the alpha2 phase of alloy 407 is shown in Fig.4.3. Owing to the fact that each lamellar colony descended from one prior alpha grain, the orientation of each (0001) $_{\alpha 2}$ spot is the orientation of the lamellar interfaces in each colony. Thus, the pole figure shown here reveals that the lamellar colonies are randomly oriented.

4.2 Fatigue crack propagation threshold testing results

The threshold stress intensity factor range (ΔK_{th}) of all samples tested at 650ºC in air with stress ratio of 0.1 is measured to be between 5.5-7 MPa$\sqrt{m}$, as summarized in Table 4.3. Two test pieces of each alloy were tested in order to obtain some indication of the repeatability of the properties. Fatigue crack growth resistance curves, fatigue crack growth rate (da/dN) versus stress intensity factor range (ΔK), are shown and compared in Fig.4.4-6. It is obvious that at this temperature, once the threshold stress intensity factor range is exceeded, the cracks accelerate rapidly with the increase of ΔK, which can be demonstrated as the cliff edge appearance of the curves at the near threshold region. This feature is quite common in TiAl alloys. The threshold value of alloy AC is slightly higher than that of alloy FC. However, the difference is subtle. Such characteristics follow through all the fatigue crack growth resistance curves, shown in Fig.4.4. It also can be seen from Fig.4.5 that there is no obvious difference in threshold between alloy 107 and 407. Alloy NL shows the most scattered threshold values. Overall, the fatigue crack propagation threshold values of these alloys is within a very narrow range.

4.3 Fatigue fracture surface features

4.3.1 Overall view

The overview of the fracture surfaces of alloy AC, FC, 107, 407 and NL is shown in Fig.4.7-9 along the diagonal of the broken test piece with the crack growth direction from right to left. A straight notch front induced by EDM is shown on the right edge, and a large area of fatigue crack growth and a final monotonic tensile fracture area is displayed from right to left. The

boundary between the fatigue and tensile fracture regions can be easily identified under optical microscopy through the shade of discolouration caused by oxidation during the fatigue test, shown in Fig.4.10. The tensile failure was carried out at room temperature and therefore gives a bright colour. Although the boundary between the fatigue and tensile fracture regions cannot be seen by SEM, the subtle topological contrast brought out by the SEM image is still discernible for the investigated material. The stress intensity factor range ΔK starts from the threshold right ahead of the EDM notch at the end of fatigue region in Fig.4.7-4.9.

It can be seen from these images that the fracture surface becomes rougher as the cracks propagate. The roughness was examined by a Laser Measurement Microscope and the results of alloy 107 and 407 are shown in Table 4.4. The given data also reveals that the roughness increased with increase of the stress intensity factor range ΔK.

Two dominant fracture mechanisms, interlamellar fracture and translamellar fracture, have been observed and are shown in Fig.4.11. In these two images, the fatigue crack propagation direction is from bottom to top, which applies to all the images of fracture surface of fatigue tested samples in this thesis, except the montages of the fracture surfaces as in Fig.4.7-9. There are no striations found on the fracture surface in the fatigue region, which would be typical for stable fatigue crack propagation for ductile materials. Some other features, such as intergranular fracture caused by the failure along equiaxed gamma grain boundaries, debonding between borides and the matrix and the transverse ridges on the translamellar fracture surfaces, are also observed.

4.3.2 Interlamellar fracture

Interlamellar fracture occurred throughout the crack growth region as can be seen by the group of facets, shown in Fig.4.11a. Those facets could be darker or brighter than their surroundings when examined by secondary electron SEM, depending on their orientations. Interlamellar fracture was observed more at the high ΔK region at the left side of the images in Fig.4.7-9. The dark facets, shown in Fig.4.11a and Fig.4.13a, are from the lamellar colonies which are parallel to or having small angles with the fracture plane. With increasing of the angle between the facet and fracture plane, the facets appear brighter and their morphology is more like a cliff-edge. However, it is difficult to see such cliff-edges by SEM at low magnification. Fig.4.12 shows two examples of interlamellar fracture surfaces with cliff-edges at high magnification. These two interlamellar fracture surfaces are from the lamellar colonies with an angle of about 50-60° off the stress axis. Although their orientation with respect to the stress axis is similar, their orientation with respect to the overall crack propagation direction is very different. In Fig.4.12a, the lamellar interface trace of the concerned colony is almost parallel to the overall crack propagation direction whilst in Fig.4.12b it is almost perpendicular to it. The details of the fracture surface of the cliff-edge interlamellar fracture were examined through rotating the sample by 60° to make the faceted surface almost perpendicular to the beam direction and are shown in Fig.4.13b. It is clear that in contrast to smooth faceted fracture surface in Fig.4.13a, the fractured lamellar interfaces in this colony are very rough. Examination on the fractured interfaces of other cliff-like interlamellar fracture revealed that both smooth surfaces and rough surfaces were observed. However, rough fractured interfaces were not observed in the colonies almost parallel to the fracture plane.

Interlamellar failure was found both on γ/α_2 interfaces and γ/γ interfaces under cyclic load. Fig.4.14 (a) - (d) shows the SEM SE images and SEM BSE images of the profile of two interlamellar fractured colonies milled by FIB (focused ion beam). The interlamellar fracture surfaces in Fig.4.14 (a) and (b) consist of several facets and steps. The α_2 laths appear bright on the milled surface in Fig.4.14 (b). It is clear that the extension of both the lamellar interface A and B on the milled section exhibit bright bands in the BSE image, therefore, the interlamellar fracture in this colony occurs on the γ/α_2 interfaces. Fig.4.14 (c) and (d) show the SE and BSE image of another interlamellar fractured colony that failed on the γ/γ interface, as the extension of the interface shows dark in the BSE image on the milled section in Fig.4.14 (d).

The orientation of interlamellar-cracked colonies observed on the fracture surface in the fatigue zones was studied using SEM by tilting the sample stage. The stage was tilted to maximise or minimise the shown area of a lamellar interface. The orientation can be worked out from the tilt angle with an accuracy of about 5° and also the angle between the facet and the overall crack propagation direction with an accuracy of about 1°. The orientation of the interlamellar-cracked colonies is described by a pole figure and the three axes are defined as follows: the direction of the applied stress, N, is in the centre; the A axis which is at the top of the pole figure is parallel to the overall crack propagation direction and the B axis to the right of the pole figure is perpendicular to the overall crack propagation direction, as shown in Fig.4.15. The orientation of the interlamellar-cracked colonies is shown in the pole figures by the poles of their lamellar interface normal and can be described by two angles. For example, two angles of a lamellar colony labelled ‘16.1’ are shown in Fig.4.16a. The first angle is the angle between lamellar interface normal and the N axis and is referred to as the ‘Orientation’

for simplicity. The second angle is the angle between the lamellar interfaces and the overall crack propagation direction which is the angle between the projection of lamellar interface normal onto the fracture plane and the A axis. In the present study, this angle is referred to as the 'Sub-Orientation'. Obviously, the orientation of the two interlamellar-cracking facets in Fig.4.12 is similar but their Sub-Orientations are different. Facet (a) is nearly parallel to the overall crack propagation direction while facet (b) in is almost perpendicular to it. 5 samples were selected for examination and the results are given in pole figures in Fig.4.16a-e. Every dot in the pole figures represents the normal of a lamellar interface from an interlamellar-cracked colony, and the stress intensity range ΔK of each colony is given next to it. The given stress intensity range ΔK here for each point on the fracture surfaces was measured by linear interpolation between the crack length of the specific point and that of the notch. As mentioned in chapter 3, the crack length is determined using D.C.P.D method. As this method can only guarantee accuracy to single decimal place of the stress intensity range values, the results given here cannot be treated as quantitative, but semi-quantitative at most.

From the points highlighted in the pole figures, several conclusions can be drawn. Firstly, interlamellar fracture can occur when the Orientation of lamellar colonies is close to 0° at both low and high ΔK levels. Secondly, interlamellar fracture of lamellar colonies with high angle Orientation can occur only at high ΔK, exhibiting cliff-edge morphology. Finally, when the Orientation is constant, the interlamellar cracking behaviour is almost not affected by different Sub-Orientations. Based on the examination of the fracture surfaces of the 10 samples tested here, it is clear that both lamellar orientation and stress intensity range ΔK influence the occurrence of interlamellar fracture and morphology of the fracture surface. At low ΔK level (up to 9-10 MPa√m), interlamellar fracture only occurs when the lamellar

interface is parallel to the fracture plane or with a deviation up to ~30° at most. The pole figures of 5 analysed samples given in Fig.4.16 all reveal these features in spite of the tiny difference of the ΔK range of each sample.

4.3.3 Translamellar fracture

Translamellar fracture was found throughout all the fracture surfaces and it is the dominant fracture mode during the whole fatigue crack propagation process. The observation in this study reveals that the morphology of a translamellar fracture surface is different at different ΔK level.

At low ΔK values, the fracture surfaces of translamellar fractured colonies are very smooth, as shown in Fig.4.17. The three colonies shown here are at ΔK values of 7.5, 6.4 and 6.5MPa√m. They all have high angle Orientations but different Sub-Orientations (A, B and AB respectively). It can be seen from the images that the morphology of the fracture surface is not affected by Sub-Orientation. In addition, some parallel linear markings are observed on the lamellae of translamellar fractured colonies. However, their direction may be different in different lamellae. Also, it seems that they are not related to the overall crack growth direction.

Compared with the fracture surfaces of translamellar cracked colonies observed at low ΔK level, the fracture surfaces at high ΔK are very different and they are much rougher, such as those in Fig.4.18. The two translamellar-cracked colonies shown in Fig.4.18 are at ΔK values of 15.5 and 16.2 MPa√m. Similarly to those shown in Fig.4.17, both of them have high angle Orientation with different Sub-Orientation. The one in Fig.4.18a has about 10° Sub-

Orientation from axis A and the other in Fig.4.18b is approximately 70°. The roughness at high ΔK values came from the large steps formed by secondary interlamellar cracking (two deep vertical interfacial cracks in Fig.4.18a) and small steps within/along each lamella. No small steps were found when ΔK is low. At high ΔK, although translamellar fracture is the predominant manner during crack propagation, interlamellar delamination is still observed throughout the fracture surface.

4.3.4 Other features

Apart from the two main fracture modes mentioned above, there are several other fracture behaviours during fatigue crack propagation in gamma titanium aluminides. The intergranular and transgranular fracture, shown in Fig.4.19 and Fig.4.20, which are caused by the failure of equiaxed gamma grains, are observed in the area of γ grains in each sample. The intergranular fracture surface in Fig.4.19a, b and c have different angles to the fracture plane. In Fig.4.19a it is nearly parallel to the fracture plane; in Fig.4.19b it is almost perpendicular to the fracture plane; and in Fig.4.19c it exhibits an intermediate angle. Thus, intergranular fracture can occur at any orientation. As the volume fraction of equiaxed gamma grains in alloy NL is higher than other alloys, large areas of intergranular fracture in Fig.4.20 are detected in this alloy. Although intergranular fracture is the predominant fracture mode for the equiaxed gamma grains, transgranular fracture still occurs, as shown in Fig.4.20 (b). There are some equiaxed gamma grains in the near-notch region (50μm from the notch in depth) on the fracture surface of sample NL1, but these features are not found in the near-notch region of sample NL2, as shown in Fig.4.21.

The second feature is the debonding between borides and the matrix. Large boride ribbons with both curvy and straight shape were observed on the fracture surfaces. Fig.4.22 (a) – (d) shows the fracture induced by the curvy boride ribbons in alloy AC and FC with a very smooth surface, revealing that the crack propagated along the interface between the borides and the matrix. Fig.4.23 (a) – (c) exhibits the sites on the fracture surface of alloy 107, 407 and NL where borides are pulled out from the matrix during crack growth, leaving a straight and flat morphology. It can be seen that the boride ribbons in Fig.4.23 (a) and (c) are almost parallel to the fracture plane, while that in Fig.4.23 (b) makes an angle about 40° to the fracture plane. Therefore, the debonding between borides and the matrix can occur during crack propagation, regardless of the orientation of borides.

Some transverse ridges, appearing to be a river pattern, are observed on the fracture surface of translamellar-cracked colonies near the interlamellar-cracked colonies In Fig.4.24a, the interlamellar-cracked colony, which is composed of several facets in the centre, is encircled by some translamellar-cracked colonies and is just at the notch, with a ΔK value of 6.3MPa.$m^{1/2}$. The river pattern on the fracture surfaces of these translamellar-cracked colonies radiates from the interlamellar-cracked colony and it reveals the real crack growth direction. The ridges converge at one point and this point is the crack initiation area. Therefore, in this image, it is obvious that the crack initiated in the colony at the centre then propagated to the adjacent colonies while the overall crack growth direction is from bottom to top.

Another example is shown in Fig.4.24b, in which the translamellar-fractured colony is below the interlamellar-fractured colony. The direction of the ridges on the translamellar facture surface is shown by the white arrow. Therefore, it is revealed that the actual crack growth

direction is from top to bottom. In Fig.4.24c, the interlamellar cracking occurred within one lamellar colony with an angle about 30° to the fracture plane. The interlamellar facture surface shown here is composed of a set of facets along the lamellar interface at different depths and the trace of tearing through the lamellae between these facets. It seems that there are no ridges on this fracture. However, when observed at high magnification, the ridges, appear to be a river pattern, as can be seen in Fig.4.24d, which is a high magnification image of area 'A' in Fig.4.24c. Therefore, the actual crack growth direction in this colony is from top to bottom, which means the crack fractured firstly on the lamellar interface A, and then propagated to lamellar interface B. This is again opposite to the overall crack growth direction.

4.4 Tensile properties

Tensile tests on alloy AC and FC were carried out with cylindrical samples at 650°C to assess the tensile behaviour of the samples with different lamellar spacing. Two test pieces were used for each alloy in order to obtain some indication of the repeatability of the properties. The results shown in Table 4.5 indicate the tensile properties of both alloys are repeatable and the ductility of both alloys is reasonable, higher than 1%. Alloy AC exhibits a slightly higher yield stress and better ductility than alloy FC. The fracture surfaces of failed test pieces were examined by SEM. The overall fracture surfaces are shown in Fig.4.25 (a) and (c) and the high magnification images are given in Fig.4.25 (b) and (d). The test pieces of both alloys failed mainly by translamellar failure.

4.5 Discussion

4.5.1 Mechanism of fatigue crack propagation in lamellar γ-TiAl and Microstructural characterisation of fracture surfaces

The fatigue crack growth curves of all the studied alloys shown in Fig.4.4-4.6 all exhibit high sensitivity of crack growth rate, da/dN to the stress intensity factor range ΔK throughout the entire range of crack propagation. This is analogous to other brittle materials. The three regions of fatigue crack propagation (near threshold, stable crack propagation i.e. Paris Region and unstable fast crack propagation) are distinguishable in spite of the limited range of ΔK of the whole crack growth.

The fatigue crack propagation mainly occurs in translamellar and interlamellar manner in the fully lamellar and near fully lamellar gamma titanium aluminides in this study, which are both brittle modes of failure. Translamellar fracture is regarded as cleavage through the adjacent lamellar plates. In the present alloys, it appears that the interlamellar fracture occurs on both γ/γ and γ/α_2 interfaces under cyclic loads. Intergranular and transgranular fracture are also representative brittle fracture modes, and these are observed in the area of γ grains. Compared with transgranular fracture, intergranular fracture is more common at 650ºC in this study.

Brittleness is the nature of lamellar gamma titanium aluminides and it is associated with the low ductility of most of this material. The ductility of lamellar TiAl alloys is usually less than 2% below their brittle-ductile transition temperature. As shown in Table 4.5, the ductility of alloy AC and FC is for both below 1.5% at the temperature up to 650 ºC. In ductile materials,

cracks and voids may form after the plastic deformation. However, the cracks in lamellar gamma titanium aluminides form at the very start of plastic deformation, which has been shown by some early studies where the first crack was detected just above the elastic limit under monotonic loads, at about 2/3-3/4 of the 0.2% proof stress [124, 125]. This intrinsic brittleness of lamellar gamma titanium aluminides is because of their complex and ordered crystal structure, which leads to dislocations with large Burgers vectors and therefore low mobility. The low transparency of interfaces for slip transfer also contributes to the brittleness of lamellar γ-TiAl alloys [126]. As a consequence, in such materials, the most efficient approach for accommodation of discontinuity of deformation from cross-lamella slip is interfacial cracking, such as interlamellar cracking and intergranular cracking. Thus the fracture surface of lamellar titanium aluminides is composed of interlamellar facets and also intergranular cracks under monotonic loads, which can be easily observed from the fracture surfaces of tensile tested samples in Fig.2.25. Fatigue fracture surfaces of lamellar titanium aluminides in this study are nearly identical to the fracture surface of tensile failed test pieces. This observation is analogous to other brittle materials and agrees with the early studies [93].

Although the fracture surfaces of fatigue tested specimens are analogous to those under monotonic loading, they exhibit their own features, especially the fracture modes (interlamellar cracking and translamellar cracking) at different stress intensity range ΔK and lamellar orientation. As shown in Fig.4.7-9, interlamellar fracture in low ΔK areas can only take place in the colonies with a low angle between the lamellar interface and crack growth plane. This implies that at low ΔK, only when the applied stress is nearly parallel to the lamellar interface normal, can it overcome the intrinsic coherency stresses of lamellar interfaces and lead to lamellar interface debonding, i.e. interlamellar cracking. Interlamellar

fractured facets are observed more in high ΔK areas than in the low ΔK areas, and interlamellar fracture in high ΔK areas can occur with any lamellar orientation, which induce lots of crack deflection. An increase in crack deflection with increasing ΔK can be confirmed with the rougher fracture surface exhibited in high ΔK regions, as shown in Fig4.7-4.9; the fracture surface is gradually rougher from right to left. This observation is consistent with the roughness examination results listed in Table 4.4. As interlamellar cracking at low ΔK only occurs when lamellar interface normal is almost perpendicular to the crack growth plane, translamellar cracking is the dominant fracture mode in low ΔK region.

Apart from the fracture mode, the morphology of interlamellar fracture and translamellar fracture surface is also influenced by stress intensity range, which has been reported in some early work but not investigated in detail [101, 127]. As shown in Fig.4.13, the fracture surface of interlamellar cracking is flatter at low ΔK than at high ΔK with high angle Orientation. This interlamellar cracking in translamellar-cracked colonies was only found in high ΔK region, which is in accordance with James' work [123]. However, there is no work published about the smooth translamellar fracture surface at low ΔK. In the present work, smooth translamellar fracture surfaces were found in the area where stress intensity range ΔK is low, as shown in Fig.4.17 (a)-(c). It is important to understand this phenomenon as these smooth fracture surfaces were all observed in near-threshold regions, which is just adjacent to the notch with low ΔK value. Based on the observation of the near-threshold region in this study, the samples fractured primarily by translamellar cracking and such smooth translamellar fracture surface should dictate the threshold.

Although it is not easy to overcome the intrinsic stress of lamellar interfaces to initiate an interlamellar fracture, the interlamellar cracking within one colony is easy and fast. The crack propagation along a lamellar interface is nearly instantaneous, thus not providing much crack resistance as cracks propagate through lamellae. Nonetheless, interlamellar cracking may change the local crack growth direction and lead to a tortuous crack path. Furthermore, the forming of interlamellar cracks itself may absorb some energy, thus providing crack resistance and retard crack propagation. The behaviour of intergranular fracture and the debonding between borides and matrix is similar to that of interlamellar fracture. When the borides or equiaxed gamma grains are not ahead of the main crack, or their interfaces are not with the same direction of the overall crack growth direction, as shown in Fig.4.19, 4.22 and 4.23, they may cause crack deflection, which is a typical toughening mechanism during fatigue crack growth.

Another observation is the different effects of Orientation and Sub-Orientation on fracture mode. Unlike Orientation, Sub-Orientation of the lamellar colonies exhibited little influence on the fracture mode during crack propagation. The effects of Orientation on fracture mode are because of their influence on slip/twinning systems. It can be easily figured out that the Schmid Factor of the slip/twinning systems is affected by Orientation but not Sub-Orientation.

In this study, some areas with opposite or oblique direction to the overall crack growth direction were observed on the fracture surface, as shown in Fig.4.24. This is due to the interlamellar cracking ahead of the main crack during fatigue crack propagation and it also leads to the severance of the ligament. This characteristic is important for the fracture of lamellar titanium aluminides and is consistent with some early study [128]. However, the observation by Chan was just made on the profile of the specimens. In this study, more

detailed observation was made on the real fracture surfaces of the specimens, exhibiting the evidence of interlamellar cracking ahead of the main crack.

4.5.2 Effects of microstructure on fatigue crack propagation threshold

The effect of lamellar spacing on fatigue crack propagation threshold was studied with alloy 4522XD which had been either air cooled or furnace cooled. The two alloys have similar colony sizes (~90μm and ~79μm) but different lamellar spacing. The lamellar spacing of alloy FC is nearly double that of alloy AC, as well as the γ lamellae thickness and α_2 lamellar spacing, as shown in Table 4.2. The volume fraction of α_2 phase decreased with decrease of cooling rate from air cooling to furnace cooling, which was reported in Mine's early work [90]. The alloy AC with small lamellar spacing only shows slightly higher fatigue crack propagation threshold (6.2/6.0 MPa.$m^{1/2}$) than that of alloy FC with larger lamellar spacing (5.7/5.8MPa.$m^{1/2}$). The yield strength of alloy AC (405/400MPa) is also slightly higher than that of alloy FC (380/384MPa). Although the improvement of fatigue threshold and yield strength by smaller lamellar spacing is subtle, the results of each condition are very stable. Therefore, both fatigue threshold and yield strength can be enhanced by smaller lamellar spacing. This is consistent with the results reported in some early work. The difference of lamellar spacing among the alloys in their work was much larger than that studied here. The lamellar spacing of the air cooled sample is about one quarter of that of the furnace cooled one, and the difference in threshold is from ~6.5 to ~8MPa.$m^{1/2}$ under three-point bending. The movement of cracks can be efficiently retarded by lamellar interfaces. As translamellar is the dominant fracture mode during crack propagation, it is easily rationalized that fine lamellar spacing can afford better fatigue crack growth resistance and high strength [90, 91, 106].

There could be an influence of colony size on fatigue crack propagation threshold, but the colony sizes of alloy 107 and 407 are very close, as well as the lamellar spacing. As a consequence, there is no difference in their threshold.

The equiaxed gamma grains mainly cause brittle intergranular fracture at elevated temperature. When there are only a few equiaxed gamma grains in the near-notch region, the fatigue threshold may not be affected by the intergranular fracture. When the fracture of equiaxed gamma grains fail with different orientation to the overall fracture plane (high angle orientation intergranular fracture), as shown in Fig.4.20 (b) and (c), crack deflection will occur, giving a tortuous fracture path, which can improve crack growth resistance. When a certain amount of intergranular cracking, of which the fracture surfaces are with the same orientation of the overall fracture plane (low angle orientation intergranular fracture), are in front of the main crack, microcrack coalescence can occur. This is a typical intrinsic damage mechanism which promotes the crack growth ahead of the crack tip. Therefore, this type of intergranular fracture in the near-notch region can give rise to a low fatigue crack propagation threshold, which can be confirmed with the lower threshold (5.5 MPa√m) of sample NL-1, with a number of low angle orientation intergranular fracture in the near-notch region. While the threshold of sample NL-2 is 7 MPa√m, with no intergranular fracture observed near the notch.

4.6 Conclusion

The samples subjected to fatigue crack propagation threshold testing fail by interlamellar cracking and translamellar cracking at 650ºC, which is similar to failure under monotonic tensile load. The fracture behaviour is determined by both lamellar orientation and stress

intensity factor range ΔK. At low ΔK level, interlamellar only occurs in lamellar colonies with lamellar interface parallel to the fracture plane, while at high ΔK level, interlamellar cracking occurs in lamellar colonies at any lamellar orientation.

The fatigue crack propagation threshold of as-cast alloy Ti4522XD shows limited sensitivity to microstructure parameters within the range investigated, such as lamellar spacing and volume faction of equiaxed gamma grains.

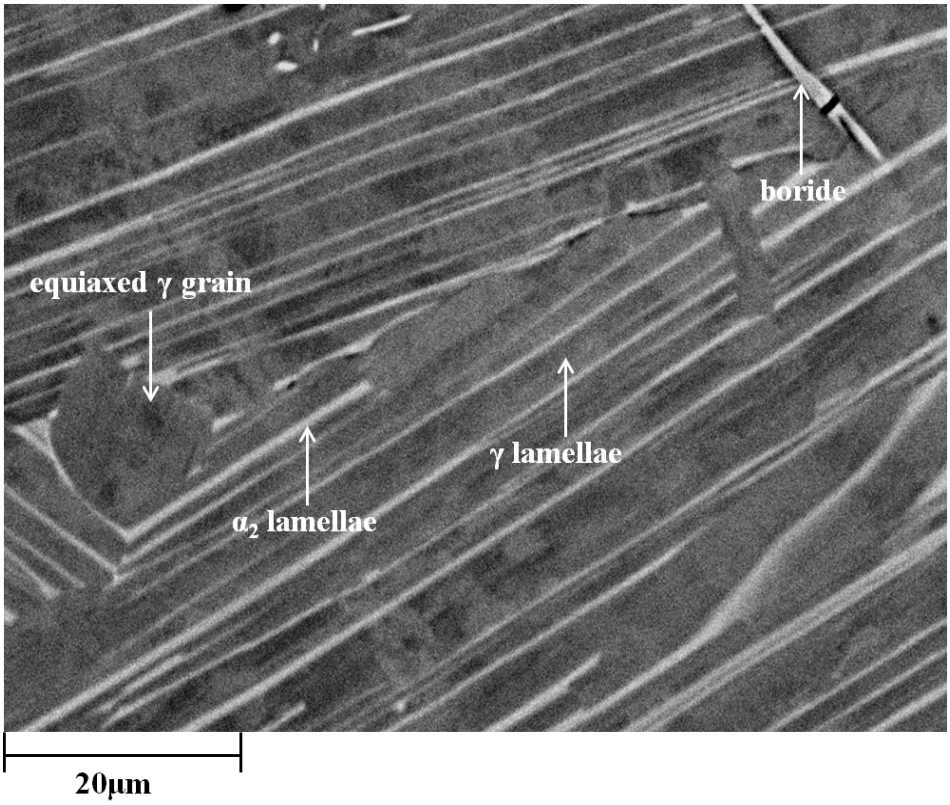

Fig.4.1 SEM back scattered electron (BSE) micrograph showing the microstructure of Ti4522XD.

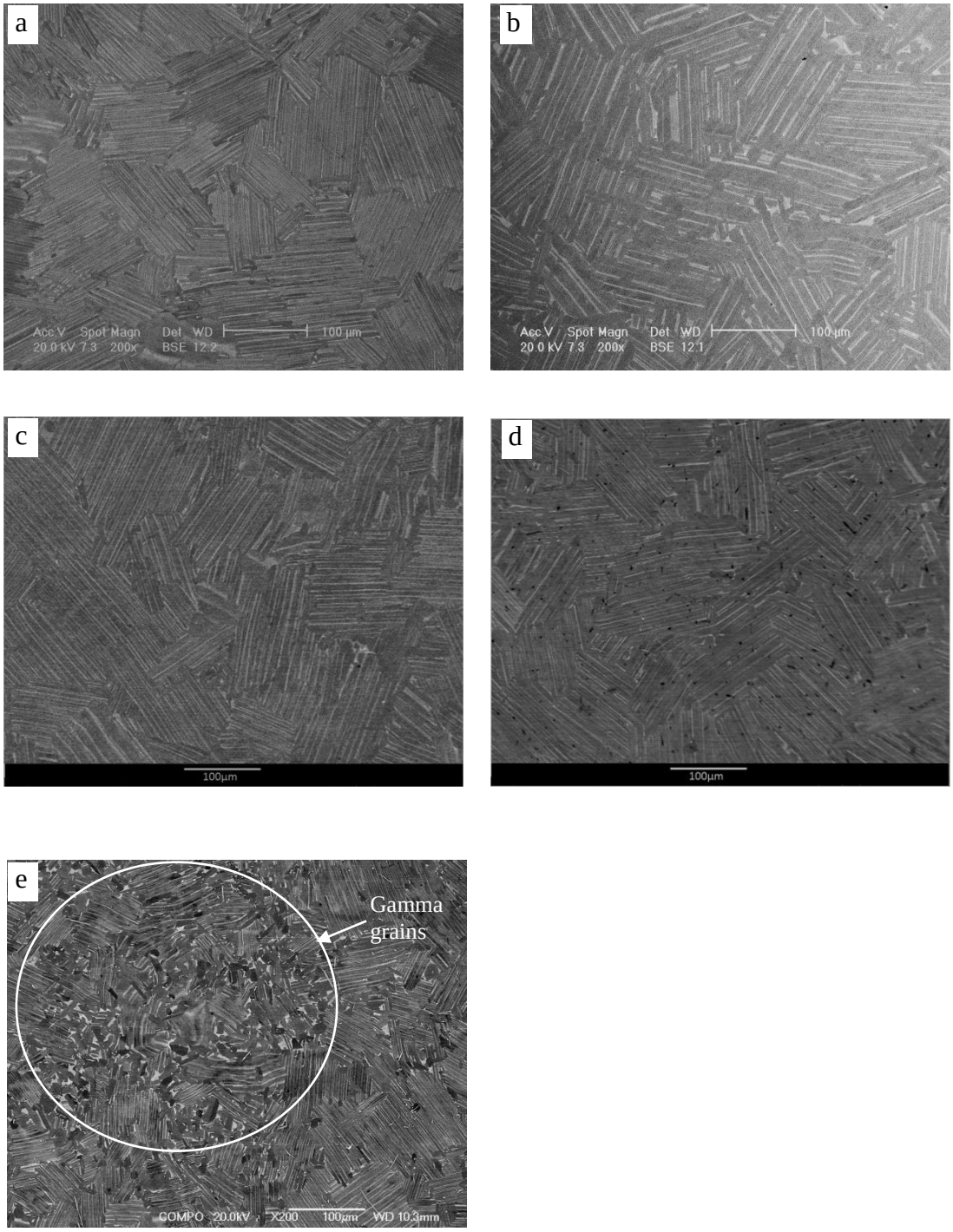

Fig.4.2 SEM BSE images showing the microstructures of five as-cast 4522XD alloys: (a) AC (thin lamellar spacing); (b) FC (thick lamellar spacing); (c) 107 (large colony size); (d) 407 (small colony size); (e) NL (large amount of equiaxed gamma grains).

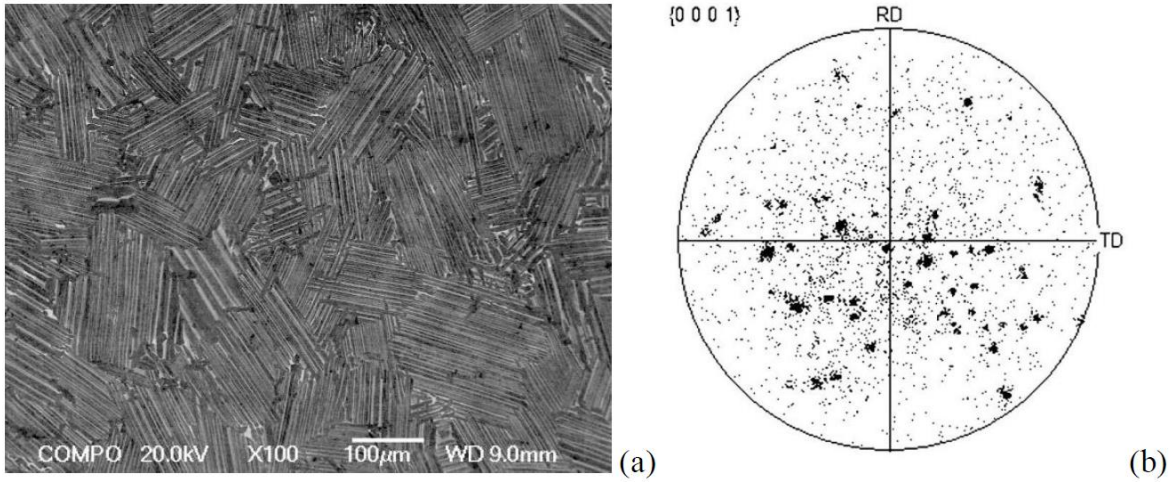

Fig.4.3 (a) SEM BSE image showing the lamellar microstructure of alloy 407 and (b) the EBSD (0001) $_{\alpha 2}$ pole figure shows the random lamellar orientation distribution.

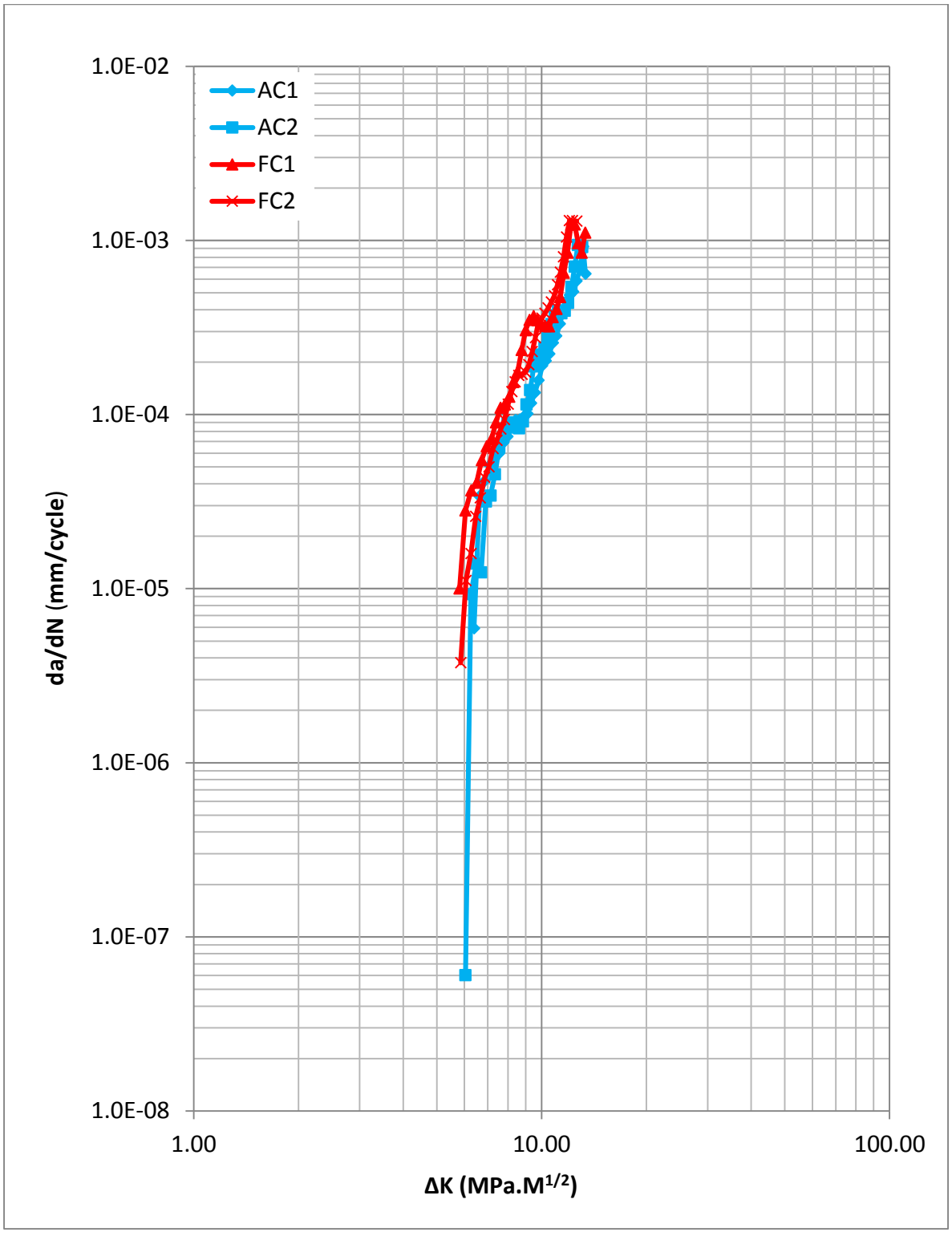

Fig.4.4 Fatigue crack growth curves of alloy AC (air cooling) and FC (furnace cooling) with different lamellar spacing.

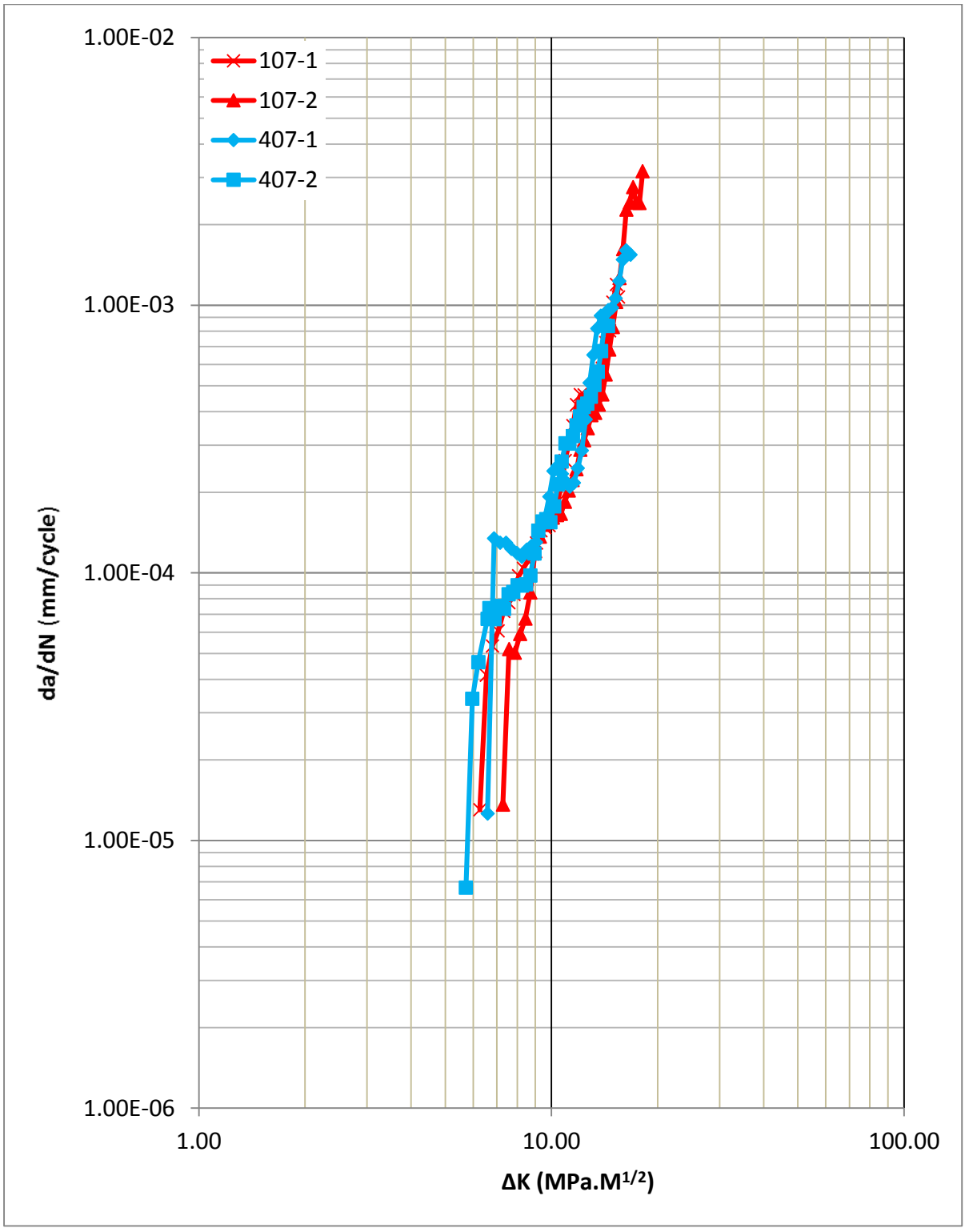

Fig.4.5 Fatigue crack growth curves of alloy 107 (large lamellar colony size) and 407 (small lamellar colony size).

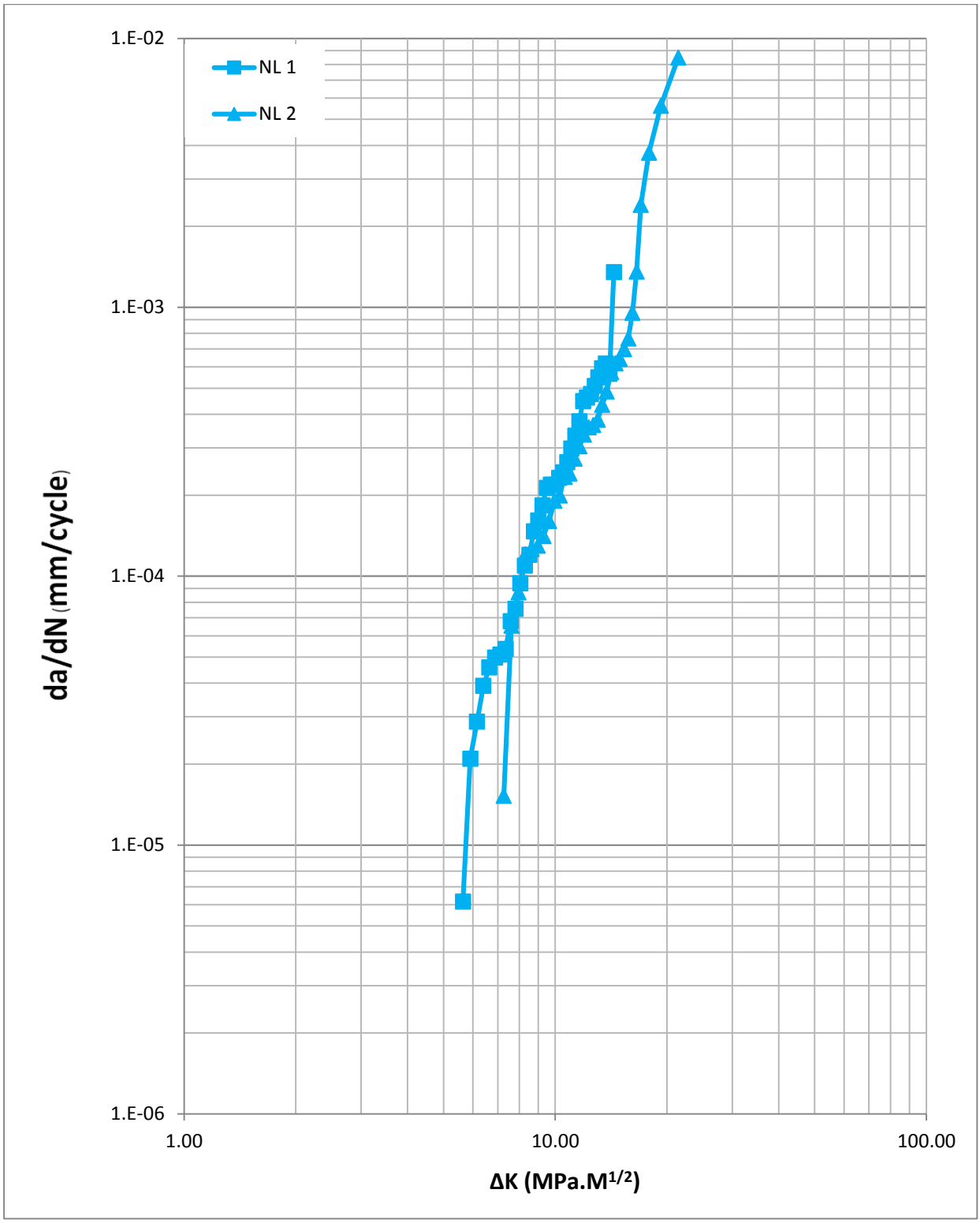

Fig.4.6 Fatigue crack growth curves of alloys NL which contain about 10% of equiaxed gamma grains.

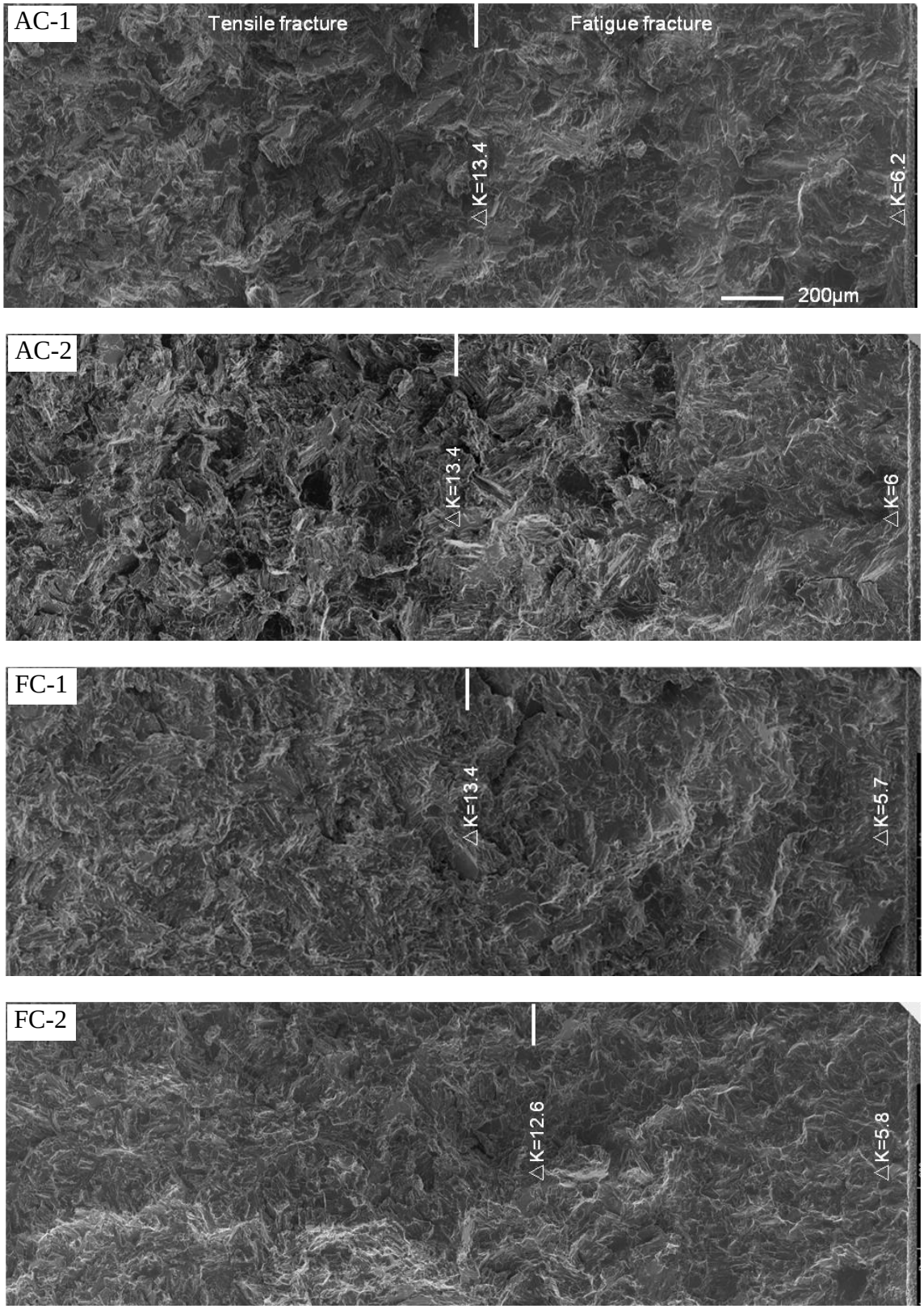

Fig.4.7 SEM montage showing the fracture surface of test pieces AC and FC. The crack propagation direction is right to left.

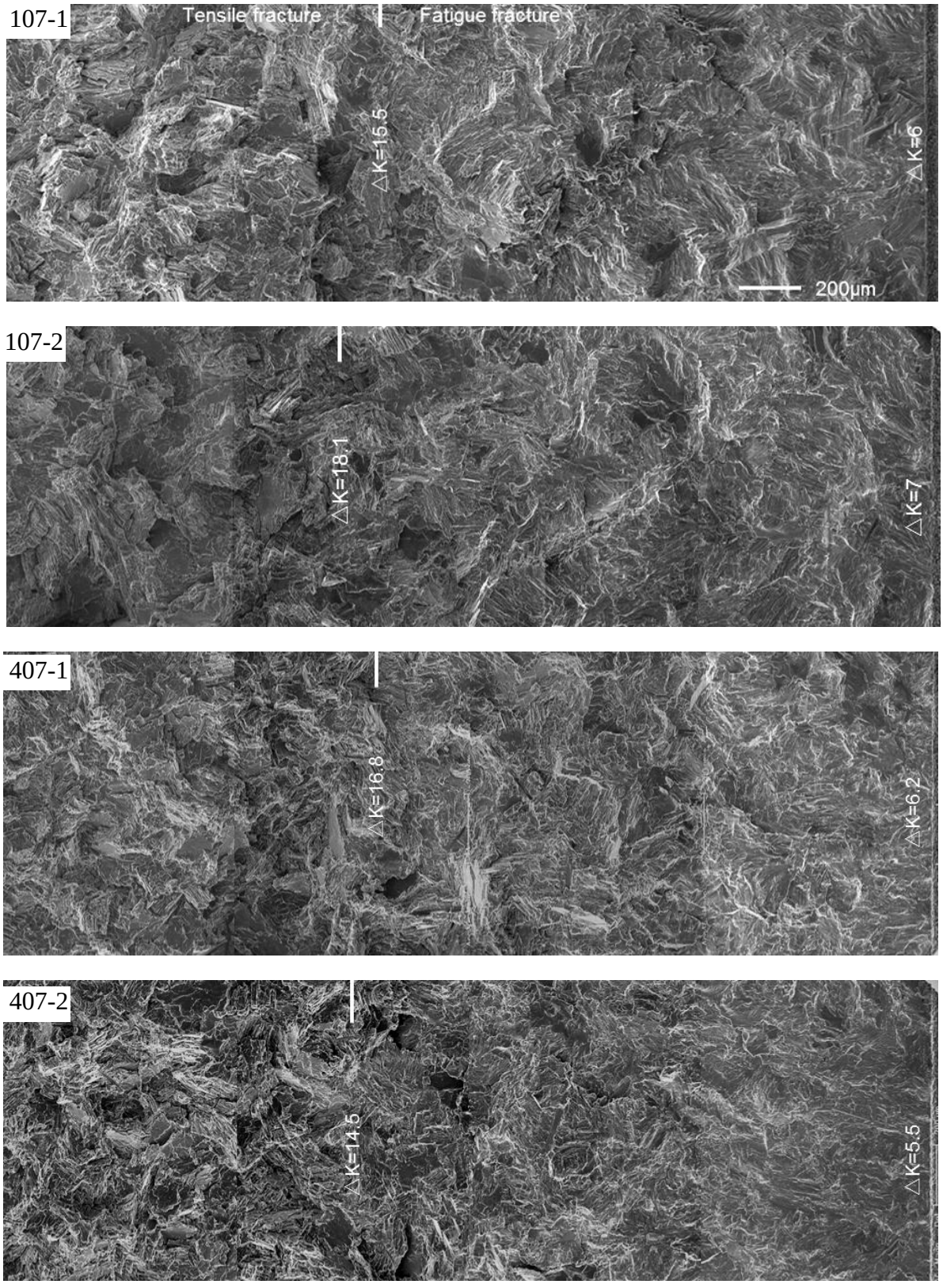

Fig.4.8 SEM montage showing the fracture surface of test pieces 107 and 407. The crack propagation direction is right to left.

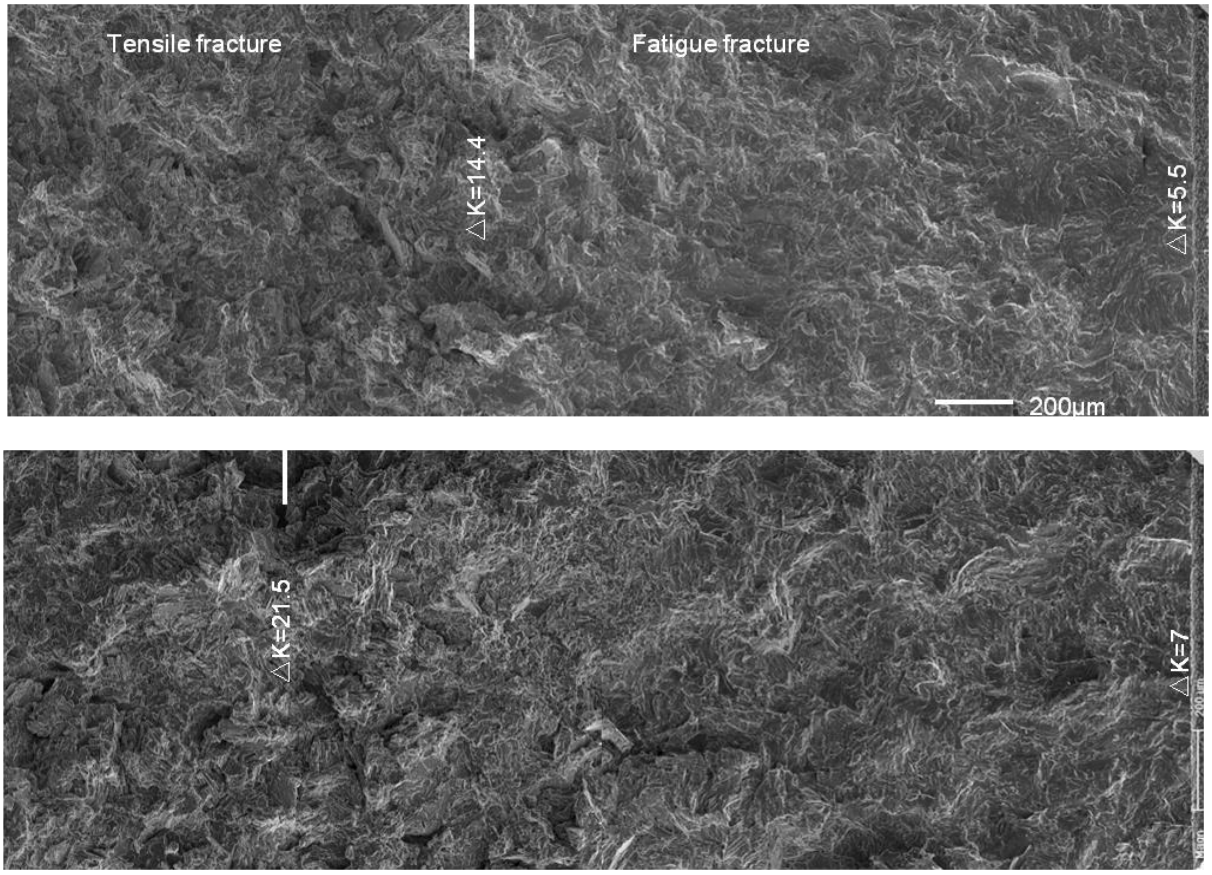

Fig.4.9 SEM montage showing the fracture surface of test pieces NL. The crack propagation direction is right to left.

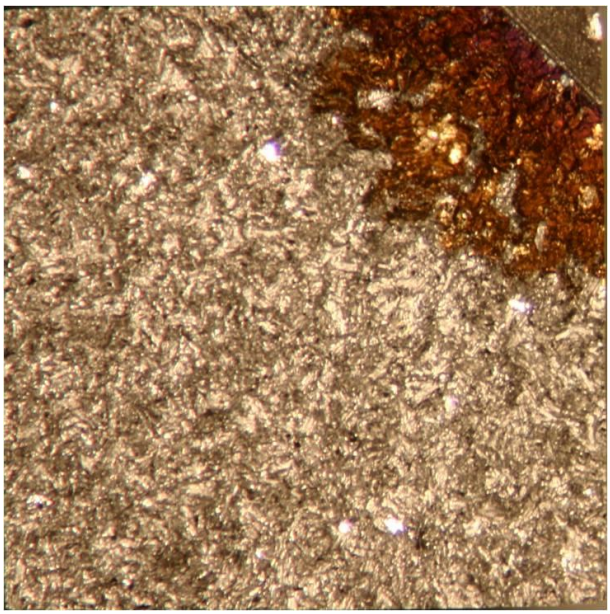

Fig.4.10 Optical microscopy image show the fracture surface of the broken test piece. The different shades of discolouration caused by oxidation indicate the fatigue and tensile fracture regions.

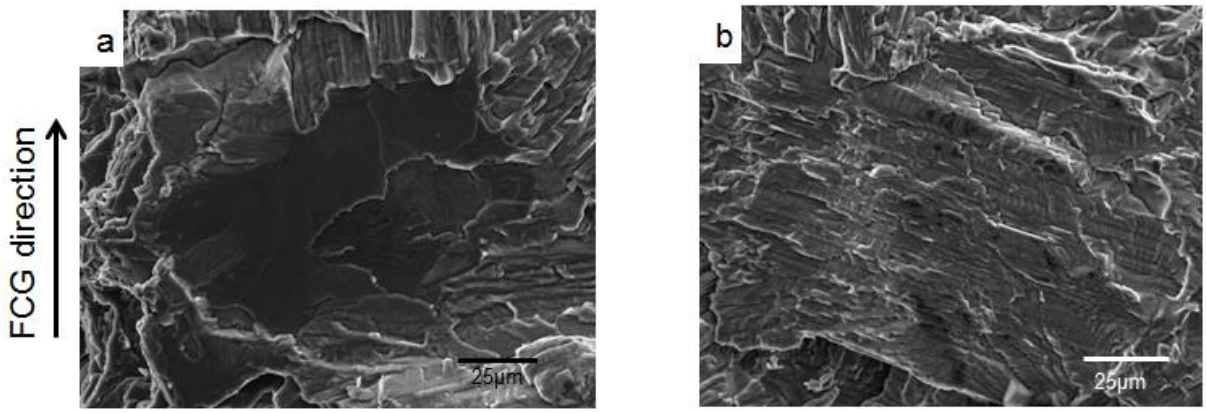

Fig.4.11 Two major fracture modes of the fracture of gamma TiAl alloys: (a) interlamellar fracture; and (b) translamellar fracture.

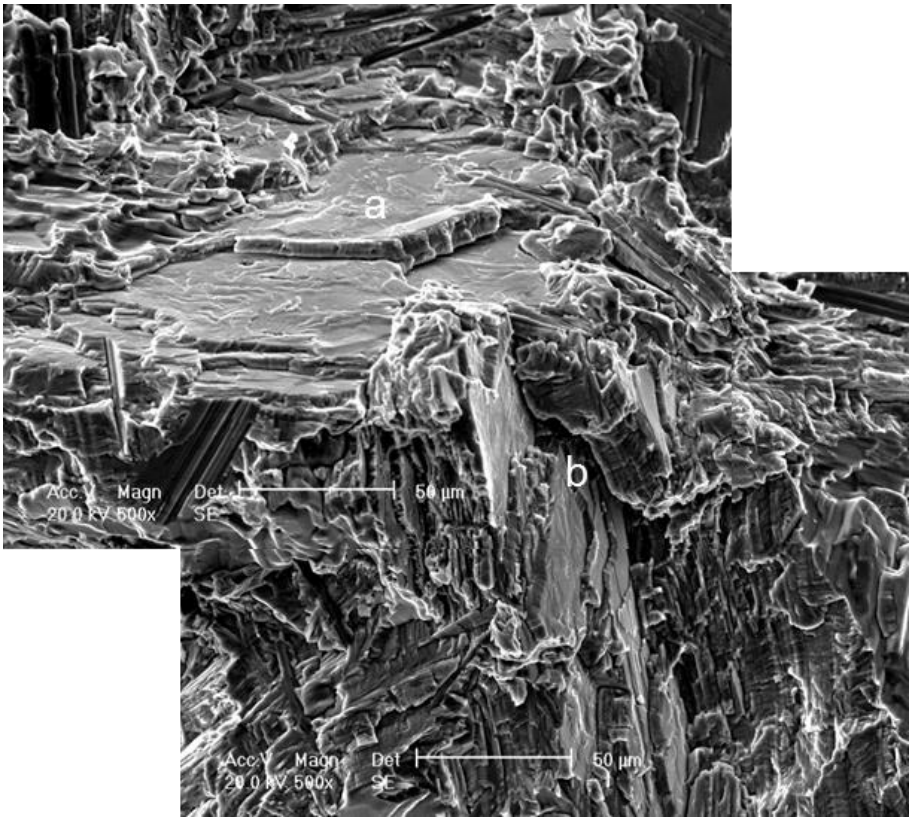

Fig.4.12 Interlamellar fracture at high ΔK region; (a) ΔK =14.5 and (b) ΔK =14.1MPa√m.

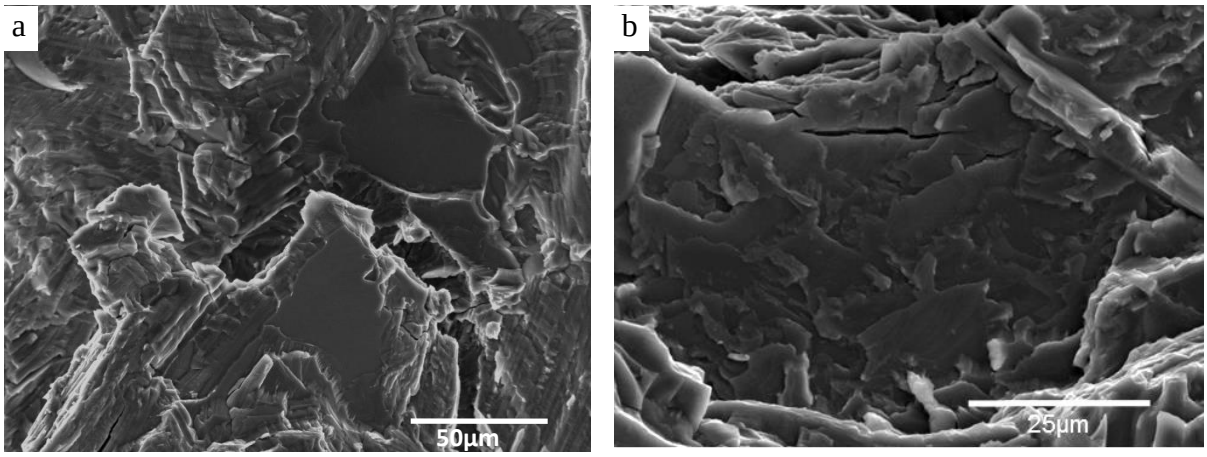

Fig.4.13 Interlamellar fracture surfaces at low ΔK region and high ΔK region; (a) ΔK=7.6, and (b) ΔK=17.5, tilted by 60º.

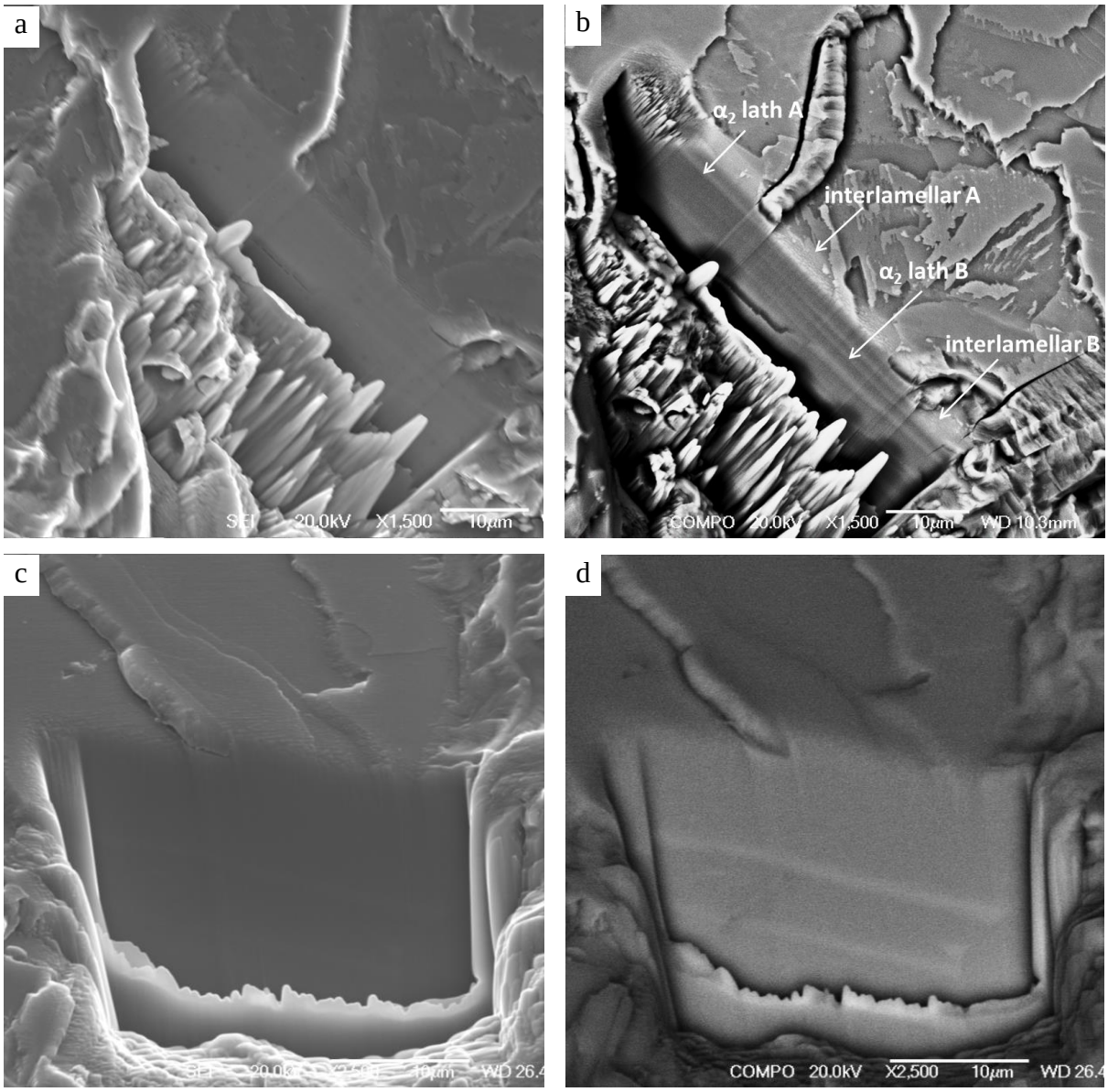

Fig.4.14 SEM SE image (a) and (c) and SEM BSE image (b) and (d) showing the profile of the interlamellar cracked colonies.

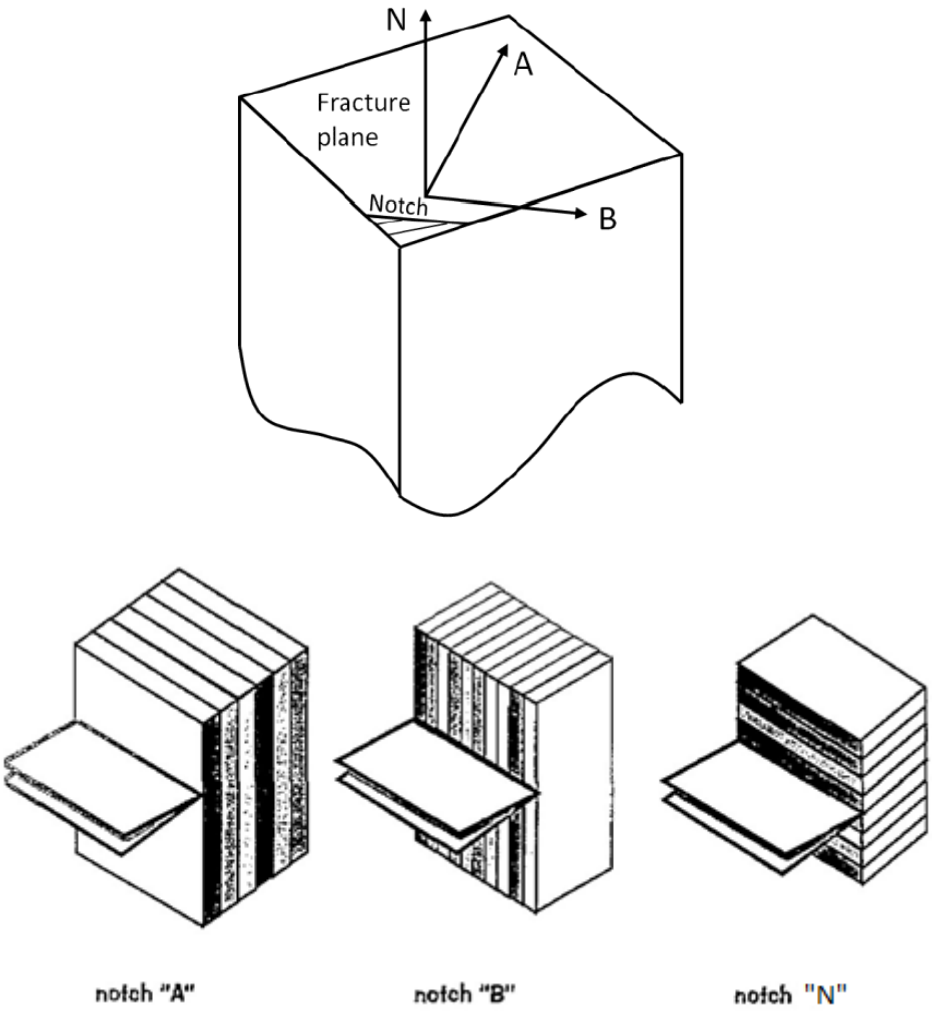

Fig.4.15 Definition of pole figure directions with respect to the stress axis and the fracture plane.

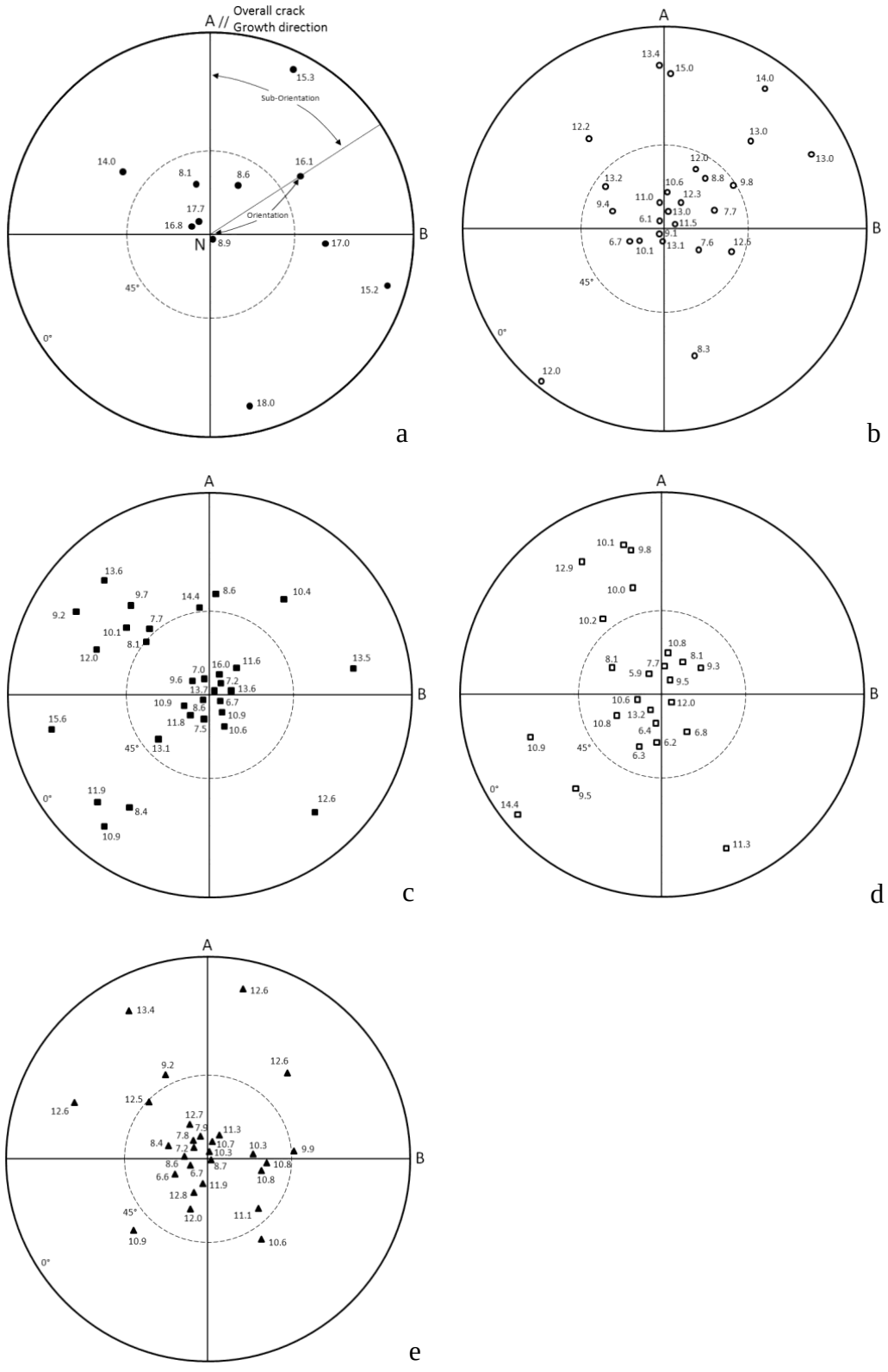

Fig.4.16 Pole figures showing the orientations of interlamellar-cracked colonies together with their local stress intensity range observed on the fracture surfaces of samples (a) and (b) with alloy 107, (c) and (d) with alloy 407 and (e) with alloy AC.

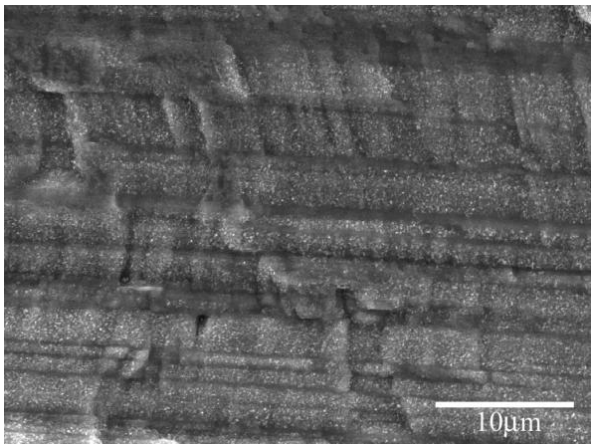

(a)

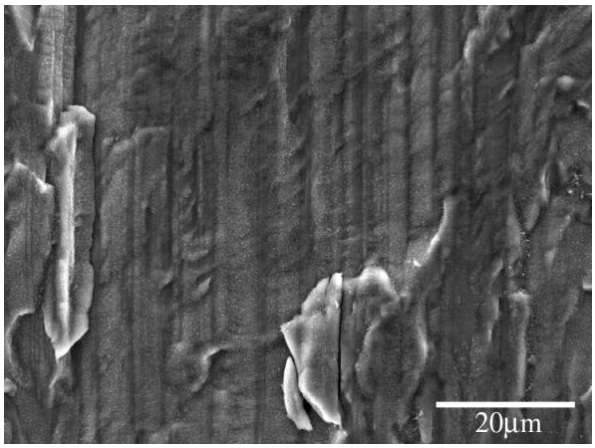

(b)

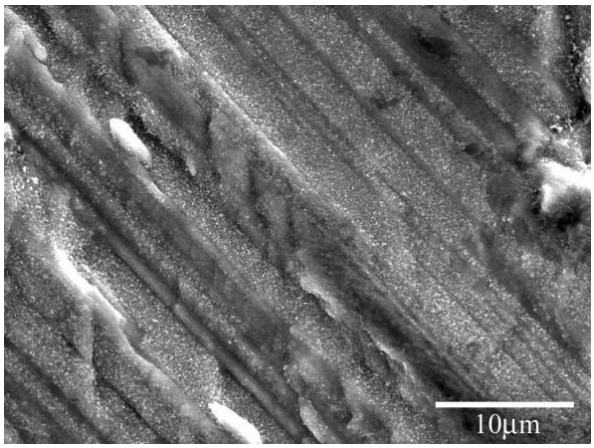

(c)

Fig.4.17 Translamellar fracture at low ΔK; (a) 7.5, (b) 6.4, and (c) 6.5MPa√m.

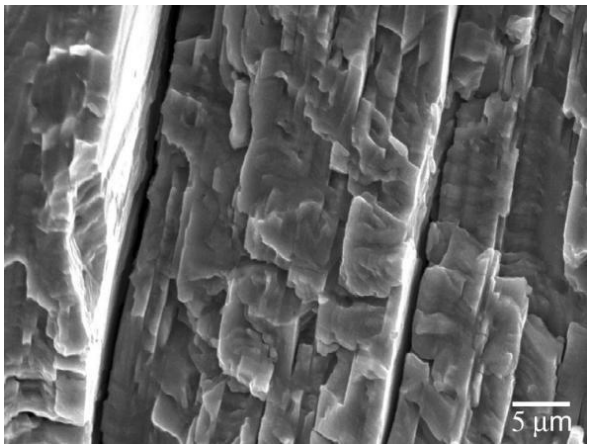

(a)

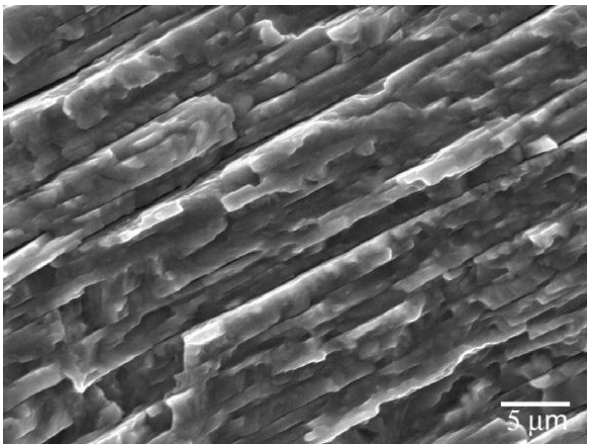

(b)

Fig.4.18 Translamellar fracture at high ΔK; (a) 15.5 and (b) 16.2MPa√m.

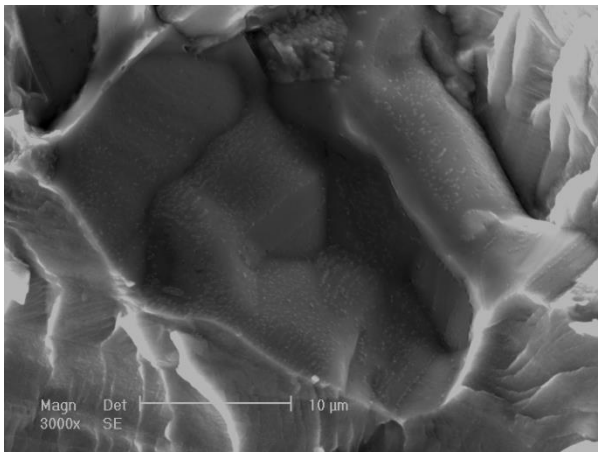

(a)

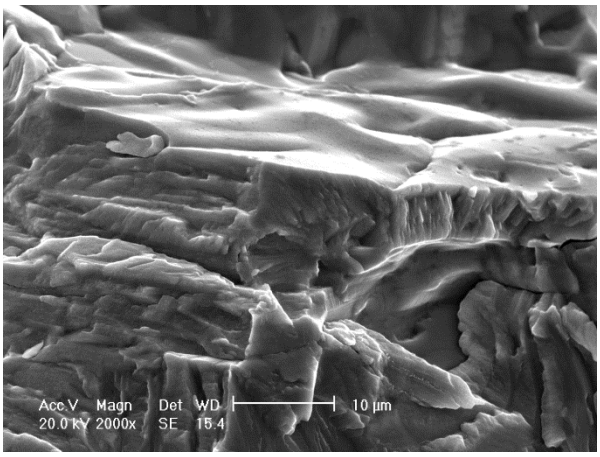

(b)

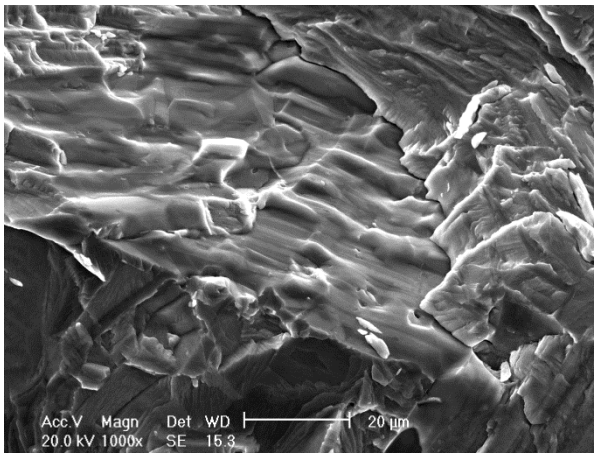

(c)

Fig.4.19 SE SEM image of intergranular fracture of equiaxed gamma grains observed on the fracture surface on alloy (a) FC and (b) and (c) 107.

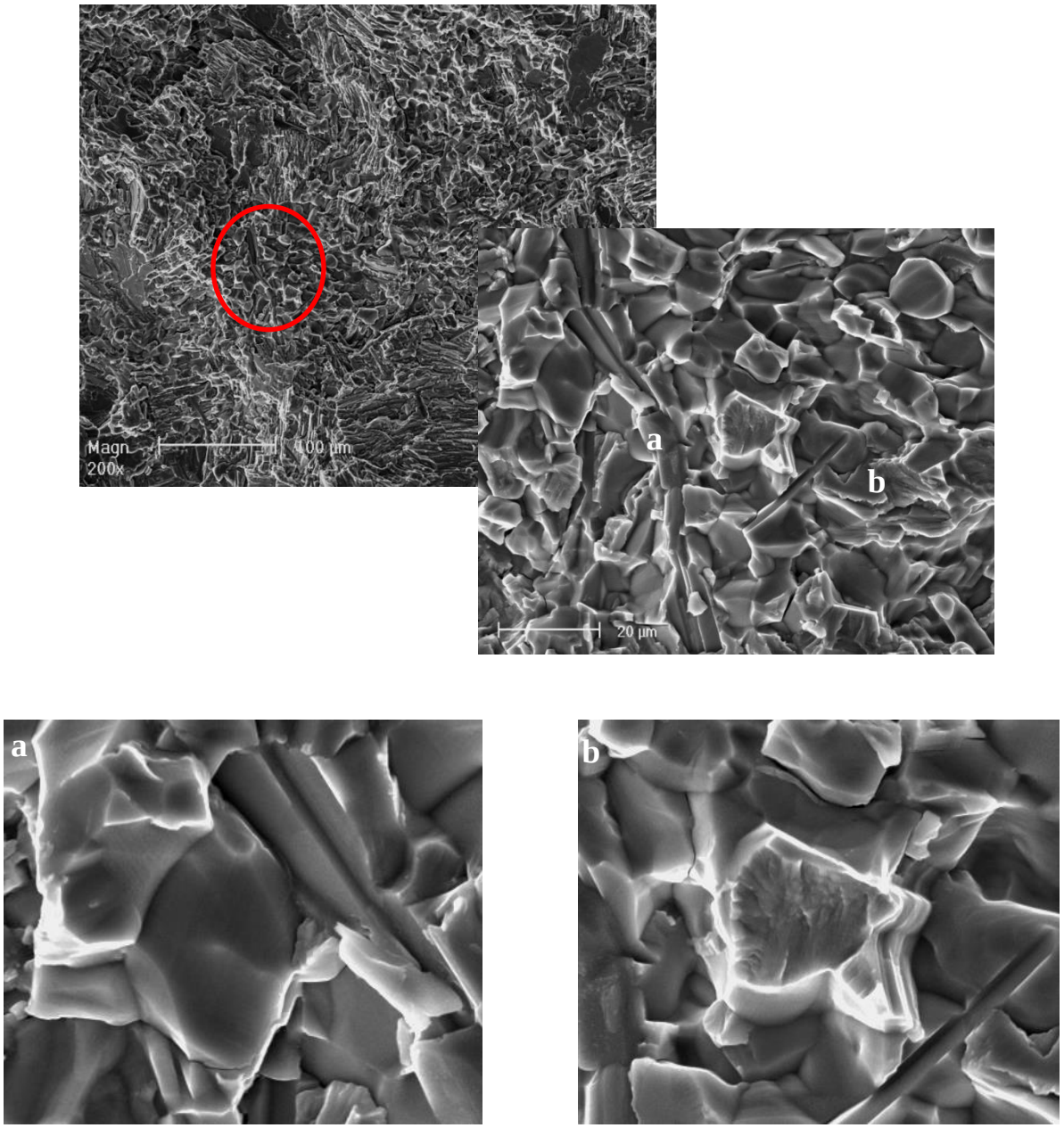

Fig.4.20 SEM SE image of (a) intergranular and (b) transgranular fracture of equiaxed gamma grains observed on the fracture surface on alloy NL.

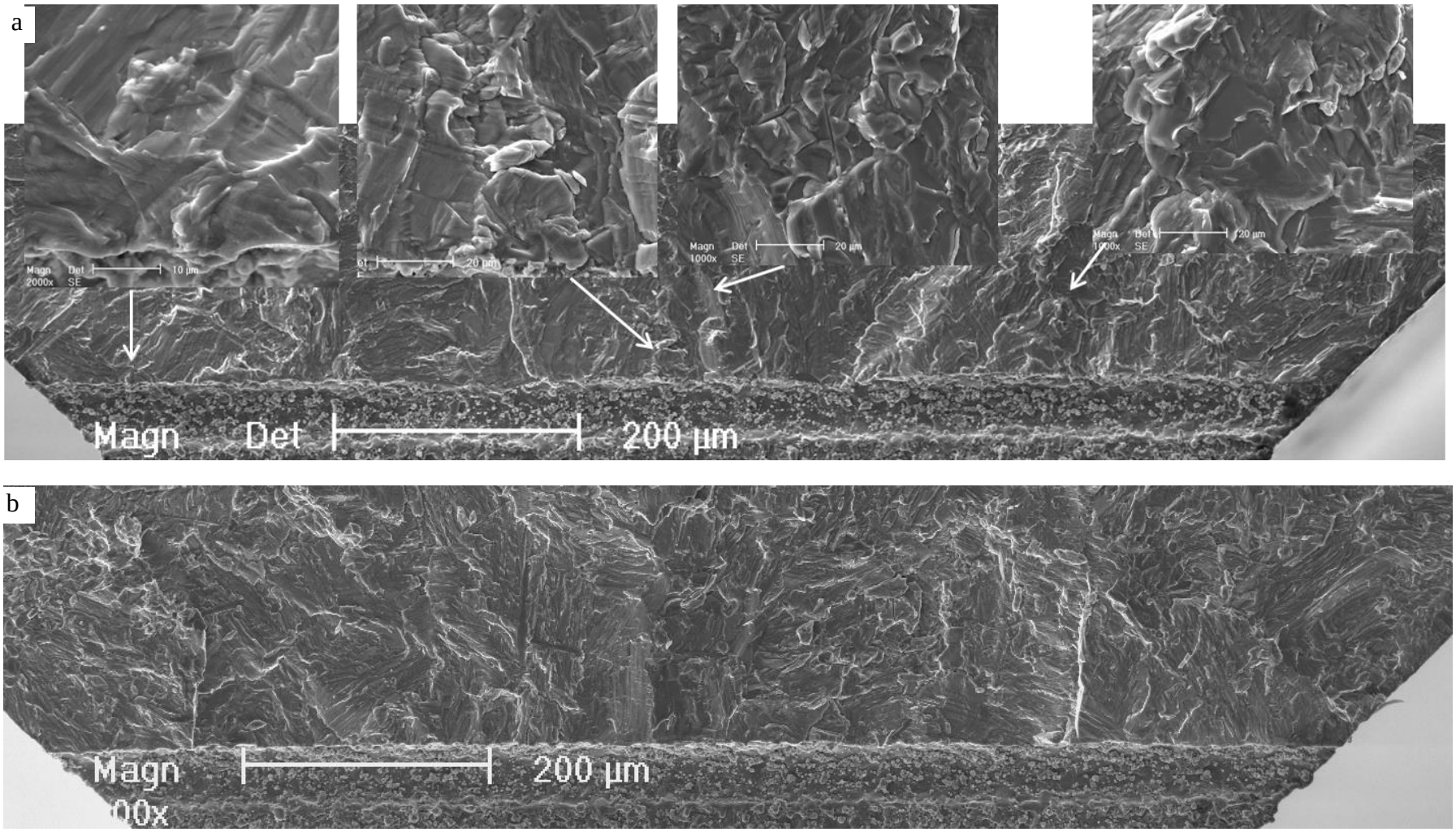

Fig.4.21 SEM SE image of fracture surfaces near the notch of alloy NL (a) NL1 and (b) NL2.

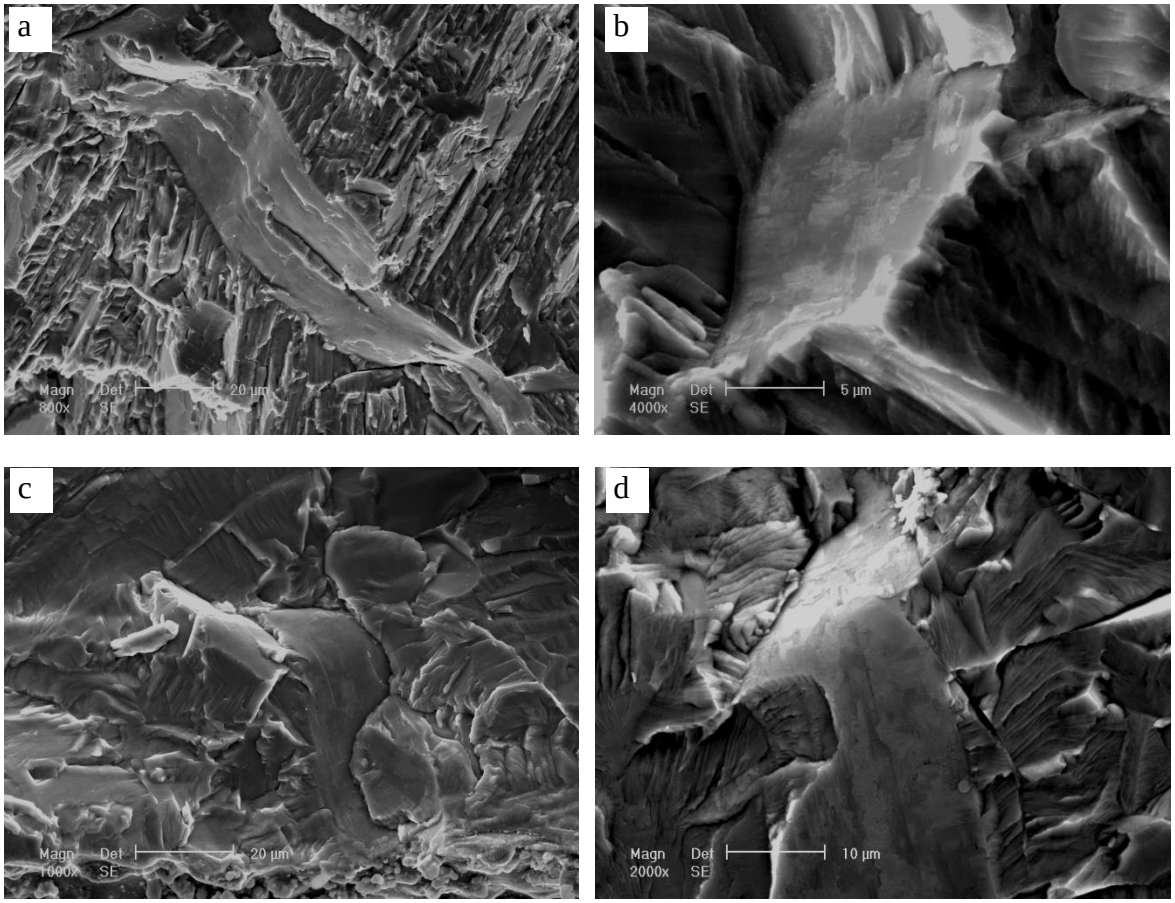

Fig.4.22 SEM SE images showing details of debonding between curvy borides and the matrix in (a) AC1, (b) AC2, (c) FC1 and (d) FC2.

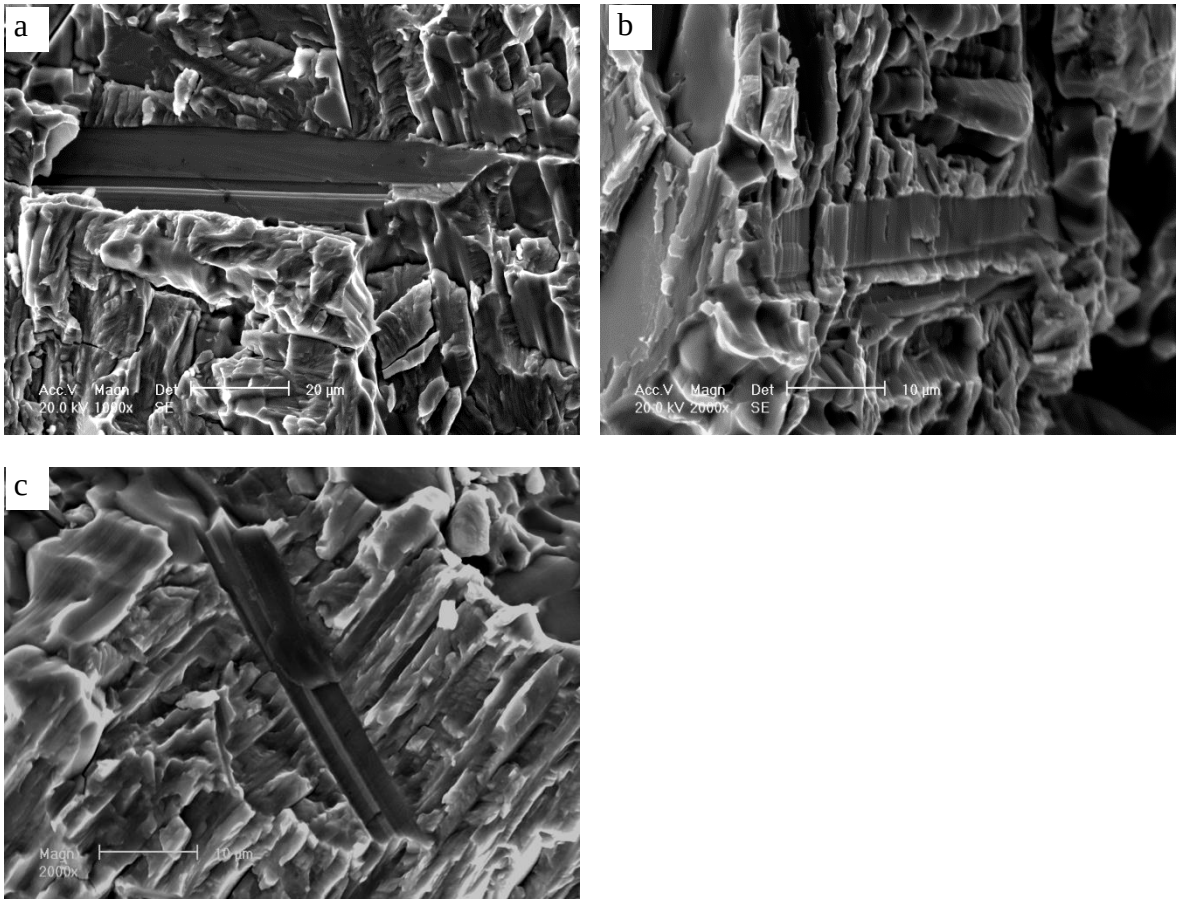

Fig.4.23 SEM images showing the debonding between boride ribbons and the matrix in alloy (a) 107, (b) 407 and (c) NL.

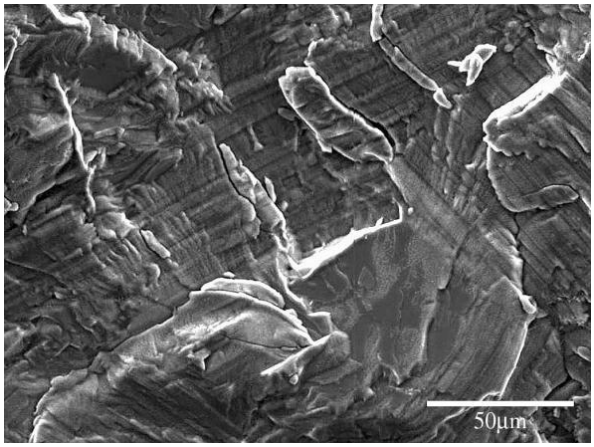

(a)

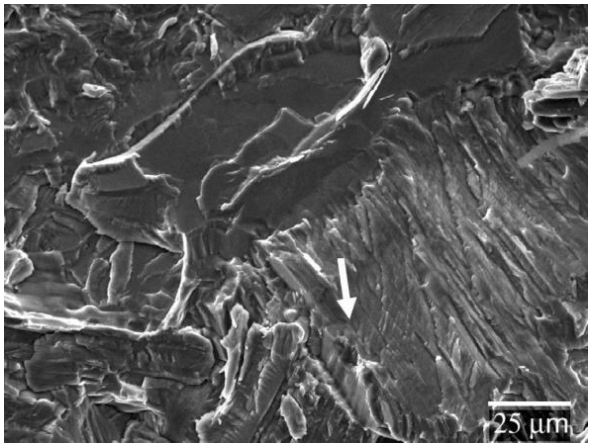

(b)

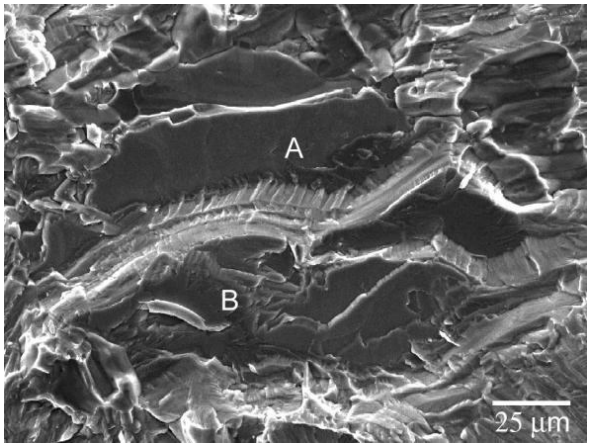

(c)

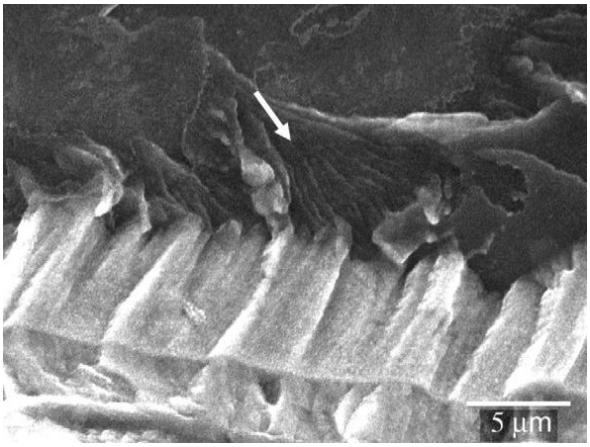

(d)

Fig.4.24 Linear features on the translamellar fracture surfaces adjacent to interlamellar fracture areas. ΔK= (a) 6.3, (b) 10.2, and (c) 8.9MPa√m, (d) is the high magnification image of (c).

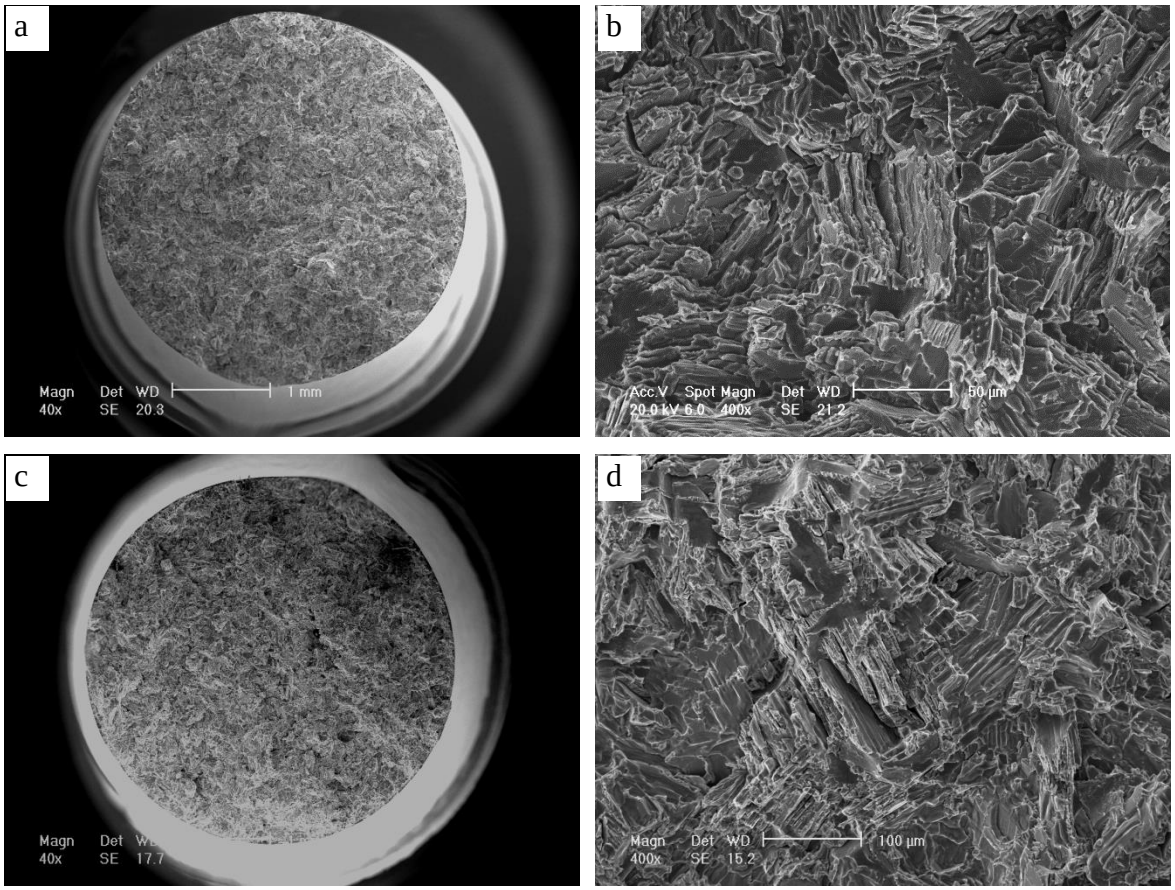

Fig.4.25 SE SEM images of fracture surfaces of the failed tensile test pieces, showing (a) and (b) from alloy AC, and (c) and (d) from alloy FC. (a) and (c) are the overall surface morphologies, and (b) and (d) are the high magnification image of the fracture surface of alloy AC and FC, respectively.

Table 4.1 Average lamellar colony size of alloy AC, FC, 107, 407 and NL

Materials	Colony size (μm)
AC	79±42
FC	90±41
107	93±51
407	79±43
NL	37±22

Table 4.2 Average α_2 lamellar spacing, γ lamellae thickness and lamellar spacing of alloy AC, FC, 107 and 407

Materials	α_2 lamellar spacing (μm)	γ lamellae thickness (μm)	lamellar spacing (μm)
AC	2.05	0.74	0.62
FC	4.31	2.15	1.54
107	3.04	1.10	0.74
407	3.54	1.39	0.99

Table 4.3 Fatigue crack propagation threshold values of alloy FC, AC, 107, 407 and NL.

Materials	ΔKth at threshold (MPa.m^1/2)	Stress ratio	Temperature (°C)
AC1	6.2	0.1	650
AC2	6.0	0.1	650
FC1	5.7	0.1	650
FC2	5.8	0.1	650
107-1	6	0.1	650
107-2	7	0.1	650
407-1	6.2	0.1	650
407-2	5.5	0.1	650
NL 1	5.5	0.1	650
NL 2	7.0	0.1	650

Table4.4 Surface roughness of alloys 107 and 407 after fatigue crack propagation threshold test

	107-1		107-2		407-1		407-2	
	ΔK (MPa.m^1/2)	Roughness Ra	ΔK (MPa.m^1/2)	Roughness Ra	ΔK (MPa.m^1/2)	Roughness Ra	ΔK (MPa.m^1/2)	Roughness Ra
ΔK_{th}	6	2.8	7	3.6	6.2	2.8	5.5	3.6
ΔK_{mid}	10.3	10.2	11.9	7.8	10.5	13.1	9.1	6.1
ΔK_{end}	15.5	26.7	18.1	13.8	16.8	18	14.5	7.4

Table 4.5 Yield strength, UTS and elongation results of alloy AC and FC at 650°C.

Materials	Yield strength (MPa)	Ultimate tensile strength (MPa)	Elongation (%)	Temperature (°C)
AC	405	541	1.4	650
AC	400	531	1.5	650
FC	380	477	1.0	650
FC	384	480	1.2	650

Chapter 5. Effects of alloy composition on Fatigue crack propagation threshold

5.1 Microstructure evaluation

Five forged alloys Ti45Al2Mn2Nb1B (at %) (Ti4522XD), Ti45Al2Nb2Ta1B (2Nb2Ta), Ti45Al2Mn2Ta1B (2Mn2Ta), Ti45Al2Mn4Nb1B (2Mn4Nb) and Ti45Al2Mn4Ta1B (2Mn4Ta), were studied in this section to investigate the alloying effects on the microstructure and properties of gamma titanium aluminides. Alloy 2Mn2Nb, i.e. 4522XD is the baseline alloy, and others are its modifications. The microstructures of this series of the five forged alloys are shown in Fig.5.1 (a)-(e). In these SEM BSE images, it is clear that all of the five alloys are of lamellar microstructure, with few equiaxed γ grains on the colony boundary and borides throughout the whole image.

The lamellar colony size and the size distribution of these lamellar colonies for each alloy are shown in Fig.5.2, from which it is clear that the microstructure of these alloys are homogeneous. The colony size of most colonies is within a range of about 20 to 60μm, only a few colonies are very large, with the colony size up to 150μm. There are no significant differences among the colony size of five forged alloys, when the standard deviation is included, as shown in Table 5.1. However, a very slight trend can be found - 2Nb2Ta and 2Mn2Ta alloys have smaller colony sizes than other three alloys. The average α_2 lamellar spacing, γ lamellae thickness and lamellar spacing of alloy 2Nb2Ta are slightly smaller than those of alloy 2Mn2Nb and 2Mn2Ta alloy, as shown in Table 5.2. Nb addition slightly decreases the volume fraction of α_2 phase, alloy 2Mn2Nb and alloy 2Mn2Ta, with α_2 phase

about 24 and 26%; alloy 2Mn4Nb and alloy 2Mn4Ta, with α_2 phase about 19% and 28%, as shown in Table 5.3. The lamellar orientation of these alloys was studied with the samples cut from the thread of the tensile testing specimens along and perpendicular to the loading direction. Their microstructures are shown in Fig.5.3, and the EBSD $(0001)_{\alpha 2}$ pole figures shown in Fig.5.4 indicate that the lamellar orientation of these five alloys are randomly distributed.

5.2 Effects of alloy composition on hardness

The hardness of these five alloys was measured with Vickers hardness method with polished samples and the applied load was 20Kgf and the results are shown in Table 5.4. It is seen that the hardness of these alloys are very similar. Only the hardness of 2Nb2Ta alloy is slightly higher than others.

5.3 Effects of alloy composition and temperature on tensile properties

5.3.1 Effects of alloy composition on tensile properties and examination of fracture surface

Tensile tests on alloy 2Mn2Nb, 2Mn2Ta, 2Nb2Ta, 2Mn4Nb and 2Mn4Ta were conducted with cylindrical samples at 650°C to assess the tensile behaviour of the samples with different alloy composition. Two test pieces were used for each composition in order to obtain some indication of the repeatability of the properties. A summary of the tensile properties of these alloys is given in Table 5.5, where outstanding consistency was noted for each set of samples. It is clear from this data that overall these alloys are brittle, with ductility

below 2% at 650°C, regardless of their composition. The ductility alloys 2Nb2Ta (1.7/1.9), 2Mn2Ta (1.6/1.9) and 2Mn4Ta (1.6/1.9) is slightly better than that of alloys 2Mn2Nb (1.4/1.5) and 2Mn4Nb (1.1/1.3).

Fractographic examinations were carried out on the failed samples by SEM. The overall fracture surfaces, as shown in Fig.5.5 (a), (c) and (e), exhibit a relatively flat morphology, revealing a brittle fracture mode of these alloys, regardless of the composition. For these fine-grained lamellar TiAl alloys, crack initiation sites are difficult to identify on the fracture surfaces, although interlamellar cracking near the test piece surface was observed in Fig.5.5 (b), (d) and (f) [129]. However, there are still some features on the fracture surfaces worth noting. The cracking in lamellar titanium aluminides mainly appears to be translamellar, although the crack occasionally propagates either along the lamellar interface as manifested by small facets or through lamellar colony boundaries as shown in Fig.5.6. Another feature on the fracture surfaces is that there are groups of fairly smooth but curvy surfaces at different orientations, which can be seen in in Fig.5.7 (a). There are neither translamellar cracking nor interlamellar cracking surfaces. Brittle intergranular fracture caused by the failure of equiaxed gamma grains is observed. The debonding between borides and matrix crack was also observed visible in Fig.5.7 (b) as flat rectangular surfaces.

5.3.2 Effects of temperature on tensile properties and examination of fracture surfaces

Tensile tests of the base line alloy 2Mn2Nb were carried out at room temperature, 450°C and 650°C. The data is given in Table 5.6. Tensile properties of this alloy show strong dependence on temperature. With increase of temperature, the yield strength decreases

gradually from room temperature to 650°C; on the other hand, the elongation goes up slightly. The overall fracture surfaces of selected samples tested in all cases are shown in Fig.5.8. They all exhibit a quite even and flat morphology, revealing a similar brittle fracture model below the brittle ductile temperature. The fracture mode at these three temperatures is very similar, mainly consisting of translamellar fracture and interlamellar fracture, as shown in Fig.5.9.

5.4 Effects of alloy composition on fatigue crack propagation threshold

5.4.1 Fatigue crack propagation threshold testing results

The fatigue crack growth resistance curves, fatigue crack growth rate (da/dN) versus stress intensity factor range (ΔK) obtained for the forged 2Mn2Nb, 2Mn2Ta, 2Nb2Ta, 2Mn4Nb and 2Mn4Ta are shown in Fig.5.10- Fig.5.14. All tests were conducted at 650°C in air with stress ratio of 0.1 Two specimens were used for each alloy in order to obtain some indication of the repeatability of the properties. From the results summarized in Table 5.7. It can be seen that the fatigue crack propagation threshold of these alloys falls in a very narrow range, between 5.6-6.3 MPa√m, and the threshold for each alloy is relatively consistent. Note that only one result for alloy 2Mn2Nb and 2Nb2Ta was obtained due to some unexpected issue of the test machine.

From the overall curves given in Fig.5.10, it is clear that like the cast alloys studied in Chapter Four, the fatigue crack growth resistance curves of the forged alloys studied here also exhibit three distinguishable regions of fatigue crack propagation, and also the crack

growth rate da/dN shows high sensitivity to stress intensity factor range ΔK, which is typical for brittle materials. Alloy 2Mn4Nb shows the highest fatigue crack growth rate while alloy 2Mn2Nb, which is the baseline alloy, shows the slowest crack growth rate or in other words the highest fatigue crack growth resistance. From the curves shown in Fig.5.11, it can be seen that with the same content of Mn, the alloy with 2Nb has a slightly higher threshold and crack growth resistance than the alloy with 2Ta. However, with the same content of Mn, when the content of Nb and Ta increases to 4Nb and 4Ta, the results are very close, as shown in Fig.5.12. In addition, the increase of Nb content from 2 to 4 leads to a decrease of both threshold and crack resistance in Fig.5.13; while the increase of Ta seems have no influence on both threshold and crack resistance, as shown in Fig.5.14.

5.4.2 Fracture surface features

The fracture surfaces of alloy 2Mn2Nb, 2Mn2Ta, 2Nb2Ta, 2Mn4Nb and 2Mn4Ta are selected and collated in Fig.5.15 and Fig.5.16. A notch was induced by EDM on the right edge, and the fatigue crack growth area and final monotonic tensile fracture area is shown from right to left. From the fractographic observations, it is noted that the failure mainly occurred by translamellar fracture and interlamellar fracture, which indicated that the test pieces failed in a brittle manner in general. The fracture surface of near threshold area (about 50μm from the notch) is relatively smooth compared with that of other area.

The behaviour of both translamellar facture mode and interlamellar fracture mode has been assessed for different ranges of stress intensity factor range ΔK. Fig.5.17 shows the morphology of translamellar fracture surface at low ΔK (6.5 for 5.17(a) which is just at the notch) and high ΔK (16.4 for 5.17(b)), respectively. At low ΔK, the fracture of translamellar

fracture is rather flat, while at high ΔK, it is much rougher. It can be also noted that the secondary interlamellar cracking was observed on the fracture surface of translamellar fracture at high ΔK, as shown in the high magnification image in Fig.5.17 (b). These secondary interlamellar cracks lead to the large steps on the fracture surface thus causing a rougher morphology of translamellar fracture at high ΔK region.

Interlamellar fracture also shows a strong dependence on the stress intensity factor range ΔK. In low ΔK region, interlamellar cracking only occurs occasionally when the lamellar interface is parallel to the fatigue crack growth plane, as shown in Fig.5.18 (a) with ΔK=6.5 MPa.$m^{1/2}$, appearing as a very flat facet. However, in high ΔK region, interlamellar fracture could occur at any orientation, appearing as a cliff-edge morphology, which is not observed in the low ΔK region, as shown in Fig.5.18 (b) and (c), with the ΔK value of 21.8 and 21.6 MPa.$m^{1/2}$. From the fracture surface shown here, it can be seen that not only interlamellar fracture, but also delamination between lamellae in the same lamellar colony was observed.

Apart from translamellar and interlamellar fracture, some other brittle fracture modes, such as the debonding between borides and matrix and intergranular fracture in the area of equiaxed gamma grains are found on the fracture surfaces. The fractured boride appears as a long facet with a few steps, as shown in Fig.5.19. The intergranular fracture is found in the area of equiaxed gamma grains, and the fracture surface can be at a different angle to the overall fracture plane, as shown in Fig.5.20. Fig.5.20 (d) shows a high magnification SEM image of intergranular fracture which is marked in Fig.5.20(c), and it can be seen that the fracture surface of intergranular cracking is very smooth.

5.5 Discussion

The studied alloys 2Mn2Ta, 2Nb2Ta, 2Mn4Nb, 2Mn4Ta and2Mn2Nb are all with fully lamellar microstructure, as shown in Fig.5.3, and the lamellar orientation is randomly distributed, as shown in the pole figures in Fig.5.4. The lamellar colony size of alloy 2Mn2Nb and 2Mn4Nb is slightly larger than other Ta containing alloys, leading to a poorer ductility than Ta containing alloys. Alloy 2Nb2Ta shows the highest yield strength among these alloys, about 10% higher than others, which may be due to its small lamellar spacing, compared with 2Mn2Nb and 2Mn2Ta.

Translamellar fracture and interlamellar fracture are the main fracture modes no matter whether the test piece is under monotonic load or cyclic load. For fatigue crack propagation threshold test, translamellar fracture is the dominant fracture behaviour throughout the entire crack growth progress. The occurrence of interlamellar fracture is strongly dependent on the lamellar orientation and stress intensity factor range ΔK. In low ΔK area, near the notch, interlamellar fracture can take place only when the lamellar interface is parallel with or at a low angle to the crack growth plane. However, it can occur in a colony where the lamellar interface makes either a low or high angle to crack growth plane in high ΔK region.

The crack propagation can be efficiently impeded when crossing the lamellar interfaces whilst moving quite fast along lamellar interfaces. Thus translamellar cracking can afford reasonable crack growth resistance while interlamellar cracking itself cannot provide much crack resistance. However, the formation of interlamellar fracture can retard crack propagation and change the local crack growth direction. Similar effect is also applied to intergranular fracture and debonding between borides and matrix. These features are

corresponding to those found in the as-cast alloy, indicating that these features are typical for fracture of lamellar gamma titanium aluminides. However, the fatigue crack propagation threshold obtained with these forged alloys is more stable than that with the as-cast alloys in general. This is mainly due to their smaller lamellar colony size, which is about half or one third of the as-cast alloys. As the notch induced by EDM is 1mm in length, there are about 10 lamellar colonies in front of the notch for the specimens made of as-cast alloys, while there are about 20-30 lamellar colonies in front of the notch for the specimen made of forged alloy. Therefore, the microstructure ahead of notch is more homogenous in the forged alloy and gives a more stable property.

The fatigue crack propagation threshold values of the alloys in the studied range are situated in a rather narrow range, from 5.6 MPa√m to 6.3 MPa√m, differing by 0.7 MPa√m, which is more concentrated than the as-cast alloys. This may result from their smaller colony size, thus having more colonies at the notch, providing a more random orientation. The relatively close threshold of these forged alloys may be due to their similar microstructure, fully lamellar microstructure, and similar microstructural parameters, such as lamellar colony size and lamellar spacing, as shown in Table 5.1 and 5.2. Effects of lamellar spacing and colony size on threshold have been studied in Chapter 4, although distinct lamellar colony sizes were not obtained as intended. Further attention will be concentrated on the lamellar orientation effects on fatigue crack propagation threshold.

5.6 Conclusion

Alloying elements, Nb and Ta, have little influence on the fatigue crack propagation threshold in the studied range. This may be because of their similar microstructure, all with

fully lamellar microstructure, and similar microstructural parameters, such as colony size, lamellar spacing and phase ratio of gamma phase.

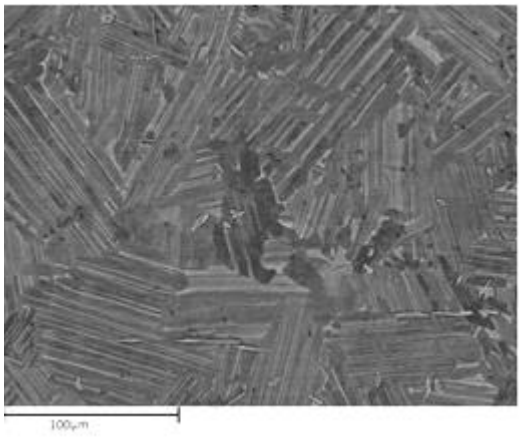

(a)

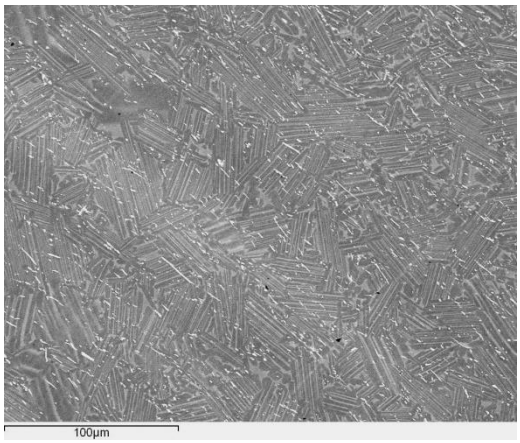

(b)

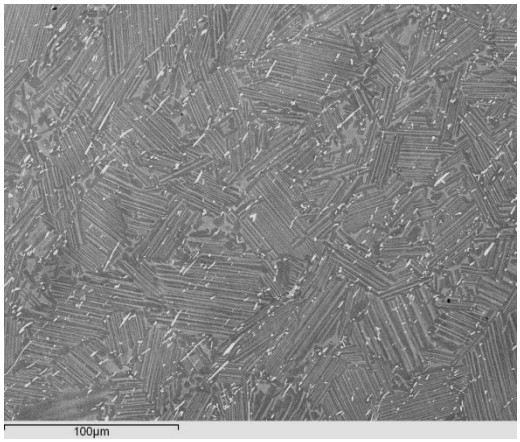

(c)

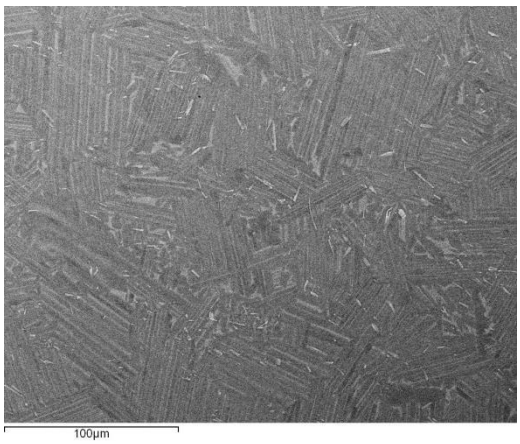

(d)

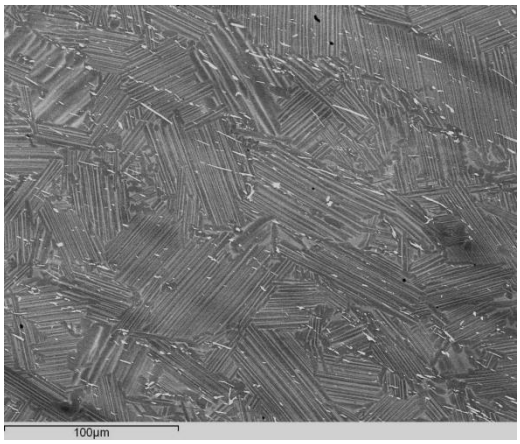

(e)

Fig.5.1 SEM BSE image showing the microstructures of five forged alloys: (a) 2Mn2Nb (Ti4522XD); (b) 2Mn2Ta; (c) 2Nb2Ta; (d) 2Mn4Nb; (e) 2Mn4Ta.

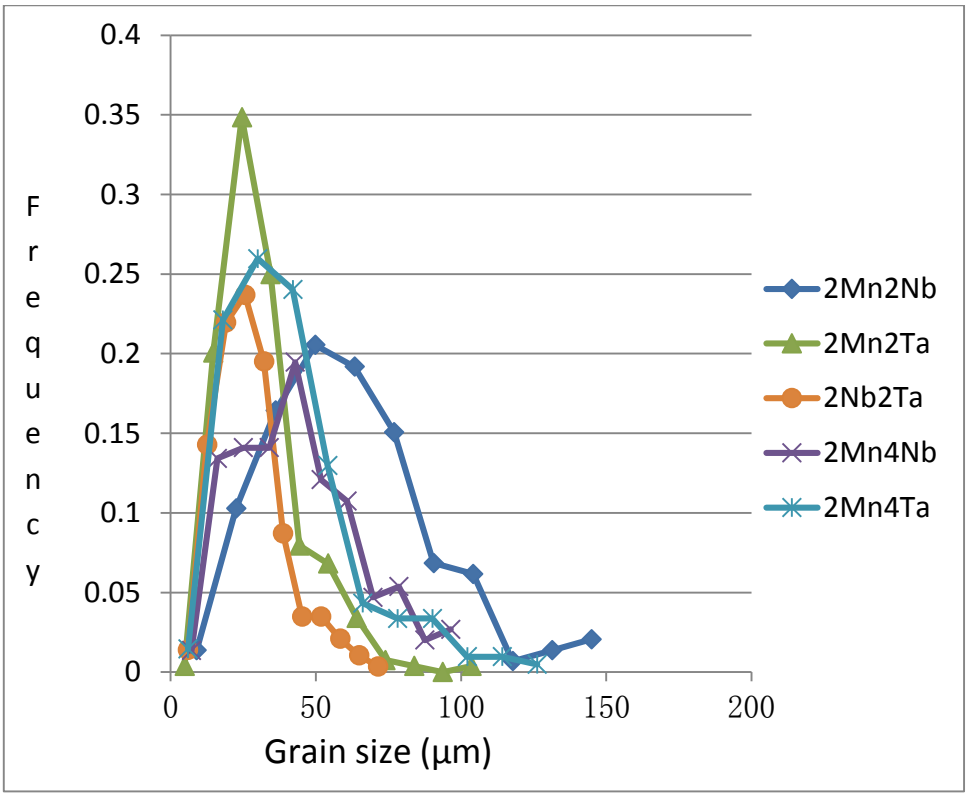

Fig.5.2 Grain size distribution of alloy 2Mn2Nb, 2Mn2Ta, 2Nb2Ta, 2Mn4Nb and 2Mn4Ta.

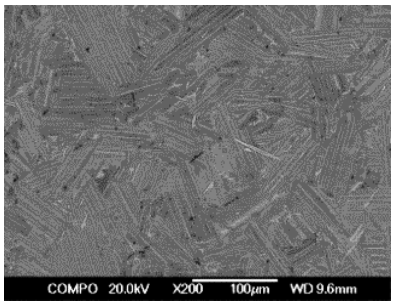

2Mn2Nb (a)

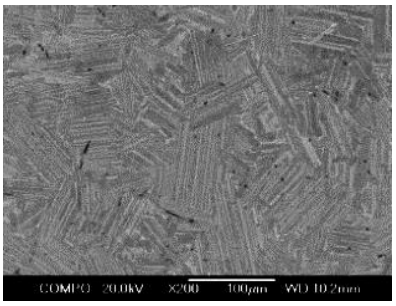

2Mn2Nb (b)

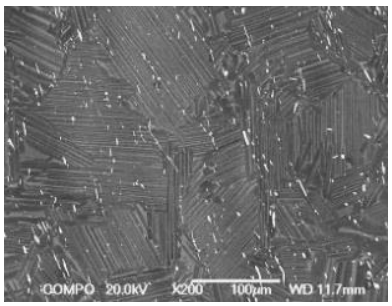

2Mn2Ta(a)

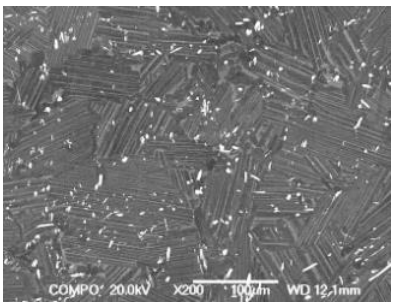

2Mn2Ta(b)

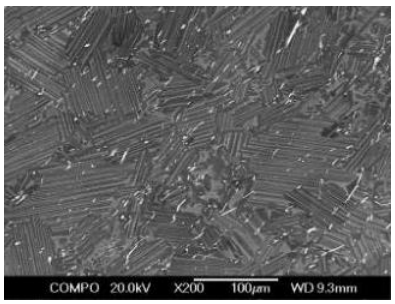

2Nb2Ta (a)

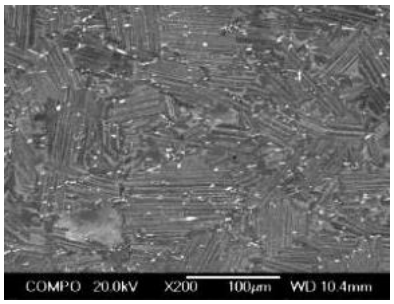

2Nb2Ta (b)

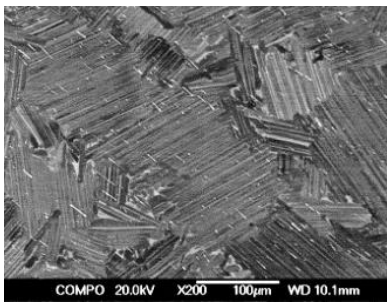

2Mn4Nb (a)

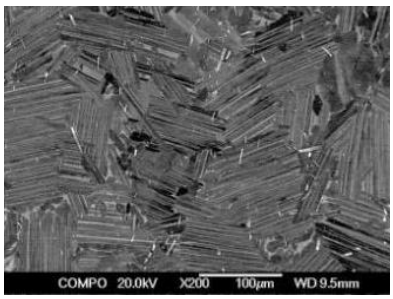

2Mn4Nb (b)

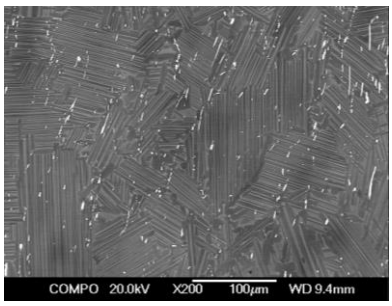

2Mn4Ta (b)

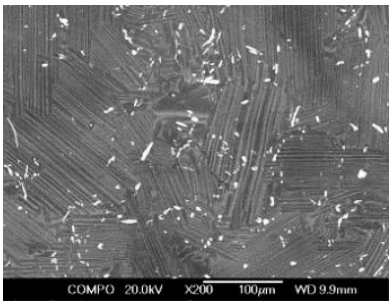

2Mn4Ta (b)

Fig.5.3 SEM BSE images showing microstructures of 2Mn2Nb, 2Mn2Ta, 2Nb2Ta, 2Mn4Nb, 2Mn4Ta samples cutting from tensile specimen (a) perpendicular to loading axis and (b) parallel to loading axis.

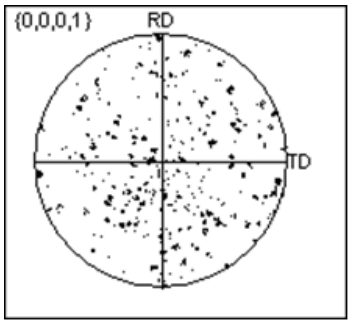

2Mn2Nb (a)

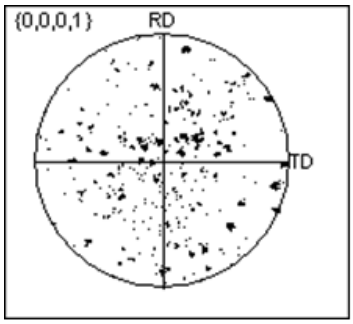

2Mn2Nb (b)

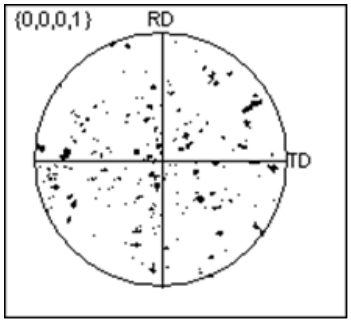

2Mn2Ta (a)

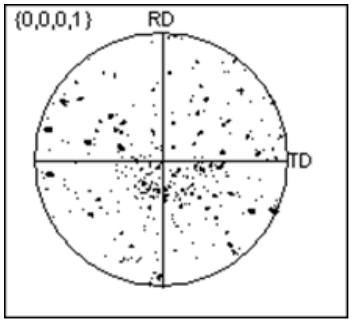

2Mn2Ta (b)

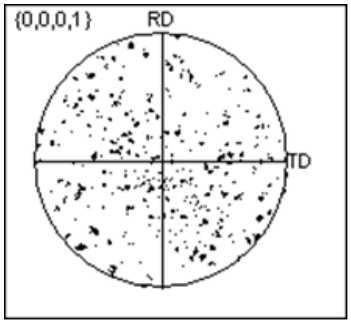

2Nb2Ta (a)

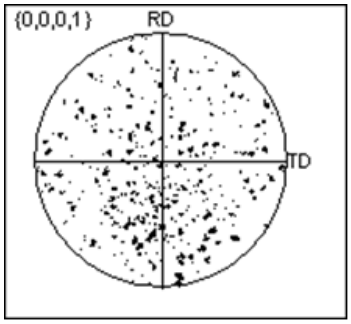

2Nb2Ta (b)

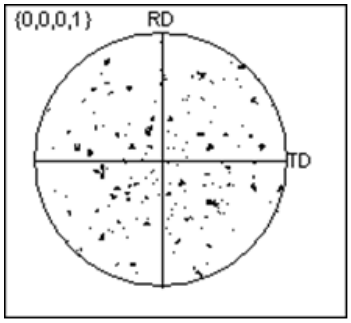

2Mn4Nb (a)

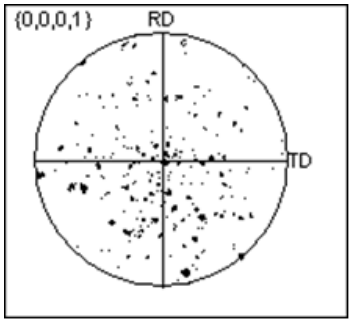

2Mn4Nb (b)

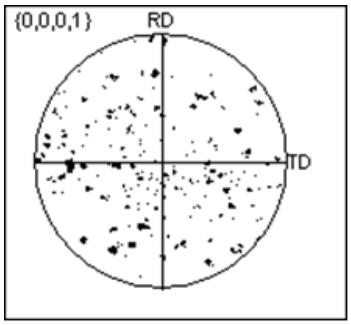

2Mn4Ta (a)

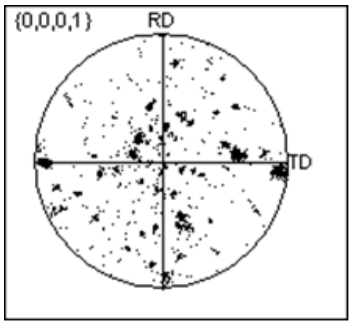

2Mn4Ta (b)

Fig.5.4 EBSD (0001)α2 pole figure showing the random lamellar orientation distribution of 2Mn2Nb, 2Mn2Ta, 2Nb2Ta, 2Mn4Nb, 2Mn4Ta of tensile specimen (a) perpendicular to loading axis and (b) parallel to loading axis.

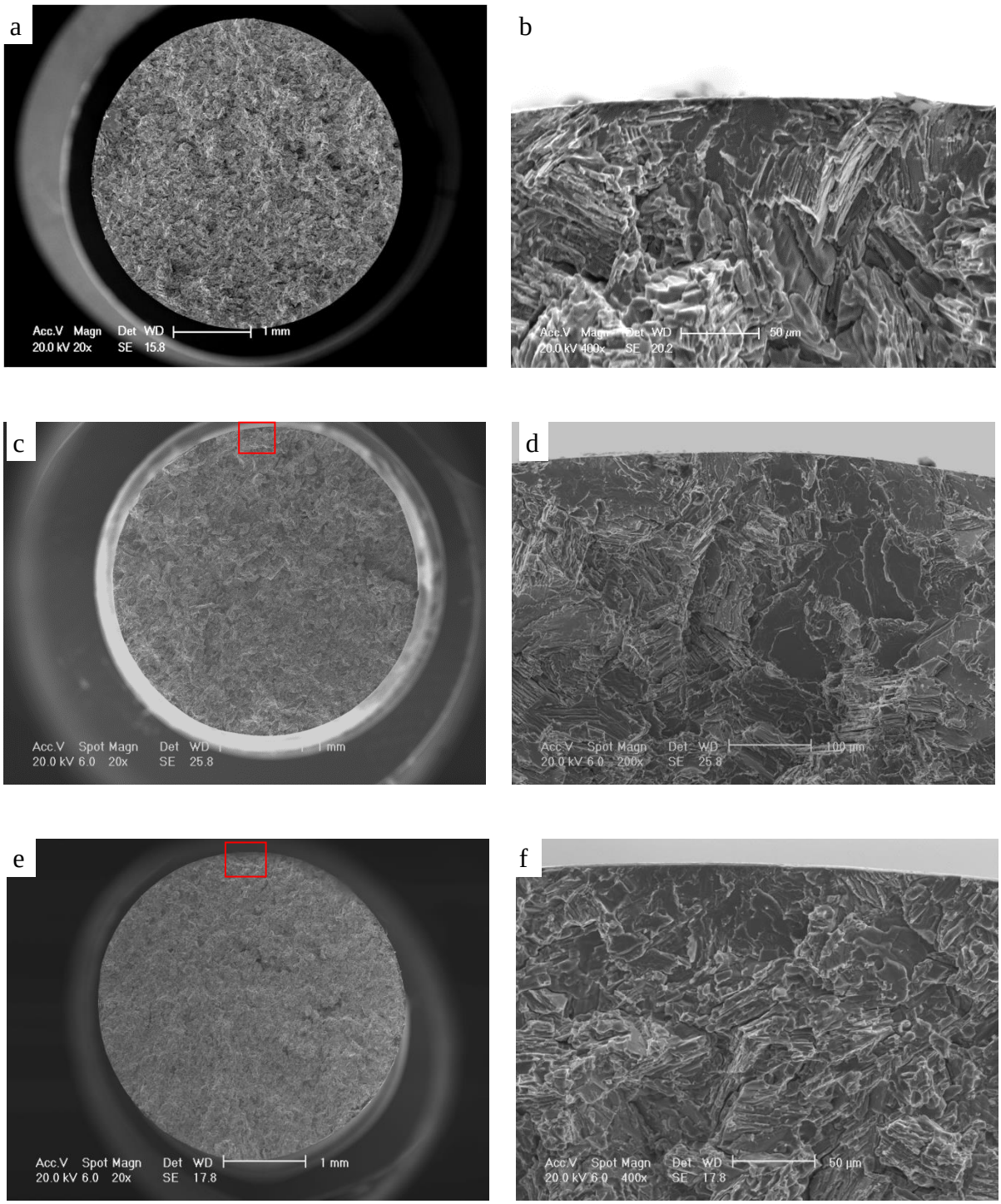

Fig.5.5 SE SEM images of fracture surfaces of the failed tensile test pieces, showing (a) and (b) from alloy 2Mn2Nb, (c) and (d) from alloy 2Mn2Ta and (e) and (f) from alloy 2Nb2Ta test pieces. (a), (c) and (e) are the overall surface morphologies, and (b), (d) and (f) are the corresponding crack initiation areas from the region marked with red rectangles in (a), (c) and (e), respectively.

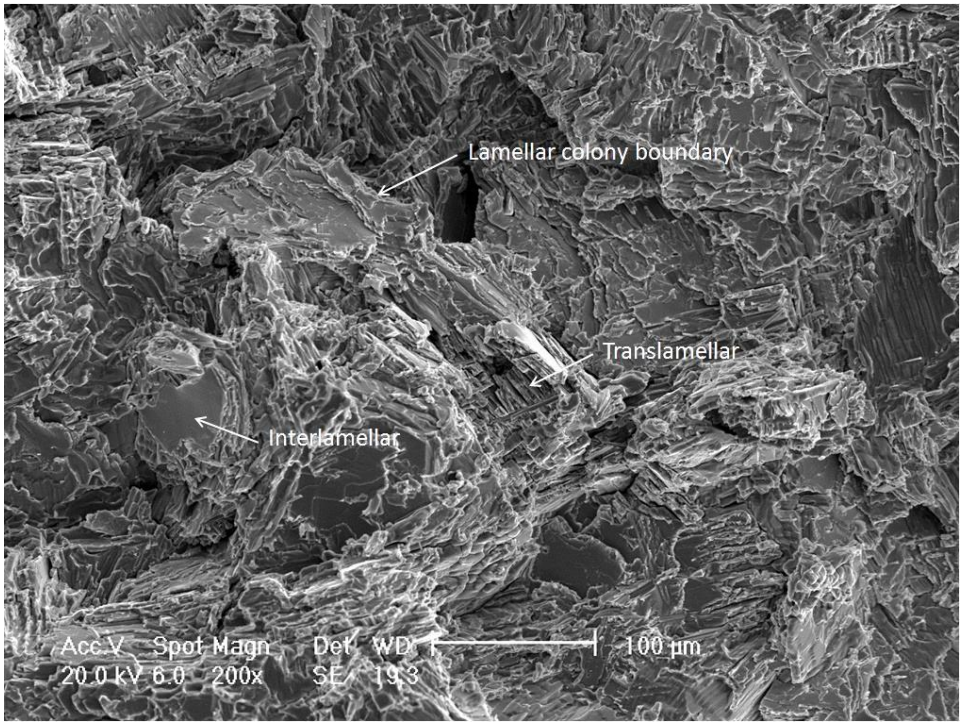

Fig.5.6 SE SEM image of fracture surface of failed tensile test pieces of alloy 2Mn2Ta, indicating the main crack propagation behaviour during tests: translamellar cracking, interlamellar cracking and lamellar colony boundary cracking.

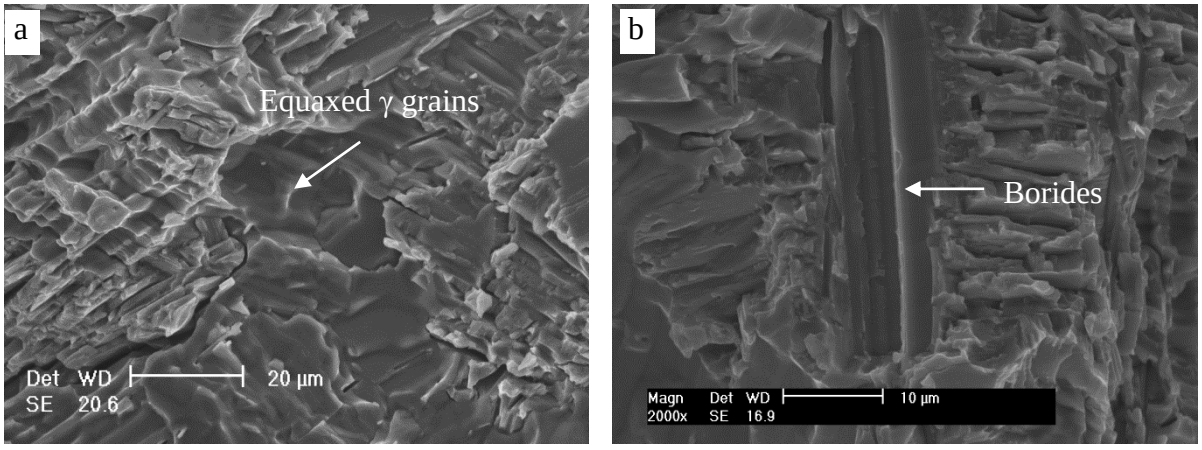

Fig.5.7 SE SEM image of fracture surfaces of alloy 2Mn4Nb (a) intergranular fracture of equiaxed gamma grains and (b) debonding between borides and matrix of alloy.

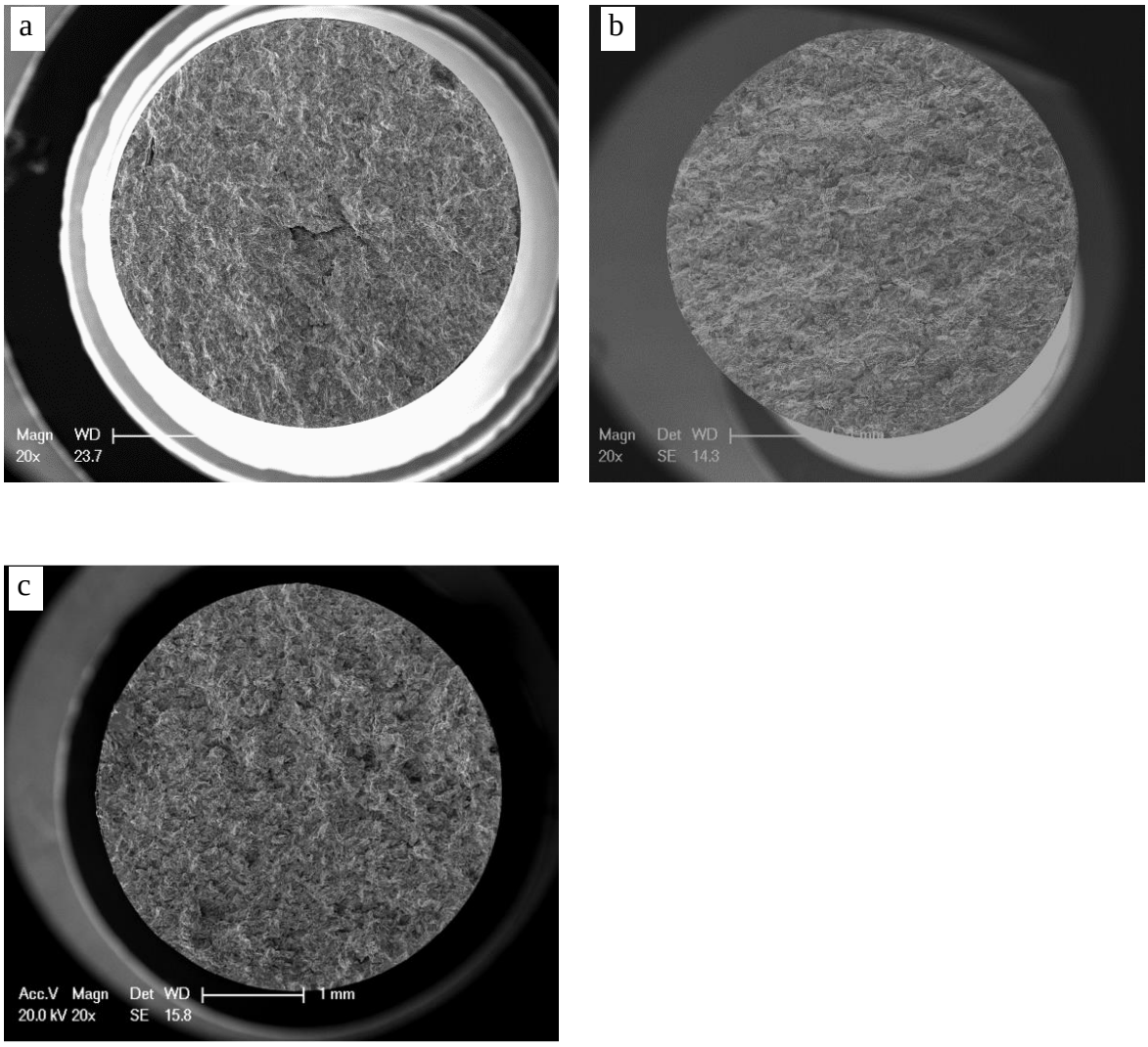

Fig.5.8 SE SEM images of fracture surfaces of the failed tensile test pieces tested at (a) room temperature, (b) 450°C and (c) 650°C.

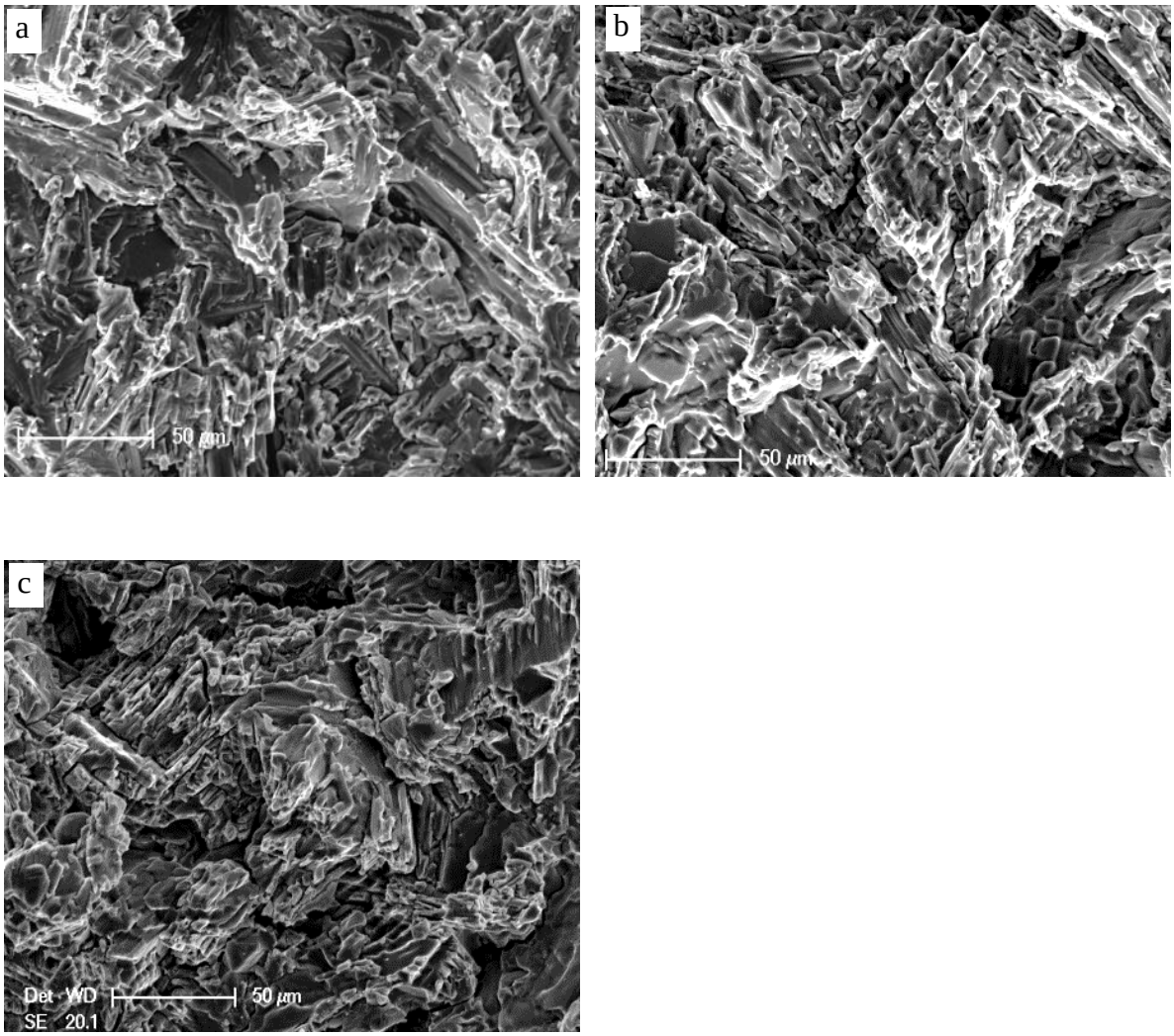

Fig.5.9 SE SEM images of fracture surfaces of the failed tensile test pieces tested at (a) room temperature, (b) 450°C and (c) 650°C.

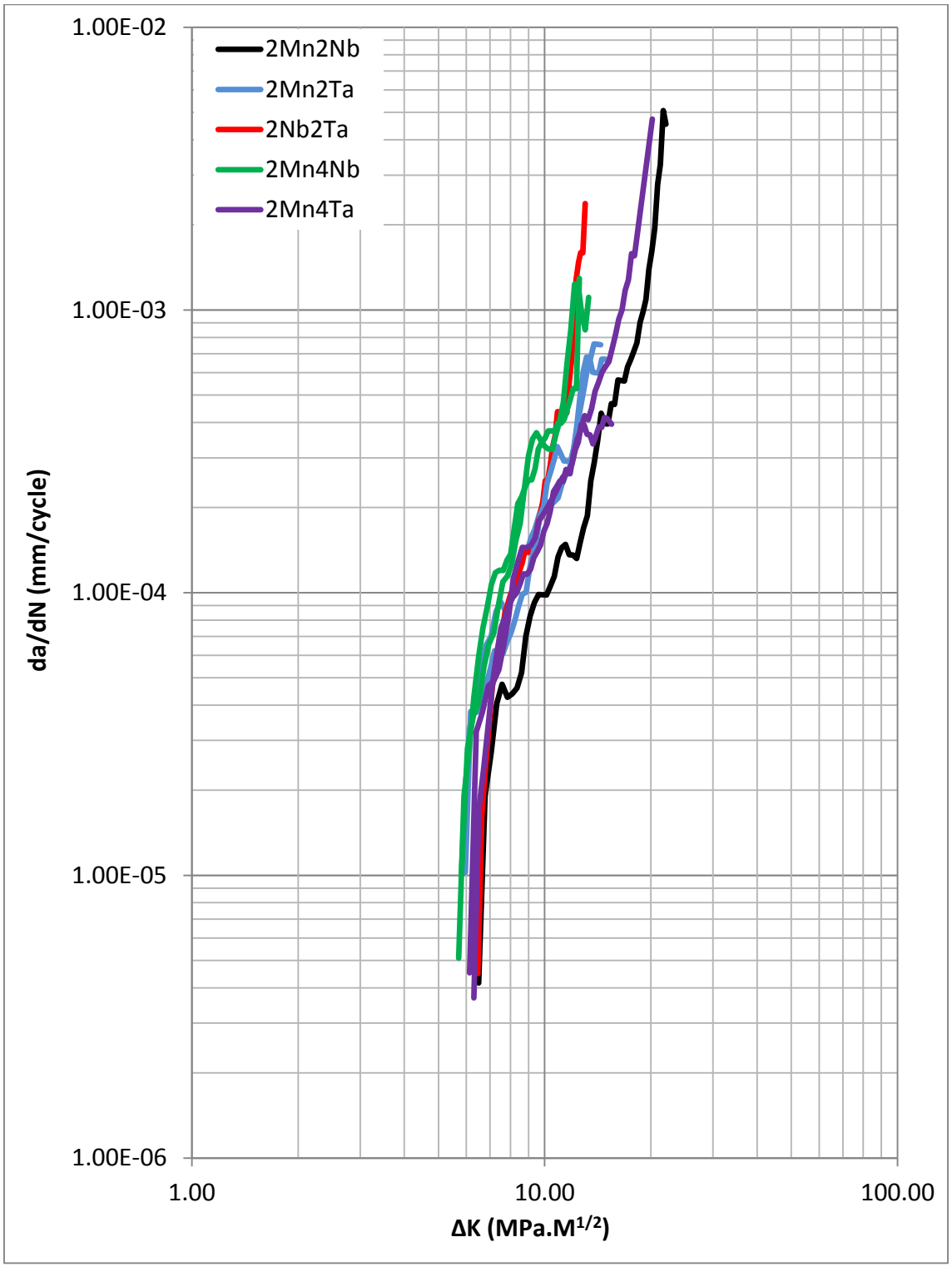

Fig.5.10 Fatigue crack growth curve of 2Mn2Nb, 2Mn2Ta, 2Nb2Ta, 2Mn4Nb and 2Mn4Ta.

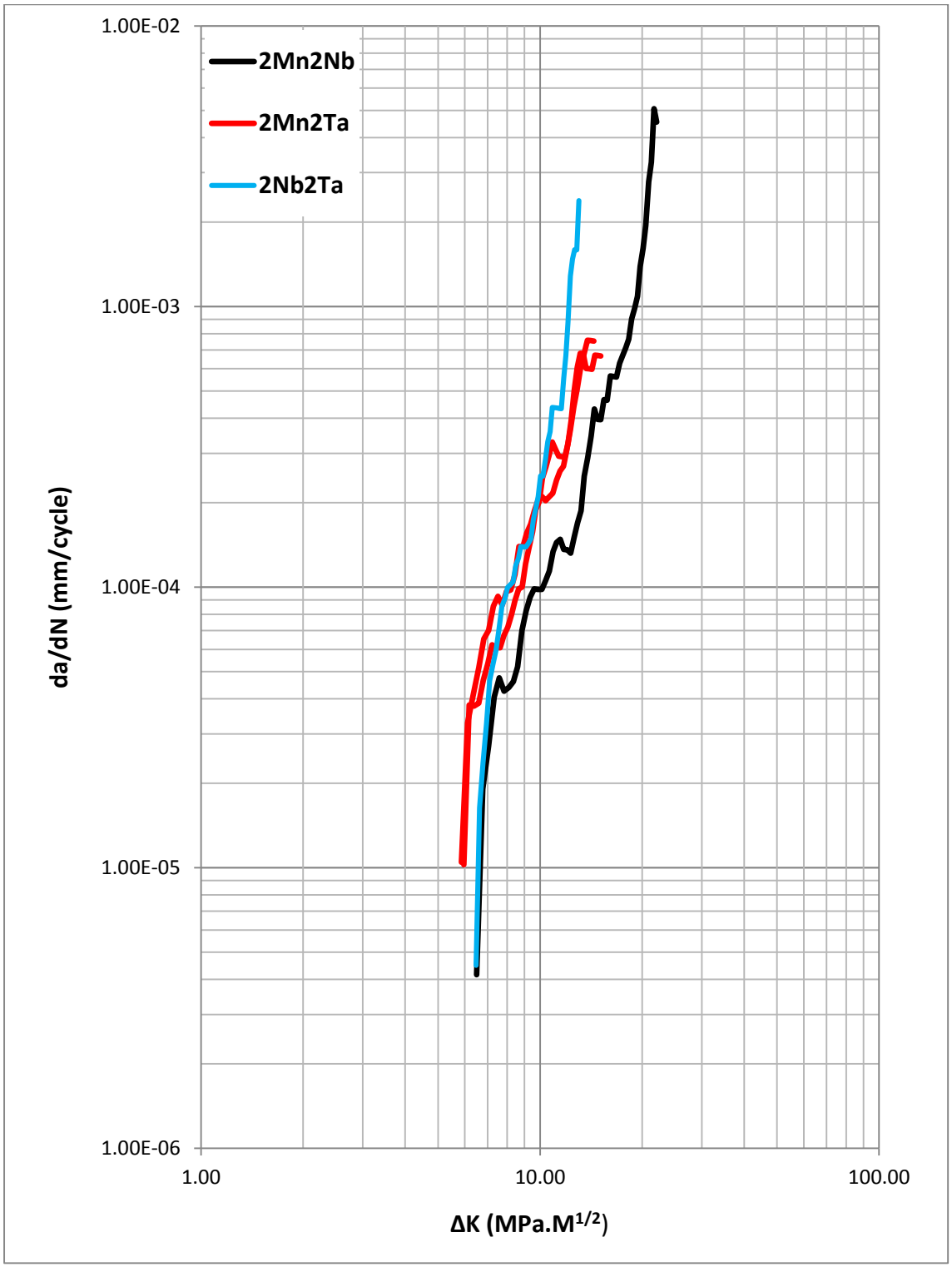

Fig.5.11 Fatigue crack growth curve of 2Mn2Nb, 2Mn2Ta and 2Nb2Ta.

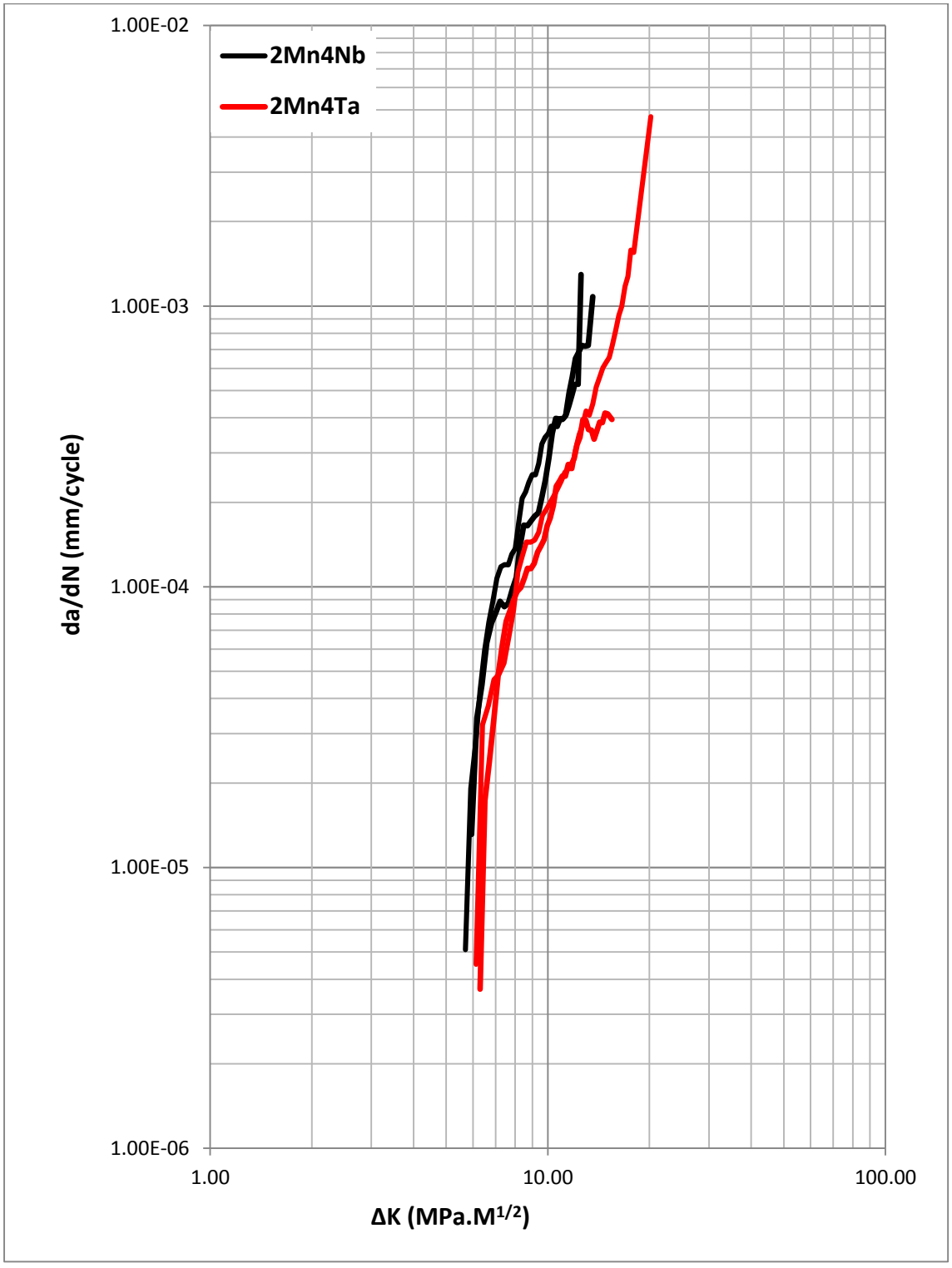

Fig.5.12 Fatigue crack growth curve of 2Mn4Nb and 2Mn4Ta.

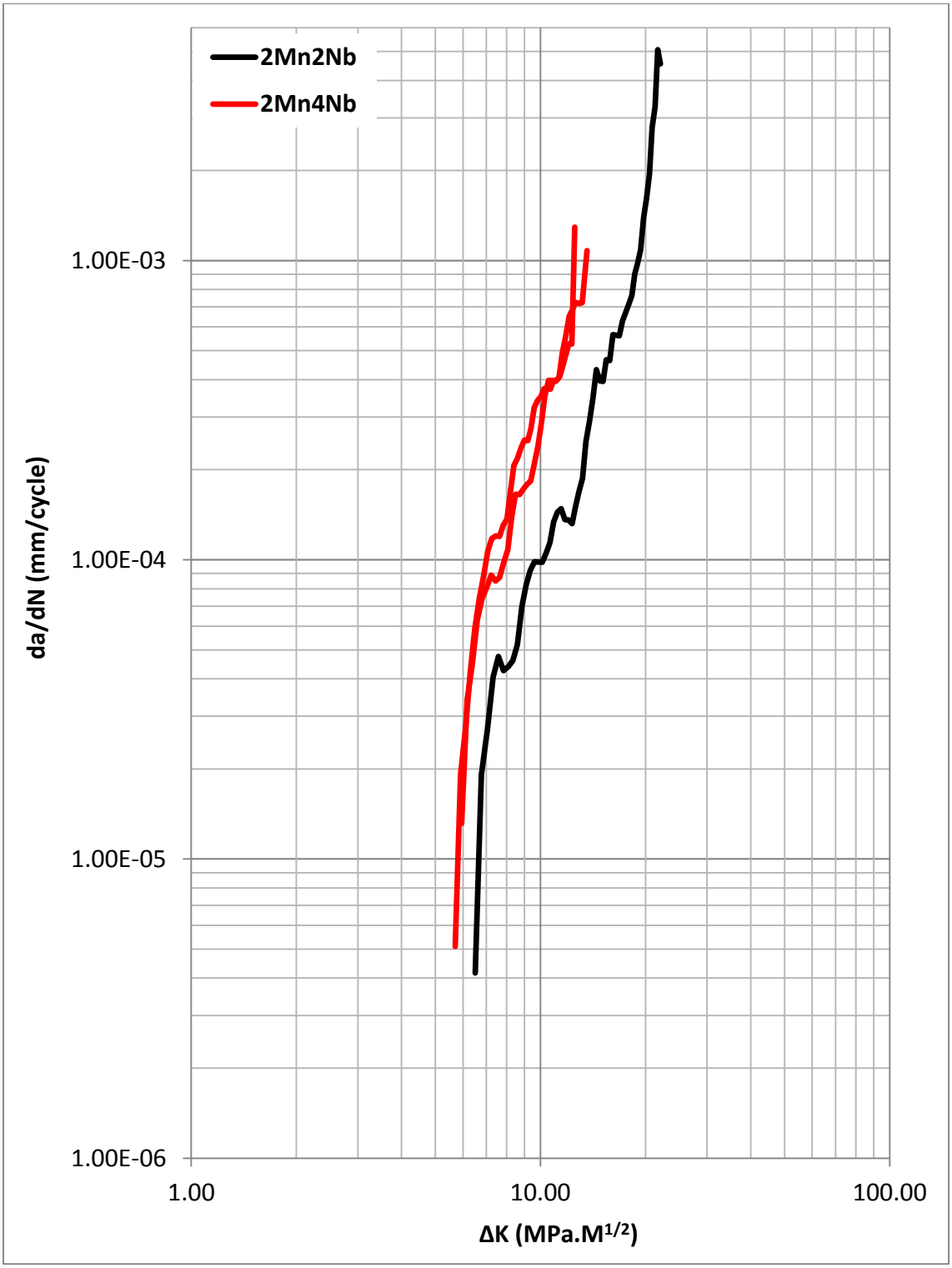

Fig.5.13 Fatigue crack growth curve of 2Mn2Nb and 2Mn4Nb.

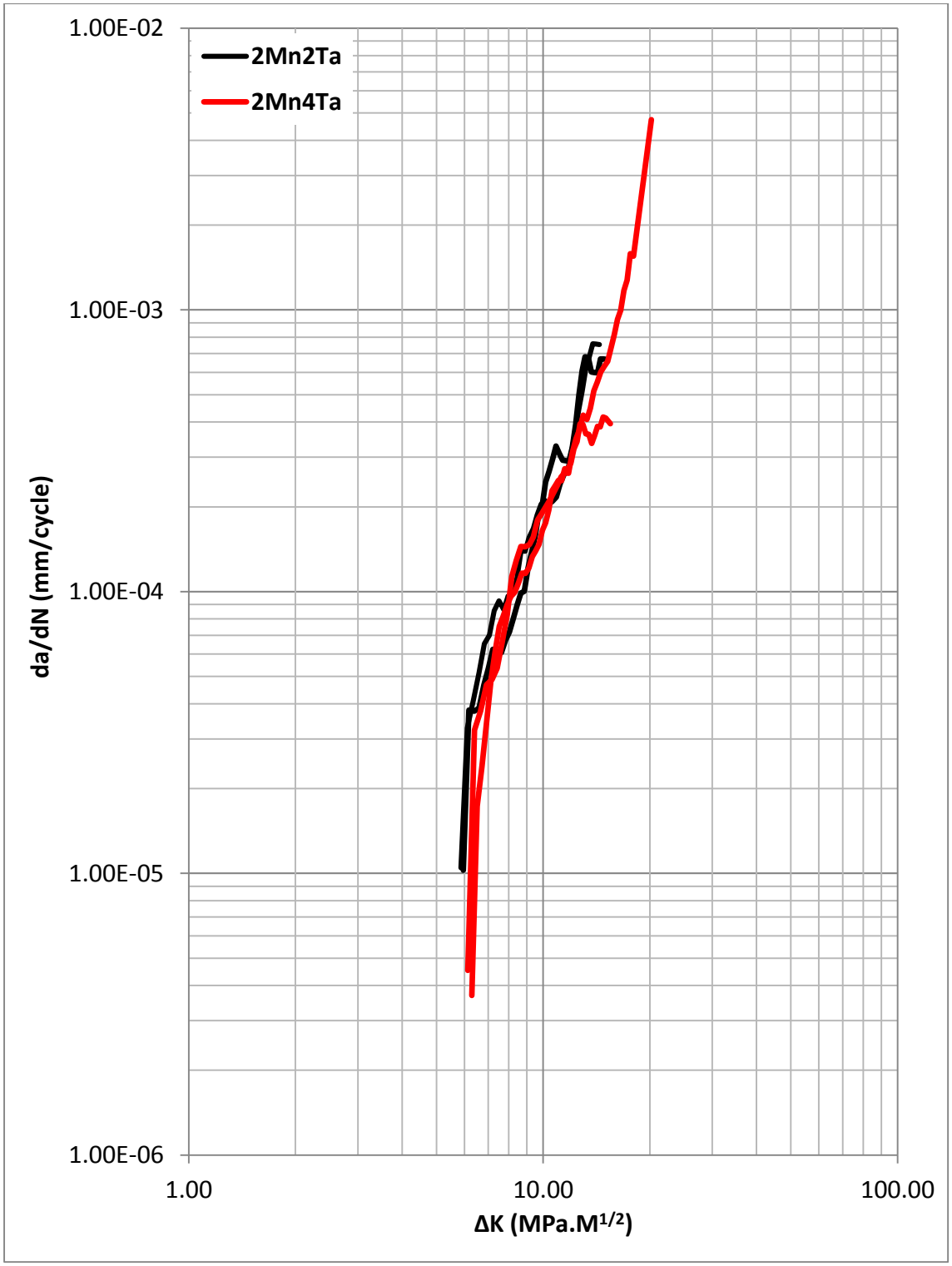

Fig.5.14 Fatigue crack growth curve of 2Mn2Ta and 2Mn4Ta.

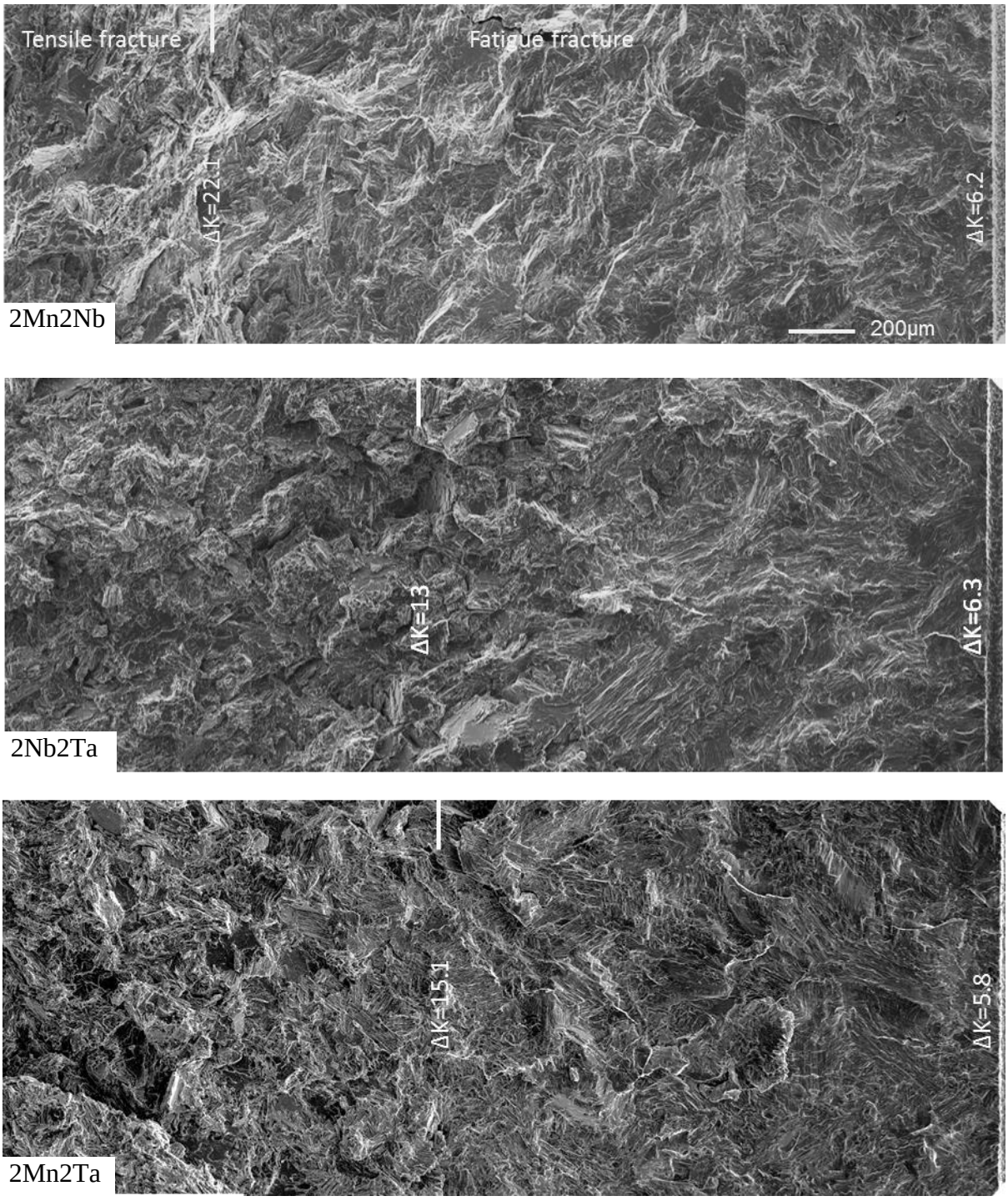

Fig.5.15 SEM montage showing the fracture surface of alloy 2Mn2Nb, 2Nb2Ta and 2Mn2Ta. The crack propagation direction is right to left.

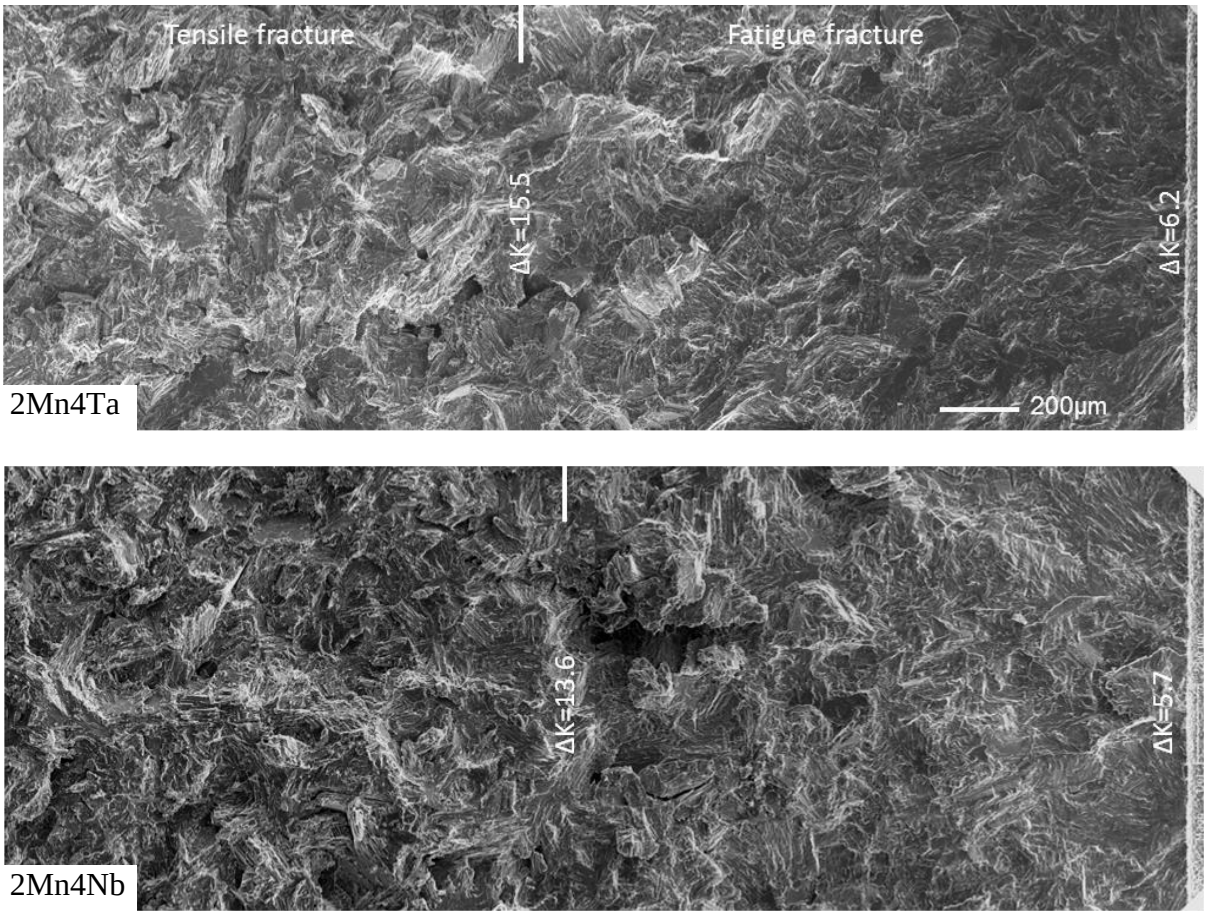

Fig.5.16 SEM montage showing the fracture surface of alloy 2Mn4Ta and 2Mn4Nb. The crack propagation direction is right to left.

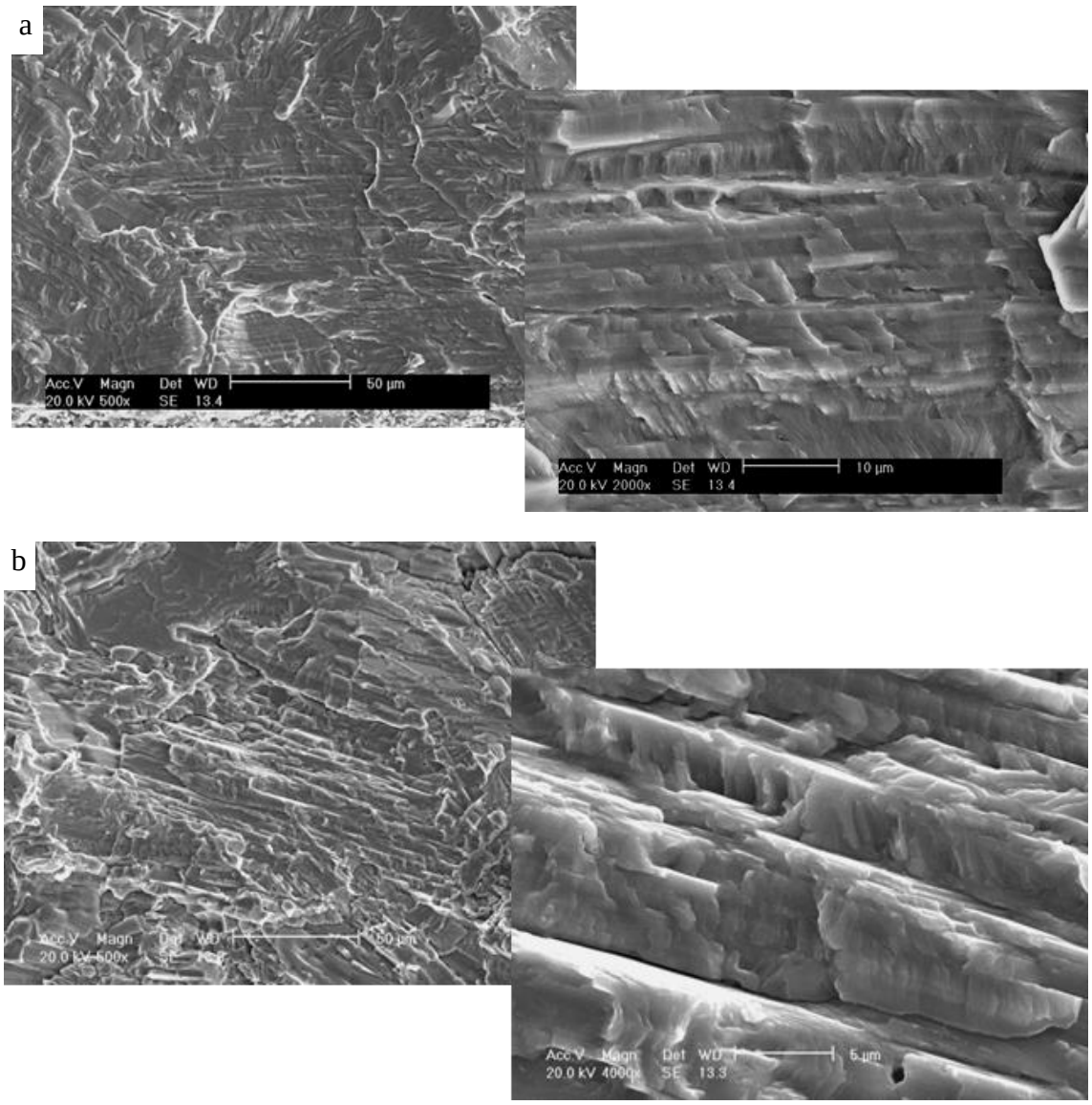

Fig.5.17 SEM SE images showing translamellar fracture surfaces of alloy 2Mn2Nb at low ΔK (a) ΔK=6.5 MPa√m and high MPa√m (b) ΔK=16.4MPa√m.

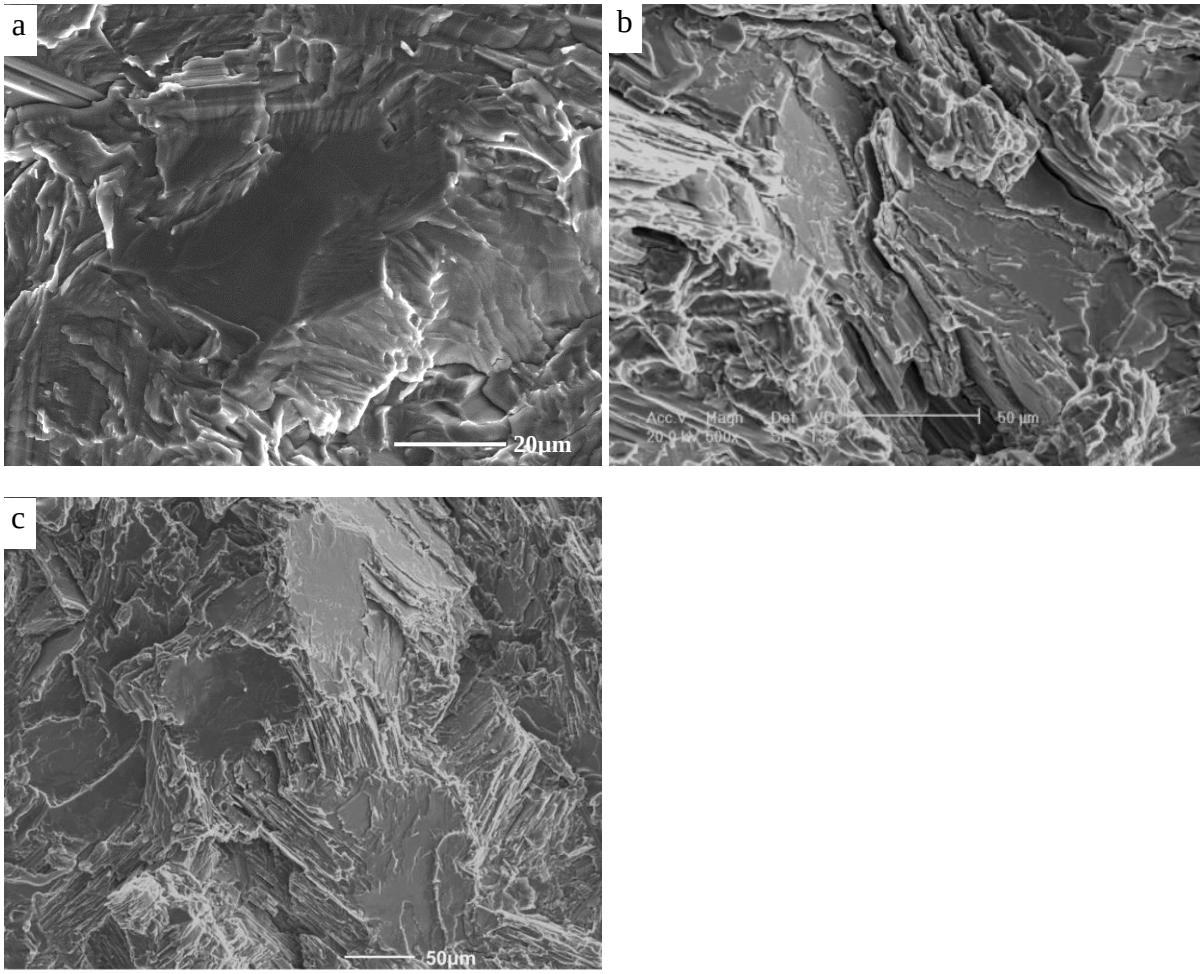

Fig.5.18 SEM SE images showing interlamellar fracture surfaces of alloy 2Mn2Nb at low ΔK (a) ΔK=6.5 MPa√m and high MPa√m (b) ΔK=21.8MPa√m and (c) alloy 2Nb2Nb ΔK=13MPa√m.

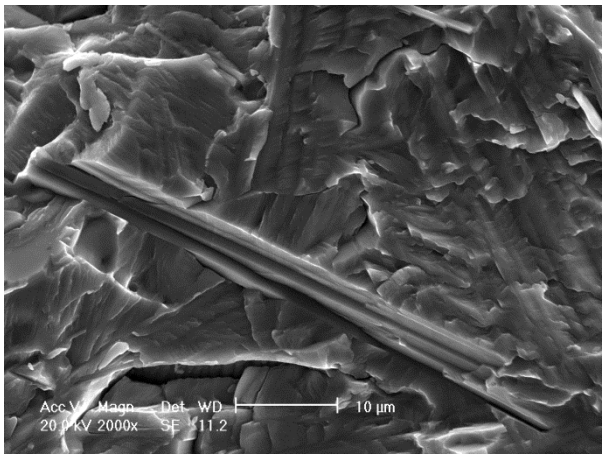

Fig.5.19 SEM SE images show the debonding between borides and matrix of alloy 2Mn2Nb.

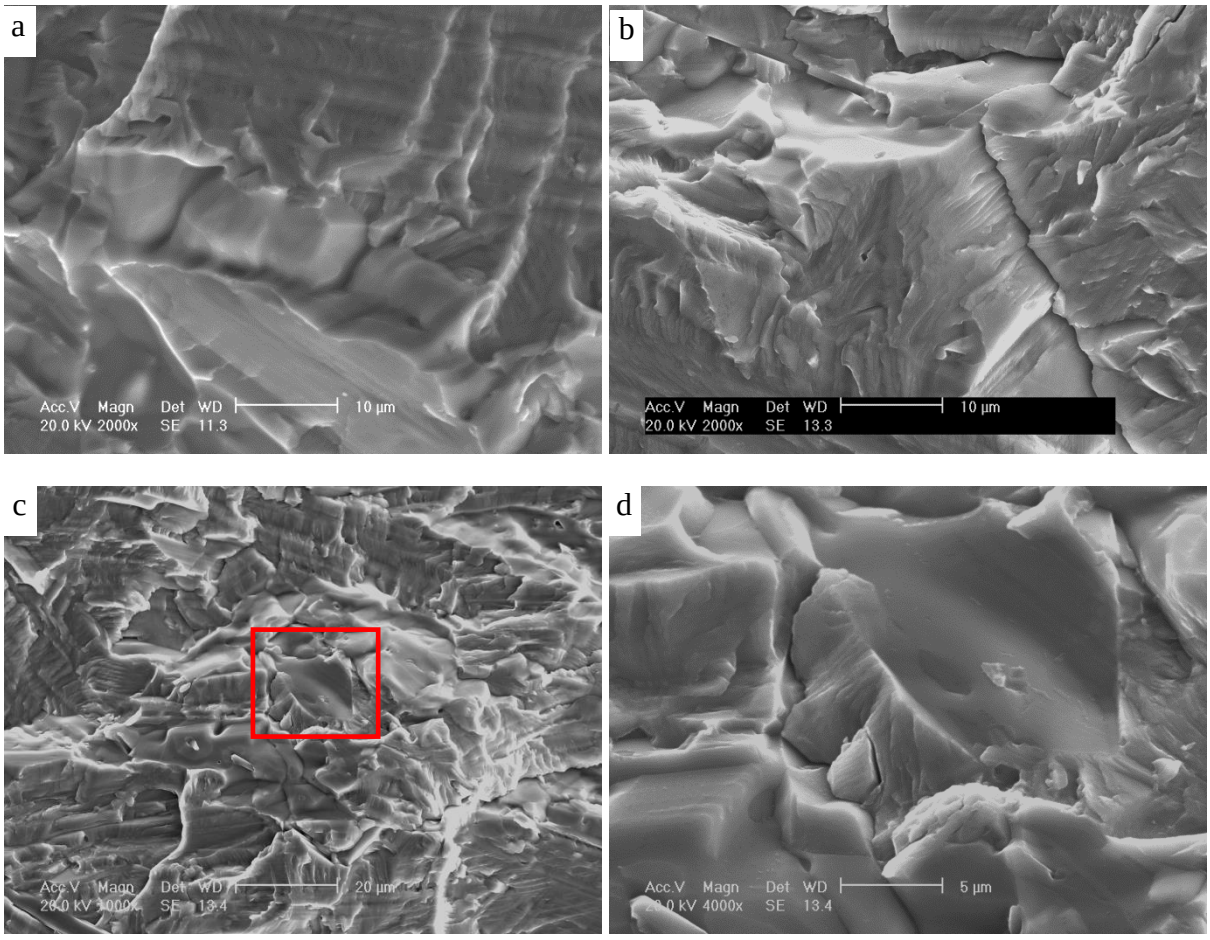

Fig.5.20 SEM SE images show intergranular fracture of equiaxed gamma grians of alloy 2Mn2Nb, (d) is the corresponding area from the region marked with red rectangle in (c).

Table 5.1 Average colony size of forged 2Mn2Nb, 2Nb2Ta, 2Mn2Ta, 2Mn4Ta and 2Mn4Nb

Materials	Average colony size (μm)
Forged 2Mn2Nb	41 ± 24
Forged 2Nb2Ta	25 ± 12
Forged 2Mn2Ta	26 ± 14
Forged 2Mn4Ta	34 ± 21
Forged 2Mn4Nb	39 ± 21

Table 5.2 Average α_2 lamellar spacing, γ lamellae thickness and lamellar spacing of forged 2Mn2Nb, 2Nb2Ta, 2Mn2Ta

Materials	α_2 lamellar spacing (μm)	γ lamellae thickness (μm)	Lamellar spacing (μm)
Forged 2Mn2Nb	1.51	0.76	0.55
Forged 2Nb2Ta	1.25	0.57	0.35
Forged 2Mn2Ta	1.85	0.79	0.59

Table 5.3 Phase ratio of α_2 and γ phases of forged 2Mn2Nb, 2Nb2Ta, 2Mn2Ta, 2Mn4Ta and 2Mn4Nb

Materials	**α_2 (%)**	**γ (%)**
Forged 2Mn2Nb	24±3	76±3
Forged 2Nb2Ta	23±2	77±2
Forged 2Mn2Ta	26±3	74±3
Forged 2Mn4Ta	28±2	72±2
Forged 2Mn4Nb	19±2	81±2

Table 5.4 Hardness of forged 2Mn2Nb, 2Nb2Ta, 2Mn2Ta, 2Mn4Ta and 2Mn4Nb

Materials	**Hardness(kgf/mm^2)**
Forged 2Mn2Nb	286 ± 4
Forged 2Nb2Ta	301 ± 4
Forged 2Mn2Ta	280 ± 3
Forged 2Mn4Ta	273 ± 2
Forged 2Mn4Nb	287 ± 3

Table 5.5 Yield strength, UTS and elongation results of forged 2Mn2Nb, 2Nb2Ta, 2Mn2Ta, 2Mn4Nb and 2Mn4Ta at 650°C.

Materials	Yield strength (MPa)	UTS (MPa)	Elongation (%)	Temperature (°C)
Forged 2Mn2Nb	400	551	1.5	650
Forged 2Mn2Nb	405	565	1.4	650
Forged 2Nb2Ta	455	628	1.7	650
Forged 2Nb2Ta	452	637	1.9	650
Forged 2Mn2Ta	400	550	1.6	650
Forged 2Mn2Ta	384	552	1.9	650
Forged 2Mn4Ta	400	567	1.9	650
Forged 2Mn4Ta	395	544	1.6	650
Forged 2Mn4Nb	420	540	1.1	650
Forged 2Mn4Nb	405	560	1.3	650

Table 5.6 Yield strength, UTS and elongation results of forged 2Mn2Nb at room temperature, 450°C and 650°C.

Materials	Yield strength (MPa)	UTS (MPa)	Elongation (%)	Temperature (°C)
Forged 2Mn2Nb	450	668	1.3	RT
Forged 2Mn2Nb	425	599	0.9	RT
Forged 2Mn2Nb	425	622	1	450
Forged 2Mn2Nb	420	611	1	450
Forged 2Mn2Nb	400	551	1.5	650
Forged 2Mn2Nb	405	565	1.4	650

Table 5.7 Fatigue crack propagation threshold of different alloys.

Materials	ΔKth at threshold (MPa.m^1/2)	Stress ratio	Temperature (°C)
Forged 2Mn2Nb	6.2	0.1	650
Forged 2Nb2Ta	6.3	0.1	650
Forged 2Mn2Ta	5.7	0.1	650
Forged 2Mn2Ta	5.8	0.1	650
Forged 2Mn4Ta	6.2	0.1	650
Forged 2Mn4Ta	6.0	0.1	650
Forged 2Mn4Nb	5.7	0.1	650
Forged 2Mn4Nb	5.6	0.1	650

Chapter 6. Effects of lamellar orientation on Fatigue crack propagation threshold[2]

The microstructures and properties of lamellar γ-TiAl alloys are strongly anisotropic, and the properties of polycrystalline lamellar γ-TiAl alloys are the average of individual lamellar colonies. Therefore, the study on lamellar γ-TiAl alloys is based on the study of individual lamellar colonies. The behaviour and properties of lamellar γ-TiAl alloys have been investigated with Polysynthetically twinned (PST) TiAl crystals. It has been found that many properties are influenced by lamellar orientation, such as tensile strength, compression strength, fatigue strength, fracture toughness. In this chapter, the lamellar orientation effect on fatigue crack propagation threshold is studied by using very coarse grained Ti46Al8Nb and Ti4522 alloy. It is possible to keep the entire notch within one single lamellar colony, therefore to investigate the influence of lamellar orientation on threshold intensity range.

[2] The contents of this chapter are based on the paper by Yang J., Li H., Hu D., Martin N., and Dixon M., Lamellar orientation effect on fatigue crack propagation threshold in coarse-grained Ti46Al8Nb. Materials Science and Technology, 2014. 30(15): pp. 1905-1910.According to Elsevier's policy, the contents of published journal articles can be included in a thesis. *http://www.elsevier.com/authors/author-rights-and-responsibilities*

6.1 Effects of lamellar orientation on Fatigue crack propagation threshold with alloy Ti46Al8Nb

6.1.1 Starting microstructure and lamellar orientation determination

The ingot of Ti46Al8Nb was HIPped at 1280°C/150MPa for 4h to offer a coarse lamellar microstructure, which could allow the notch to be made within one lamellar colony. The alloy was etched and observed using optical microscopy, and the microstructure is shown in Fig.6.1. As can be seen from the image, the lamellar colonies are very coarse and the sizes of some colonies are over 1mm. The α_2 lamellar spacing, γ lamellae thickness and lamellar spacing were measured and they are 2.35μm, 1.73μm and 1.11μm. As the notch is 1mm in length and 0.5mm in depth, it is possible to make the notch within one lamellar colony. However, some small colonies are still formed during solidification and some equiaxed gamma grains are also formed during HIPping. Therefore, careful observation on the surface of each face of the test pieces was carried out with an optical microscope and the position of the notch was accurately selected and induced by an EDM which can be accurate to 1μm.

Although the test pieces were carefully prepared, there are still some specimens where the notch was not made in one lamellar colony. Only the specimens where the notch was in one colony or most of the notch (70% or greater) within one colony were chosen for further study. After fatigue testing, the samples were broken by monotonic tensile load. To determine the lamellar orientation, one half of each sample was ground and polished to the EDM notch trail to provide a flat and longitudinal surface for SEM examination, shown as the shaded plane L in Fig.6.2(a). The orientation of the lamellar colony in front of the notch is determined by two angles α and β. They are both the angle between the lamellar interface trace and notch, but α

is on the fracture plane while β is on plane L, as shown in Fig.6.2 (b). For the specimen where the orientation cannot be analysed by SEM imaging, the orientation measurement was done by EBSD on plane L.

The lamellar orientation can be expressed in a pole figure as Fig.6.3 (a). The three axes of the pole figure are defined as follows: the direction of the applied stress, N, is in the centre; the A axis which is at the top of the pole figure is parallel to the overall crack propagation direction on the fracture plane and the B axis to the right of the pole figure is perpendicular to the overall crack propagation direction. Obviously, in the centre of the pole figure, N, the lamellar interface is perpendicular to the loading axis and in the 90º orientation; and at the circumference the lamellar interface is parallel to the loading axis and in the 0º orientation. Accordingly, the three different orientations of lamellar colony, A notch, B notch and C notch, are also shown in Fig.6.3 (b). The orientation of A notch is perpendicular to the loading axis and parallel to the overall crack growth direction, therefore, it is the intersection of A axis and circumference in the pole figure. Similarly, the orientation of B notch is also perpendicular to the loading axis but perpendicular to the overall crack growth direction, thus it is the intersection of B axis and circumference in the pole figure. The orientation of Notch C is parallel to the loading axis and it is in the centre of the pole figure [82, 84, 111].

The SEM images and EBSD results of 11 tested samples are shown in Fig.6.4-6.14. The definition of axes in the EBSD pole figure is different from that in the lamellar orientation pole figure. The loading axis is in the centre in the lamellar orientation pole figure while it is at the circumference in the EBSD pole figure. The overall crack growth direction is at the top or bottom of the circumference in the lamellar orientation pole figure while it is in the centre in the EBSD direction. The lamellar orientations of the tested samples are summarised in the

pole figure in Fig.6.15. From the pole figure shown in Fig.6.15, it can be seen that 11 test pieces were selected for further analysis, and they are with different orientation to the loading axis, from 0º to 90º. Among these test pieces, not every notch is made within one lamellar colony. The close dots in the pole figure indicate where a single lamellar colony is in front of the notch and the open dots indicate where more than one lamellar colony is in front of the notch.

6.1.2 Fatigue crack propagation

The fatigue crack growth resistance curves, fatigue crack growth rate (da/dN) versus stress intensity factor range (ΔK) are shown in Fig.6.16. The threshold stress intensity factor range (ΔK_{th}) tested at 650ºC in air with stress ratio of 0.1 is measured to be between 4.3 to 7.2MPa√m as summarised in Table.6.1. There is a significant difference of almost 3MPa√m between samples with near 0º orientation to near 90º orientation. From the results shown in Table 6.1, it can be seen that specimens 1, 4, 8 and 9 shows the highest level of threshold, from 6.5 to 7.2 MPa√m, and the lamellar colonies in front of the notch of these specimens are all with low angle orientation, which is near 0º as shown in the pole figure in Fig.6.15. Furthermore, it seems that the threshold is not affected by the notch orientation, as the notch orientation of these four specimens is A-notch, B-notch and A-B notch. The intermediate threshold values are obtained with specimens with near 90º orientation (specimen 468-7 and 468-12), and the lowest level of threshold is obtained with the specimens with intermediate orientation. Clearly, the dominant factor affecting the threshold value is the angle between the lamellar interface normal and loading axis, which is named lamellar orientation in this thesis for short. The sub-orientation, which is the angle between lamellar interface and the overall crack growth direction, i.e. axis A, does not seem to affect the threshold value no

matter whether the lamellar orientation is near 0º or intermediate. The relationship between threshold and lamellar orientation is shown in Fig.6.17. It can be seen that the threshold value drops from the highest value to the lowest value at about 30-50º with increase of lamellar orientation and increases again after that.

Fig.6.18 shows the fatigue crack growth resistance curve of specimen 468-12 and its fracture surface. It can be seen that the fatigue crack curve shown here is different from others. The crack growth rate increases at the beginning, but decreases gradually after the ΔK of about 6.2MPa.$m^{1/2}$ and reaches the slowest growth rate at a ΔK level of 7.2 MPa.$m^{1/2}$. This is because it is the boundary between the first and second lamellar colony in this range, as shown in Fig.6.18 (b). Therefore, the fatigue crack growth rate is also dependent on the lamellar orientation.

6.1.3Fracture surface analysis

The fracture surface analysis of the selected specimens, with various lamellar orientations, was carried out by SEM. As the study is focused on the effects of lamellar orientation on fatigue crack propagation threshold, the analysis of fracture surface concentrated on the area which is related to the threshold. Only the microstructure in a very limited region in front of the notch is related to the fatigue crack propagation threshold and the rest is concerned with the fatigue crack propagation. There is no definition of the size of fracture surface which is related to the threshold. However, by the analysis of a certain amount (more than 30) of experimental data, it is noted that the steady crack propagation is found to be detected from the distance about 10-70μm from the notch owing to the resolution of the D.C.P.D. method, and the average value is 40μm. Thus, the area of 50μm from the notch is selected for the

study of the relationship between microstructure and threshold, and the rest in the fatigue area is in the fatigue crack propagation regime.

The fracture surfaces of two near 0° orientation, A- notch sub-orientation specimens (468-1 and 468-4) are shown in Fig.6.19. As can be seen from Fig.6.4 and Fig.6.5, the notch of the specimen 468-1 is within one lamellar colony, while that of specimen 468-4 is in two colonies, of which nearly 70% is with the similar orientation with 468-1. The crack grows from bottom to top which is the same as in the previous fracture surface images (Fig.6.4-6.14) and following ones. The fracture surface of specimen 1 (with A-notch) in front of the notch in Fig.6.19 (a) is very smooth, and this can be attributed to the nearly entire translamellar fracture throughout the fracture surface. The details of the fracture surface are shown in Fig.6.19 (b) by the high magnification image of an area which is approximately 80μm from the notch in Fig.6.19 (a). The whole fracture surface of specimen 468-4 is given in Fig.6.19 (c), and it can be seen that the dominant colony on the left is with a sub-orientation of A-notch and the right colony is with a sub-orientation of A-B notch. The details of the main colony are shown in Fig.6.19 (d), and the fracture surface at this area is also very smooth.

The fracture surface of specimen 468-8 (with B-notch) ahead of the notch is shown is Fig.6.20 (a). It is noted that the roughness of the fracture surface of specimen 468-8 differs with the distance from the notch, i.e. ΔK. A high magnification image of the middle of Fig.6.20 (a) is given in Fig.6.20 (b). It can be seen that apart from translamellar cracking, interlamellar cracking is also observed on the fracture surface. Both the rougher fracture surface and the occurrence of interlamellar fracture are due to the increase of the stress intensity factor range ΔK with the increasing distance from the notch, which has been discussed in the previous chapter.

Fig.6.21 (a) shows the fracture surface of specimen 468-9 from the notch, of which the dominant lamellar colony is near 0º orientation. The area on the left of the red line in is the dominant colony, and it has a sub-orientation of A-B notch. Fig.6.21 (b) shows the details of the fracture surface about 80μm from the notch by a high magnification image. The facture surface is rather flat, and only translamellar fracture was observed on the fracture surface. This is similar to that observed in the specimens with A-notch.

The fracture surfaces of the whole notch area of specimen 7 and 12 are shown in Fig.6.22 (a) and (c). The notch of both specimens are not within only one lamellar colony, but most of the notch (more than 70%) is within a lamellar colony which is close to 90º orientation named C notch, and the lamellar interface is parallel to the fracture plane. Therefore, the interlamellar fracture is the dominant fracture mode in front of the notch. Fig.6.22 (b) and (d) shows the details of the interlamellar fracture ahead of the notch and it can be seen that the crack propagates through cleavage on the lamellar interface.

As shown on the whole fracture surface of each specimen shown in Fig.6.4 (a)-Fig.6.14 (a), the fracture surface of the specimens with low fatigue crack propagation threshold are different from those with high threshold values. The lamellar orientation of the specimens with low threshold values is between 20º and 70º, which is the soft orientation in PST crystals. The fracture surface of specimen 468-5 in front of the notch is shown in Fig.6.23 (a) and the fracture surface in very rough. The orientation of the lamellar colony at the notch is about 30º. It can be seen that there are two bright areas, which are marked by the black arrows, just ahead of the notch. In these areas, the first cracks formed under a load which is lower than that threshold. The growth of early cracks can be detected by the chart recorder, but it stops after slight growth. As threshold is the stress intensity factor range in the beginning of the

continuous crack growth, higher load was applied if no crack growth is detected for another 2 hours after the early cracks. The detail of the early crack is shown in Fig.6.23 (b) with a depth about 10μm from the notch. There is lots of oxidation on the fracture surface, revealing that the crack propagation stops for a long time at the testing temperature. The fracture of these cracks is combined with interlamellar cracking and translamellar cracking, and there are some reefs on the fracture surface. These reefs are in the direction parallel to the overall crack growth direction. The formation of these reefs is due to the intersection between two adjacent fracture planes across the lamellae. The cracks start to propagate by translamellar fracture and along the lamellar interface with some small steps. Some early cracks stopped at the top of this area and others continued.

Early cracks are also observed on the fracture surface of other samples with soft orientation. The behaviour of early cracks is different. Fig.6.24 shows two early crack areas with different size observed on the fracture surface of specimen 468-6. The semi-elliptical area in Fig.6.24 (a) is about 150μm in width and 70μm in depth from the notch, while that in Fig.6.24 (b) is only about 50μm in width and 10μm in depth from the notch. A large area of regularly spaced early cracks of specimen 468-15 is shown in Fig.6.25. It can be seen that the crack propagated before the final continuous propagation. The cracks were arrested for the first time at a depth of about 20μm from the notch and then arrested at a depth of nearly 50μm from the notch for the second time. Two early cracks of specimen 468-16 are shown in Fig.6.26 (a) and (b). The cracks in Fig.6.25 (a) propagated twice before continuous growth while that in Fig.6.26 (b) propagated only once. The cracks in Fig.6.26 (a) were first arrested at a depth of about 30μm and then propagated about another 10μm before the second arrest. Therefore, there can be more than one early crack area in one specimen, and the cracks may

propagate more than once before continuous growth. The size of the area of the early cracks is also different, even in the same sample.

From the results of fatigue threshold of the five specimens with soft lamellar orientation, it can be seen that the threshold of specimen 468-10 is higher than that of the other four specimens. No early cracks were observed ahead of the notch in specimen 468-10, while they were found in the other four specimens. Thus, early cracks might be one factor which reduces the fatigue threshold.

6.2 Effects of lamellar orientation on Fatigue crack propagation threshold of alloy Ti4522

6.2.1 Starting microstructure and lamellar orientation determination

The ingot of alloy Ti4522 was also HIPped to provide a coarse lamellar microstructure to induce the notch within one lamellar colony. Optical microscopy was applied on the etched samples for the starting microstructure observation, and an optical micrograph is shown in Fig.6.27. The α2 lamellar spacing, γ lamellae thickness and lamellar spacing were measured and they are 1.29μm, 0.97μm and 0.58μm, respectively. The lamellar colonies in this alloy are relatively coarse and some of the colonies are over 1mm. However, as with the coarse Ti46Al8Nb alloy, a certain amount of small lamellar colonies and equiaxed gamma grains are formed during solidification and HIPping, respectively. Therefore, the machining of the notch requires careful design, and the notch was induced using the same procedure as for alloy Ti46Al8Nb. 16 samples were machined for testing. However, after the optical microscopy

observation on the four surfaces of each sample, it was found that only eight samples were able to provide a large lamellar colony to form the notch within one colony.

The orientation of the lamellar colony/colonies at the notch were finally determined by the angle between the lamellar interface trace and notch on the fracture plane and that angle on plane L in Fig.6.2, termed angle α and β, respectively. According to the fracture surface analysis of the tested samples, it can be seen that among these samples, four samples were found with the notch in one lamellar colony, and their fracture surfaces are shown in Fig.6.28 (a) – Fig.6.31 (a). The BSE SEM images of plane L are shown in Fig.28 (b) – Fig.6.31 (b). Thus, a pole figure can be used to represent the lamellar orientation of these samples, as shown in Fig.6.32. The dots denote the lamellar orientation of each sample at the notch. For the other four samples, 4522-8, 4522-13, 4522-14 and 4522-15, two lamellar colonies were observed ahead of the notch, and they occupied comparable length at the notch, as shown in Fig.6.33.

6.2.2 Fatigue crack propagation

The fatigue crack propagation data was processed and the results are summarised in the fatigue crack growth resistance curves in Fig.6.34, expressed as fatigue crack growth rate (da/dN) versus stress intensity factor range (ΔK). The threshold stress intensity factor range (ΔK_{th}) tested at 650ºC in air with stress ratio of 0.1 is measured to be between 4.8 to 7MPa√m and summarised in Table.6.2, with a significant difference of 2.2MPa√m.

From the pole figure shown in Fig.6.32, it can be seen that there are two samples 4522-3 and 4522-12 with very low angle orientation, which is almost at the circumference. Sample 4522-

3 is typical A-notch sub-orientation, and sample 4522-12 is with A-B notch sub-orientation. They present the highest fatigue crack propagation threshold values, 7MPa√m and 6MPa√m. Sample 4522-7 is within about 10º orientation, and the threshold value is 5.7 MPa√m. Sample 4522-5 is in the soft orientation, about 60º, and it shows the lowest threshold value among these four samples. This trend is the same as that observed with alloy Ti46Al8Nb, high threshold at hard orientation and low threshold at soft orientation.

6.2.3Fracture surface analysis

The fracture surfaces of sample 4522-5, 4522-7, 4522-12 and 4522-14 were observed by SEM with the aim of defining the effect of lamellar orientation on fatigue crack propagation threshold. Therefore, the fractography was concentrated in the near threshold area. As mentioned in paragraph 6.1.3, based on experience, the area of 50μm from the notch is treated as the near threshold area for the study of the relationship between lamellar orientation and threshold, and the rest in the fatigue area is in the fatigue crack propagation regime.

The fracture surfaces of one 0º orientation, A-notch sub-orientation sample, sample 4522-3, are shown in Fig.6.35. It can be seen from Fig.6.35 (a) that the overall fracture surface of sample 4522-3 is very flat, as the cracks propagates by translamellar fracture throughout this area. Fig.6.35 (b) shows the details of the fracture surface at about 50μm from the notch, and only translamellar fracture is observed. This is analogous to that found with alloy 46Al8Nb at a similar orientation.

Fig.6.36 shows the fracture surfaces of sample 4522-12, which is at 0º orientation and A-B notch sub-orientation. As can be seen from Fig.6.36 (a), the cracks in front of the notch all grow by translamellar cracking. Again, the high magnification image in Fig.6.36 (b) shows the fracture surface of the area at about 50μm from the notch. The fracture surface is very smooth, and translamellar cracking is the exclusive fracture mode observed here. The lamellar colony in front of the notch of sample 4522-7 is at about 10º orientation and A-B notch sub-orientation. The fracture surface of the near notch area shown Fig.6.37 (a) is rather flat, and it is composed of entirely translamellar fracture. Fig.6.37 (b) shows a high magnification image of the smooth translamellar fracture surface, which is about 50μm from the notch.

Sample 4522-5 is the only sample with soft orientation among the 4522 samples, and it shows the lowest threshold value. Fig.6.38 (a) shows the fracture surface of the full notch area of sample 4522-5. A large semi-elliptical area almost covering the whole notch length is observed on the fracture surface with a depth up to 200μm. The cracks propagated at a lower stress intensity factor range than the threshold and stopped at the edge of this area, and they are regarded as early cracks. Some early cracks stopped at the top edge of this area and others continued. Fig.6.38 (b) and (c) shows the details of the early cracks, and it can be seen that the cracks in this site propagate by dominant translamellar cracking and minor interlamellar cracking.

In summary, with alloy Ti45Al2Mn2Nb, samples with hard orientation, near 0º orientation, shows higher fatigue crack propagation threshold than that with soft orientation, although only four samples could be selected for further analysis. The fracture surfaces of three hard oriented samples show entirely smooth translamellar fracture with no early cracks, while that

of the soft orientated sample is composed of both translamellar fracture and interlamellar fracture, thus presents a rougher morphology. These features are similar to those for alloy Ti46Al8Nb.

6.3 Discussion

6.3.1 Lamellar orientation effect on fatigue crack propagation threshold with alloy Ti46Al8Nb

As can be seen from Fig.6.17, the fatigue crack propagation threshold of alloy Ti46Al8Nb with lamellar microstructure is strongly dependent on its lamellar orientation as a saddle shape and also the fatigue crack growth rate is influenced by the lamellar orientation. This agrees with the early work by Bowen [82]. Inui studied the lamellar orientation effect on tensile/compression yield stress at room temperature with PST TiAl intermetallic, and a similar saddle-shaped relationship was found between the yield stress and lamellar orientation [109]. In consequence, similar features of deformation behaviour must exist between monotonic deformation and cyclic deformation in TiAl lamellar crystals. The deformation behaviour in PST TiAl alloys under monotonic loading has been completely investigated, and it was shown that the deformation is dictated by the critical resolved shear stress (CRSS) and the Schmid factor of the slip/twinning systems [109, 110]. In general, the applied stress level under monotonic loading is much higher than that under cyclic loading, normally 2-4 times higher than the latter. For the forged and as-cast alloys with fine lamellar microstructure studied in this thesis, the applied stress in tensile testing is about 3 times of that in fatigue crack propagation testing. However, the deficiency in the overall stress level under cyclic loading could be made up by the stress concentration in front of the crack tip.

Thus, the deformation behaviour of lamellar colonies could be the same during both monotonic and fatigue crack growth testing.

As can be seen from the fracture surfaces, the cracks propagate by translamellar fracture mode in most lamellar orientations, except for those close to 90º, which is a hard orientation with N-notch. For the N-notch orientation, the lamellae were detached by the forward crack tip. It was found that the cracks detached the lamellae on the cross-lamella {111} planes by twinning and banding of ordinary and superdislocation slip in an earlier post mortem TEM study [113]. Similar results were also obtained by the in-situ TEM examination of the tensile deformed PST TiAl crystals [114, 115]. For the lamellar colonies with 0º orientation, deformation can only take place on the cross-lamella {111} planes as the Schmid factor for the deformation on the interfacial (111) plane is zero. The highest fatigue crack propagation threshold and high tensile/compression yield stress is obtained at this orientation.

The short dislocation gliding distance at 0º hard orientation gives rise to a high tensile and compression yield stress. When the lamellar orientation diverges from 0º orientation, the deformation on the interfacial (111) plane can be activated, and the dislocation gliding distance increases. The increasing gliding distance of dislocations on the interfacial (111) plane leads to a decrease of the yield stress according to the Hall-Petch relationship. Therefore, lamellar orientation affects the yield stress through its influence on dislocation gliding distance. The dislocation gliding distance is also limited by the lamellae thickness. However, the influence of lamellar orientation on fatigue crack propagation threshold cannot be explained by this mechanism. This is because yielding is only a prerequisite for fatigue crack propagation, the formation and opening up of new micro cracks in front of the main crack is also crucial.

To form and open up the new micro cracks, slip/twinning on the interfacial (111) planes may need to be included. The Schmid factor calculation for slip/twinning on the cross-lamella {111} planes was made for lamellar orientation in a 120° sector of $[\bar{1}01]$-$[01\bar{1}]$-[111], covering lamellar orientation from 0-90° and a 120° rotation about interface normal. The results indicated that there was no significant effect of lamellar orientation on the Schmid factor. This is because no matter what the lamellar orientation is, at least one slip or twinning system on the cross-lamella {111} planes is found to have a very high Schmid factor. There are 6 γ variants and each variant has 3 cross-lamella {111} planes. On each plane there is one twinning system, one ordinary dislocation slip system and two superdislocation slip systems [101] and [011]. In consequence, there are at least 72 deformation systems for each orientation and it is very likely to find a high Schmid factor. Therefore, the cross-lamella deformation cannot fully explain the lamellar orientation effect on fatigue crack propagation threshold.

The twin boundaries and slip bands can be formed by cross-lamellar deformation, and they are potential paths for the propagation of the main crack. However, the main crack can advance only when it is opened up. Deformation on the interfacial (111) plane could help to open up the new cracks at the twin boundaries and slip bands on the cross-lamellar {111} planes by intersection with them. At the intersection out-of-plane dislocation debris can be left and cracks can be formed by the dislocation debris when they are sufficiently accumulated. Such an effect on opening up cracks on grain boundaries has been documented [130]. The intensity of deformation activity on the interfacial (111) planes should be related to the opening of new cracks. Furthermore, it is determined by the lamellar orientation.

Therefore, the effects of lamellar orientation on fatigue crack propagation threshold could be explained by this way. Further study is required.

Unlike the relationship between lamellar orientation and yield stress in PST TiAl alloys, the fatigue crack propagation threshold of samples with near 90º orientation only show an intermediate value. At this orientation, deformation should only exist on the cross-lamella {111} planes. Moreover, it could be the inter-reaction between deformation systems in the contiguous lamellae which help to open the new crack on the interfaces. Therefore, there should be difficulty in the deformation in both lamellae because of the limited gliding distance, and fast crack propagation can counteract this difficulty. Thus, an intermediate threshold value is obtained at this orientation.

6.3.2 Lamellar orientation effect on fatigue crack propagation threshold with alloy Ti4522

Although only 4 useful data were obtained with alloy Ti4522, the lamellar orientation effect on fatigue crack propagation threshold is still noticeable. The high threshold value was obtained with samples near 0º orientation, and lower threshold value was obtained with the sample with soft orientation.

For samples with near 0º hard orientation, the obtained fatigue crack propagation threshold values were within the range of 5.7 MPa√m – 7 MPa√m. At similar orientation, Ti46Al8Nb alloy shows a threshold range from 6.5 MPa√m to 7.3 MPa√m. There is only one Ti4522 sample with soft orientation about 50º, and the threshold value is 5.2 MPa√m. The threshold of Ti46Al8Nb samples at soft orientation, 30º-50º, is within a range of 4.3-5.4MPa√m.

Therefore, the fatigue crack propagation threshold of alloy Ti4522 is also affected by lamellar orientation and the possible mechanism has been discussed in the previous paragraph, and also, the threshold value seems not affected by the different alloy composition.

As can be seen from the fracture surfaces, translamellar cracking is the dominant fracture mode when the samples are near 0º hard orientation and soft orientation. Fairly smooth fracture surfaces were observed with hard orientation samples and rougher fracture surfaces were observed with the soft orientation sample, accompanied with early cracks. These features are in accordance with those found with Ti46Al8Nb alloy, indicating that the crack growth behaviour is also not influenced by the different alloy composition. However, further study is still needed.

6.4 Conclusion

Fatigue crack propagation threshold shows strong dependence on lamellar orientation, based on the work on coarse grained Ti46Al8Nb and Ti4522 alloy with lamellar microstructure. The relationship between fatigue crack propagation threshold and lamellar orientation is similar to that between yield stress and lamellar orientation. The highest threshold was obtained in the lamellar colonies with lamellar interface parallel to the loading axis while the low threshold was obtained in the colonies with an orientation in a range of 30º to 50º.

Within the investigated range, the refractory element, Nb, shows no improvement to the fatigue crack propagation threshold.

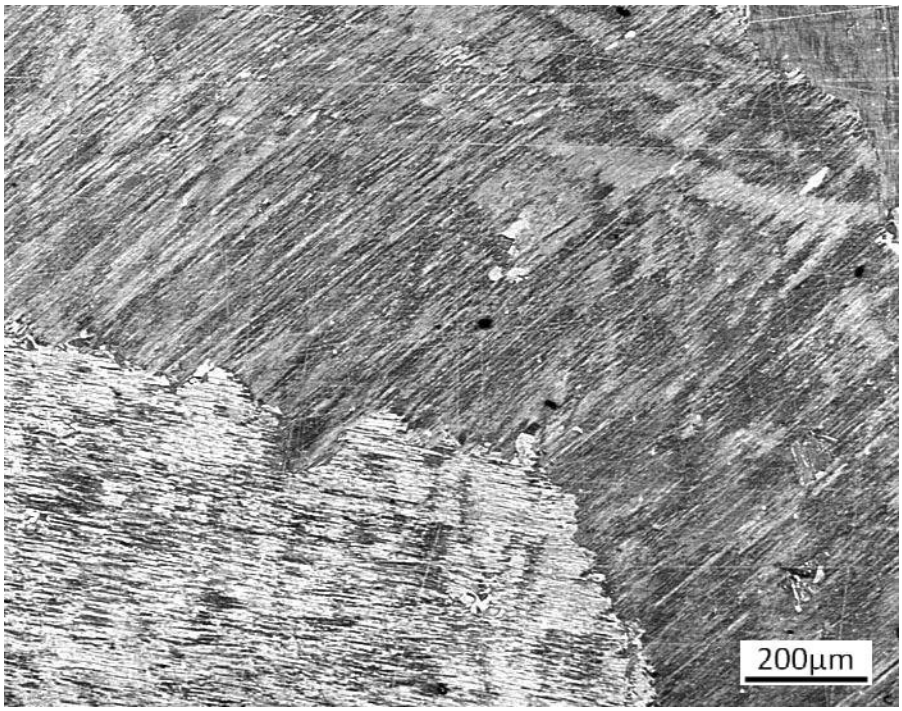

Fig.6.1 Optical micrograph image showing the coarse lamellar microstructure of the Ti46Al8Nb ingot.

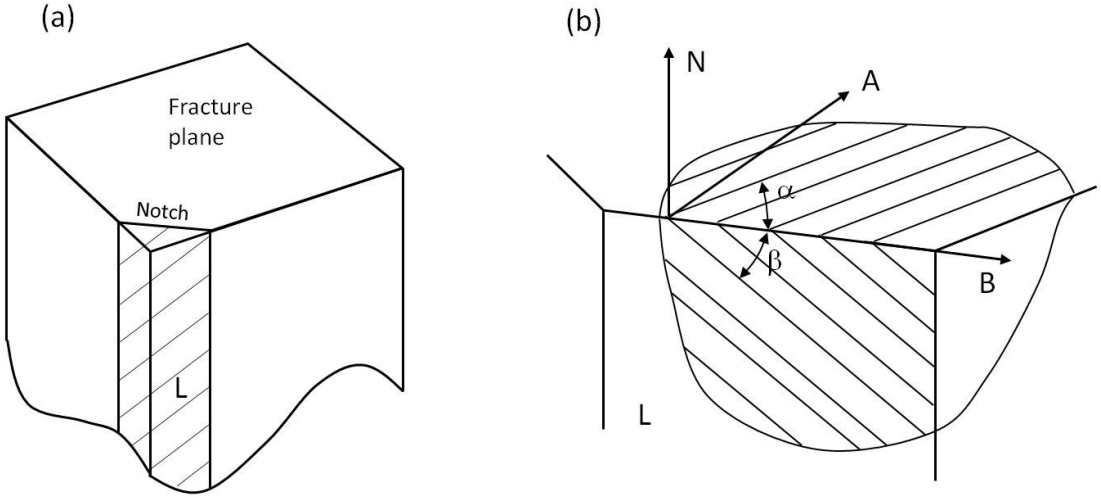

Fig.6.2 (a) Configuration of the surface planes in the testpieces for lamellar orientation determination and (b) intersection between lamellar interfaces and the surface planes.

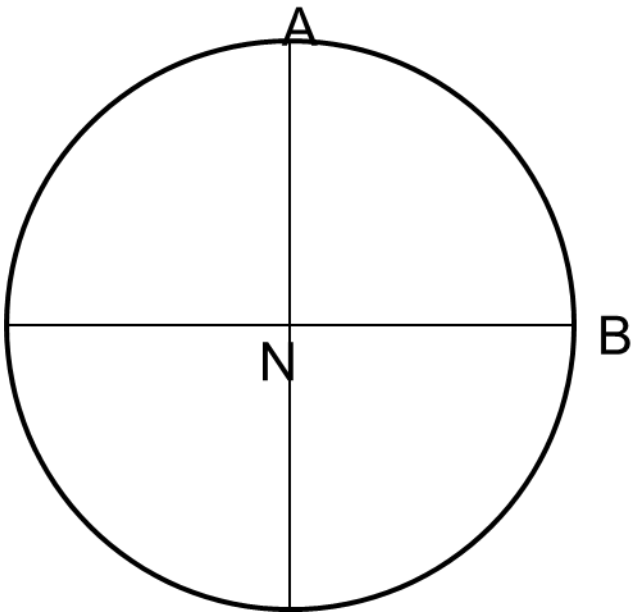

(a)

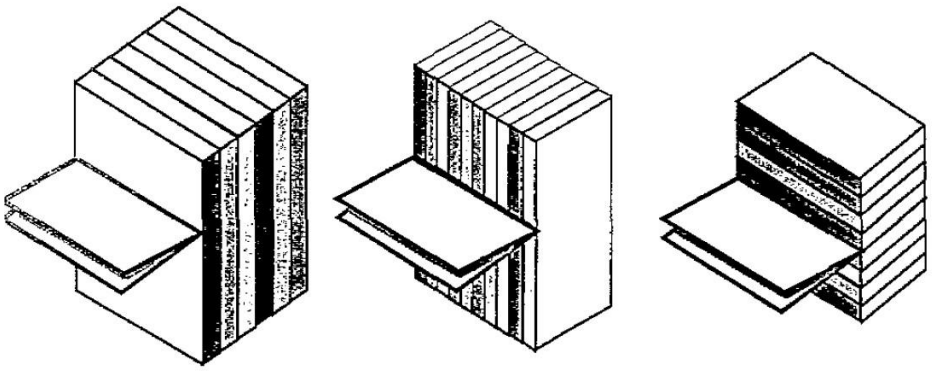

A notch B notch C notch (b)

Fig.6.3 Definition of lamellar orientation type with respect to pole figure directions.

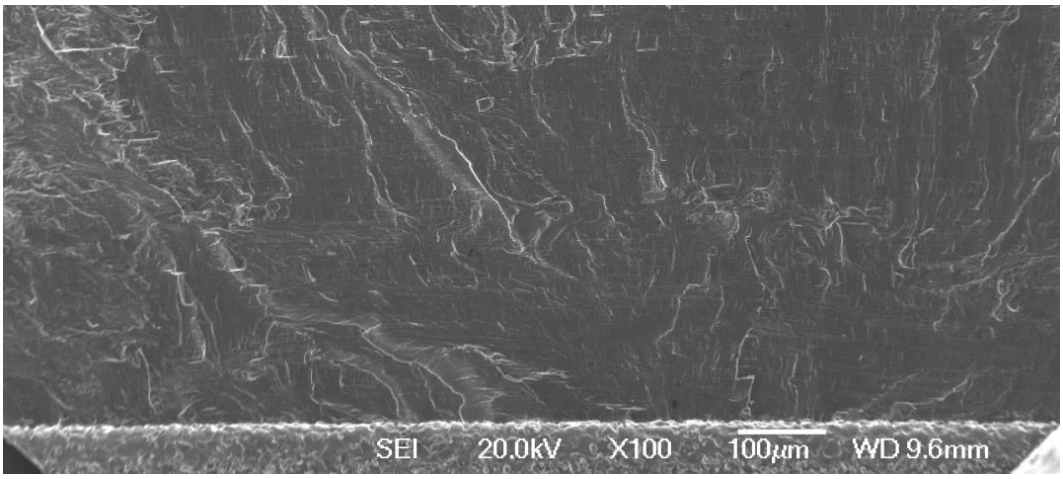

(a)

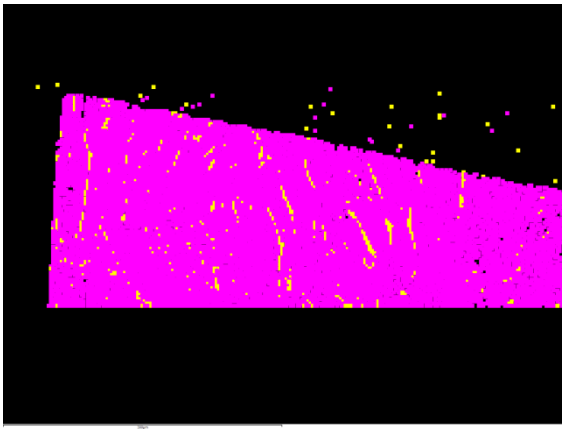
(b)

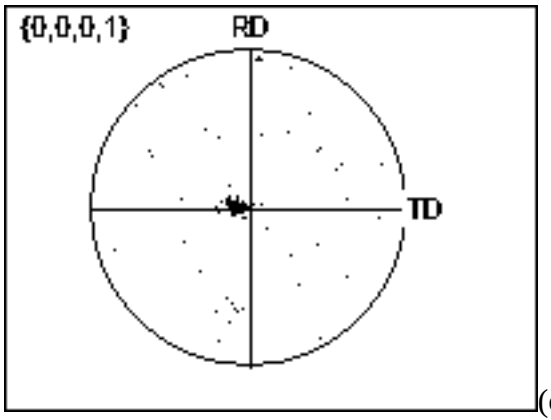

(c)

Fig.6.4 SEM SE image (a) showing the fracture surface of Specimen 468-1; EBSD mapping (b) on the plane L and pole figure (c) showing the orientation of the lamellar colony.

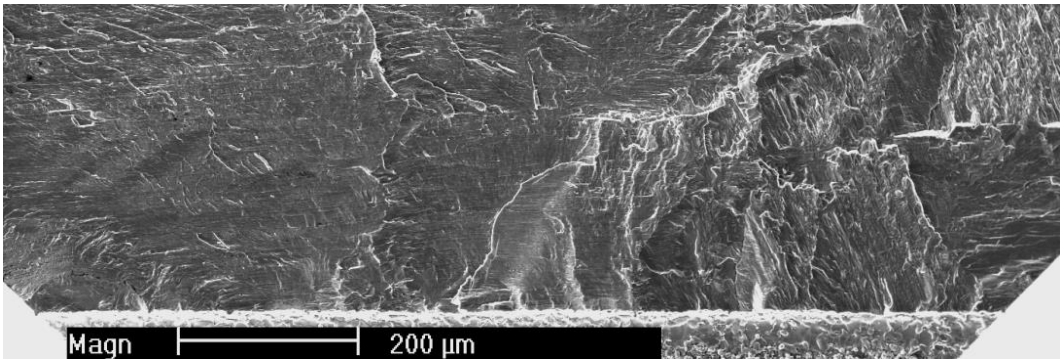

(a)

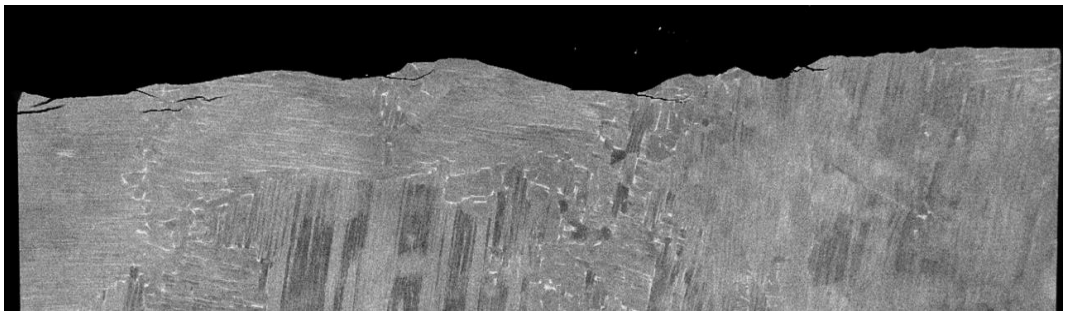
(b)

Fig.6.5 SEM SE image showing the lamellar interface trail on the fracture plane (a) and SEM BSE image showing the lamellar interface trail on the plane L (b) of Specimen 468-4.

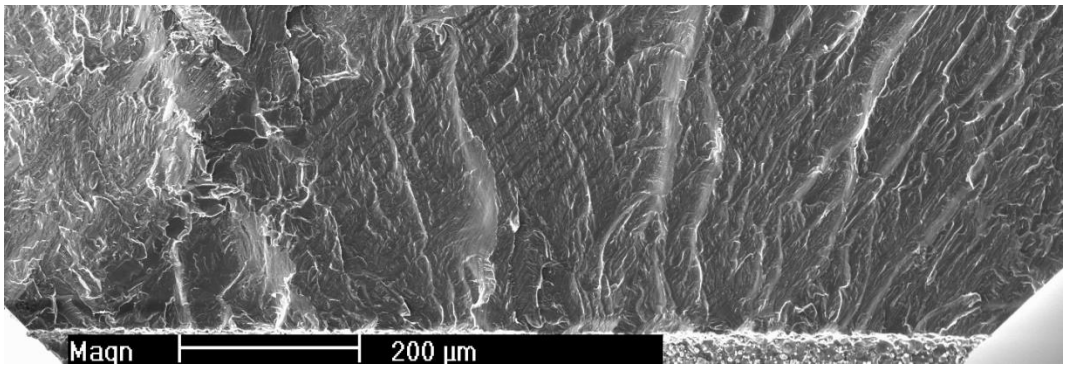

(a)

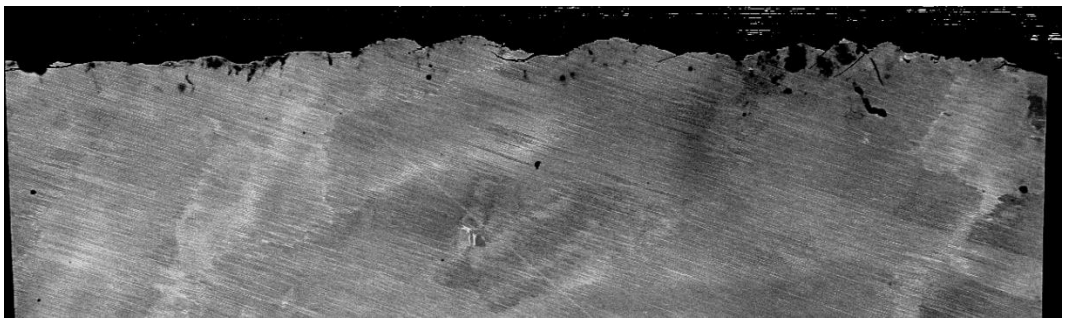
(b)

Fig.6.6 SEM SE image showing the lamellar interface trail on the fracture plane (a) and SEM BSE image showing the lamellar interface trail on the plane L (b) of Specimen 468-5.

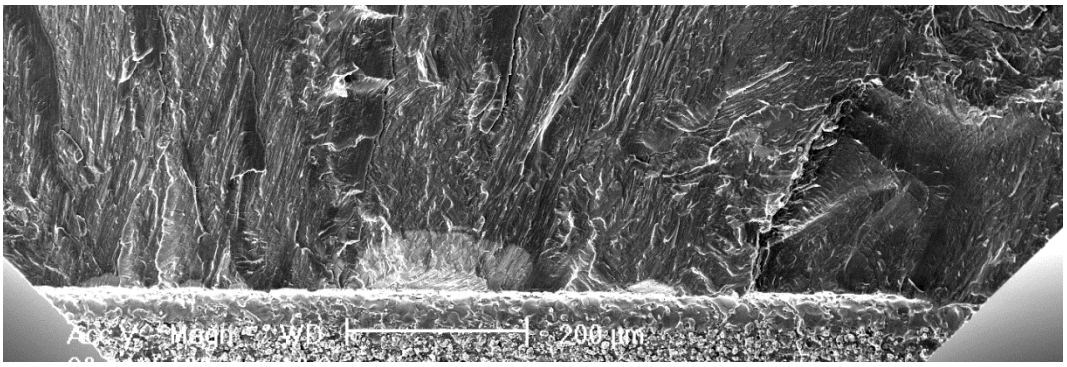

(a)

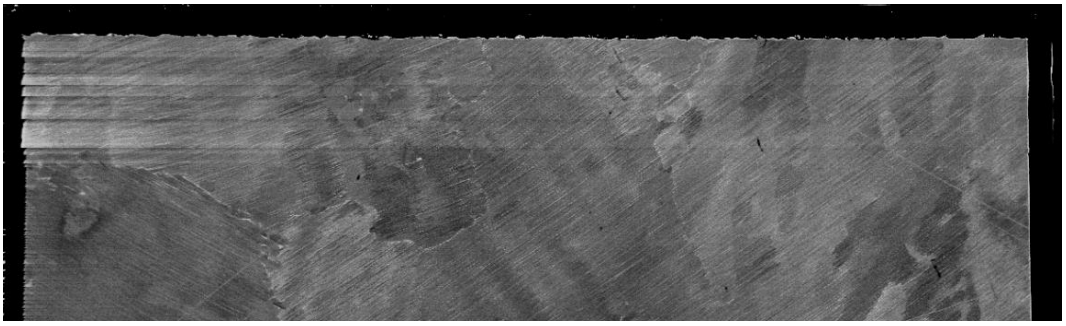

(b)

Fig.6.7 SEM SE image showing the lamellar interface trail on the fracture plane (a) and SEM BSE image showing the lamellar interface trail on the plane L (b) of Specimen 468-6.

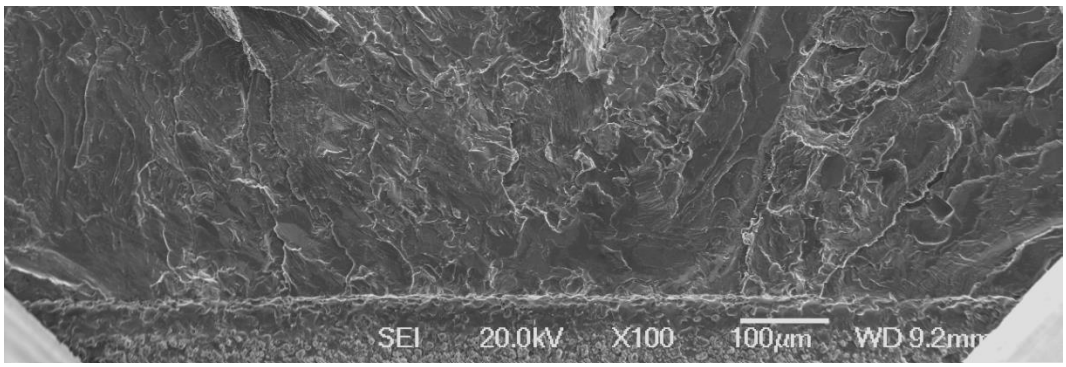

(a)

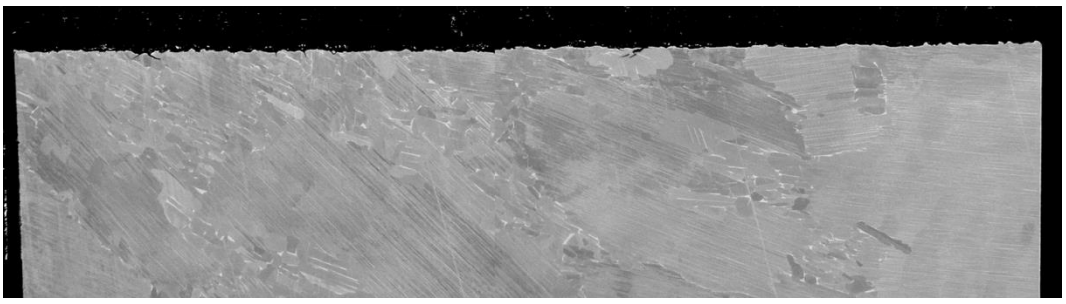

(b)

Fig.6.8 SEM SE image showing the lamellar interface trail on the fracture plane (a) and SEM BSE image showing the lamellar interface trail on the plane L (b) of Specimen 468-7.

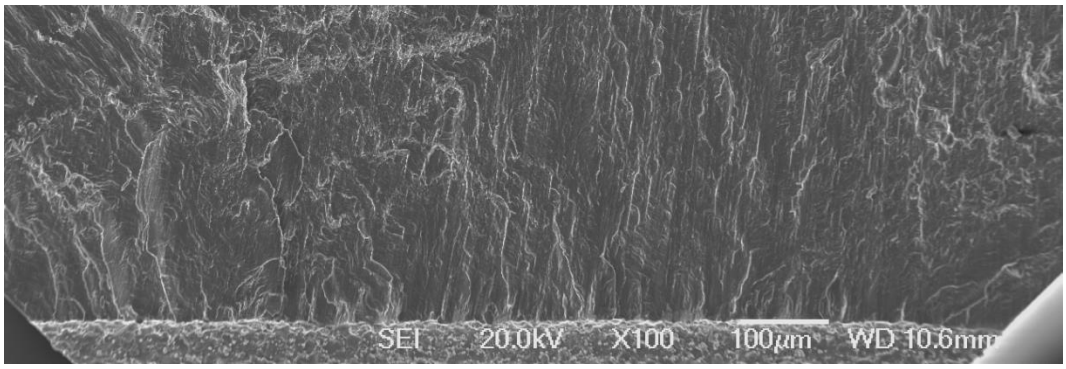

(a)

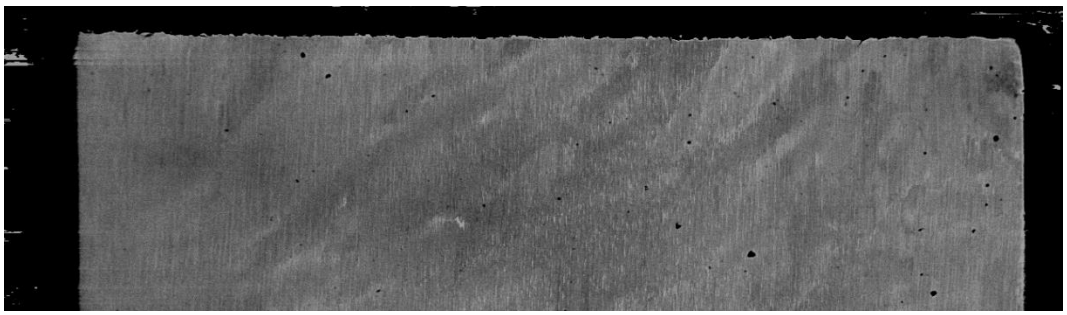
(b)

Fig.6.9 SEM SE image showing the lamellar interface trail on the fracture plane (a) and SEM BSE image showing the lamellar interface trail on the plane L (b) of Specimen 468-8.

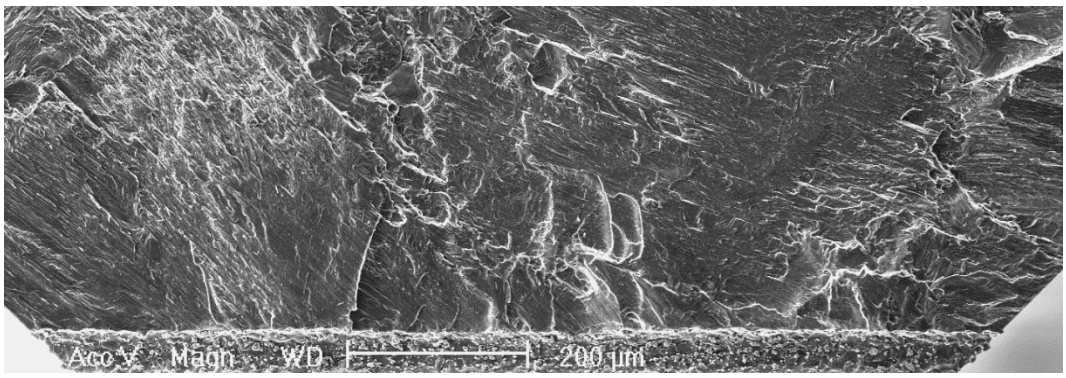

(a)

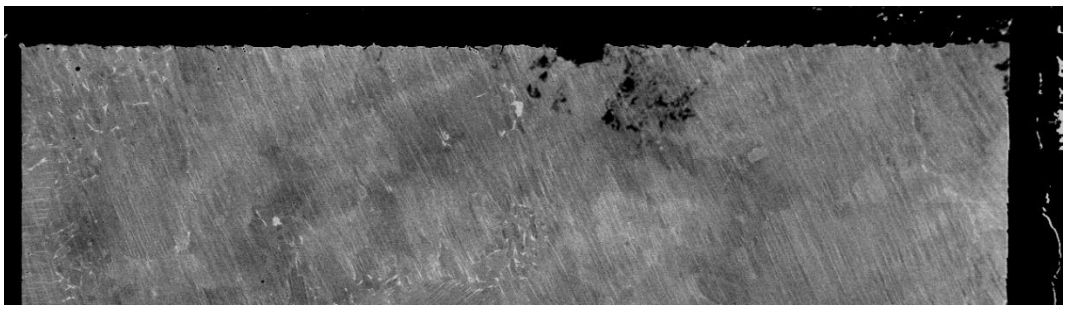
(b)

Fig.6.10 SEM SE image showing the lamellar interface trail on the fracture plane (a) and SEM BSE image showing the lamellar interface trail on the plane L (b) of Specimen 468-9.

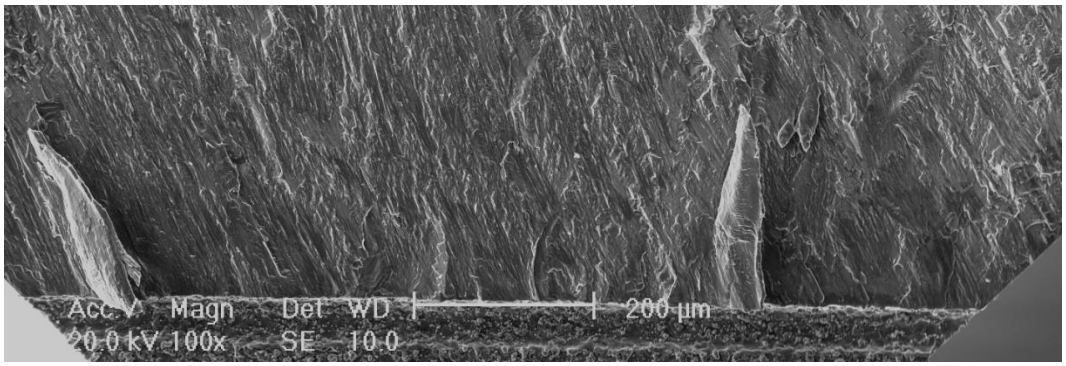

(a)

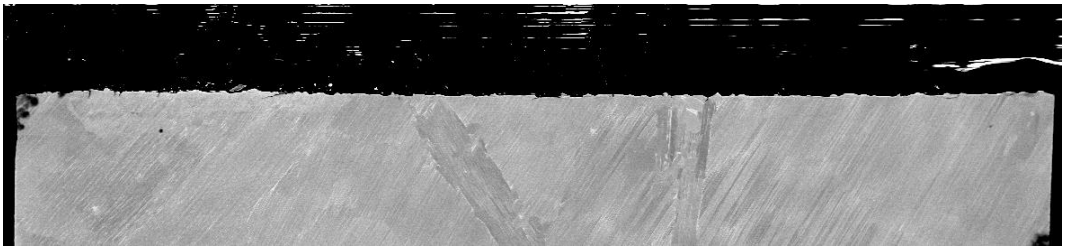

(b)

Fig.6.11 SEM SE image showing the lamellar interface trail on the fracture plane (a) and SEM BSE image showing the lamellar interface trail on the plane L (b) of Specimen 468-10.

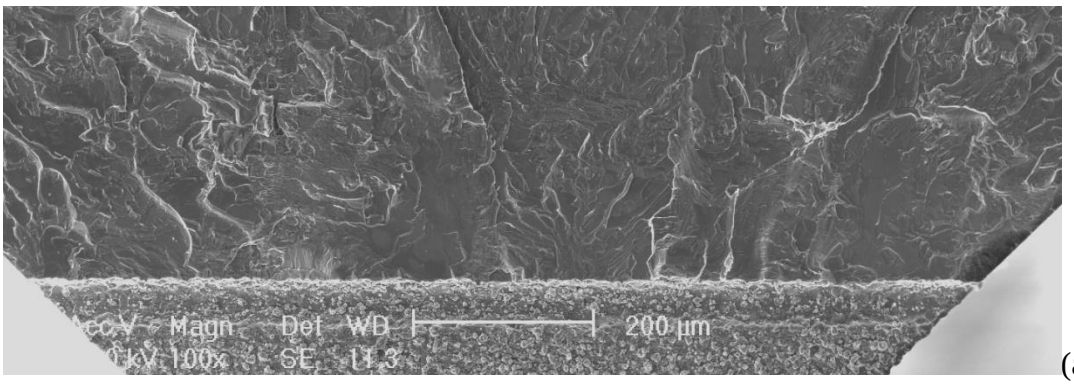

(a)

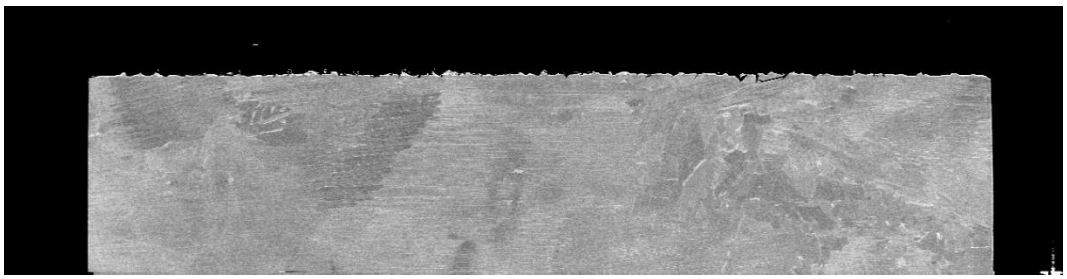

(b)

Fig.6.12 SEM SE image showing the lamellar interface trail on the fracture plane (a) and SEM BSE image showing the lamellar interface trail on the plane L (b) of Specimen 468-12.

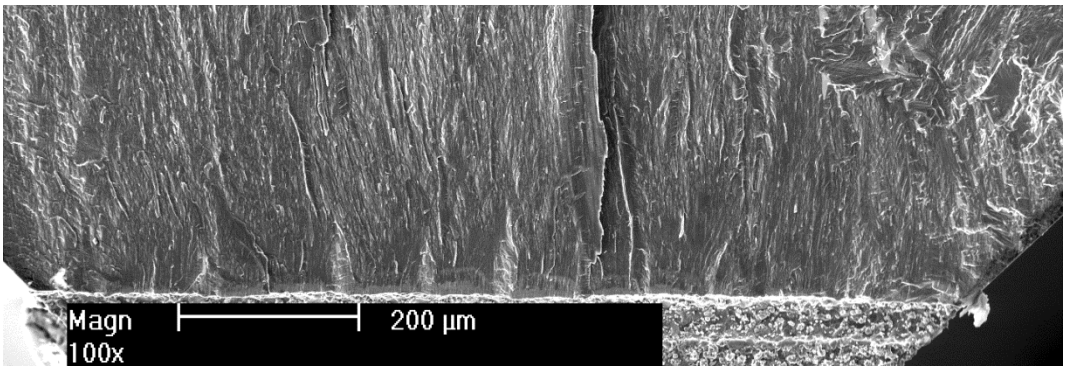

(a)

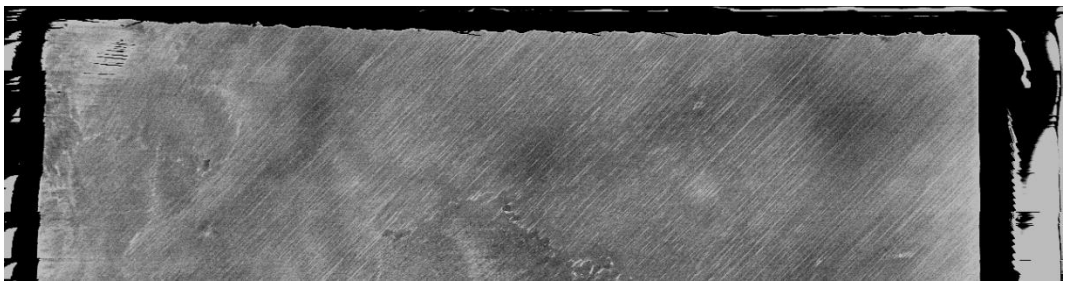
(b)

Fig.6.13 SEM SE image showing the lamellar interface trail on the fracture plane (a) and SEM BSE image showing the lamellar interface trail on the plane L (b) of Specimen 468-15.

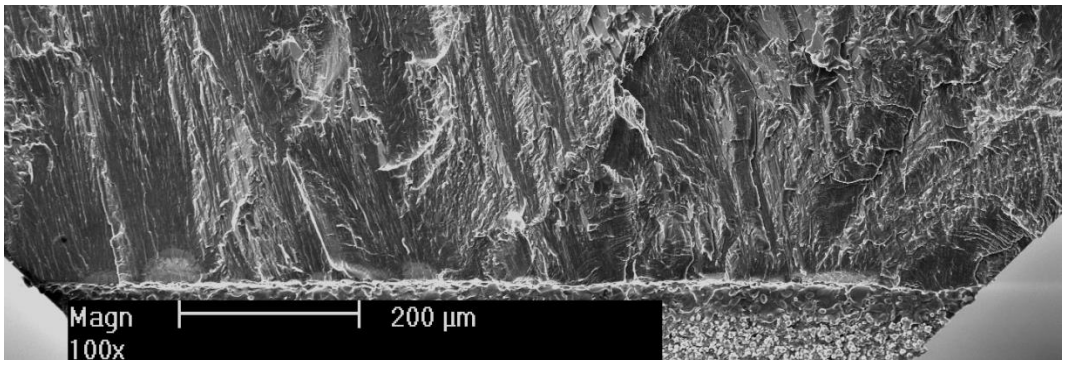

(a)

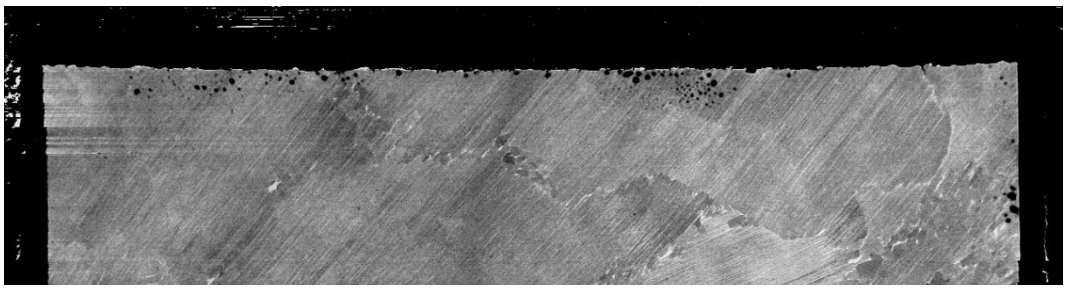
(b)

Fig.6.14 SEM SE image showing the lamellar interface trail on the fracture plane (a) and SEM BSE image showing the lamellar interface trail on the plane L (b) of Specimen 468-16.

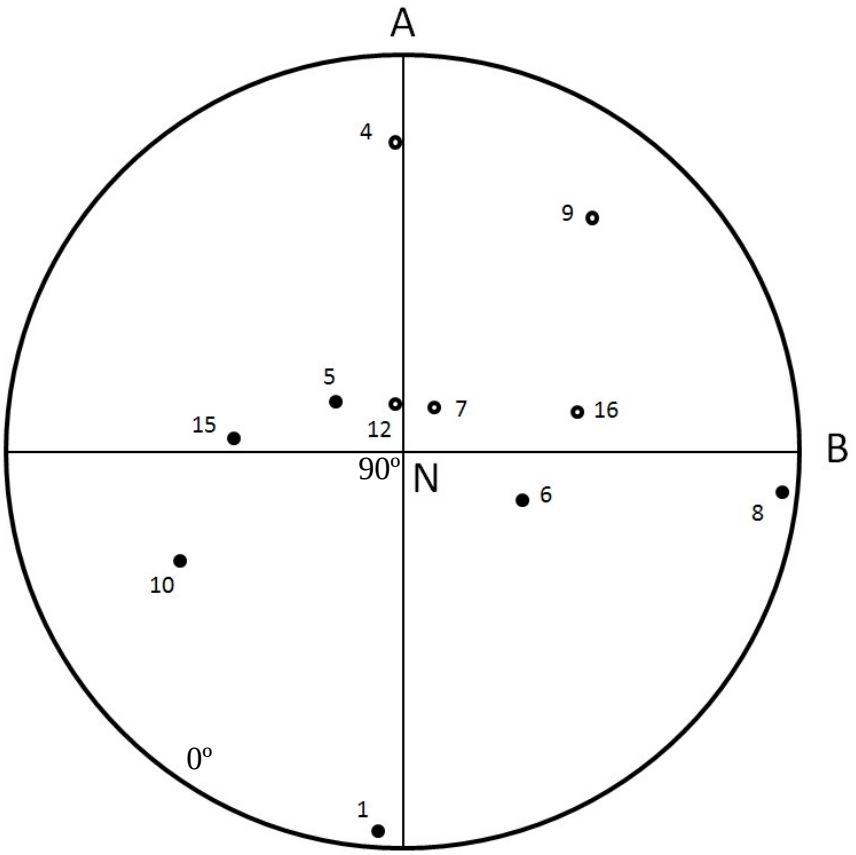

Fig.6.15 Pole figure showing the orientation of the lamellar colony at the notch. The open dots denote that more than one lamellar colony is at the notch and the close dots denote a single lamellar colony at the notch.

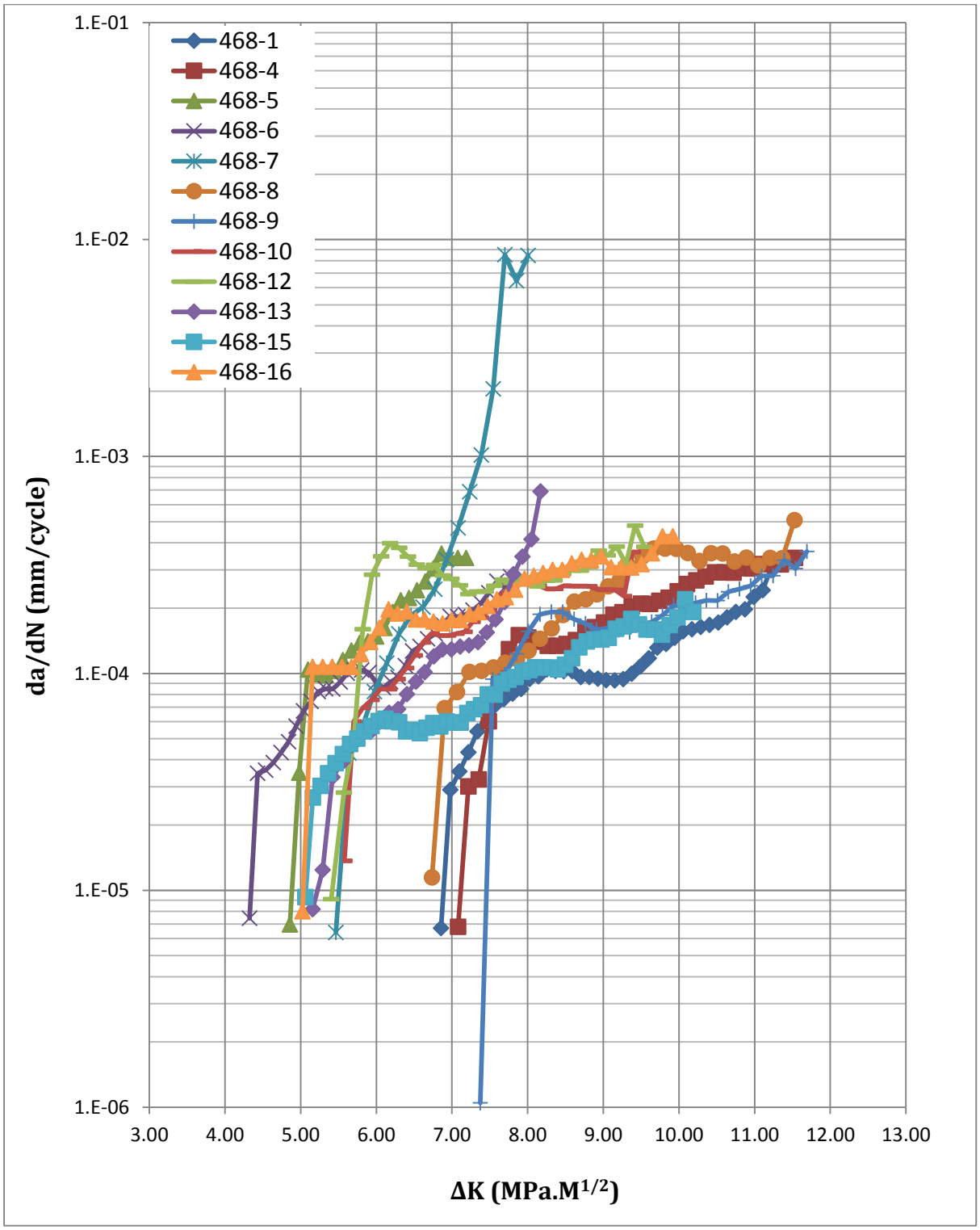

Fig.6.16 Typical fatigue crack propagation curves of Ti46Al8Nb at 650°C with R=0.1.

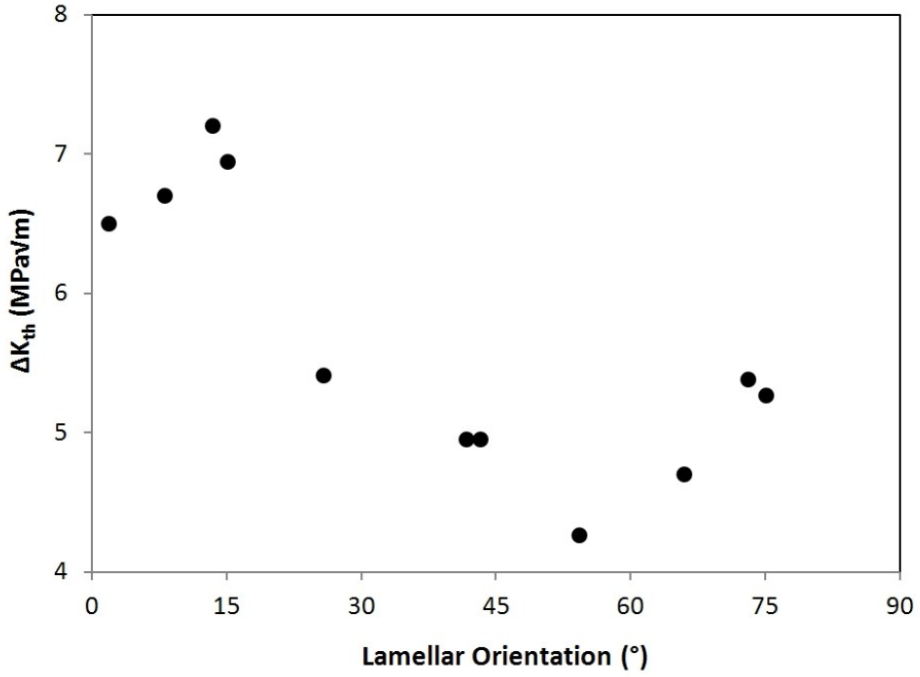

Fig.6.17 Variation of fatigue crack propagation threshold with lamellar orientation (defined as the angle between N and the pole).

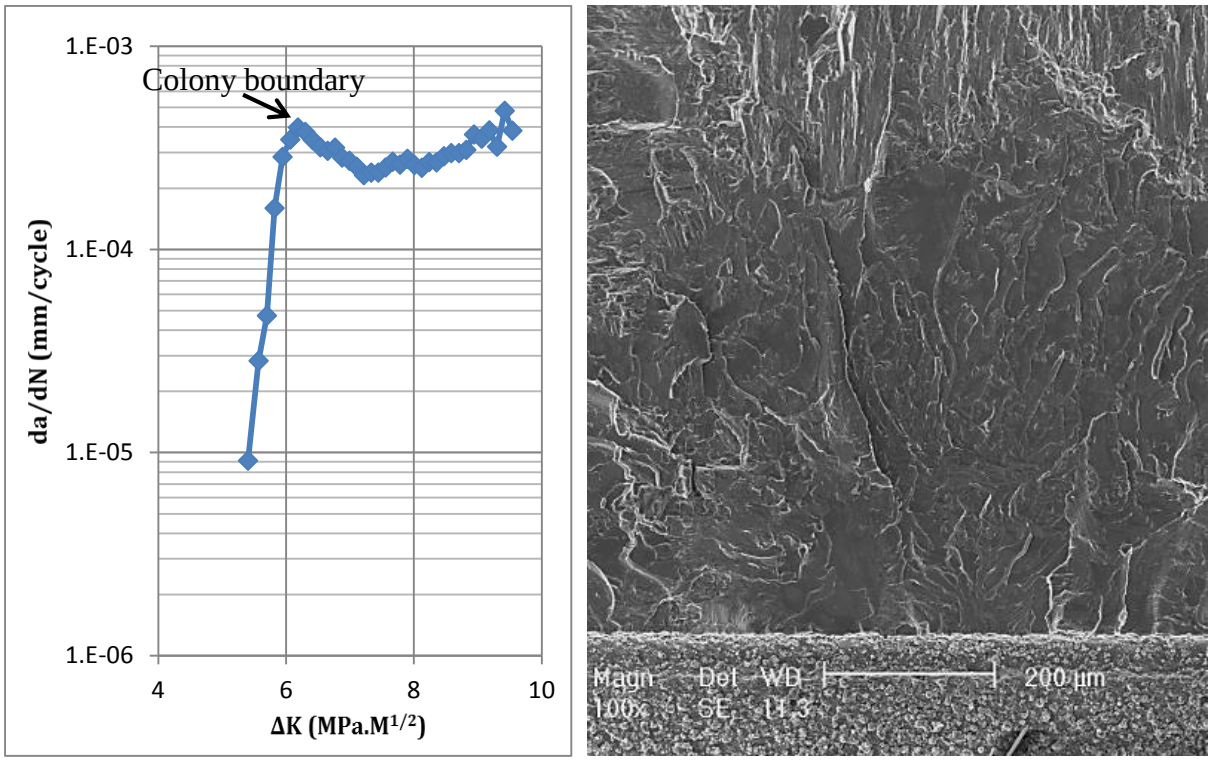

(a) (b)

Fig.6.18 (a) fatigue crack growth curve of sample 468-12; (b) SEM SE image shows the fracture surface of sample 468-12.

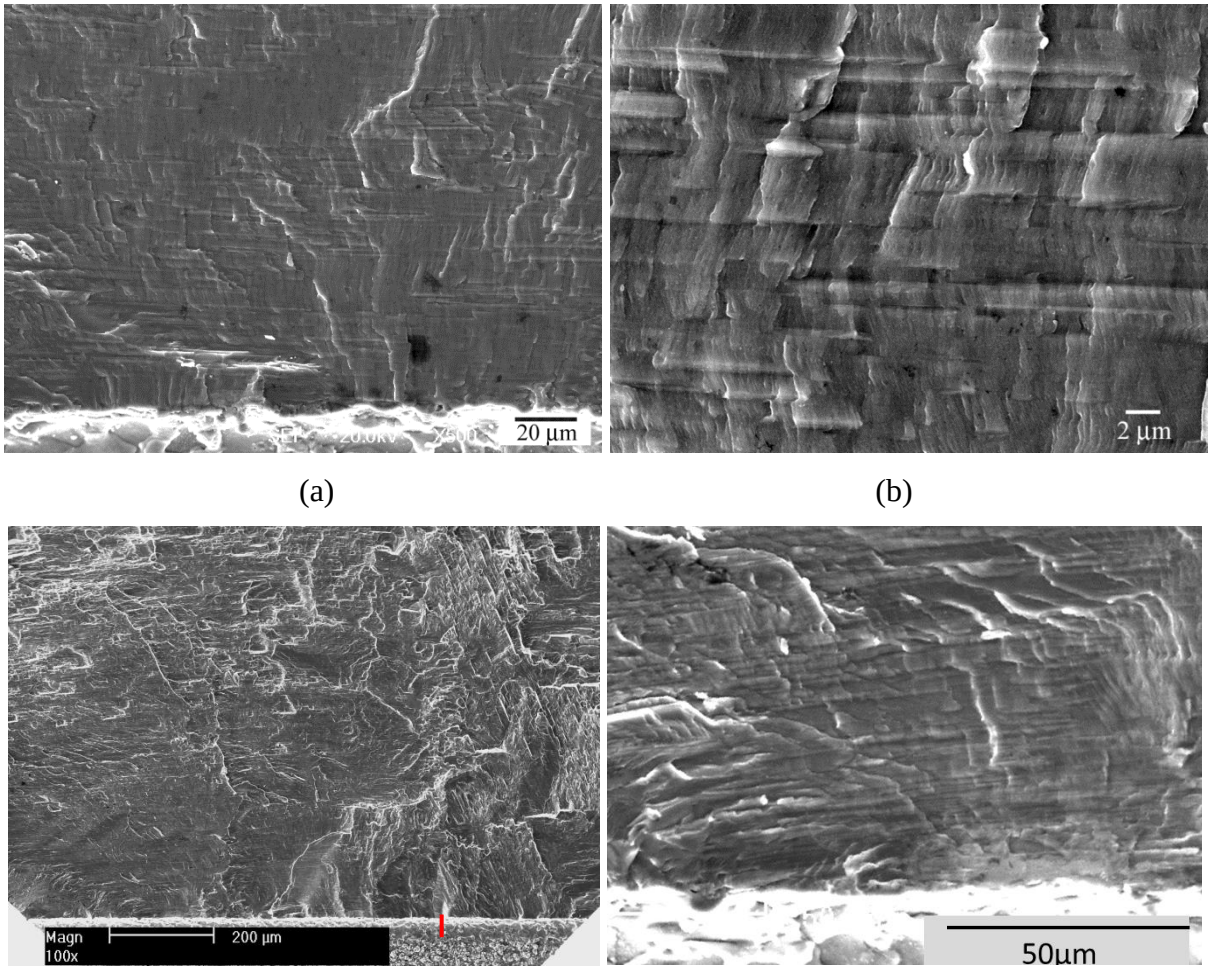

Fig.6.19 SEM SE images showing the facture surfaces of samples with near 0º orientation and near A-notch sub-orientation: (a) the near threshold area of sample 468-1; (b) the high magnification image of translamellar cracking in sample 468-1 about 80µm from the notch; (c) the full notch area of sample 468-4; (d) the high magnification image of translamellar cracking of sample 468-4.

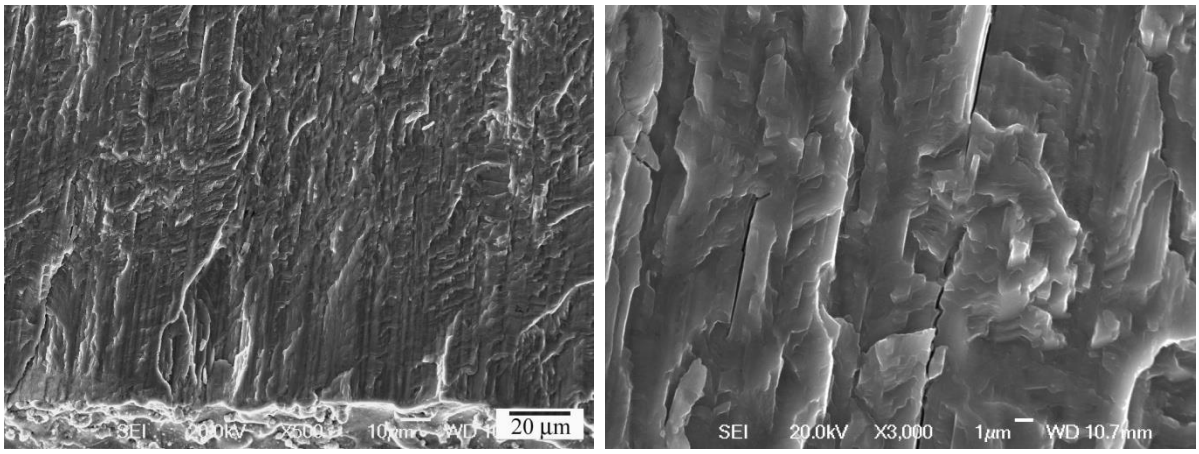

(a) (b)

Fig.6.20 SEM SEM images showing (a) the fracture surface of sample 468-8, and (b) the details.

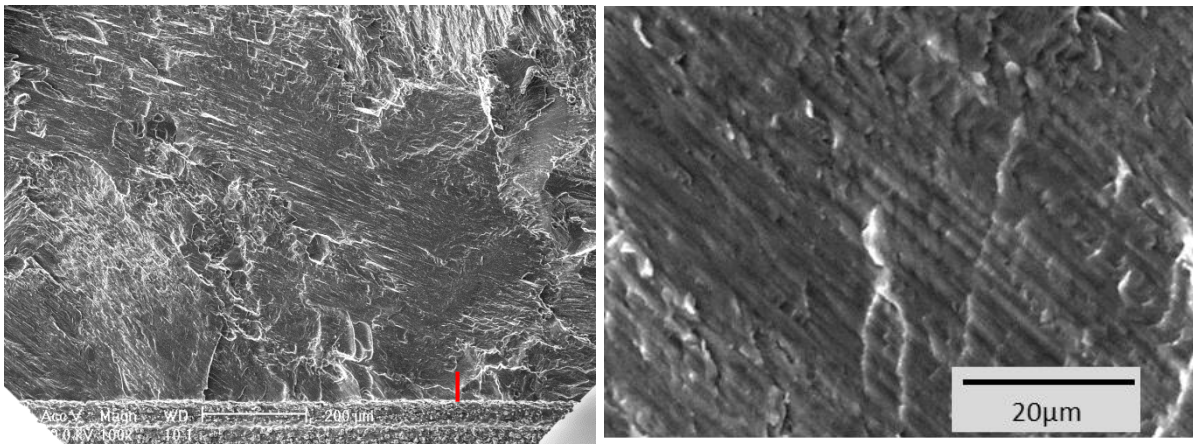

(a) (b)

Fig.6.21 SEM SE images showing (a) the fracture surface of sample 468-9, and (b) the details of the dominant lamellar colony on the left.

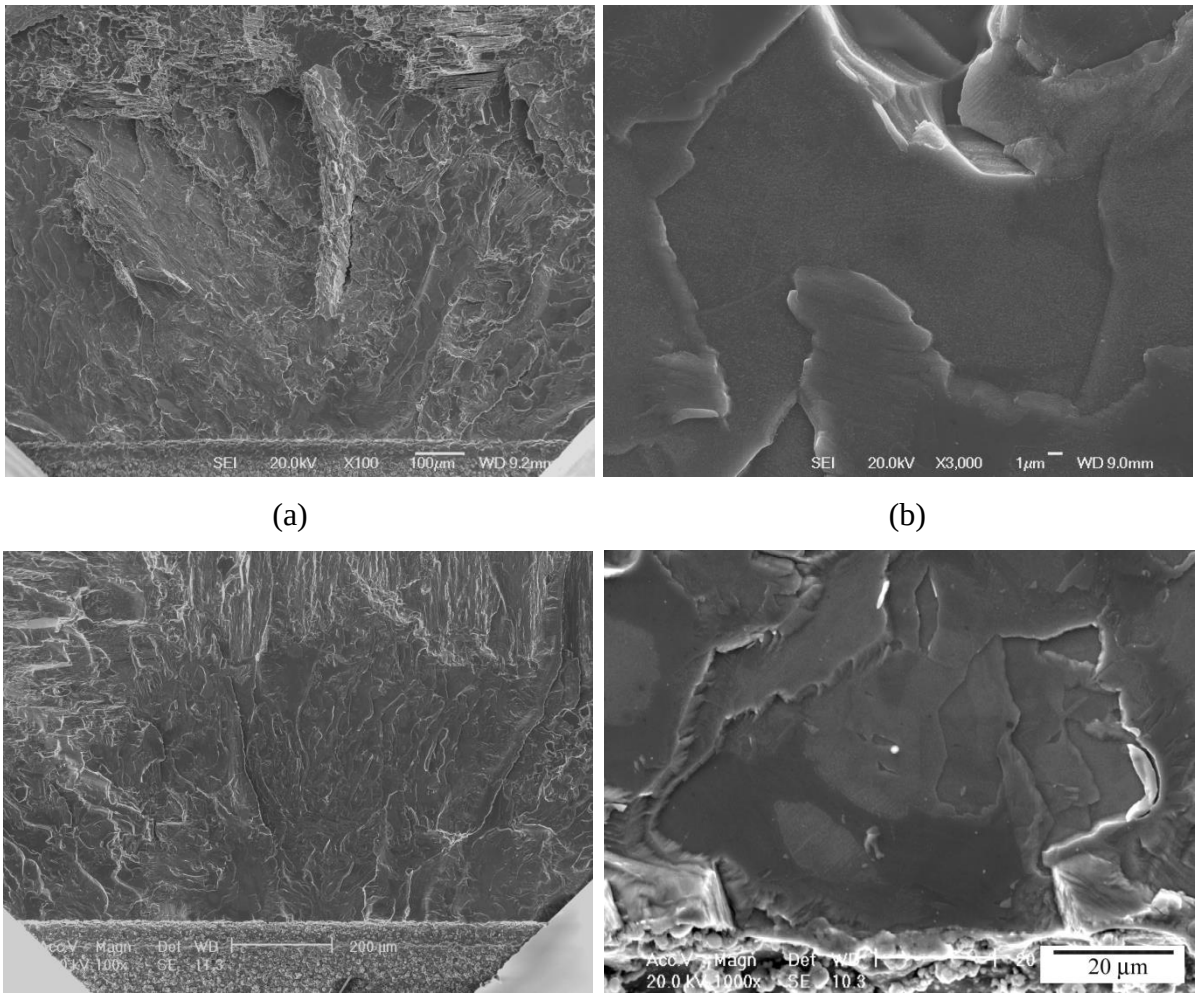

(a) (b)

(c) (d)

Fig.6.22 SEM SE images showing the fracture surfaces of samples with near 90º orientation: (a) the full notch area of sample 468-7; (b) the interlamellar cracking facet of sample 468-7: (c) the full notch area of sample 468-12: (d) the interlamellar cracking facet of sample 468-12.

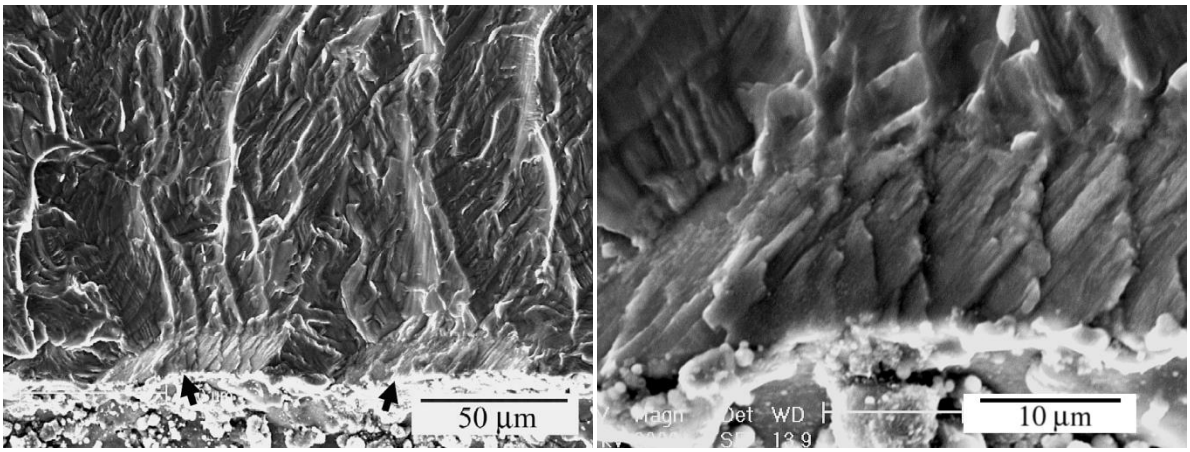

(a) (b)

Fig.6.23 SEM SE images showing the fracture surface of sample 468-5: (a) the near notch site; (b) the early cracks.

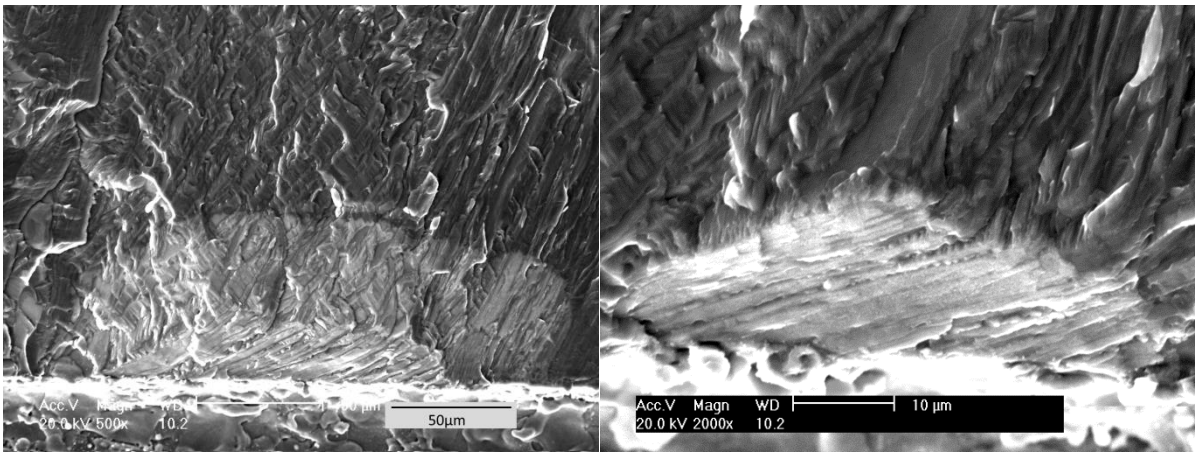

(a) (b)

Fig.6.24 SEM SE images showing (a) and (b) the early cracks observed on the fracture surface of sample 468-6.

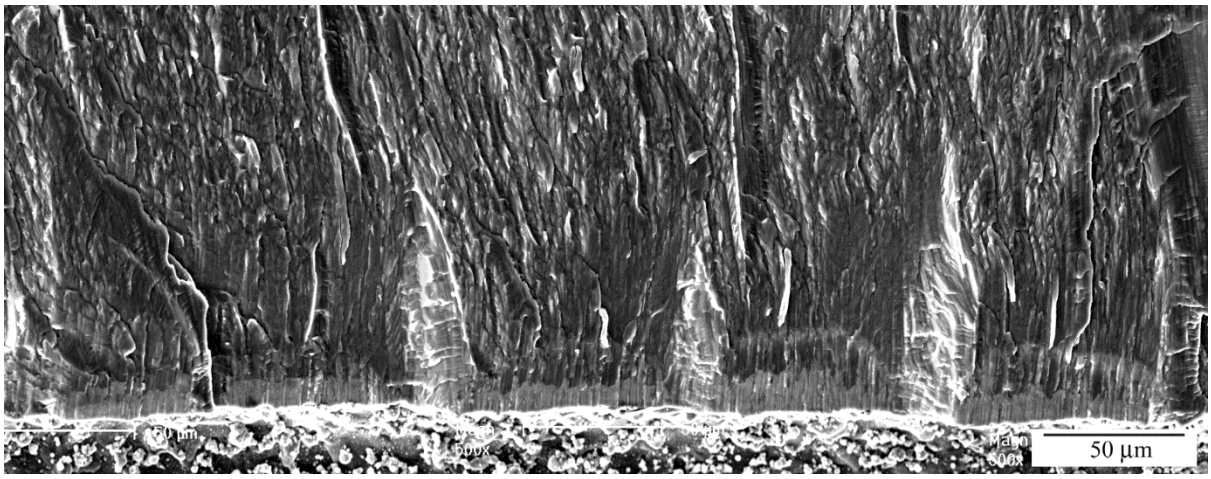

Fig.6.25 SEM SE image showing the fracture surface of sample 468-15 with a soft orientation. Regularly spaced early cracks are shown at the notch.

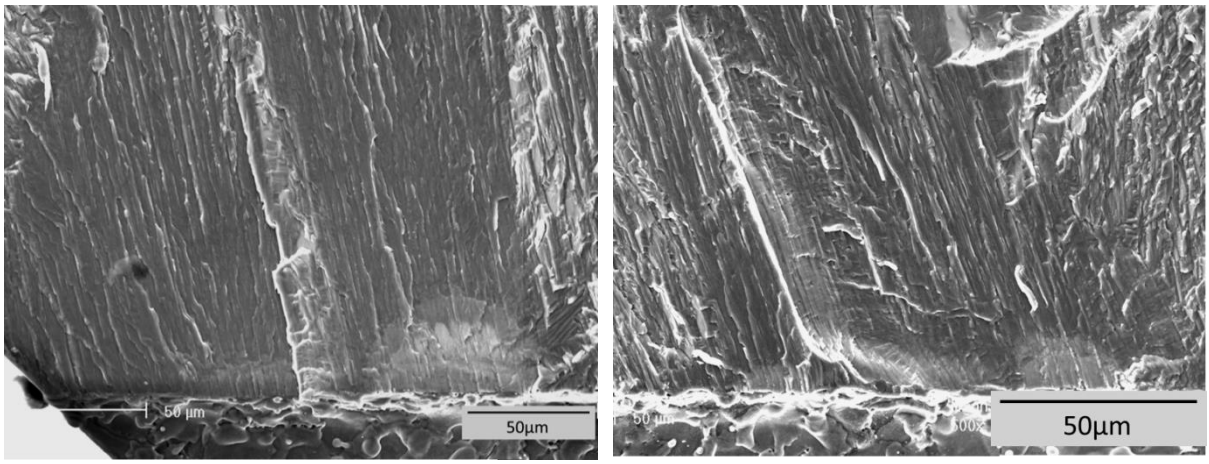

(a) (b)

Fig.6.26 468-16 SEM SE images showing (a) and (b) the early cracks observed on the fracture surface of sample 468-16.

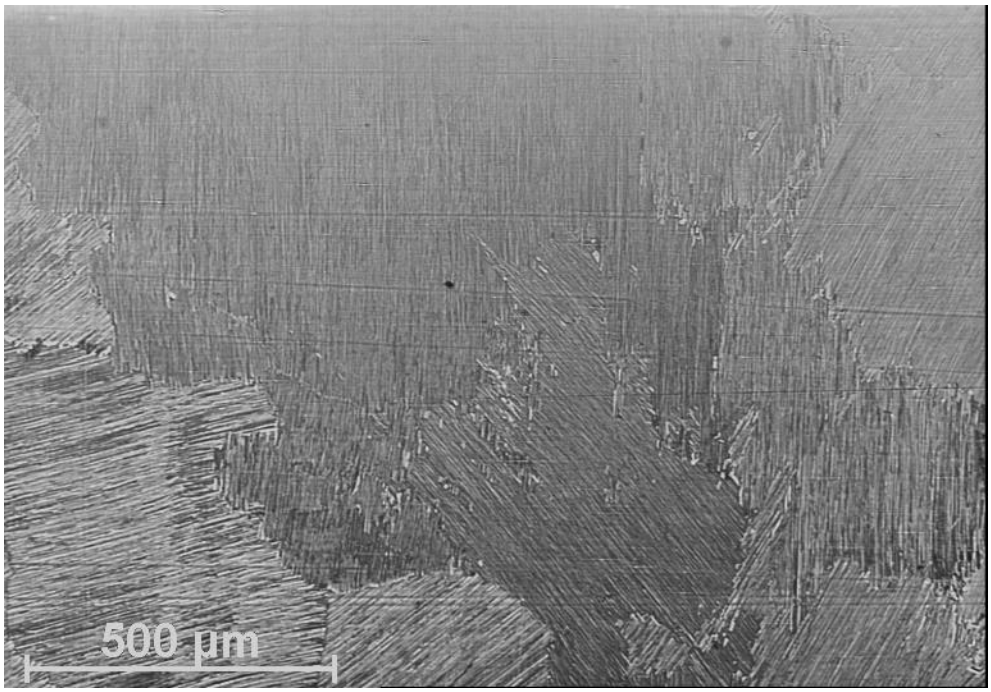

Fig.6.27 Optical micrograph image showing the coarse lamellar microstructure of the Ti4522Al ingot.

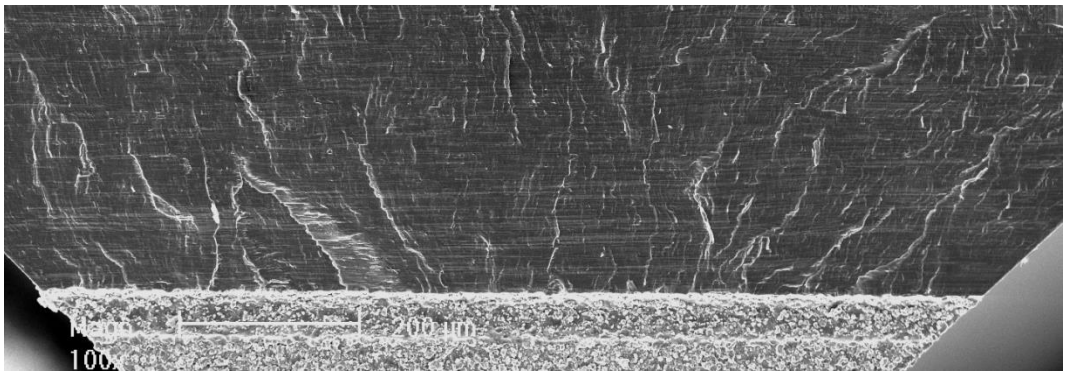

(a)

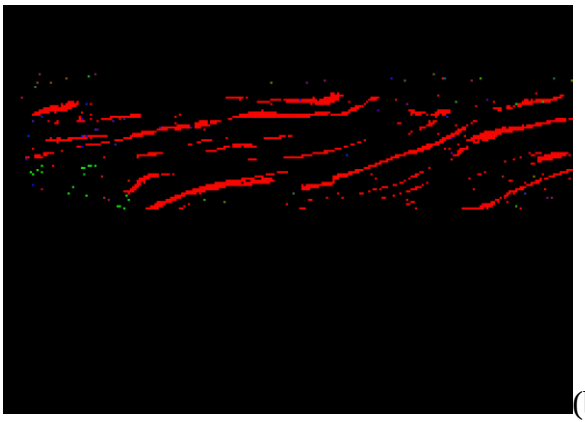
(b)

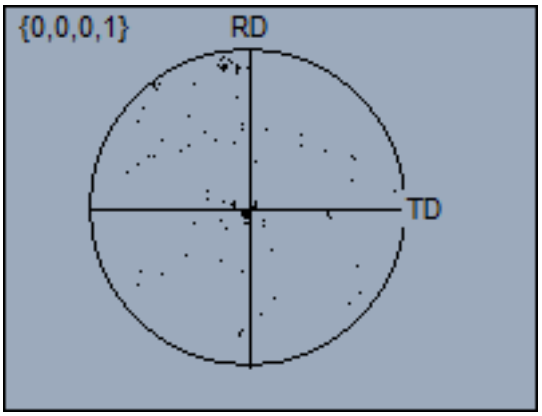

(c)

Fig.6.28 SEM SE image showing (a) the lamellar interface trail on the fracture plane, SEM BSE image showing (b) the lamellar interface trail on the plane L and (c) pole figure of Specimen 4522-3.

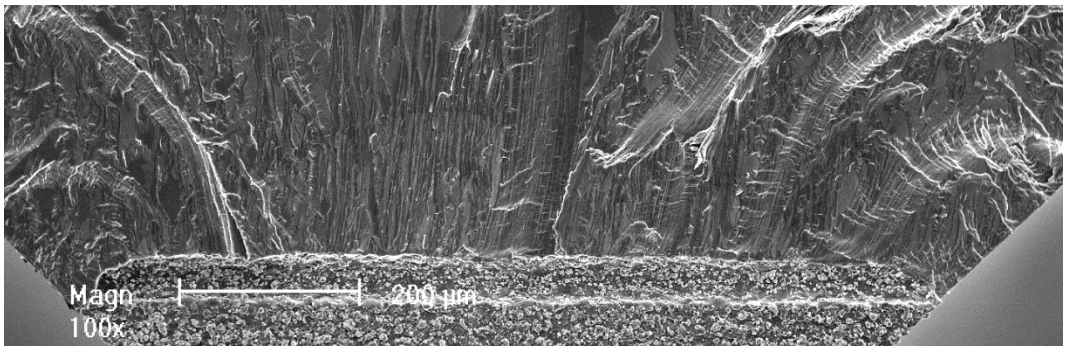

(a)

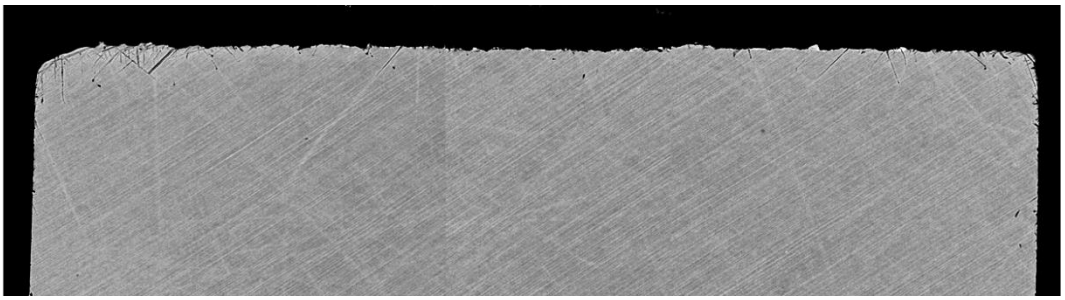
(b)

Fig.6.29 SEM SE image showing the lamellar interface trail on the fracture plane (a) and SEM BSE image showing the lamellar interface trail on the plane L (b) of Specimen 4522-5.

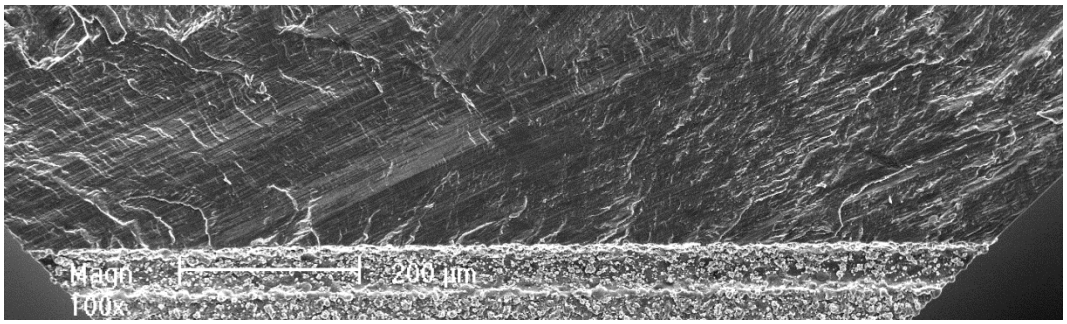

(a)

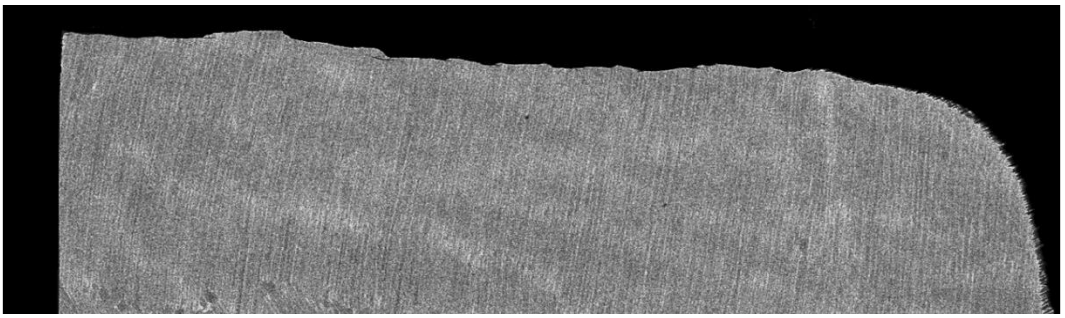
(b)

Fig.6.30 SEM SE image showing the lamellar interface trail on the fracture plane (a) and SEM BSE image showing the lamellar interface trail on the plane L (b) of Specimen 4522-7.

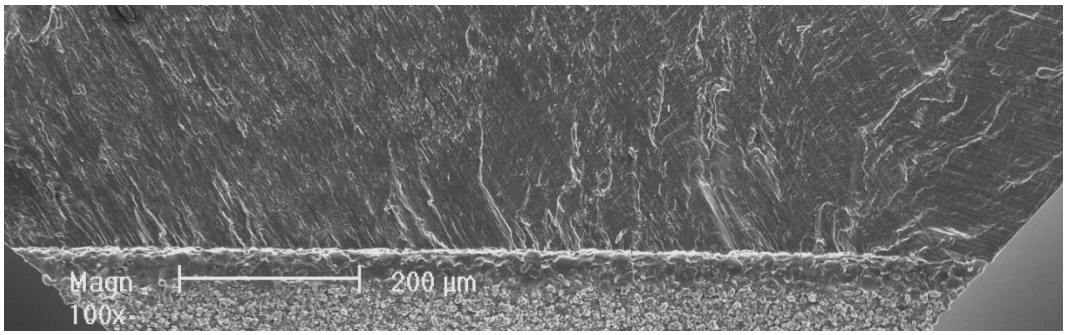

(a)

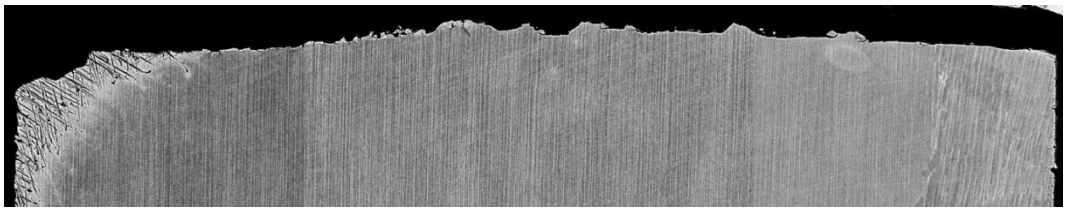
(b)

Fig.6.31 SEM SE image showing the lamellar interface trail on the fracture plane (a) and SEM BSE image showing the lamellar interface trail on the plane L (b) of Specimen 4522-12.

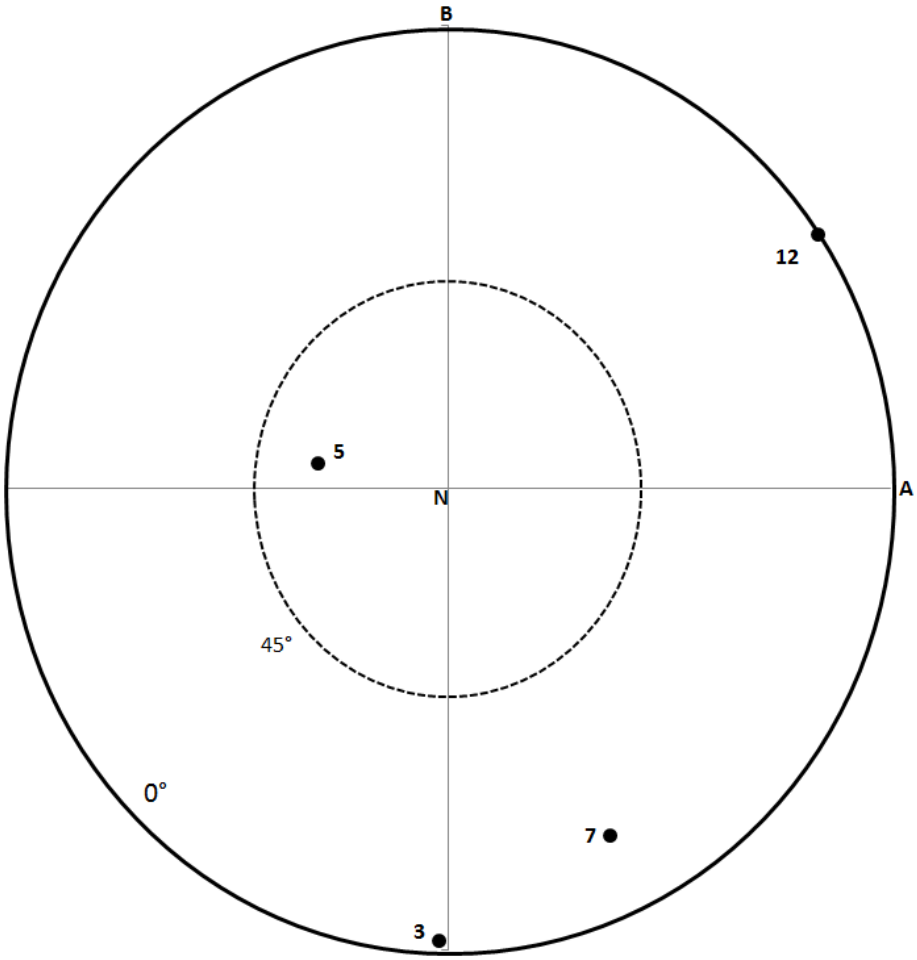

Fig.6.32 Pole figure showing the orientation of the lamellar colony at the notch. The open dots denote that more than one lamellar colony is at the notch and the close dots denote a single lamellar colony at the notch.

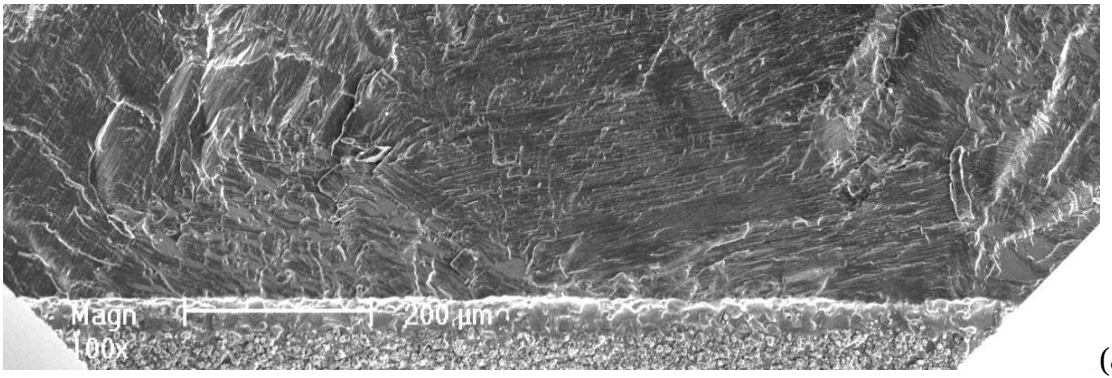

(a)

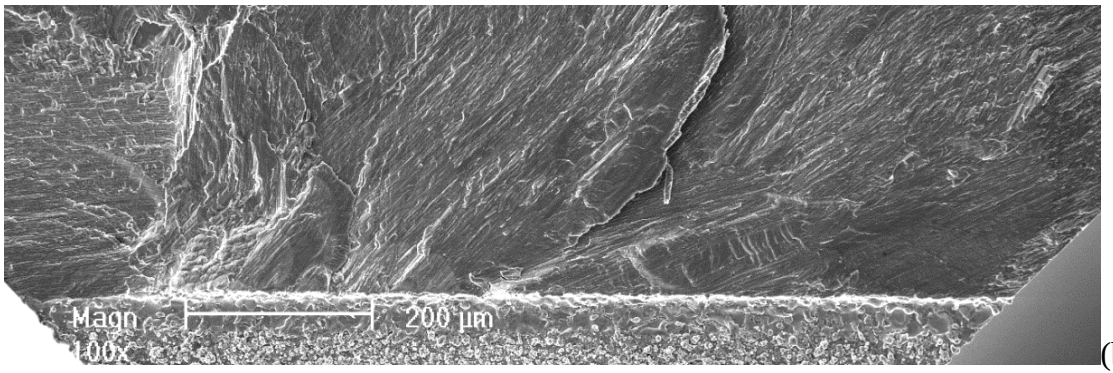

(b)

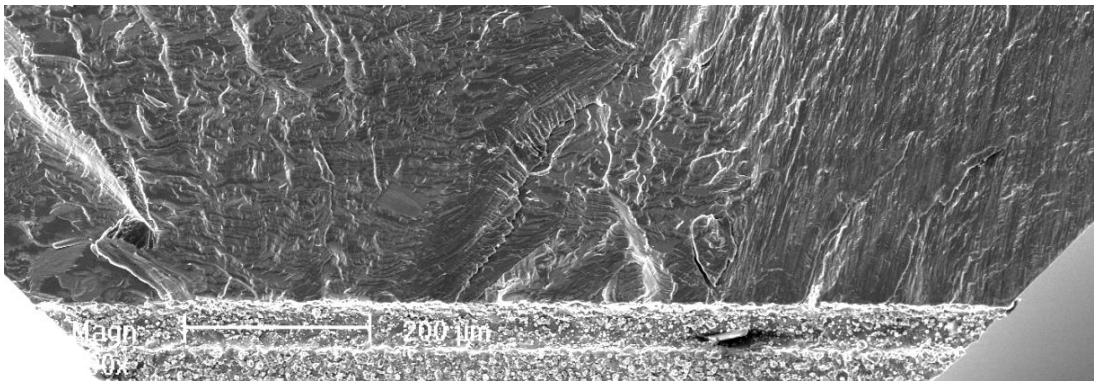

(c)

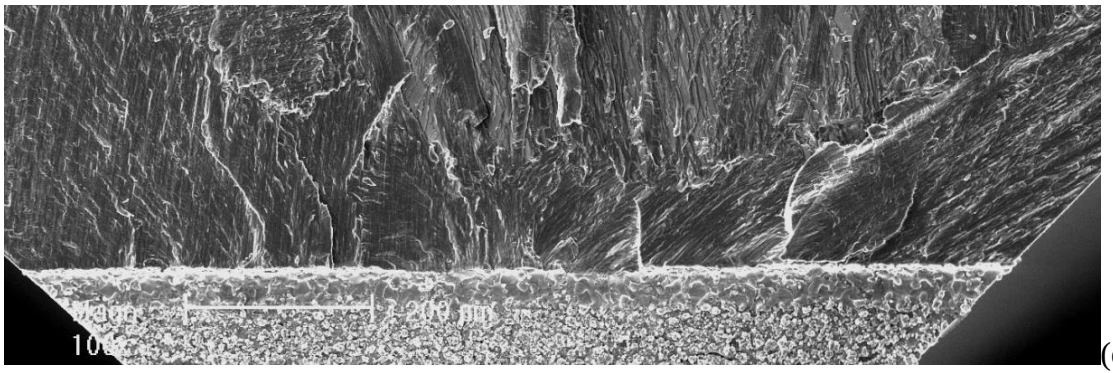

(d)

Fig.6.33 SEM SE image showing the fracture surface at the notch of (a) sample 4522-8, (b) 4522-13, (c) 4522-14 and (d) 4522-15.

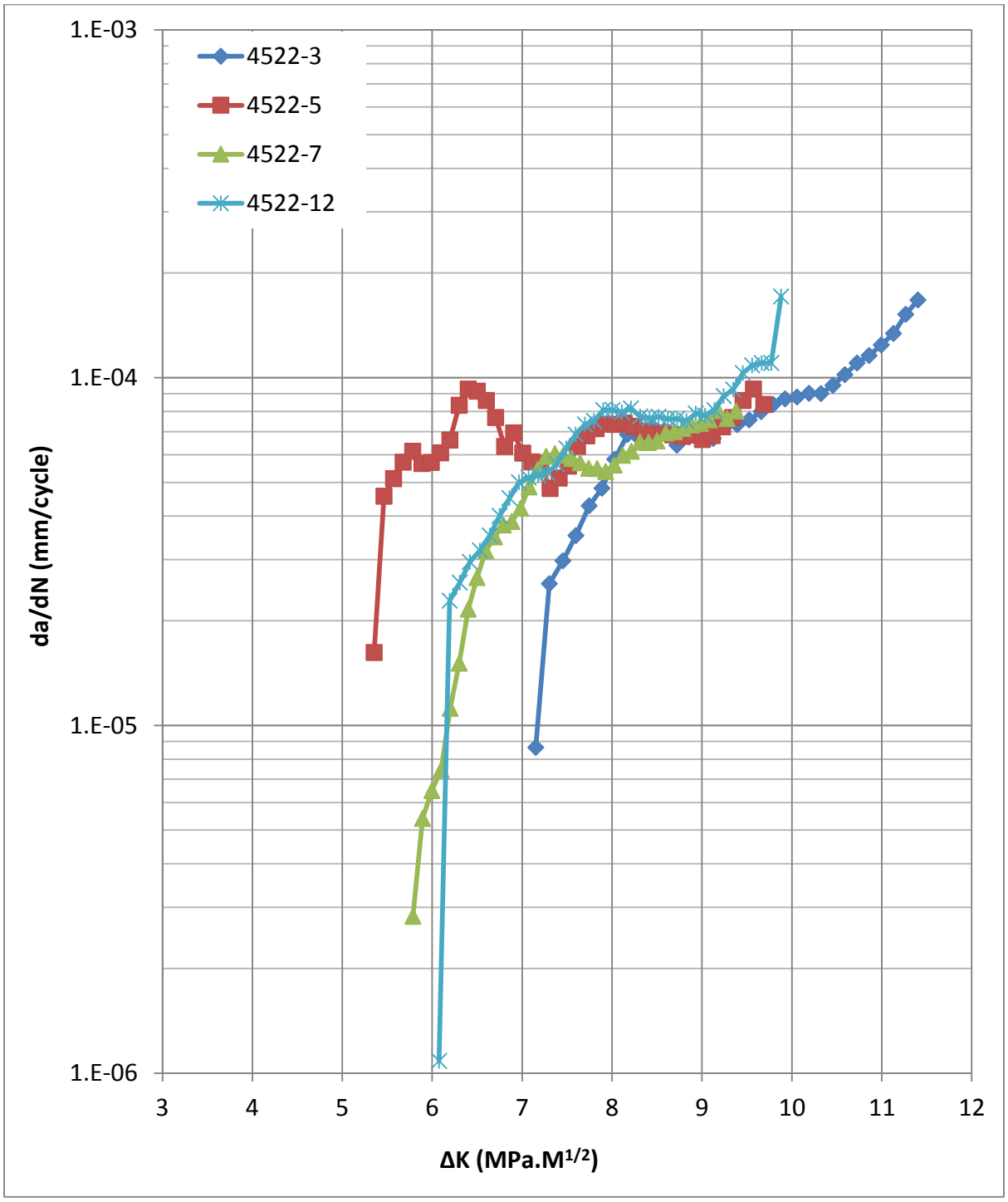

Fig.6.34 Typical fatigue crack propagation curves of Ti4522 at 650°C with R=0.1.

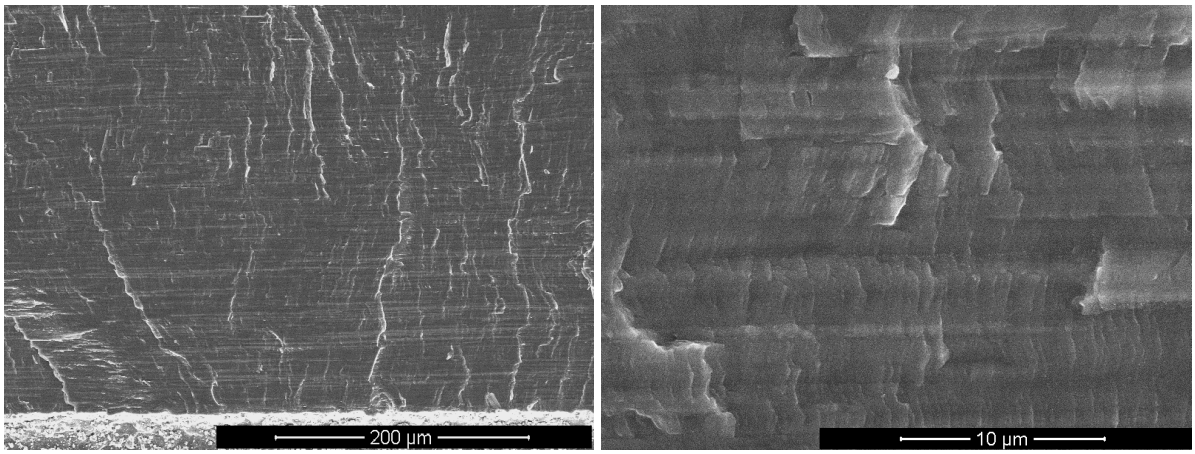

(a) (b)

Fig.6.35 SEM SE images showing the fracture surface of sample 4522-3 with 0º orientation, A-notch sub-orientation: (a) near threshold site; (b) the details of the facture surface at near threshold area.

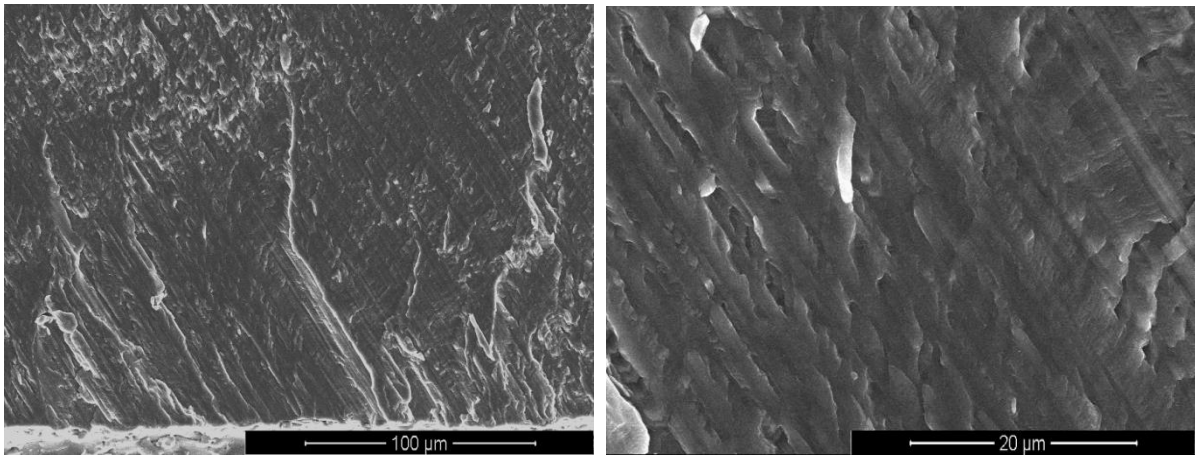

(a) (b)

Fig.6.36 SEM SE images showing the facture surfaces of samples 4522-12 with 0º orientation, A-B notch sub-orientation: (a) near threshold site; (b) the details of the facture surface at near threshold area.

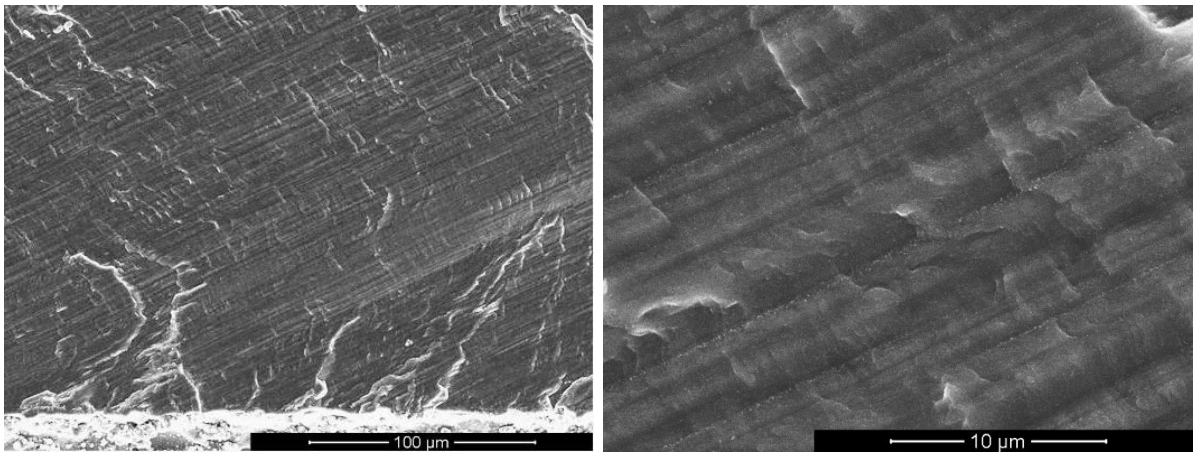

(a) (b)

Fig.6.37 SEM SE images showing the facture surfaces of samples 4522-7 with near 0º orientation, A-B notch sub-orientation: (a) near threshold site; (b) the details of the facture surface at near threshold area.

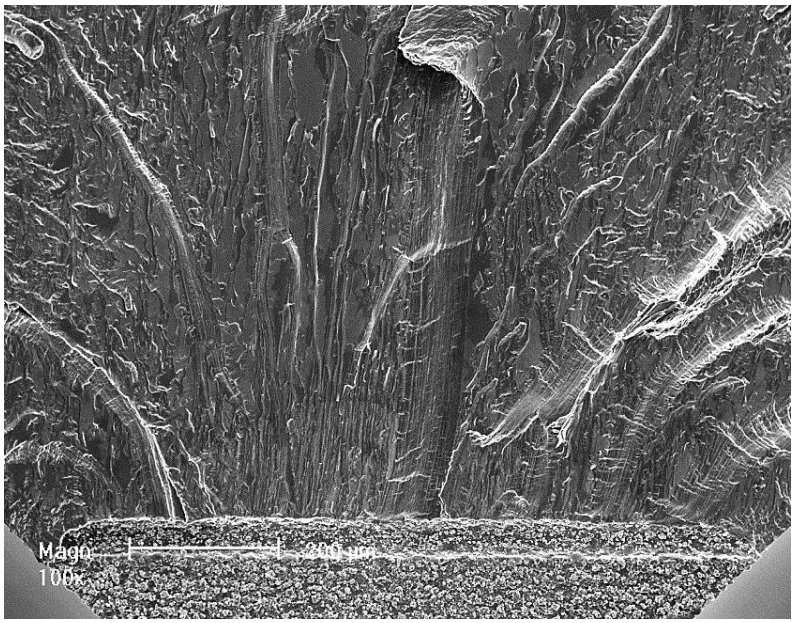

(a)

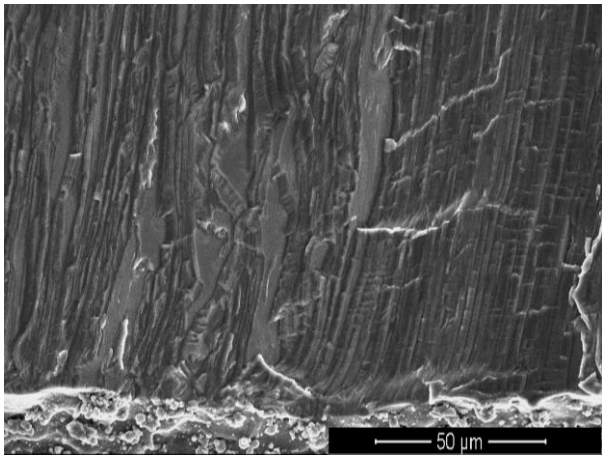

(b)

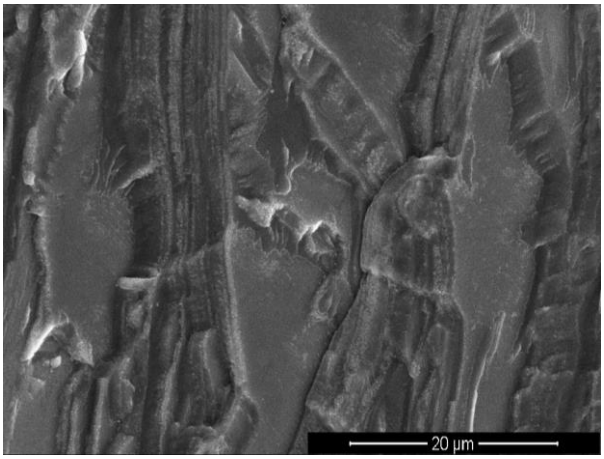

(c)

Fig.6.38 SEM SE images showing the fracture surfaces of sample 4522-5 with soft orientation: (a) the full notch area; (b) the early crack and (c) details of early cracks.

Table.6.1 Fatigue crack propagation threshold value and orientation of alloy Ti46Al8Nb

Sample No.	ΔK_{th} (MPa$\sqrt{m}$)	Orientation
468-1	6.7	Hard orientation, A-notch
468-4	7.0	Hard orientation, A-notch
468-5	4.7	Soft orientation
468-6	4.3	Soft orientation
468-7	5.4	Hard orientation, C-notch
468-8	6.5	Hard orientation, B-notch
468-9	7.2	Hard orientation, A-B notch
468-10	5.4	Soft orientation
468-12	5.3	Hard orientation, C-notch
468-15	5.0	Soft orientation
468-16	5.0	Soft orientation

Table.6.2 Fatigue crack propagation threshold value and orientation of alloy Ti46Al8Nb

Sample No.	ΔK_{th} (MPa$\sqrt{m}$)	Orientation
4522-3	7	Hard orientation, A-notch
4522-5	5.2	Soft orientation
4522-7	5.7	Hard orientation, A-B notch
4522-8	5.9	Two colonies
4522-12	6	Hard orientation, A-B notch
4522-13	5.5	Two colonies
4522-14	4.8	Two colonies
4522-15	6.5	Two colonies

Chapter 7. Conclusions and future work

This chapter gives the main conclusions of the work reported in this thesis. Several issues addressed in this work which needs further investigations and suggestions for further work are listed after the main conclusions.

7.1 Conclusions

1. The samples subjected to fatigue crack propagation threshold testing fail by interlamellar cracking and translamellar cracking at 650ºC, which is similar to failure under monotonic tensile load. The fracture behaviour is determined by both lamellar orientation and stress intensity factor range ΔK. Interlamellar cracking occurs in lamellar colonies at any lamellar orientation at high ΔK level, while that only occurs in lamellar colonies with lamellar interface parallel to the fracture plane at low ΔK level.

2. The fatigue crack propagation threshold of as-cast alloy Ti4522XD shows limited sensitivity to microstructure parameters in the studied range, such as lamellar spacing and volume faction of equiaxed gamma grains.

3. Alloying elements, Nb and Ta, have little influence on the fatigue crack propagation threshold. This may be because of their similar microstructure, all with fully lamellar microstructure, similar colony size, lamellar spacing and phase ratio of gamma phase.

4. Fatigue crack propagation threshold shows strong dependence on lamellar orientation, with alloy Ti46Al8Nb and alloy Ti4522 with coarse lamellar microstructure. The relationship

between fatigue crack propagation threshold and lamellar orientation is similar to that between yield stress and lamellar orientation. The highest threshold was obtained in the lamellar colonies with lamellar interface parallel to the loading axis while the low threshold was obtained in the colonies with an orientation about 30º-50º.

5. High Nb content, 8Nb, shows no improvement to the fatigue crack propagation threshold, compared with the alloy with 2Nb.

7.2 Future work

1. The Ti4522XD alloys with different microstructural parameters exhibited similar properties which may be due to the small difference in the microstructure. Therefore, it would be of interest to investigate the influence of microstructure at different levels.

2. The fatigue crack propagation threshold showed a strong dependence on lamellar orientation. It was considered that the threshold could be affected by the lamellar orientation through its influence on the intensity of deformation activity on the interfacial (111) plane, which needs further investigation.

3. The alloy elements, Nb and Ta, had no influence on fatigue crack propagation threshold, no matter whether the alloy was of 2Nb, 4Nb or 8Nb. Therefore, it is suggested that the fatigue properties of lamellar γ-TiAl cannot be improved by addition of Nb and Ta. However, further study is still required on the deformation behaviour with different additions.

4. Ti45Al2Nb2Ta shows much higher tensile yield strength than the other alloys, while it does not show any increase in fatigue crack propagation threshold. Thus, it may be of interest to study the deformation behaviour under monotonic tensile loading and cyclic loading.

References

1. Schulze G.E.R., *Metallphysik*. 1967. Berlin: Akademie – Verlag.

2. Kim Y.W., *Ordered Intermetallic Alloys, Part : Gamma Titanium Aluminides ///* JOM, 1994. 7: p. 30.

3. Jarvis D. J. and Voss D., *IMPRESS Integrated Project—An overview paper*. Materials Science and Engineering: A, 2005. 413–414: pp. 583-591.

4. Wu X., *Review of alloy and process development of TiAl alloys*. Intermetallics, 2006. 14(10–11): pp. 1114-1122.

5. Loria, E.A., *Quo vadis gamma titanium aluminide*. Intermetallics, 2001. 9(12): pp. 997-1001.

6. Kim Y.W., *Intermetallic alloys based on gamma titanium aluminide.* JOM, 1989. 41(7): pp. 24-30.

7. Schuster J.C. and Palm M., *Reassessment of binary aluminium-titanium phase diagram*. Journal of Phase Equilibria and Diffusion, 2006. 27(3): pp. 255-277.

8. Yamaguchi M., Inui H., and Ito K., *High-temperature structural intermetallics*. Acta Materialia, 2000. 48(1): pp. 307-322.

9. Blackburn M.J., *Some aspects of phase transformations in titanium alloys.* In: Jaffee R.I. and Promisel N, editors. The science, technology and applications of titanium, 1970: pp. 633-643.

10. Kim Y.W., *Microstructural evolution and mechanical properties of a forged gamma titanium aluminide alloy*. Acta metal.mater, 1992. 40, No.6: pp. 1121-1134.

11. Kim Y.W., *Strength and ductility in TiAl alloys*. Intermetallics, 1998. 6(7–8): pp. 623-628.

12. Cheng T.T., *The mechanism of grain refinement in TiAl alloys by boron addition — an alternative hypothesis*. Intermetallics, 2000. 8(1): pp. 29-37.

13. Hu D., Huang A. J., Novovic D., and Wu X., *The effect of boron and alpha grain size on the massive transformation in Ti–46Al–8Nb–xB alloys.* Intermetallics, 2006. 14(7): pp. 818-825.

14. Larsen D.E., Christodoulou L., Kampe S.L., and Sadler R., *Investment-cast processing of XDTM near-γ titanium aluminides*. Materials Science and Engineering: A, 1991. 144(1–2): pp. 45-49.

15. Hu D., Yang C., Huang A., Dixon M., and Hecht U., *Solidification and grain refinement in Ti45Al2Mn2Nb1B.* Intermetallics, 2012. 22: pp. 68-76.

16. Hu D., *Effect of composition on grain refinement in TiAl-based alloys*. Intermetallics, 2001. 9(12): pp. 1037-1043.

17. Yang J., Wang J.N., Wang Y., Xi Q., and Zhang B., *Control of the homogeneity of the lamellar structure of a TiAl alloy refined by heat treatment.* Intermetallics, 2001. 9(5): pp. 369-372.

18. Wang J.N. and Xie K., *Refining of coarse lamellar microstructure of TiAl alloys by rapid heat treatment.* Intermetallics, 2000. 8(5–6): pp. 545-548.

19. Yang J., Wang J.N., Xia Q., and Wang Y., *Effect of cooling rate on the grain refinement of TiAl-based alloys by rapid heat treatment.* Materials Letters, 2000. 46(4): pp. 193-197.

20. Hu D., Huang A.J., and Wu X., *On the massive phase transformation regime in TiAl alloys: The alloying effect on massive/lamellar competition.* Intermetallics, 2007. 15(3): pp. 327-332.

21. Voice W.E., Henderson M., Shelton E.F.J., and Wu X., *Gamma titanium aluminide, TNB.* Intermetallics, 2005. 13: pp. 959-964.

22. Appel F., Clemens H., and Oehring M., *Recent process in the development of gamma titanium aluminide alloys.* Advanced Engineering Materials, 2000. 2 (11): pp. 699-720.

23. Clemens H., Wallgram W., Kremmer S., Güther V., and Otto A., *Design of Novel β-Solidifying TiAl Alloys with Adjustable β/B2-Phase Fraction and Excellent Hot-Workability*. ADVANCED ENGINEERING MATERIALS, 2008. 10(8): pp. 707-713.

24. Güther V., Rothe C., Winter S., and Clemens H., Metallurgy, *Microstructure and Properties of Intermetallic TiAl Ingots*. BHM Berg- und Hüttenmännische Monatshefte, 2010. 155(7): pp. 325-329.

25. Jarvis D.J., and Voss D., *IMPRESS Integrated Project – An overview paper.* Materials Science and Engineering: A, 2005. 413-414: pp. 583-591.

26. Lapin J., TiAl-based alloys: *present status and future perspectives*. Metals, 2009. 19-21(5): pp. 1-12.

27. Yoshihara M. and Miura K., *Effects of Nb addition on oxidation behavior of TiAl.* Intermetallics, 1995. 3(5): pp. 357-363.

28. Tsuyama S., Mitao S., and Minakawa K., *Alloy modification of γ-base titanium aluminide for improved oxidation resistance, creep strength and fracture toughness.* Materials Science and Engineering: A, 1992. 153(1–2): pp. 451-456.

29. Shida Y. and Anada H., *The influence of ternary element addition on the oxidation behaviour of TiAl intermetallic compound in high temperature air.* Corrosion Science, 1993. 35(5–8): pp. 945-953.

30. Kawabata T., Tamura T., and Izumi O., *Effect of Ti/Al ratio and Cr, Nb, and Hf additions on material factors and mechanical properties in TiAl.* Metallurgical Transactions A, 1993. 24(1): pp. 141-150.

31. Pérez P., Haanappel V. A. C., and Stroosnijder M. F., *The effect of niobium on the oxidation behaviour of titanium in N_2/20% O_2 atmospheres.* Materials Science and Engineering: A, 2000. 284(1–2): pp. 126-137.

32. Lin J.P., Zhao L.L., Li G.Y., Zhang L.Q., Song X.P., Ye F., and Chen G.L., *Effect of Nb on oxidation behavior of high Nb containing TiAl alloys.* Intermetallics, 2011. 19(2): pp. 131-136.

33. Jiang H., Hirohasi M., Lu Y., and Imanari H., *Effect of Nb on the high temperature oxidation of Ti–(0–50 at.%)Al.* Scripta Materialia, 2002. 46(9): pp. 639-643.

34. McKee D.W. and Huang S.C., *The oxidation behavior of gamma-titanium aluminide alloys under thermal cycling conditions.* Corrosion Science, 1992. 33: pp. 1899-1914.

35. Zhang W.J. and Appel F., *Effect of Al content and Nb addition on the strength and fault energy of TiAl alloys*. Materials Science and Engineering: A, 2002. 329–331: pp. 649-652.

36. Liu Z.C., Lin J.P., Li S.J., and Chen G.L., *Effects of Nb and Al on the microstructures and mechanical properties of high Nb containing TiAl base alloys*. Intermetallics, 2002. 10(7): pp. 653-659.

37. Appel F., Oehring M., and Wagner R., *Novel design concepts for gamma-base titanium aluminide alloys.* Intermetallics, 2000. 8(9–11): pp. 1283-1312.

38. Tsujimoto T., Hashimoto K., and Nobuki M., *Alloy design for improvement of ductility and workability of alloys based on intermetallic compound TiAl*. Materials Transactions, JIM, 1992. 33(11): pp. 989-1003.

39. Yamaguchi M. and Inui H., *TiAl compounds for structural applications*. In Darolia R., Lewandoski J.J., Liu C.T., Martin P.L., Miracle D.B., Nathal M.V., editors. Structural Intermetallics. Warrendale (PA): TMS: 1993: pp. 127-142.

40. Huang S.C., *Microstructures and property Tradeoffs in Wrought TiAl-Base Alloys.* Metallurgical Transactions A, 1992. 23A: pp. 375-377.

41. Qiu, C.Z., Liu Y., Huang L., Liu B., Zhang W., He Y.H., and Huang BY., *Tuning mechanical properties for β(B2)-containing TiAl intermetallics.* Transactions of Nonferrous Metals Society of China, 2012. 22(11): pp. 2593-2603.

42. Larson E., *Effects of XD^{TM} TiB_2 volume fraction on the microstructure of a cast near-gamma titanium aluminide alloy.* MRS Symposium R, 1990. 194(Spring): pp. 285-294.

43. Inkson B.J., Boothroyd C.B., and Humphreys C.J., *Boron segregation in a (Fe, V, B) TiAl based alloy.* J. Phys. IV France, 1993. 3: pp. 397-402.

44. Godfrey A.B., *Grain refinement of a gamma-based titanium aluminide using microalloy additions.* in the School of Metallurgy and Materials, 1996. The University of Birmingham: Birmingham, UK.

45. Hu D., *Effect of boron addition on tensile ductility in lamellar TiAl alloys.* Intermetallics, 2002. 10(9): pp. 851-858.

46. Kawabata T., Tadano M., and Izumi O., *Effect of Carbon and Nitrogen on Mechanical Properties of TiAl Alloys.* ISIJ International, 1991. 31(10): pp. 1131-1167.

47. Park H.S., Nam S.W., Kim N.J., and Hwang S.K., *Refinement of the lamellar structure in TiAl-BASED intermetallic compound by addition of carbon.* Scripta Materialia, 1999. 41(11): pp. 1197-1203.

48. Loiseau A. and Lasalmonie A., *Influence of the thermal stability of TiAl on its creep behaviour at high temperatures.* Materials Science and Engineering, 1984. 67(2): pp. 163-168.

49. Umakoshi Y., Nakano T., and Yamane T., *The effect of orientation and lamellar structure on the plastic behavior of TiAl crystals.* Materials Science and Engineering: A, 1992. 152(1–2): pp. 81-88.

50. Lin, D., Wang, Y., Liu, J., and Law, C.C., *The effects of temperature, strain rate and minor boron on tensile properties of wrought Ti-47Al-2Mn-2Nb alloy*. Intermetallics, 2000. 8(5-6): pp. 549-558.

51. Appel F. and Wagner R., *Microstructure and deformation of two-phase γ-titanium aluminides.* Materials Science and Engineering: R: Reports, 1998. 22(5): pp. 187-268.

52. Mercer C. and Soboyejo W.O., *Fatigue crack growth in cast gamma titanium aluminides.* Acta Materialia, 1997. 45(10): pp. 4385-4396.

53. Liu C.T., Schneibel J.H., Maziasz P.J., Wright J.L., and Easton D.S., *Tensile properties and fracture toughness of TiAl alloys with controlled microstructures*. Intermetallics, 1996. 4(6): pp. 429-440.

54. Cheng T.T., Willis M R., and Jones I.P., *Effects of major alloying additions on the microstructure and mechanical properties of γ-TiAl.* Intermetallics, 1999. 7(1): pp. 89-99.

55. Zhang W.J., Deevi S.C., and Chen G.L., *On the origin of superior high strength of Ti–45Al–10Nb alloys.* Intermetallics, 2002. 10(5): pp. 403-406.

56. Kim Y.W. and Dimiduk D.M., *Process in the understanding of gamma titanium aluminides.* JOM, 1991 (August): pp. 40-47.

57. Maruyama K., Takahashi T., and Oikawa H., *Different origins of grain size and composition effects on creep in TiAl.* Materials Science and Engineering: A, 1992. 153(1–2): pp. 433-437.

58. Maruyama K., Yamamoto R., Nakakuki H., and Fujitsuna N., *Effects of lamellar spacing, volume fraction and grain size on creep strength of fully lamellar TiAl alloys.* Materials Science and Engineering: A, 1997. 239–240: pp. 419-428.

59. Takahashi T., Nagai H., and Oikawa H., *Effects of grain size on creep behaviour of Ti-50 mol.%Al intermetallic compound at 1100 K*. Materials Science and Engineering: A, 1990. 128(2): pp. 195-200.

60. Zhu H., Seo D.Y., Maruyama K., and Au P., *Effect of microstructure on creep deformation of 45XD TiAl alloy at low and high stresses*. Materials Science and Engineering: A, 2008. 483–484: pp. 533-536.

61. Beddoes J., Wallace W., and Zhao L., *Current understanding of creep behaviour of near γ-titanium aluminides.* International Materials Reviews, 1995. 40(5): pp. 197-217(21).

62. Es-Souni M., Bartels A., and Wagner R., *Creep behaviour of near γ-TiAl base alloys: Effects of microstructure and alloy composition.* Materials Science and Engineering: A, 1995. 192–193, Part 2: pp. 698-706.

63. Appel F., Christoph U., and Oehring M., *Creep deformation in two-phase titanium aluminide alloys*. Materials Science and Engineering: A, 2002. 329–331: pp. 780-787.

64. Chen W.R., Triantafillou J., Beddoes J., and Zhao L., *Effect of fully lamellar morphology on creep of a near γ-TiAl intermetallic*. Intermetallics, 1999. 7(2): pp. 171-178.

65. Kim B.G., Kim G.M., and Kim C.J., *Oxidation behavior of TiAl-X (X = Cr, V, Si, Mo or Nb) intermetallics at elevated temperature*. Scripta Metallurgica et Materialia, 1995. 33(7): pp. 1117-1125.

66. Yang R., Cui Y.Y., Dong L.M., and Jia Q., *Alloy development and shell mould casting of gamma TiAl.* Journal of Materials Processing Technology, 2003. 135(2–3): pp. 179-188.

67. Meier G.H. and Pettit F.S., *The oxidation behavior of intermetallic compounds.* Materials Science and Engineering: A, 1992. 153(1–2): pp. 548-560.

68. Rakowski J.M., Pettit F.S., Meier G.H., Dettenwanger F., Schumann E., and Ruhle M., *The effect of nitrogen on the oxidation of γ-TiAl.* Scripta Metallurgica et Materialia, 1995. 33(6): pp. 997-1003.

69. Rakowski J.M., Meier G.H., Pettit F.S., Dettenwanger F., Schumann E., and Rühle M., *The effect of surface preparation on the oxidation behavior of gamma TiAl-base intermetallic alloys*. Scripta Materialia, 1996. 35(12): pp. 1417-1422.

70. Gil A., Hoven H., Wallura E., and Quadakkers W.J., *The effect of microstructure on the oxidation behaviour of TiAl-based intermetallics*. Corrosion Science, 1993. 34(4): pp. 615-630.

71. Maurice V., Despert G., Zanna S., Josso P., Bacos M.P., and Marcus P., *XPS study of the initial stages of oxidation of α_2-Ti_3Al and γ-TiAl intermetallic alloys.* Acta Materialia, 2007. 55(10): pp. 3315-3325.

72. Bacos, M.P., Morel, A., Naveos, S., Bachelier-locq, A., Josso, P., and Thomas, M., *The effect of long term exposure in oxidising and corroding environments on the tensile properties of two gamma-TiAl alloys.* Intermetallics, 2006. 14(1): pp. 102-113.

73. Draper S L., Lerch B.A., Locci I.E., Shazly M., and Prakash V., *Effect of exposure on the mechanical properties of Gamma MET PX.* Intermetallics, 2005. 13(9): pp. 1014-1019.

74. Sun C.T. and Jin Z.-H., *Fracture mechanics.* 2012: Academic Press

75. Griffith A.A., *The phenomena of rupture and flow in solids*. Philosophical Transactions of the Royal Society of London,. Vol.221, no. 587 A. Mathematical and Physical Sciences ;. 1920, London: Harrison.

76. http://en.wikipedia.org/wiki/Stress_intensity_factor.

77. Ewalds H.L. and Wanhill R.J.H. *Fracture mechanics*. 1984, London: Edward Arnold.

78. Suresh S., *Fatigue of materials*. 2nd Edition ed. 1998, Cambridge: Cambridge University Press.

79. Zhu S.J., Peng L.M., Moriya T., and Mutoh Y., *Effect of stress ratio on fatigue crack growth in TiAl intermetallics at room and elevated temperatures*. Materials Science and Engineering: A, 2000. 290(1–2): pp. 198-206.

80. Donahue R.J., Clark H.M., Atanmo P., Kumble R., and McEvily A.J., *Crack opening displacement and the rate of fatigue crack growth*. International Journal of Fracture Mechanics, 1972. 8(2): pp. 209-219.

81. Soboyejo W.O., Deffeyes J.E., and Aswath P.B., *Investigation of room- and elevated-temperature fatigue crack growth in Ti-48Al.* Materials Science and Engineering: A, 1991. 138(1): pp. 95-101.

82. Bowen P., Chave R.A., and James A.W., *Cyclic crack growth in titanium aluminides*. Materials Science and Engineering: A, 1995. 192–193, Part 1: pp. 443-456.

83. James A.W. and Bowen P., *Elevated temperature crack growth resistance of TiAl under monotonic and cyclic loading.* Materials Science and Engineering: A, 1992. 153(1–2): pp. 486-492.

84. Tsutsumi M., Takano S., Kitamura T., and Ohtani R., *Fatigue crack propagation in a cast TiAl intermetallic compound at high temperature*. Intermetallics, 1996. 4, Supplement 1: pp. S77-S83.

85. Campbell J.P., Rao K.T.V., and Ritchie R.O., *On the role of microstructure in fatigue-crack growth of γ-based titanium aluminides.* Materials Science and Engineering: A, 1997. 239–240: pp. 722-728.

86. Kruzic J.J., Campbell J.P., and Ritchie R.O., *On the fatigue behavior of γ-based titanium aluminides: role of small cracks.* Acta Materialia, 1999. 47(3): pp. 801-816.

87. Pippan R., Hageneder P., Knabl W., Clemens H., Hebesberger T., and Tabernig B., *Fatigue threshold and crack propagation in γ-TiAl sheets.* Intermetallics, 2001. 9(1): pp. 89-96.

88. Filippini M., Beretta S., Patriarca L., Pasquero G., and Sabbadini S., *Defect tolerance of a gamma titanium aluminide alloy.* Procedia Engineering, 2011. 10: pp. 3677-3682.

89. Hénaff G. and Gloanec A., *Fatigue properties of TiAl alloys*. Intermetallics, 2005. 13(5): pp. 543-558.

90. Mine Y., Takashima K., and Bowen P., *Effect of lamellar spacing on fatigue crack growth behaviour of a TiAl-based aluminide with lamellar microstructure.* Materials Science and Engineering: A, 2012. 532: pp. 13-20.

91. Choi C., Kim H.J., Lee Y., Kim Y.W., and Lee C.S., *Effects of microstructural parameters on the fatigue crack growth of fully lamellar γ-TiAl alloys.* Materials Science and Engineering: A, 2002. 329–331: pp. 545-556.

92. Shiota H., Tokaji K., and Ohta Y., *Influence of lamellar orientation on fatigue crack propagation behavior in titanium aluminide TiAl.* Materials Science and Engineering: A, 1998. 243(1–2): pp. 169-175.

93. RITCHIE R.O., *Mechanisms of fatigue-crack propagation in ductile and brittle solids.* International Journal of Fracture, 1999. 100: pp. 55-83.

94. Worth B.D., Larsen J.M., Balsone S.J., and Jones J.W., *Mechanisms of ambient temperature fatigue crack growth in Ti-46.5Al-3Nb-2Cr-0.2W.* Metallurgical and Materials Transactions A, 1997. 28(3): pp. 825-835.

95. Venkateswara Rao K.T., Kim Y.W., Muhlstein C.L., and Ritchie R.O., *Fatigue-crack growth and fracture resistance of a two-phase (γ + α2) TiAl alloy in duplex and lamellar microstructures.* Materials Science and Engineering: A, 1995. 192–193, Part 1: pp. 474-482.

96. Sadananda K. and Vasudevan A.K., *Fatigue crack growth behaviour in titanium aluminides.* Materials Science and Engineering: A, 1995. 192–193, Part 1: pp. 490-501.

97. Balsone S.J., Larsen J.M., Maxwell D.C., and Jones J.W., *Effects of microstructure and temperature on fatigue crack growth in the TiAl alloy Ti-46.5Al-3Nb-2Cr-0.2W.* Materials Science and Engineering: A, 1995. 192–193, Part 1: pp. 457-464.

98. Mutoh Y., Zhu S.J., Hansson T., Kurai S., and Mizuhara Y., *Effect of microstructure on fatigue crack growth in TiAl intermetallics at elevated temperature.* Materials Science and Engineering: A, 2002. 323(1–2): pp. 62-69.

99. Larsen J.M., Worth B.D., Balsone S.J., and Jones J.W., *An overview of the structural capability of available gamma titanium aluminide alloys*. In: Kim Y.W. and Wagner R, editors. Gamma titanium alumides. Warrendale (PA): (TMS): 1995. pp. 821-834.

100. Liu C.T., Maziasz P.J., Clemens D.R., and Schneibel J.H., *Room and elebated temperature mechanical properties of a PM TiAl alloy Ti-47Al-2Cr-2Nb* In: Kim Y.W. and Wagner R, editors. Gamma titanium alumides. Warrendale (PA): (TMS): 1995. pp. 679-688.

101. Balsone S.J., Worth B.D., Larsen J.M., and Jones J.W., *Fractographic study of fatigue crack growth processes in a fully lamellar γ-tiAl alloy.* Scripta Metallurgica et Materialia, 1995. 32(10): pp. 1653-1658.

102. Kong M.C., Axinte D., and Voice W., *Aspects of material removal mechanism in plain waterjet milling on gamma titanium aluminide.* Journal of Materials Processing Technology, 2010. 210(3): pp. 573-584.

103. Cao R., Li L., Chen J.H., and Zhang J., *Study on compression deformation, damage and fracture behavior of TiAl alloys: Part II. Fracture behavior.* Materials Science and Engineering: A, 2010. 527(10–11): pp. 2468-2477.

104. Zheng R.T., Zhang Y.G., and Chen C.Q., *Microcrack nucleation and its effect on the plastic deformation of FL γ-TiAl alloy.* Journal of Materials Science, 2004. 39(5): pp. 1721-1725.

105. Huang Z. W., Bowen P., Davey S., and Blenkinsop P.A., *Crystallographic Features of Intralamellar Fracture in a Fully Lamellar TiAl Based Alloy.* Scripta Materialia, 1998. 38(7): pp. 1117-1123.

106. Chan K.S. and Kim Y.W., *Effects of lamellae spacing and colony size on the fracture resistance of a fully-lamellar TiAl alloy*. Acta Metallurgica et Materialia, 1995. 43(2): pp. 439-451.

107. Umakoshi Y., Yasuda H.Y., and Nakano T., *Plastic anisotropy and fracture behavior of cyclically deformed TiAl polysynthetically twinned crystals.* Materials Science and Engineering: A, 1995. 192–193, Part 1: pp. 511-517.

108. Yokoshima S. and Yamaguchi M., *Fracture behavior and toughness of PST crystals of TiAl.* Acta Materialia, 1996. 44(3): pp. 873-883.

109. Inui H., Oh M.H., Nakamura A., and Yamaguchi M., *Room-temperature tensile deformation of polysynthetically twinned (PST) crystals of TiAl.* Acta Metallurgica et Materialia, 1992. 40(11): pp. 3095-3104.

110. Kishida K., Inui H., and Yamaguchi M., *Deformation of lamellar structure in TiAl-Ti3Al two-phase alloys.* PHILOSOPHICAL MAGAZINE A, 1998. 78(1): pp. 1-28.

111. Hénaff G., Bittar B., Mabru C., Petit J., and Bowen P., *Fatigue crack propagation resistance of a Ti48Al2Mn2Nb alloy in the as-cast condition.* Materials Science and Engineering: A, 1996. 219(1–2): pp. 212-220.

112. Wissuchek D.J., Lucas G.E., and Evans A.G., *The effects of lamellar orientation and bridging ligaments on fracture and fatigue of fully lamellar Ti-48Al-2Cr-2Nb* In: Kim Y.W. and Wagner R, editors. Gamma titanium alumides. Warrendale (PA): (TMS): 1995. pp. 875-882.

113. Huang Z.W., Bowen P., and Jones I.P., *Transmission electron microscopy investigation of fatigue crack tip plastic zones in a polycrystalline γ-TiAl-based alloy.* Phil Mag, 2001. 81(9): pp. 2183-2197.

114. Lu Y.H., Zhang Y.G., Qiao L.J., Wang Y B., Chen C Q., and Chu W.Y., *In-situ TEM study of fracture mechanisms of polysynthetically twinned (PST) crystals of TiAl alloys.* Materials Science and Engineering: A, 2000. 289(1–2): pp. 91-98.

115. Yao K., Xiao J., and Zhang J., *In-situ deformation of TiAl PST crystals in TEM.* Intermetallics, 2000. 8(5–6): pp. 569-573.

116. Chen M. and Lin D., *The influence of lamellar structure on crack propagation in tow-phase TIAl alloys.* In: Kim Y.W. and Wagner R, editors. Gamma titanium alumides. Warrendale (PA): (TMS): 1995. pp. 903-912.

117. Nakano T. and Umakoshi Y., *Effect of boron addition on the plastic behaviour of polysynthetically twinned crystals of TiAl.* Intermetallics, 1994. 2(3): pp. 185-191.

118. US Patent 4915903, Process For Forming Composites Having An Intermetallic Containing Matrix. 1990.

119. Jeon J H., Godfrey A.B., Blenkinsop P.A., Voice W., and Hahn Y.D., *Recrystallization in cast 45-2-2 XD™ titanium aluminide during hot isostatic pressing.* Materials Science and Engineering: A, 1999. 271(1–2): pp. 128-133.

120. Wayne V., *The future use of gamma titanium aluminides by Rolls-Royce.* Aircraft Engineering and Aerospace Technology, 1999. 71.4: pp. 337.

121. Roth M. and Biermann H., *Thermomechanical Fatigue Behavior of the Intermetallic γ-TiAl Alloy TNB-V5 with Different Microstructures.* Metallurgical and Materials Transactions A, 2010. 41(3): pp. 717-726.

122. Zhou Y., Wang J.Q., Zhang B., Ke W., and Han E.H., *High-temperature fatigue property of Ti46Al8Nb alloy with the fully lamellar microstructure*. Intermetallics, 2012. 24: pp. 7-14.

123. Tetsui T., *Effects of high niobium addition on the mechanical properties and high-temperature deformability of gamma TiAl alloy*. Intermetallics, 2002. 10(3): pp. 239-245.

124. Hu D., Huang A., Jiang H., Mota-Solis N., and Wu X., *Pre-yielding and pre-yield cracking in TiAl-based alloys.* Intermetallics, 2006. 14(1): pp. 82-90.

125. Wu X., Jiang H., Huang A., Hu D., Mota-Solis N., and Loretto M.H., *Microstructural study of pre-yielding and pre-yield cracking in TiAl-based alloys*. Intermetallics, 2006. 14(1): pp. 91-101.

126. Hu D. and Loretto M.H., *Slip transfer between lamellae in fully lamellar TiAl alloys*. Intermetallics, 1999. 7(11): pp. 1299-1306.

127. James A.W., University of Birmingham, PhD thesis 1996.

128. Chan K.S. and Shih D.S., *Fundamental aspects of fatigue and fracture in a TiAl sheet alloy*. Metallurgical and Materials Transactions A, 1998. 29(1): pp. 73-87.

129. Hu D., Jiang H., and Wu X., *Microstructure and tensile properties of cast Ti-44Al-4Nb-4Hf-0.1Si-0.1B alloy with refined lamellar microstructures*. Intermetallics, 2009. 17(9): pp. 744-748.

130. Simkin B.A., Ng B.C., Crimp M.A., and Bieler T.R., *Crack opening due to deformation twin shear at grain boundaries in near-γ TiAl.* Intermetallics, 2007. 15(1): pp. 55-60.

Published work

1. Yang J., Li H., Hu D., and Dixon M., *Microstructural Characterisation of Fatigue Fracture Surfaces of a Lamellar TiAl Alloy.* Intermetallics, 2014. 45: pp. 89-95.
2. Yang J., Li H., Hu D., Martin N., and Dixon M., *Lamellar orientation effect on fatigue crack propagation threshold in coarse-grained Ti46Al8Nb.* Materials Science and Technology, 2014. 30(15): pp. 1905-1910.